Hydrogen dynamics in solids : quantum diffusion and plastic phase transition in hydrates under pressure

Niccolo Avallone

PhD Thesis

Doctoral School 397

Physics and Chemistry of Materials

Hydrogen dynamics in solids: quantum diffusion and plastic phase transition in hydrates under pressure

---

To obtain the title of

PhD of Sorbonne Université

defended by

Niccolò Avallone

on December 15^{th}, 2023

Prepared at Institut des NanoSciences de Paris

funded by Institut des Sciences du Calcul et des Données

under the supervision of Fabio Finocchi *and* Riccardo Spezia

Jury

Reviewers	Paola Gallo	Università degli Studi Roma Tre
	Grégory Geneste	CEA DAM
Examiners	Livia Bove	Sorbonne Université, CRNS, EPFL
	Fausto Martelli	IBM Research Europe
Advisor	Fabio Finocchi	Sorbonne Université, CRNS
Co-Advisor	Riccardo Spezia	Sorbonne Université, CNRS

Contents

Table of Contents ii

1 Introduction 1
- 1.0.1 Nuclear quantum effects, phase transitions and hydrogen bonds . . 2
- 1.0.2 Hydrogen diffusion and super-ionic phases . . . 3
- 1.0.3 Ammonia hydrates under pressure . . . 4
- 1.0.4 Plastic crystals and disordered molecular alloys . . . 5
- 1.0.5 Ammonia Hemi-Hydrates under pressure . . . 7
- 1.0.6 Structure of the manuscript . . . 8

2 Langevin-based molecular dynamics methods for nuclear dynamics 11
- 2.1 Born-Oppenheimer approximation . . . 13
  - 2.1.1 Potential energy surface . . . 14
- 2.2 Molecular Dyamics methods . . . 17
  - 2.2.1 Integration of Newton's second law . . . 18
- 2.3 Classical Langevin Thermostat . . . 20
  - 2.3.1 Canonical sampling via Langevin equation . . . 20
  - 2.3.2 Integration of equations of motion via Langevin MD . . . 21
  - 2.3.3 Classical Langevin barostat . . . 22
- 2.4 Path Integral Molecular Dynamics . . . 25
  - 2.4.1 Path Integral formalism . . . 25
  - 2.4.2 Path Integral Molecular Dynamics for statistical properties . . . 26
  - 2.4.3 Ring-Polymer Molecular Dynamics . . . 28
  - 2.4.4 Nuclear quantum effects in RPMD . . . 30
  - 2.4.5 The RPMD estimators of energy and pressure . . . 31
  - 2.4.6 Integration of the equations of motion in RPMD . . . 32
- 2.5 Quantum Thermal Bath . . . 32
- 2.6 Adaptive Quantum Thermal Bath . . . 35
  - 2.6.1 Zero-Point Energy Leakage . . . 35
  - 2.6.2 Adaptation routine of adQTB . . . 36
- 2.7 Path-integral Quantum Thermal Bath . . . 37
- 2.8 Conclusion: where the methods are used in this work . . . 41
- Appendix . . . 42
  - A Liouville operator formalism . . . 42
  - B Harmonic Analysis of Stationary Stochastic Processes . . . 43

3 Nuclear Quantum Effects on hydrogen diffusion: a model study 45
- 3.1 Diffusion in solids . . . 47
  - 3.1.1 Brownian motion and the Langevin equation . . . 47
  - 3.1.2 Particle in an external potential . . . 49
- 3.2 Exactly solvable model . . . 50
  - 3.2.1 Sum-over-states method . . . 50
  - 3.2.2 Free particle . . . 51
  - 3.2.3 Particle in a fixed periodic lattice . . . 53
- 3.3 Hydrogen diffusion in a 2D lattice . . . 54

3.3.1 Model systems . . . 55
3.3.2 Simulation setup of MD-based methods . . . 57
3.3.3 Diffusion coefficient in a fixed lattice: quantum vs. classical . . . 58
3.3.4 Quantum Thermal Bath: a critical analysis . . . 61
3.3.5 Path-Integral Quantum Thermal Bath: a possible compromise? . . . 66
3.4 Isotope effect . . . 69
3.5 Diffusion in flexible lattice . . . 71
3.6 Conclusions . . . 71
Appendix . . . 73
A Quantum diffusion coefficient calculations . . . 73
B Diffusion coefficient tables . . . 74
C Diffusion events and friction dependence . . . 74
D Zero-point-energy leakage correction . . . 77

4 Plastic phase of Ammonia Hemi-Hydrate 81
4.1 Molecular dynamics simulations setup . . . 83
4.1.1 Description of the input AHH-II structure . . . 83
4.1.2 Computational details of MD-based methods . . . 85
4.2 Thermodynamics . . . 87
4.2.1 Establishing the phase transition . . . 87
4.2.2 Structural properties: structure factors and pair distribution functions 90
4.2.3 Evolution of the hydrogen bond network . . . 98
4.2.4 Discussion of thermodynamics results . . . 102
4.3 Dynamical characterization of the AHH plastic phase . . . 103
4.3.1 Hydrogen bonds lifetimes . . . 103
4.3.2 Molecule dipoles rotations . . . 106
4.3.3 Hydrogen rotations and molecular diffusion . . . 108
4.3.4 Formation of the disordered molecular alloy . . . 112
4.4 Addition of Nuclear Quantum Effects . . . 116
4.4.1 Intermediate ordered structure of AHH-II . . . 118
4.5 General conclusions . . . 122
Appendix I . . . 124
A Metastability and simulation times . . . 124
B Comparison between quantum MD methods . . . 127
Appendix II: simulations beyond P=6GPa . . . 129
C Compression at 300K . . . 131
D Compression at 500K . . . 132
E Cooling at 18GPa and decompressing at 300K . . . 135
F Tables . . . 137

Conclusions 141

Bibliography 158

Chapter 1

Introduction

This work is a theoretical investigation of quantum dynamical properties of hydrogen-rich solid materials, focusing in particular on hydrogen diffusion and plastic phase transitions in hydrogen bonded systems, such as water and ammonia mixtures.

The first part of the thesis aim at assessing different approximate molecular dynamics method to compute the diffusion coefficient of protons/hydrogen atoms moving in a solid material. This problem is far from being trivial if we take into account the quantum nature of the protons. Indeed, although the laws of quantum mechanics offer a complete and exact solution to the problem, the impossibility of solving the many-body quantum dynamics analytically for realistic systems poses numerical and theoretical issues. Our approach was to create a quantum diffusion model which can be solved analytically and use it as a controlled playground to test different molecular dynamics techniques. Although we could not find a definitive solution to the problem, we are now able to assess more precisely the advantages and the limits of each method.

The second part of the work focuses on the properties of water and ammonia mixtures, known as ammonia hydrates, at high pressure. Ammonia hydrates are notably hydrogen-rich systems, whose solid structure is based on intermolecular hydrogen bonds. We were able to access measured observables via to a collaboration with an experimental group at Sorbonne University, and we were asked to find a theoretical explanations of the complex phase transitions occurring in this systems. Thus, we set up a simulation framework accounting for a large number (above 10^5) of atoms for times of tens of nanosecond per trajectory. From the analysis of the molecular dynamics data, we are able to explain the crystal-plastic transition mechanism in the P-T range of [300K-600K] and [2GP-10GPa], which might be a cornerstone for further investigations of the entirety of solid hydrates at high pressure.

In the following Sections, we give a brief account of the complex phenomena we have to deal with in our theoretical investigation of quantum hydrogen diffusion and plastic phase transitions in hydrates at high pressure.

1.0.1 Nuclear quantum effects, phase transitions and hydrogen bonds

The major theoretical challenge in condensed matter physics is the impossibility to solve the Schrödinger equation for a large number of degrees of freedom. A first step to deal with complex quantum multi-atomic systems can be to adiabatically decouple the electronic and nuclei degrees of freedom (Born-Oppenheimer approximation). Once the electronic ground state energy is determined with the nuclei at rest, the latter, because of their heavier mass, are often considered as classical objects following Newton's laws of motion. This classical representation of the atomic nuclei allows to dramatically simplify the calculations and it provides satisfactory results for heavy atoms. However, at low temperatures or when light atoms are considered, the classical framework cannot provide an exhaustive description of microscopic phenomena. Indeed, the nuclei can show several purely quantum properties, known as Nuclear Quantum Effects (NQEs) [1]. Note that there is no general classification of light and heavy nuclei, but, in order to have an approximate idea of the importance of NQEs, it is possible to consider the de Broglie thermal wavelength

$$\lambda_B = \frac{h}{\sqrt{2\pi m k_B T}} \tag{1.1}$$

where k_B is the Boltzmann constant, T the temperature, m the mass of the particle and h the Planck constant. If λ_B is of the order of the characteristic length scale of the system, the quantum nature of the nuclei cannot be neglected. Experimental evidences of NQEs have shown that they are present not only in typical quantum regimes, such as at low temperature [2], or in extreme conditions, as high pressure [3], but also surprisingly close to ambient conditions, as in the case of reactions involving proton transfer [4] or displaying isotopic effects [5, 6].

Moreover, NQEs are necessary to accurately reproduce the phase diagram of some materials, such as ferroelectric crystals like $BaTiO_3$ [7] or pure water [8]. Indeed, ice presents many exotic phases under pressure, which can be observed for examples on planets inside [9] and outside [10] our Solar system. Let us consider an example more in details [3, 11]. Ice under pressure has a quantum-driven phase transition between the so-called phase VII and the phase X. In the former, ice has a cubic structure with disordered hydrogen bonding. As pressure increases to 65GPa, Raman and infrared spectra show a transition towards the more symmetric phase X. At the atomic scale, simulations show that the distance d_{OO} between oxygen atoms decreases with pressure up to the point it becomes impossible to define a convalent and a H-bond, but the hydrogen sits in the middle of the OO distance. Analogous quantum-driven phase transitions can be observed in salty ice as well [6].

The standard definition of an hydrogen bond is an inter-molecular, non-covalent interaction between a strongly polar donor-hydrogen (DH) group and another electronegative atom, called acceptor (A). As a general notation in this work, any hydrogen bond denoted as DH$\cdots$A. Typical elements forming hydrogen bonds are nitrogen, oxygen or fluorine; they can be homonunclear or heteronuclear; DA distances span a range between 2.5-3.3Å, shorter by about 1Å than the typical distances of Van der Waals bonds. Moreover, hydrogen bonds are directional: on the donor side, hydrogen bonds generally favor the linearity, which distinguishes them from Van der Waals interactions. Therefore, not only elongation or compression of distances, but also distortions to the directionality of the bond could

result in its weakening and breaking. Hydrogen bond energies span from about -0.2 kcal mol^{-1} to -40 kcal mol^{-1} [12]. The strength of a bond depends on the nature of the donor and the acceptor, the distance d_{HA}, the angle θ_{DHA}, the local environment and back-bonds. The two order of magnitudes of possible energies add depth to the already complex picture given by hydrogen bonds to crystal and biological systems. Indeed, strong hydrogen bonds could be of comparable strength of covalent interactions, whereas weak hydrogen bonds could contribute less than Van der Waals interactions to the cohesion and structure of polarizable systems. Hydrogen bonds are responsible for many phenomena, from the structure of brucite minerals in the Earth's mantle [13], to the properties of DNA [14]. For water and ammonia, their hydrogen bonds have 'moderate' energies [15] between -3 kcal mol^{-1} and -6.5 kcal mol^{-1} at ambient conditions [16].

The effect of nuclear quantum effect on hydrogen bonds is not straightforward. Both theoretical calculations and experimental studies have shown that in general NQEs or ZPE effects tend to weaken weak hydrogen bonds, and strengthen the strong ones [17–19]. The reason lies in the competition between the anharmonic intermolecular bond bending and the intramolecular bond stretching. Moreover, the addition of nuclear quantum effects in dynamical simulations can drastically change the properties of simple molecules such as water, as they accelerate reorientation dynamics [20] and increase donor-hydrogen distance, lowering the H-bond strength [21, 22]. Similar effects are observed in ammonia dimers [23]. This effect plays a role in the bonds symmetrization in ice [24] and the formation of ionic phases via proton transfer mechanisms [25–27].

1.0.2 Hydrogen diffusion and super-ionic phases

The first part of this thesis focuses on the quantum dynamics problem of proton/hydrogen diffusion in solid materials [28, 29]. Proton conduction and diffusion is at the core of technological developments for hydrogen production and storage [30–32]. It is also present in biological system, such as water wires [33], which have also promising applications in fuel cells.

We have mentioned previously the phenomenon of proton transfer observed in several hydrogen bonded materials [25–27]. NQEs are also central in the discussion of proton/hydrogen diffusion. In general, NQEs, in this case mainly zero-point energy (ZPE) and tunneling, tend to enhance the proton diffusion, particularly at low temperatures: for a classical proton, diffusion is completely suppressed at low T, whereas it is not the case for the quantum particle. An exact and numerically treatable method to describe hydrogen diffusion in condensed matter systems, that includes all nuclear quantum effects, is not yet available. Therefore, the first part of this thesis work has been devoted to assess approximate methods that can simulate the hydrogen dynamics, from which one could extract time-correlation functions and the relevant quantities to describe diffusion, such as the diffusion coefficient and the free-energy barriers. In order to make the problem treatable, we set up a model system where a light particle with the hydrogen mass diffuses through a two-dimensional network of heavy atoms. The interaction between the light and heavy particles can be modified at will, in order to enhance (or depress) specific quantum effects, from zero-point-energy driven diffusion barriers to deep tunneling regimes. Our simu-

lations show that Langevin-based mixed quantum-classical approaches, such as quantum baths, unfortunately provide a biased description of diffusion and cannot be used to that aim in real systems. However, we benchmark other path-integral-based methods, which can be valid alternatives for studying quantum-driven diffusion, especially on the short times.

In real materials, proton often diffuses through complex mechanisms. The interplay between the diffusing particle and the network dynamics is an open problem, sometimes referred to as phonon-assisted hopping [34]. In our 2D model we can quantify this contribution to diffusion. The next step would be to study hydrogen diffusion at extreme conditions of temperature and pressure. For instance, in brucite under very high pressure, proton dynamics consists of two-step processes that should combine to make the particle travel through the solid [13].

Under extreme pressure conditions, proton diffusion is a the core of an exotic phenomenon, known as superionicity, which combines two apparently incompatible features. i.e. solid rigidity and liquid-scale mobility [35]. Superionic phases were firstly predicted and observed in water (phase XVIII) at pressure conditions compatible to the interior of iced planets such as Uranus and Neptune [36, 37]. Solid ammonia [38] and ammonia hydrates [39] under extreme pressures are also systems in which superionic phases are or might be present. A superionic phase is predicted also in hydride LaH_{10} [40]. Therefore, the availability of reliable and efficient simulation methods which include NQEs is pivotal for the discovery and prediction of superionic phases, and the development of possible applications [41].

1.0.3 Ammonia hydrates under pressure

After having mentioned how nuclear quantum effects affect the hydrogen/proton diffusion, the occurrence of phase transitions and the formation and breaking of hydrogen bonds, we introduce the systems under study in the second part of this work, namely ammonia hydrates at high pressure (2GPa $\leq P \leq$ 25GPa).

Three main types of ammonia hydrates exist at ambient pressure [42, 43], depending on their stoichiometric composition: 1:2 NH_3-H_2O ratio is know as Ammonia Di-Hydrate (ADH), 1:1 NH_3-H_2O ratio as Ammonia Mono-Hydrate (AMH) and finally 2:1 NH_3-H_2O ratio as Ammonia Hemi-Hydrate (AHH). The domains of existence of these species as a function of the concentration of ammonia molecules are shown on diagram in Figure 1.1. For the present work, however, we consider these mixture, in particular AHH, under high pressures.

The study of ammonia hydrates at high pressure has seen important developments throughout the recent years due to their astrochemical relevance. Indeed, ammonia hydrates are abundant elements in the outer solar system and they are crucial in the composition and formation of icy giants planets, such as Uranus and Neptune, and icy moons, such as Titan and Triton [45–47]. The explanation of exotic magnetic fields of icy planets [48] could be crucially linked to the different icy phases of ammonia, water and methane mixtures present in the core of these planets. Due to the relative abundance of water com-

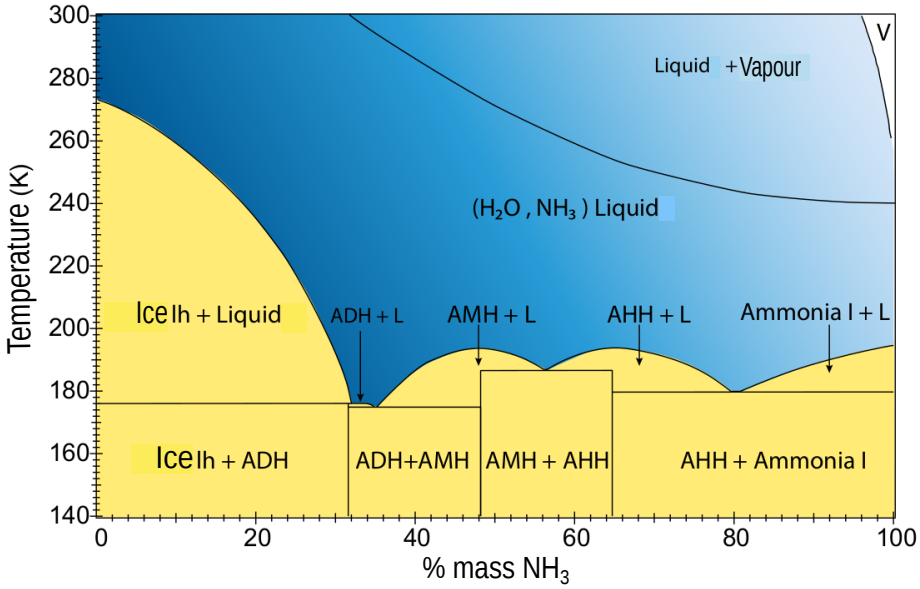

Figure 1.1: Existing phases of Ammonia Hydrates at ambient pressure [43]. Redraw from Figure in [44] (pag. 34).

pared to ammonia in both inner and outer Solar systems, the study of phase diagrams of water-rich ammonia hydrates, (ADH and AMH) at extreme pressures, coherent with inner planetary conditions, had produced numerous results. For instance, observations of density profiles of Uranus and Neptune estimated an ammonia content to be around 8% [49, 50] of the total mass; the nebula in the nearby of Saturn has an estimated 10-15% of ammonia content [51]. On the other hand, water-poor AHH was considered unlikely to exists in nature and it had been disregarded for long time.

However, a dehydration process under pressure for both water-rich hydrates (AMH and ADH) was highlighted, presenting a mixture of water and ammonia hydrates with higher concentration of NH_3 than previously expected. First examples of dehydration under compression were found in the ADH phase diagram, in which the ADH-IV phase transforms in mixture of AMH-IV and ice-VII at 300K and 3.4GPa [52, 53]. The same dehydration behavior was found to be true for AMH under compression [54]: liquid with 1:1 water-ammonia ratio decomposes in AHH phase II and ice-VII at 3.5GPa and room temperature. Later studies confirmed these results [55, 56]. Dehydration processes make AHH a possible candidate for the interior of icy planets. For instance, the $\tilde{1}$0-15% of ammonia content of Saturn nebula, which normally translates to roughly half ADH and half ice, could instead consist of $\tilde{8}$0% ice and $\tilde{2}$0% AHH instead [54, 55].

1.0.4 Plastic crystals and disordered molecular alloys

Ammonia hydrates under high pressure present a large variety of phases, both experimentally observed or theoretically predicted. Here, we briefly describe two of them, namely the plastic phase and disorder molecular alloy (DMA) phase.

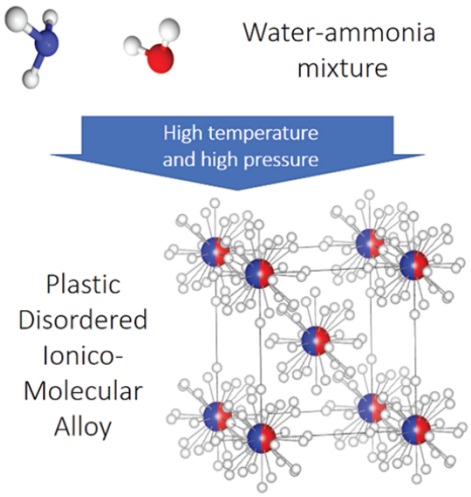

Figure 1.2: Representation of DMA/DIMA phase of AMH from Zhang et al. [57].

Traditionally, a 'plastic crystal', also designed by the acronym ODIC (Orientational Disorder In Crystal), refers to a molecular system in which the molecular centers of mass sits on a (often cubic) crystal site, while molecular orientations are dynamically disordered [58]. This is connected with the so-called 'globular' shape of molecules and the fact that inter-molecular interactions are much weaker than intra-molecular ones. The plastically crystalline phase has historically been seen as intermediate between the crystal and the liquid [59]. Note that self-diffusion coefficients were also measured in plastic crystals via radiotracer techniques [60, 61]. In the case of hydrates, the inter-molecular interactions are mainly the hydrogen bonds, while often in other molecular crystals Van der Waals interactions play a major role [62]. The orientational distribution of the molecule in a plastic crystal phase are seldom isotropic [1].

Noticeable example of plastic crystal can be found in pure ammonia under pressure ($\geq$ 1GPa). A plastic phase (II) is obtained by compressing the liquid ammonia at about 220K [38, 50]. It has a hexagonal closed-packed structure (*hcp*), and presents partial or full rotation disorder depending on the T-P conditions. Finally, in the case of ammonia hydrates, plastic behavior has been observed for instance by Zhang et al. [57] for AMH ice VII at high temperatures (from about 400K to 600K). In particular, they computed the reorientational diffusion coefficient of hydrogen atoms of ammonia molecules via quasi-elastic neutron scattering (QENS) measurements, which quantify the timescale of the rotational disorder of ammonia molecules. Several theoretical studies have also predicted the presence of a plastic phase for pure water (ice VII) above 2GPa, for a wide range of pressures and temperatures [64–67] and rotational behavior under pressure was measured by Bove et al. [68].

The definition of disordered molecular alloy (DMA) was first introduced by Loveday and Nelmes [69] for a new molecular structure observed in AMH phase under pressure (AMH-VI). It designates a crystal with two (or more) molecular species, presenting a well defined geometrical order, where the species are randomly distributed in the structure from the chemical point of view. This type of disorder is also called substitutional disorder. Ammonia hydrates present this type of crystal for all three stoichiometric compositions: ADH [53],

[1] Important applications of plastic crystals can be found in the field of solid-state ionic conductors [63].

AMH [69] and AHH [70, 71]. Moreover, if ionization of the molecules is present, due to a proton transfer from water molecules to ammonia molecules ($H_2O+NH_3 \rightarrow HO^- + NH4+$), the alloy takes the name of disordered ionic molecular alloy (DIMA), which has also been observed in AMH [57, 72], AHH [73] and ADH [44]. Figure 1.2 gives an example of *bbc* cell of AMH with substitutional disorder on the *bbc* sites.

In summary, Zhang et al. [57] determined AMH-VII to be a DIMA phase with plastic behavior. Hence, three main types of disorder are present in AMH-VII: substitutional, compositional and rotational.

1.0.5 Ammonia Hemi-Hydrates under pressure

Ammonia Hemi-Hydrate (AHH) has a known phase (AHH-I) at low temperature and ambient pressure[42]. Wilson et al. [70] studied this phase under compression, finding it stable until 1GPa, then another structure appears until around 5GPa and 300K.

Two main phases of AHH have been established under high pressure. The first phase, named AHH-II in analogy of ADH-II, was found by compression of AMH liquid, as stated above [54]. Further compression of this phase finds no significant changes below 20GPa at room temperature. At higher pressures, a cubic *bcc* structure is observed, called AHH-DMA for its similarities with disordered molecular alloy of AMH [69] and ADH [53]. The same phase was also obtained by heating AHH-II between 4 and 8GPa.

Theoretical calculations have hitherto matched onto the experimental results only partially. Naden Robinson et al. [74] performed 0K, high pressure calculation on the AHH-II structure, which appears to be stable up to 23GPa; for higher values of pressure, they predict a DIMA phase. Moreover, fully ionized AHH [75] and plastic and super-ionic phases [39] are predicted in P-T ranges outside the scope of this work.

The AHH phase diagram in the range 0-30GPa and 300K-600K has been recently explored in detail via Raman and infrared spectroscopy, and X-ray diffraction by Andriambariarijaona et al. [44, 73]. Figure 1.3 shows the updated phase diagram of AHH in this T-P region. Two new solid phases were highlighted in the region where only AHH-DMA was previously observed:

- AHH-pbcc: anew phase with a *bcc* structure and plastic behavior. Moreover, the this phase is believed to be a DMA phase;
- AHH-qbcc: a new DMA phase is obtained, with quasi *bcc* structure;
- the metastable region between 10GPa and 19GPa, and 300K and 450K. Simple compression of AHH-II structure at 300K does not present any phase transition until the AHH-DIMA phase at $\tilde{1}$8GPa. If the AHH-qbcc found at 500K and 15GPa is cooled at fixed pressure, the AHH-II is not recovered at 300K.

The theoretical exploration of these systems requires molecular dynamics simulations with large amount of atoms, to account for its complexity due to temperature and pressures effects, and hydrogen bond structure.

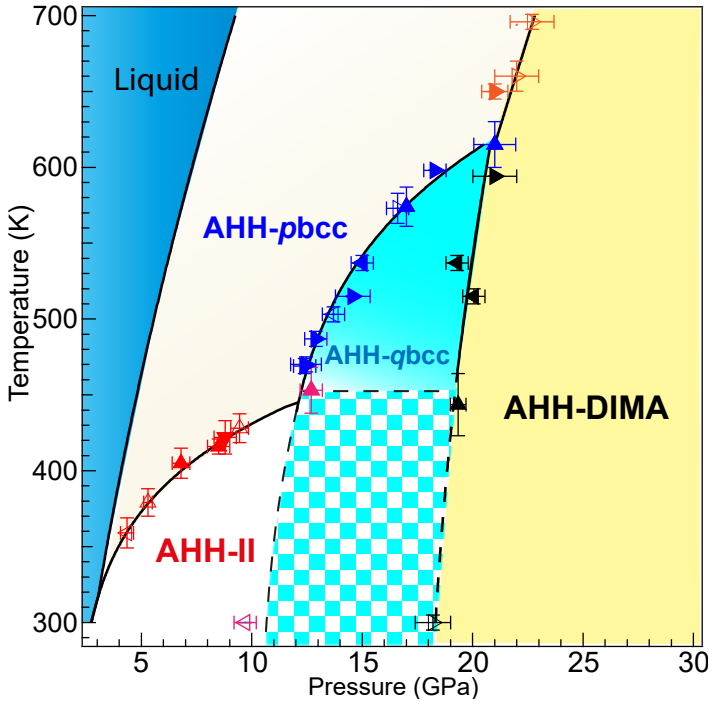

Figure 1.3: Updated phase diagram of AHH under pressure from the work of Andriambariarijaona et al. [44, 73].

1.0.6 Structure of the manuscript

This work is divided in three main Chapters:

1. the Chapter 2 focuses on the main computational techniques used in this work, within the Born-Oppenheimer approximation. The main idea is to compare two main classes of methods which account for the quantum effects in the nuclei's dynamics: the quantum thermal bath methods (both standard and adaptive versions), and the ring-polymer approximation of path integral molecular dynamics [76]. We also present an hybrid version of the two classes, which uses a colored bath to accelerate the convergence of the ring-polymer dynamics [77];

2. the Chapter 3 consists mainly in a comparison between the methods previously explained on the problem of diffusion of a quantum particle. None of the existing techniques is able to solve this problem exactly, which poses the issue of which method is the best practical approximation to use for a simulation of quantum diffusion. Our approach is to create a exactly solvable model (2D rigid lattice) which allows to assess the advantages and the limits of each method;

3. finally, Chapter 4 exposes the theoretical investigation of the crystal-plastic phase transition in ammonia hemi-hydrate (AHH) under high pressure. Our analysis is based on the experimental work of Andriambariarijaona et al. [44, 73]. We use some of the molecular dynamics techniques explained before, coupled with a force field potential. We are able to simulate a system of 10^5 atoms for times of the order of tens

of nanoseconds per trajectory. Our goal is to find a microscopic explanation of the phase transition between the crystal solid of AHH-II and the plastic solid observed at higher temperatures.

Chapter 2

Langevin-based molecular dynamics methods for nuclear dynamics

2.1 Born-Oppenheimer approximation . . . 13
2.1.1 Potential energy surface . . . 14
2.2 Molecular Dyamics methods . . . 17
2.2.1 Integration of Newton's second law . . . 18
2.3 Classical Langevin Thermostat . . . 20
2.3.1 Canonical sampling via Langevin equation . . . 20
2.3.2 Integration of equations of motion via Langevin MD . . . 21
2.3.3 Classical Langevin barostat . . . 22
2.4 Path Integral Molecular Dynamics . . . 25
2.4.1 Path Integral formalism . . . 25
2.4.2 Path Integral Molecular Dynamics for statistical properties 26
2.4.3 Ring-Polymer Molecular Dynamics . . . 28
2.4.4 Nuclear quantum effects in RPMD . . . 30
2.4.5 The RPMD estimators of energy and pressure . . . 31
2.4.6 Integration of the equations of motion in RPMD . . . 32
2.5 Quantum Thermal Bath . . . 32
2.6 Adaptive Quantum Thermal Bath . . . 35
2.6.1 Zero-Point Energy Leakage . . . 35
2.6.2 Adaptation routine of adQTB . . . 36
2.7 Path-integral Quantum Thermal Bath . . . 37
2.8 Conclusion: where the methods are used in this work . . . 41
Appendix . . . 42
A Liouville operator formalism . . . 42
B Harmonic Analysis of Stationary Stochastic Processes . . . 43

In this chapter, we present the main equations and the numerical details of the computa-

tional methods used in this work. We firstly introduce the Born-Oppenheimer approximation, which adiabatically separates the general quantum problem into an electronic and nuclei part. We briefly explain the approach of force fields to model electronic potential, which is used in the Chapter 4. Then, we introduce the molecular dynamics methods used to solve the nuclei equations of motion. They all are trajectory-based methods and they are linked to the Langevin equation as sampling tool for the canonical ensemble. We distinguish them in classical methods, which treats the nuclei as pure classical objects, and quantum methods, whose goal is to include the nuclear quantum effects, with various degrees of approximation. All these methods are compared in the Chapter 3 on the problem of the diffusion of a quantum particle in a solid; also, some of them are used in the Chapter 4 for full-scale atomic simulations of ammonia hydrates under high pressure.

2.1 Born-Oppenheimer approximation

The full quantum-mechanical description of a 3D system of M nuclei of positions $\mathbf{R} = \{\mathbf{R}_1, \ldots, \mathbf{R}_M\}$ and N electrons of positions $\mathbf{r} = \{\mathbf{r}_1, \ldots, \mathbf{r}_N\}$ is given by the time-dependent Schrödinger equation

$$\imath\hbar\frac{\partial}{\partial t}\psi(\mathbf{R}, \mathbf{r}, t) = \hat{\mathcal{H}}\psi(\mathbf{R}, \mathbf{r}, t) \tag{2.1}$$

where ψ is the wavefunction describing the system (nuclei and electrons) and $\hat{\mathcal{H}}$ is the Hamiltonian operator, which reads

$$\hat{\mathcal{H}} = \sum_{i=1}^{M}\frac{\hbar^2\nabla_i^2}{2m_i} + \sum_{j=1}^{N}\frac{\hbar^2\nabla_j^2}{2m_e} + \hat{U}_{n,n}(\mathbf{R}) + \hat{U}_{e,e}(\mathbf{r}) + \hat{U}_{nuc,e}(\mathbf{R}, \mathbf{r}) \tag{2.2}$$

where m_i are the nuclei masses, m_e is the electron mass, $\hbar$ is the reduced Plank constant, and we neglected the spin-orbit interactions and the presence of an external field. The nuclei and electronic interactions have the form of a Coulomb potential

$$\begin{cases} \hat{U}_{n,n}(\mathbf{R}) = \frac{1}{2}\sum_{i\neq j}^{M}\frac{Z_i Z_j e^2}{|\mathbf{R}_i - \mathbf{R}_j|} \\ \hat{U}_{e,e}(\mathbf{r}) = \frac{1}{2}\sum_{i\neq j}^{N}\frac{e^2}{|\mathbf{r}_i - \mathbf{r}_j|} \\ \hat{U}_{nuc,e}(\mathbf{R}, \mathbf{r}) = -\sum_{i=1}^{N}\sum_{j=1}^{M}\frac{Z_j e^2}{|\mathbf{r}_i - \mathbf{R}_j|} \end{cases} \tag{2.3}$$

where e is the unitary charge. The interaction between nuclei and electrons makes the Hamiltonian non separable, as it depends jointly on the nuclei and electrons coordinates. We assume that the Hamiltonian operator does not depend explicitly on time. Hence, we can also introduce the time-independent Schrödinger equation

$$\hat{\mathcal{H}}\psi(\mathbf{R}, \mathbf{r}) = E\psi(\mathbf{R}, \mathbf{r}) \tag{2.4}$$

where the eigenstate $\psi(\mathbf{R}, \mathbf{r})$ is the stationary state and the eigenvalue E is the energy associated to the stationary state $\psi(\mathbf{R}, \mathbf{r})$. If we use the solution of Eq. (2.4) in Eq. (2.1), the evolution of the quantum state in time is

$$\psi(\mathbf{R}, \mathbf{r}, t) = e^{-iEt/\hbar}\psi(\mathbf{R}, \mathbf{r})(0)$$

However, neither Eq. (2.4) nor Eq. (2.1) are generally solvable exactly for many-body systems, as the complexity of the numerically exact solution of these equations scales exponentially with the number of degrees of freedom. Approximations of the Hamiltonian operator (2.2) and the wave-function $\psi(\mathbf{R}, \mathbf{r})$ are needed to tackle the problem quantum many-body problem.

A common and powerful assumption we can make at this point is the adiabatic separation the nuclei and electronic degrees of freedom, which takes the name of Born-Oppenheimer (BO) approximation [78]. It is based on the observation that all nuclei of a quantum system are much heavier than the electrons ($m_i \gg m_e,\ \forall i$).In general, the BO approximation allows the separation of variables in the wave-function

$$\psi(\mathbf{R}, \mathbf{r}) = \chi_{nuc}(\mathbf{R})\phi_e(\mathbf{r}; \mathbf{R}) \tag{2.5}$$

where the nuclei positions $\mathbf{R}$ are fixed parameters in the electronic wave-function $\phi_e(\mathbf{r};\mathbf{R})$. Indeed, they are considered stationary for the electrons, which adiabatically adapt to any change of nuclei position. Thus, electrons are considered to be always in the ground state configuration corresponding to a given nuclear configuration. The BO approximation recasts the problem of Eq. (2.4) in two separate sub-problems. Firstly, we look for the solution of the time-independent Schrödinger equation for the electrons

$$\hat{\mathcal{H}}_{el}\phi(\mathbf{r};\mathbf{R}) = \epsilon_{el}(\mathbf{R})\phi(\mathbf{r};\mathbf{R}) \tag{2.6}$$

where

$$\hat{\mathcal{H}}_{el}(\mathbf{R}) = \sum_{j=1}^{N} \frac{\hbar^2\nabla_j^2}{2m_e} + U_{nuc,nuc}(\mathbf{R}) + \hat{U}_{e,e}(\mathbf{r}) + \hat{U}_{nuc,e}(\mathbf{r};\mathbf{R})$$

and the electronic eigenvalue $\epsilon_{el}(\mathbf{R})$ is the ground state energy of $\hat{\mathcal{H}}(\mathbf{R})$ that depends parametrically on on the set of nuclei coordinates, and takes the name of adiabatic potential energy surface (PES). The second problem is the solution of the nuclei dynamics. Assuming the PES to be known, the nuclei are affected by an external effective potential $U_{eff}(\mathbf{R}) = \epsilon_{el}(\mathbf{R})$. Then, they can be described as quantum particles [79], following the time-dependent Schrödinger equation

$$\imath\hbar\frac{\partial}{\partial t}\chi_{nuc}(\mathbf{R},t) = \left[\sum_{i=1}^{M} \frac{\hbar^2\nabla_i^2}{2m_i} + U_{eff}(\mathbf{R})\right]\chi_{nuc}(\mathbf{R},t) \tag{2.7}$$

or further approximated as classical particle, following Newton second law. This classical representation of the atomic nuclei allows to dramatically simplify the calculations and it provides satisfactory results for heavy atoms. However, when light atoms are considered in the system [1], the classical framework cannot provide an exhaustive description of microscopic phenomena. Indeed, light nuclei present a number of purely quantum properties, known as Nuclear Quantum Effects (NQEs).

We spend few words now on the solution of the electronic problem, before giving the details of the computational techniques to solve the nuclei equations of motion.

2.1.1 Potential energy surface

The electronic ground state $\epsilon_{el}(\mathbf{R})$ of Eq. (2.6) can be approximated using a variety of methods, depending on the required accuracy and on the computational resources available. Some approaches, within certain approximations, rely on an explicit calculation of the ground state energy, which allows to treat relatively large systems, up to hundreds of atoms. In other cases, the Born-Oppenheimer energy is modeled through analytical expressions, that depend on the nuclei position and on parameters that are fitted to best reproduce results of electronic structure calculations and possibly experimental observations.

As pictured in Figure 2.1, the PES is in general a complex function depending on all the atomic coordinates, and might posses global/local minima, saddle points and critical

[1] i.e. when the mass of nuclei is such that the de Broglie wave-length (1.1) is of the same order of characteristic lengths of the system.

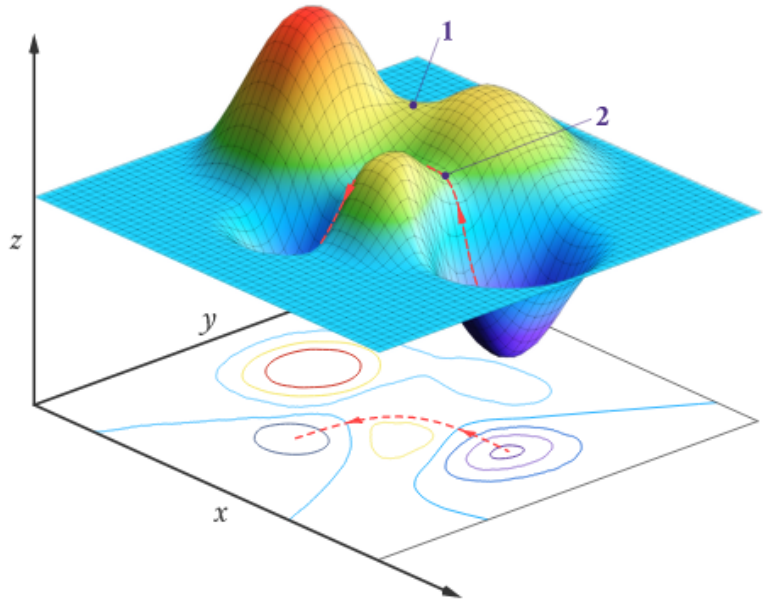

Figure 2.1: 2-D contour map and corresponding Potential Energy Surface for a hypothetical endothermic reaction (from [80])

points. Its accurate description is crucial in molecular simulations and it is a challenging issue still today, as the many-body problem of Eq. (2.6) has no trivial solution. Possible approaches to compute the electronic structure are the so-called *ab initio* techniques. They are quantum mechanical or semi-empirical methods which solve Eq. (2.6) within several approximations. High-level theory, yet expensive, methods are for example Configuration Interaction and Coupled Cluster methods [81], for system of the order of few atoms. For larger systems, one of the most popular approach is the Density Functional Theory (DFT) [82], based on the recast of the electronic problem in terms of electron density, instead of the wave-function [83]. *Ab initio* methods such as DFT techniques are vastly used in solid state simulations, but their computational cost allows to simulate systems up to hundreds of atoms and for timescales of the order of tens of ps. In this work, instead, we mostly use the force field approach, described in the following Section, with which is possible to simulate systems up to the million atoms and for times up to the order of the μs [84, 85].

Force field description

As *ab initio* techniques are not feasible for large systems, the molecular mechanics (MM) approach have been developed to treat a number of atoms beyond some hundreds [86]. The BO potential energy surface is approximated via analytical expressions that are based on physical/chemical intuition. The dynamics of this ensemble of atoms is determined by empirical functions, known as force field (FF), with the following general form

$$U = \underbrace{U_{bond} + U_{angle} + U_{b\theta} + U_{oop} + U_{tor}}_{bonded} + \underbrace{U_{VdW} + U_{el}}_{non-bonded} \tag{2.8}$$

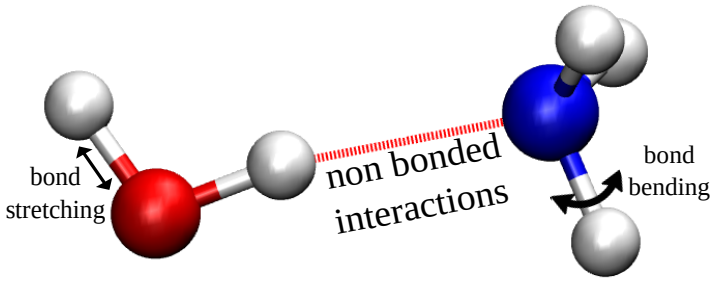

Figure 2.2: Water-ammonia dimer with force-field bonded and non-bonded terms.

where usually the bonded terms are five and they describe the short-range interactions: bond stretching, angle bending, bond-angle cross term, out-of-plane bending and torsional rotation. In this work, however, we deal only with simple molecules such as water and ammonia, for which torsional rotation are not present. In standard (non-polarizable) force fields, the non-bonded terms are instead given by the long-range Van der Walls interactions and the electrostatic interactions. Figure 2.2 shows the water-ammonia dimer (oxygen in red, nitrogen in blue, hydrogen atoms in white) and the schematic drawing of the main terms of the force field interaction. In all FFs, the energy terms based on sets of parameters optimized in a systematic way to reproduce either quantum chemistry calculations and/or experimental results. This means that the transferability of FF is limited to the data available on a specific system. Popular FFs are AMBER [87], OPLS [88] and CHARMM [89]. Notice that traditional FFs approximate the electrostatic potential term with fixed partial charges models, neglecting anisotropic features of charge distribution and polarization, which is the response of the charge distribution to the environment [90]. This means that any difference in the environment would not change the set of charge parameters. Thus, many polarizable force fields have been developed in recent years to deal with different types of environment, such as AMOEBA (Atomic Multipole Optimized Energetics for Biomolecular Applications) [91] model. Moreover, most of the force field models are non reactive, which means that it is not possible to break and form chemical bonds. Consistent efforts are made today in order to overcome these problems, as well as the transferability, with the use of machine-learning techniques to accurately reconstruct interatomic potentials from *ab initio* datasets [84, 92, 93].

In this work, we use the Optimized Potentials for Liquid Simulations All Atoms (OPLS-AA) [88, 94] for the ammonia molecules and the Simple Point-Charge flexible (SPC/fw) [95, 96] for the water molecules. Both FFs are included in the TinkerHP package [97]. In our case, the general form of the potential has three main terms:

$$U_{OPLS} = \underbrace{U_{bond} + U_{angle}} + U_{non-bonded}$$

Intermolecular bonds and angles are shaped as harmonic potentials, as

$$\begin{cases} U_{bond} = \sum_{bonds} k_r (r - r_0)^2 \\ U_{angles} = \sum_{angles} k_\theta (\theta - \theta_0)^2 \end{cases} \tag{2.9}$$

where r_0 and θ_0 are the equilibrium coordinates, and the force constants k_r and k_θ, which ensure the flexibility of the model and determine the stretching and bending frequencies. The non-bonded terms include Coulomb interactions for all atoms and Van-der-Waals-like interactions (with a Lennard-Jones form) for the heavy atoms (oxygen and nitrogen in our case). Indeed, in this simple form, the hydrogen bonds are considered to be well described by electrostatic terms [12, 98]. The general form of non-bonded parts of the potential is

$$U_{non-bond} = \sum_i \sum_{i>j} \left\{ \frac{q_i q_j e^2}{|r_i - r_j|} + 4\epsilon_{ij} \left[\left(\frac{\sigma_{ij}}{|r_i - r_j|} \right)^{12} - \left(\frac{\sigma_{ij}}{|r_i - r_j|} \right)^{6} \right] \right\} \tag{2.10}$$

where q are the partial atomic charges and the set of parameters include Lennard-Jones radii σ and well-depths ϵ. Standard combining rules are used, such as $\sigma_{ij} = (\sigma_{ii}\sigma_{jj})^{1/2}$ and $\epsilon_{ij} = (\epsilon_{ii}\epsilon_{jj})^{1/2}$.

The OPLS-AA force field has been developed for simulations of liquids and it corrected the amine hydration problem by balancing the hydrogen bond strengths [99]. It has also been used for various applications, such as study of organic liquids [100] and RNA [101], the treatment of halogen bonds [102] and searching of hydrogen-bond-donating catalysts [103]. On the other hand,the SPC flexible model has been thoroughly tested on various properties of liquid water, such as viscosity dependence on temperature [104], dielectric constant [105], activation energies and activation volumes [106] and supercriticality [107]; it was used for simulations of channel and nanopore systems [108]. As mentioned before, the force field approach allows to simulate systems up to millions of atoms and for simulations times of the order of the μs [84, 85]. In our case, we have performed molecular dynamic simulations of the ammonia hydrate systems from 10^5 up to one million atoms, for timescales of the order of tens of nanoseconds per trajectory.

2.2 Molecular Dyamics methods

Molecular Dynamics (MD) techniques are useful numerical tools to investigate physical, chemical and biophysical systems at molecular and atomic scale [109]. Classical MD consists in the simulation of the trajectories of the atomic nuclei, within the Born-Oppenheimer approximation, by numerically solving their newtonian equations of motion. This provides a clear classical picture of the properties of the system andallows to compute both static and dynamic properties of the system.

Considering the nuclei as quantum objects is way more complex. Today few approaches, such as the multi-configurational time-dependent Hartree (MCTDH) method [110] that allow to solve the Schrödinger equation for relatively complex systems, but they are still limited to a few tens of degrees of freedom. Therefore, solving numerically Schrödinger's evolution equation (2.7) for the nuclei wave-function is impossible for realistic condensed matter system, as the problem scales exponentially with the number of degrees of freedom. For static properties at thermal equilibrium, reliable results can be obtained within Feynman Path Integral (PI) formalism of quantum mechanics. However, the study of dynamical properties in quantum system remains a theoretical challenge for which different approximations have been proposed, but none of them is general and reliable for all real systems.

In this work, we focus on molecular methods which make use of a quantum bath (based on the generalized Langevin equation (GLE)) to include nuclear quantum effects in the simulations [76]. Some of these approaches are based on the PI formalism and take the name of Ring-Polymer Molecular Dynamics (RPMD) [111–113] and Centroid Molecular Dynamics (CMD) [114]. However, they rely on approximations to compute dynamical properties, whose accuracy cannot be systematically assessed *a priori* [115] and they are particularly costly from a computational point of view. On the other hand, in this work, we are particularly interested in one of the alternative approaches to the PI formalism, based on a generalized Langevin equation, namely the Quantum Thermal Bath (QTB) [116] and its refinement, the adaptive QTB (adQTB) [117]. This is an approximated method which is able to access directly dynamical properties from particle trajectories, and to introduce the zero-point energy with a computational cost of the same order of standard classical MD [118, 119]. Finally, we mention the existence of other trajectory-based method, such as the semi-classical initial value representation (SCIVR) methods [120], or based on the generalized Langevin equation [121], which are out of the scope of this work.

In the following Sections, we introduce the basic concepts of molecular dynamics methods, starting with the solution of Newton's equation (Section 2.2.1), and the classical Langevin thermostat (Section 2.3). Then, we introduce the Path integral formalism (Section 2.4) before the explanation of the main methods used in this work based on the PI formalism, namely the Ring-Polymer Molecular Dynamics ((Section 2.4.3). Finally, we explain the Quantum Thermal Bath methods, standard an adaptive versions (Sections 2.5 and 2.6 respectively) and the hybrid version with RPMD (Section 2.7).

2.2.1 Integration of Newton's second law

MD simulations consists in integrating directly the equations of motion of the nuclei in order to have a full knowledge of the trajectory of the system in the phase space. This is particularly useful to study time-dependent properties, which are not always linked to an equilibrium ensemble.

Let us consider a general system of three-dimensional N classical particles. The general classical hamiltonian for the system is

$$H(\mathbf{r},\mathbf{p}) = \sum_{i=1}^{N} \frac{\mathbf{p}_i^2}{2m_i} + U(\mathbf{r}) \tag{2.11}$$

where each particle has mass m_i, position $\mathbf{r}_i$ and momentum $\mathbf{p}_i = m_i \frac{d\mathbf{r}_i}{dt}$. The potential energy of the system $U(\mathbf{r})$ depends in general on all particles positions, and its first derivative with respect to particle i gives the force $\mathbf{f}_i = -\nabla_{\mathbf{r}_i} U(\mathbf{r})$. Therefore, each particle follows Newton's second lawor the equivalent Hamilton's equations of motion

$$\begin{cases} \frac{d\mathbf{r}_i}{dt} = \frac{\partial H(\mathbf{x},\mathbf{p})}{\partial \mathbf{p}_i} = \frac{\mathbf{p}_i}{m_i} \\ \frac{d\mathbf{p}_i}{dt} = -\frac{\partial H(\mathbf{x},\mathbf{p})}{\partial \mathbf{x}_i} = \mathbf{f}_i(\mathbf{x}) \end{cases} \tag{2.12}$$

These equations describe the evolution of the system, drawing a trajectory $(\mathbf{x}(t), \mathbf{p}(t))$ in the phase space. They have two major properties: energy conservation and time reversibil-

ity under change $\mathbf{x}' = \mathbf{x}(-t), \mathbf{p}' = -\mathbf{p}(-t)$. Conservation of energy is particularly relevant, because it means that, no matter how long the total time of the evolution of the system, the points explored by the trajectory in the phase space are always on a isoenergetic (hyper-)surface. In a statistical mechanics contexts, energy conservation defines the microcanonical ensemble (N, V, E), as fixed energy $H = E$ is constant in time.

Temporal averages of macroscopic observables can be computed from the evolution of the microscopic particles of the system, obtained via molecular dynamics techniques. Consider a general observable $O(\mathbf{x}(t), \mathbf{p}(t))$, which depends explicitly on the system trajectory in the phase space. Its time average is

$$\bar{O} = \lim_{T\to\infty} \frac{1}{T} \int_0^T O(\mathbf{x}, \mathbf{p}) dt$$

Numerical computation of $(\mathbf{x}, \mathbf{p})$ is given by the integration of Hamilton equations, for example using the Verlet algorithm [122]. Starting from an initial point $(\mathbf{x}_0, \mathbf{p}_0)$, for each discrete time step Δt, we compute the forces acting on the system and update positions and momenta iteratively, until we reach the final point.

Note that MD simulations which aim at studying equilibrium properties are usually based on the following assumption, namely the Ergodic hypothesis, which states that ensemble averages of macroscopic observable are equivalent to their time averages, $\langle O \rangle = \int d\mathbf{x} d\mathbf{p} O(\mathbf{x}, \mathbf{p}) \rho(\mathbf{x}, \mathbf{p})_{eq.}$, where $\rho(\mathbf{x}, \mathbf{p})$ is the probability density function of the given ensemble at equilibrium. The Ergodic hypothesis is true in the case of Hamilton's equations in the thermodynamic limit, i.e for very large number of particles at fixed density. Indeed, sampling from the (N, V, E) ensemble is perfectly equivalent to the exploration of the (hyper-)surface at constant energy from a single trajectory, if the total time of the simulation is long enough to allow the system to explore all possible states.

As the time-dependent trajectory of the system $(\mathbf{x}(t), \mathbf{p}(t))$ is directly computed via any MD techniques, we can compute the Time Correlation Functions (TCF) between observables [123–125]. TCFs have the same role in non-equilibrium statistical mechanics as the partition functions have in equilibrium statistical mechanics. Many transport coefficients, which are associated and characterize non-equilibrium or transport property of the system, can be expressed in terms of TCFs. Furthermore, they can be also related to many experimental techniques, such as spectroscopy and measurements of rate constants. The definition of classical TCF at given time τ is

$$C_{AB}(\tau) = \langle A(0)B(\tau) \rangle = \frac{1}{\mathcal{Z}} \int d\mathbf{x}\, d\mathbf{p}\, A(\mathbf{x}(0), \mathbf{p}(0), 0) B(\mathbf{x}(\tau), \mathbf{p}(\tau), \tau)\, \rho(\mathbf{x}(0), \mathbf{p}(0))_{eq.} \quad (2.13)$$

where A and B are the two general observables which can depend in general explicitly on time, $\rho(\mathbf{x}, \mathbf{p})$ is the probability density function of the given ensemble at equilibrium, and $\mathcal{Z}$ is the canonical partition function.

2.3 Classical Langevin Thermostat

As we mentioned in the previous section, simply integrating Hamilton's equations leads to the exploration of the isoenergetic surface $H(\{x_i, p_i\}) = E, \forall i = 1, \ldots, 3N$. A more realistic situation is a system exchanging energy with its environment, and at fixed temperature. These conditions are expressed by the Canonical ensemble (N, V, T). Here, the system is in contact with a virtually infinite thermal source, called thermostat or bath. Unlike the total energy of the system coupled to the bath, the energy of the system alone is not conserved, but it is possible to show that, in the thermodynamic limit i.e. for large number of particles $N \gg 1$ at constant density, energy fluctuations tend to vanish.

Moreover, in the canonical ensemble it is valid the Equipartition theorem, which imposes a constraint on the kinetic energy of a system of N classical particles at thermal equilibrium.

Theorem 1 (Equipartition Theorem) *For each particle of mass m in a 3D space at thermal equilibrium with a bath at temperature T, then:*

$$\langle \frac{1}{2} m v_i^2 \rangle = \frac{3}{2} k_B T \tag{2.14}$$

where $v_i = |\boldsymbol{v}_i|$.

In other words, each velocity degrees of freedom contributes on average to the total kinetic energy proportionally to the temperature T. The velocity distribution follows the Maxwell-Boltzmann distribution.

In order to sample from the (N, V, T) ensemble, various MD methods are used, both deterministic [126–128] and stochastic [129, 130]. The main idea is to modify the velocities of the system via a thermostat, in such way that the Equipartition theorem holds true. Deterministic algorithms, such as Nose-Hoover's [127, 131], usually obtain the correct velocities by integrating a new equation of motion of one (or multiple) new variable $\xi(t)$, which gives the coupling between Hamilton's equations and the thermal bath. In this work, we make use of a stochastic thermostat instead, based on the Langevin equation, which is able to samples the correct distribution for the (N, V, T) ensemble without the integration of additional variables.

2.3.1 Canonical sampling via Langevin equation

The Langevin equation [132] was originally introduced to model an actual physical process, the Brownian motion, whereas in the MD algorithm it is a simulation tool to ensure the sampling from the (N, V, T) ensemble. This stochastic equation provides a simple and efficient way to couple the equations of motion with a thermostat which gives the correct classical energy distribution [133–135]. The main idea is imposing the correct Canonical energy distribution by the addition of two contributions: a damping force with a friction parameter γ and a stochastic force $\mathbf{R}(t)$ that allows to randomize the velocities.

For simplicity, we consider the problem of N three-dimensional particles. The Langevin equations of motion of the particle i are:

$$\begin{cases} \frac{d\mathbf{r}_i}{dt} = \frac{\mathbf{p}_i}{m_i} \\ \frac{d\mathbf{p}_i}{dt} = -\gamma \mathbf{p}_i + \mathbf{f}_i + \mathbf{R}(t) \end{cases} \tag{2.15}$$

The term $-\gamma \mathbf{p}_i$ is the damping force acting on the particle i, $\mathbf{f}_i = -\nabla_{\mathbf{r}_i} U$ is an conservative force given by the presence of an external potential $U = U(\mathbf{r}_1, \ldots, \mathbf{r}_N)$. The random force $\mathbf{R}(t)$ is assumed to be a white noise, i.e. a stationary random process, with the following properties for each degree of freedom

$$\begin{cases} \langle R_j(t) \rangle = 0 \\ \langle R_j(t) R_k(t+\tau) \rangle = 2 m_i \gamma k_B T \delta(\tau) \delta_j^k \end{cases} \tag{2.16}$$

It is possible to show that these equations of motion ensure that the system reaches the equilibrium with the proper Boltzmann distribution and the proper classical energy density [124], with the consequence of recovering the Equipartition theorem 1.

2.3.2 Integration of equations of motion via Langevin MD

In order to integrate the Langevin equations of motion, we apply the so called BAOAB integration scheme, which outperforms previous possible integration schemes of the Langevin equation [133–135]. The numerical integration scheme splits the equations of motion (2.15) in three blocks, called A, B and O

$$\begin{pmatrix} d\mathbf{r}_i \\ d\mathbf{p}_i \end{pmatrix} = \underbrace{\begin{pmatrix} \mathbf{p}_i/m_i \\ 0 \end{pmatrix} dt}_{A} + \underbrace{\begin{pmatrix} 0 \\ \mathbf{f}_i \end{pmatrix} dt}_{B} + \underbrace{\begin{pmatrix} 0 \\ -\gamma \mathbf{p}_i dt + \sqrt{2\gamma m_i k_B T} d\mathbf{W} \end{pmatrix}}_{O} \tag{2.17}$$

where $\mathbf{W}(t)$ is a 3-dimensional vector of independent Wiener processes [136]. Each term corresponds to the integration of a single block of the equations of motion that can be solved exactly. The symmetric decomposition in terms of Liouville operator (see Appendix A for more details) is

$$e^{\imath \hat{\mathscr{L}} \Delta t} \simeq e^{\imath \hat{\mathscr{L}}_B \Delta t/2} e^{\imath \hat{\mathscr{L}}_A \Delta t/2} e^{\imath \hat{\mathscr{L}}_O \Delta t} e^{\imath \hat{\mathscr{L}}_A \Delta t/2} e^{\imath \hat{\mathscr{L}}_B \Delta t/2} \tag{2.18}$$

which has an overall error $\mathcal{O}(\Delta t^3)$, negligible for a small integration step Δt. Therefore, the explicit steps of the BAOAB integration scheme for the position $\mathbf{r}_i$ and momentum $\mathbf{p}_i$ of each particle of the system are the following:

- step **B**: momenta are updated of an half-step $\Delta t/2$ with the forces computed in the positions $\mathbf{r}(t)$, as:
$$\mathbf{p}_i(t + \Delta t/2) = \mathbf{p}(t) + \mathbf{f}_i(\mathbf{r}(t)) \Delta t/2$$
- step **A**: the positions are updated with the momenta of a half-step Δt. Explicitly, this is:
$$\mathbf{r}_i(t + \Delta t/2) = \mathbf{r}_i(t) + \frac{\mathbf{p}_i(t + \Delta t/2)}{m_i} \Delta t/2$$

- step **O**: the core of the Langevin thermostat is the updating of the velocities by the effect of the thermostat, which is obtained by two terms, the frictional force and the random force

$$\tilde{\mathbf{p}}_i(t+\Delta t) = \mathbf{p}_i(t)e^{-\gamma\Delta t} + \sqrt{(1-e^{-2\gamma\Delta t})\, m_i k_B T}\mathbf{G} \tag{2.19}$$

  where the components of the vector **G** are Gaussian random number $\mathcal{G}$, sampled independently at every step Δt from a normal distribution with zero mean and unitary variance i.e. $\mathcal{G} \sim \mathcal{N}(0,1)$.

- step **A** (symmetric):

$$\mathbf{r}_i(t+\Delta t/2) = \mathbf{r}_i(t) + \frac{\tilde{\mathbf{p}}_i(t+\Delta t) + \mathbf{p}_i(t+\Delta t/2)}{m_i}\Delta t/2$$

- step **B** (symmetric):

$$\mathbf{p}_i(t+\Delta t) = \mathbf{p}(t+\Delta t/2) + \tilde{\mathbf{p}}_i(t+\Delta t) + \mathbf{f}_i(\mathbf{r}(t+\Delta t))\Delta t/2$$

Figure 2.3 shows the pseudo-code of the BAOAB integration of Langevin thermostat coupled to Hamilton's equations. A qualitative criteria to choose the integration step is to compare it with the largest vibrational frequency of the system, or the shortest period. Therefore, the integration step is chosen as $\Delta t \ll 1/\nu_{max}$. The computation can be optimized by noticing that the second B step at time step t can be grouped with the first B step at the next time step. This allows to compute only once per step the forces - usually the most time-demanding computation in a MD algorithm - and update the momenta with **f** of a full step Δt, instead of $\Delta t/2$ twice.

Particular attention must be given to the friction parameter γ. Indeed, it is also the strength of the coupling of the equations of motion with the thermal bath. Strong coupling allows a faster thermalization, but the dynamical properties would be disturbed. Indeed, the effect of larger γ broadens the spectral peaks as the friction increase. To explain this effect, let us consider the case of a damped harmonic oscillator of frequency ω. The effect of the damping term is an exponential decrease of the amplitude of oscillations. In the frequency domain, this means that the spectra is not anymore a $\delta(\omega)$, but the spectral profile is given by a Lorentzian distribution. As long as the damping term is kept in a small range of values, the broadening of the spectra has no serious consequence on the dynamics. However, for large values of γ compared to the typical frequencies of the system, we fall in the over-damped regime and the dynamics is compromised. As we focus on the dynamical process of diffusion in Chapter 3 and 4, the effect of the friction is systematically checked, as it could have a strong impact on the diffusion coefficient.

2.3.3 Classical Langevin barostat

In most experiments (notably in the one made on ammonia hydrates at the core of this work), the thermodynamic parameters that are controlled are the pressure P, as well as the temperature T. The relevant ensemble is thus the iso-temperature isobaric ensemble

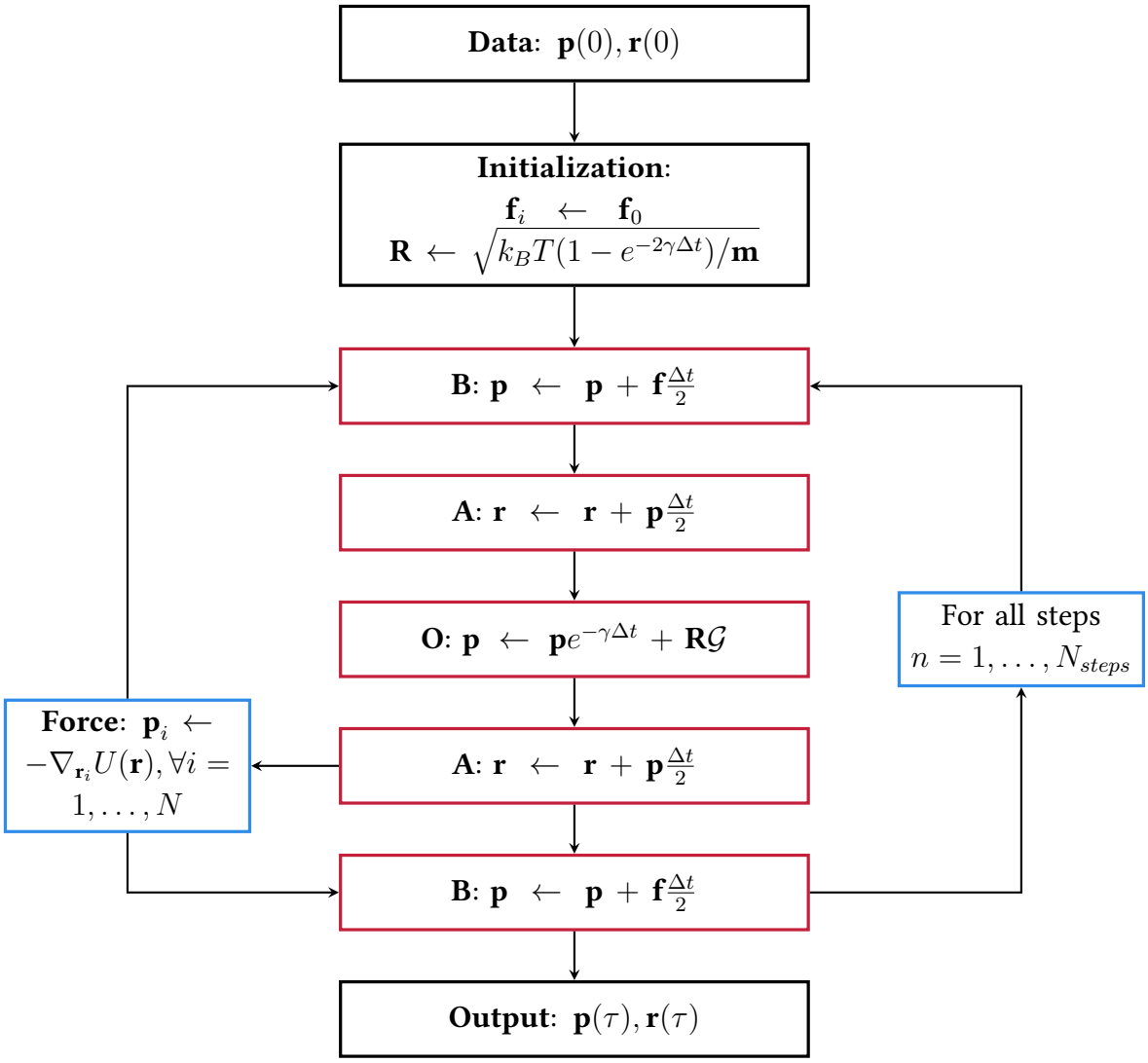

Figure 2.3: Flowchart of the Langevin thermostat with BAOAB integration scheme, where $\mathcal{G} \sim \mathcal{N}(0,1)$

(N, P, T), in which the total volume varies. Different numerical barostat have been designed for molecular dynamics at constant pressure, such as the MTK approach [124, 137] or the stochastic cell rescaling [138]. In this work, however, we use the approach of the Langevin equation as numerical tool to integrate the equations of motion coupled to both a thermostat and a barostat. The method used in this case is the Langevin Piston (LP) method by Feller et al. [139].

The main idea to allow the volume to vary is to include a additional degree of freedom - a piston - with a fictitious mass μ of units $[mass \times length^{-4}]$. This idea was originally developed by Andersen [140], in the so called Extended System (ES) method, and by Berendsen [141], within the Weak Coupling (WC) method. However, the piston dynamics in the WC method is overdamped, while it has no damping in the ES method. Feller et al. uses the Langevin equation for the piston dynamics in order to avoid too strong oscillations of the volume (for well-chosen parameters), and to sample correctly the (N, P, T) ensemble.

The equations of motion of one of N particles in 3D with the barostat attached have then the following form, completely analogous to Eq. (2.15):

$$\begin{cases} \frac{d\mathbf{r}_i}{dt} = \frac{\mathbf{p}_i}{m_i} + \frac{1}{3}\frac{1}{V}\frac{dV}{dt}\mathbf{r}_i \\ \frac{d\mathbf{p}_i}{dt} = \mathbf{f}_i - \frac{1}{3}\frac{1}{V}\frac{dV}{dt}\mathbf{p}_i \\ \frac{d^2V}{dt^2} = \frac{1}{\mu}\left[P(t) - P_{ext}\right] - \gamma_V\frac{dV}{dt} + R(t) \end{cases} \tag{2.20}$$

where $P(t)$ is the instantaneous pressure, P_{ext} is the imposed pressure; γ_V is the friction parameter for the volume V dynamics and μ is the piston fictitious mass. The stochastic process $R_V(t)$ is Gaussian, with zero mean and variance given by

$$\langle R_V(t)R_V(t+\tau)\rangle = \frac{2\gamma k_B T\delta(\tau)}{\mu}$$

Note that the instantaneous pressure $P(t) = P(\mathbf{r}, \mathbf{p})$ is estimated from the MD simulation including the virial term as

$$P(\mathbf{r}, \mathbf{p}) = \frac{1}{3V}\sum_{i=1}^{N}\left(\frac{\mathbf{p}_i^2}{2m_i} + \mathbf{r}_i \cdot \mathbf{f}_i\right) \tag{2.21}$$

The general case of the previous barostat is in the anisotropic situation, i.e. where the lattice parameters might vary differently as a consequence of the applied pressure. In Chapter 4 we make use of a orthorhombic version of the method, for which we briefly gives some details. The complete anisotropic method can be found in the book of Tuckermann [124]. We introduce the orthorhombic box matrix, made by the three box dimension

$$\hat{h} = \begin{pmatrix} a & 0 & 0 \\ 0 & b & 0 \\ 0 & 0 & c \end{pmatrix} \tag{2.22}$$

where a, b and c are the orthorhombic box parameters, and the total volume is $V = det(\hat{h}) = abc$. The pressure now is given by a 3×3 tensor, called also stress tensor, whose elements are written as

$$\sigma_{\alpha,\beta}(\mathbf{r}, \mathbf{p}) = \frac{1}{det(\hat{h})}\sum_{i=1}^{N}\left(\frac{(\mathbf{p}_i \cdot \hat{\mathbf{e}}_\alpha)(\mathbf{p}_i \cdot \hat{\mathbf{e}}_\beta)}{2m_i} + (\mathbf{r}_i \cdot \hat{\mathbf{e}}_\alpha)(\mathbf{f}_i \cdot \hat{\mathbf{e}}_\beta)\right) \tag{2.23}$$

where $\hat{\mathbf{e}}_\alpha, \hat{\mathbf{e}}_\alpha$ are the elementary vectors of directions $\alpha, \beta = x, y, z$. Hence, the isotropic instantaneous pressure estimator is given by

$$P(\mathbf{r}, \mathbf{p}) = \frac{1}{3}Tr\left[\hat{\sigma}(\mathbf{r}, \mathbf{p})\right] \tag{2.24}$$

In order to write the equations of motion of the Langevin barostat in the orthorhombic case, we introduce the 3×3 tensor of box momenta $\hat{p}_h = \mu\frac{d\hat{h}}{dt}\hat{h}^{-1}$, with μ the piston mass. The equations of motion for a particle i then read

$$\begin{cases} \frac{d\mathbf{r}_i}{dt} = \frac{\mathbf{p}_i}{m_i} + \frac{\hat{p}_h}{\mu}\mathbf{r}_i \\ \frac{d\mathbf{p}_i}{dt} = \mathbf{f}_i - \frac{\hat{p}_h}{\mu}\mathbf{p}_i \\ \frac{d^2h_{\alpha,\alpha}}{dt^2} = \frac{1}{\mu}\left[\sigma_{\alpha,\alpha}(\mathbf{r}, \mathbf{p}) - \sigma^{ext}_{\alpha,\alpha}\right] - \gamma\frac{dh_{\alpha,\alpha}}{dt} + R_V(t) \end{cases} \tag{2.25}$$

where only the diagonal terms $\alpha = \beta$ of are present and the $\hat{\sigma}^{ext}$ is the imposed stress tensor.

We have conclude now the Section on classical molecular dynamics methods. In the next Sections, we introduce the quantum bath methods used in our theoretical investigation [76], which are state-of-the-art methods to introduce nuclear quantum effects (NQEs) for the nuclei dynamics.

2.4 Path Integral Molecular Dynamics

2.4.1 Path Integral formalism

Feynman's Path Integrals (PI) formalism [142] is a framework of quantum mechanics alternative to Schrödinger's wave mechanics and Dirac's theory. Feynman's theory is closer to the classical picture, as it preserves the concept of trajectories of the particles. In the following section we briefly show how the path integral formalism is used as a reliable computational tool to include statistical NQEs in the trajectory-based formalism of MD. For the following exposition, we mostly refer to [124].

Heuristic picture of Feynman's Path Integrals is the following. Let us consider a one-dimensional (for simplicity) quantum particle with position operator $\hat{x}$ and momentum operator $\hat{p}$. The Hamiltonian operator is defined as:

$$\hat{\mathcal{H}} = \frac{\hat{p}^2}{2m} + \hat{V}(\hat{x}) \tag{2.26}$$

where m is the mass of the quantum particle, $\hat{T} = \frac{\hat{p}^2}{2m}$ is the kinetic energy operator and $\hat{V}(\hat{x})$ is the potential energy operator. Bear in mind that the kinetic and potential operators do not commute. The particle starts in position x and we perform a measure in position x'. According to the laws of quantum mechanics, until a measure is performed, we are completely ignorant on the possible path the quantum particle is following. Therefore, instead of introducing a probability distribution for the particle's position, we state Feynman's hypothesis [142]: the quantum particle follows a virtually infinite number of paths from the starting point x to the point in which its position is measured x', weighted by a certain probability amplitude.

We know that the real-time dynamics of the quantum system is given by the real-time propagator operator $\hat{\mathcal{U}}(t) = e^{-\frac{\imath \hat{H} t}{\hbar}}$. If the system is initially prepared in state $|x\rangle$ and it evolves until state $|x'\rangle$. We define the amplitude as the time propagator's coordinate-space matrix element as

$$\mathcal{U}(x, x', t) = \langle x' | \, e^{-\frac{\imath \hat{\mathcal{H}} t}{\hbar}} \, | x \rangle \tag{2.27}$$

The PI evaluation of this amplitude using Feynman's hypothesis is then the following. We state the Lie-Trotter product formula [143]

$$e^{\lambda(A+B)} = \lim_{N \to \infty} \left(e^{\lambda A/N} e^{\lambda B/N} \right)^N \tag{2.28}$$

for two general operators $n \times n$ A and B, and a real parameter λ. This formula is generalized by the Baker–Campbell–Hausdorff formula for non commutative operators [144]. For a finite N, the error is $\mathcal{O}(\lambda^2)$ i.e. of the second order in λ. We apply the Trotter splitting on Eq. (2.27) for P steps. The expression of the real-time propagator is therefore

$$\hat{U}(x, x', t) = \lim_{P \to \infty} \left(\frac{mP}{2\pi\imath\hbar t} \right)^{P/2} \int_{x=x_1}^{x'=x_{P+1}} dx_2 \dots dx_P \\ \exp\left[-\frac{\imath}{\hbar} \sum_{k=1}^{P} \left(\frac{mP}{2t}(x_{k+1} - x_k)^2 - \frac{t}{2P}(V(x_{k+1}) - V(x_k)) \right) \right] \quad (2.29)$$

where $\hbar$ is the reduced Planck constant. The index k discretized the path into $P \to \infty$ intermediate positions between x and x', which are the only fixed point of the path. Although this formula is very useful conceptually and for the development of perturbation and exact theories, this expression is not practical for numerical computations because of the phase term $e^{\imath(\dots)}$ which undergoes strong oscillations and is very difficult to converge. This is the so-called sign problem [145]. Before giving some details on an approximated method for computing real-time dynamical properties with the PI formalism (Section 2.4.3), we introduce in the next Section the formalism of Path Integral Molecular Dynamics for the computation of statical properties.

2.4.2 Path Integral Molecular Dynamics for statistical properties

Although the PI formalism does not provide exact tools to deal with real-time quantum dynamics, it can be used to compute statistical properties of the quantum system, in particular from the quantum distribution function. We state now the basic concept for the method. Given the Hamiltonian operator (2.26), we can define the density matrix element in coordinates' space as

$$\rho(x, x', \beta) = \langle x' | \frac{e^{-\beta\hat{\mathcal{H}}}}{\hat{\mathcal{Z}}} | x \rangle \quad (2.30)$$

where $\hat{\mathcal{Z}}$ is the quantum partition function of the system. The diagonal elements $\rho(x, x, \beta)$ give the probability to find the system in the state x. Formally, one can therefore write the following relation between the two operators

$$\hat{\rho}(\beta) = \frac{e^{-\beta\hat{\mathcal{H}}}}{\hat{\mathcal{Z}}} = \hat{\mathcal{U}}(-\imath\beta\hbar) \quad (2.31)$$

Hence, thanks to this mathematical correspondence, our quantum system has two possible propagators:

- the density matrix $\hat{\rho}(\beta)$ corresponds to the imaginary-time propagator, where we defined the imaginary time as $-\imath\beta\hbar$;
- the real-time propagator $\hat{\mathcal{U}}(t)$, which can be obtained from $\hat{\rho}$ by defining an imaginary inverse temperature $\beta = \frac{\imath t}{\hbar}$.

The precise mathematical relation between $U(t)$ and $\hat{\rho}(\beta)$ is given by a Wick rotation in the complex plane [146]. Analogously as before, we can write an explicit expression of the density matrix using the Trotter splitting (2.77) for the imaginary-time interval $-\imath\beta\hbar$ in P steps, as

$$\hat{\rho}(x,x',\beta) = \lim_{P\to\infty}\left(\frac{mP}{2\pi\beta\hbar^2}\right)^{P/2}\int_{x=x_1}^{x'=x_{P+1}} dx_2\dots dx_P \\ \exp\left[-\frac{1}{\hbar}\sum_{k=1}^{P}\left(\frac{mP}{2\beta\hbar}(x_{k+1}-x_k)^2+\frac{\beta\hbar}{2P}(V(x_{k+1})-V(x_k)\right)\right] \tag{2.32}$$

For a finite P, the Trotter break-up procedure is valid if β/P is small enough such the non-commuting kinetic and potential energy operators can be separated. From the density matrix we can obtain the quantum Canonical partition function (QCPF), defined as

$$\mathcal{Z}(\beta) = Tr\left[e^{-\beta\hat{\mathcal{H}}}\right] \tag{2.33}$$

which in the PI formalism has the following explicit expression

$$\mathcal{Z}(\beta) = \lim_{P\to\infty}\left(\frac{mP}{2\pi\beta\hbar^2}\right)^{P/2}\int dx_1\dots dx_P \\ \exp\left[-\frac{1}{\hbar}\sum_{k=1}^{P}\left(\frac{mP}{2\beta\hbar}(x_{k+1}-x_k)^2+\frac{\beta\hbar}{2P}V(x_k)\right)\right] \tag{2.34}$$

Note that a crucial simplification is given by the trace of Eq. (2.33), which imposes the condition $x_1 = x_{P+1}$. Once the QCPF is know, the quantum thermodynamical properties can be obtained, using the following definition for the ensemble average of an operator $\hat{O}$:

$$\langle\hat{O}\rangle = \frac{1}{\mathcal{Z}}Tr\left[\hat{O}\hat{\rho}\right]$$

Moreover, the imaginary-time quantum propagator is an interesting tool for molecular simulations: at fixed P, the expression (2.34) resembles that of a classical partition function, but in an extended phase space in P dimensions (instead of 1 for the physical system). Classical sampling techniques (Monte Carlo or Molecular Dynamics) can therefore be applied to this problem. Note also that the classical limit is recovered for high temperatures, i.e. in the limit $\beta \to 0$.

The Path-Integrals Molecular Dynamics (PIMD) is a reliable method to compute quantum static properties by sampling the canonical partition function [147–149]. The main idea of PIMD is to exploit the classical isomorphism derived naturally from the expression of the quantum Canonical partition function (QCPF) (2.34). This isomorphism allows to introduce a molecular dynamic scheme with classical Hamiltonian and classical equations of motion right at the core of the quantum problem. Indeed, the QCPF (2.34) can be seen as the classical partition function of a ring-polymer (RP) with P beads moving in a classical potential $V(\vec{x})$ (see Figure 2.4). Introducing the momenta $p_1,\dots,p_P$ in order to sample

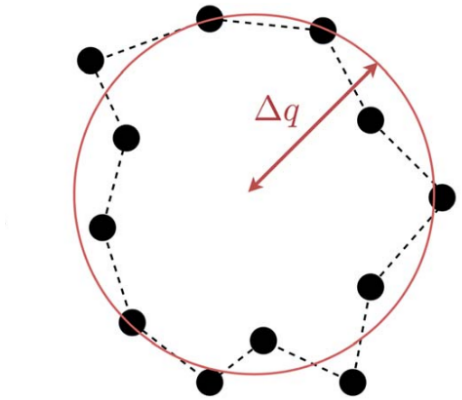

Figure 2.4: Schematic representation of the ring-polymer for a free quantum particle with gyration radius given by (2.42) (from [112])

statistical properties using the ring-polymer dynamics, Eq. (2.34) is written as

$$Z^{(P)}(\beta) = \frac{1}{(2\pi\hbar)^P} \int dp_1 \dots dp_P \int dx_1 \dots dx_P \exp\left[-\beta_P \sum_{k=1}^{P} \left(\frac{p_k^2}{2m} + \frac{1}{2} m\omega_P^2 (x_{k+1} - x_k)^2 + V(x_k)\right)\right] \tag{2.35}$$

where we defined the effective temperature $\beta_P = \frac{\beta}{P}$, the $\omega_P = \frac{1}{\beta_P \hbar}$ as chain frequency of the coupled beads in the ring-polymer, and we applied the periodic condition $x_1 = x_{P+1}$. Hence, $\{x_k, p_k\}$ are the positions and momenta of the $k = 1, \dots, P$ beads. This corresponds to a classical effective Hamiltonian for the ring-polymer of the following form:

$$H_{cl}^{(P)}(\{x_k, p_k\}) = \sum_{k=1}^{P} \left(\frac{p_k^2}{2m} + \frac{1}{2} m\omega_P^2 (x_{k+1} - x_k)^2 + \frac{1}{P} V(x_k)\right) \tag{2.36}$$

Thus, the classical equations of motion of the ring-polymer are written as

$$\begin{cases} \frac{dx_k}{dt} = \frac{p_k(t)}{m} \\ \frac{dp_k}{dt} = -\frac{\partial V}{\partial x_k} - m\omega_P^2 (2x_k - x_{k+1} - x_{k-1}) \end{cases} \tag{2.37}$$

This classical isomorphism is exact in the limit of infinite number of beads, i.e. $\hat{\mathcal{Z}}(T) = \lim_{P\to\infty} Z_{RP}^{(P)}(L, T)$. For a finite number of P beads, PIMD converges to the exact expectation values when $P \sim \beta\omega_{max}$, where ω_{max} is the frequency of the fastest normal mode, making PIMD a computationally expensive technique. Thus, some accelerating approaches reducing the number of beads have been developed [150, 151], such that, for large enough values of P, statical properties are accurately computed.

2.4.3 Ring-Polymer Molecular Dynamics

As stated in Section 2.4.1, the computation of dynamical properties within the PI formalism. Several path-integral based approximations have been developed in order to tackle this

problem, such as Linearized Semi-Classical Initial Value Representation (LSC-IVR) [152] and Centroid Molecular Dynamics (CMD) [114]. In this work, we focus on one of these PI-based methods, namely the Ring Polymer Molecular Dynamics (RPMD) [111–113] and its thermostatted version ((T)RPMD) [153].

The main goal of the method is to compute the dynamical properties of a quantum system via an approximated version of the real-time correlation functions. In analogy with the classical TCF (2.13), we can define, for two observables with operators $\hat{A}$ and $\hat{B}$, we define then the standard form of the quantum TCF [124] as

$$C_{AB}(t) = Tr\left[\hat{\rho}\,\hat{A}e^{\imath\hat{H}t/\hbar}\hat{B}e^{-\imath\hat{H}t/\hbar}\right] \tag{2.38}$$

where $e^{\imath\hat{H}t/\hbar}$ and $e^{-\imath\hat{H}t/\hbar}$ are the forward and backward time propagators respectively and $\hat{B}(t) = e^{\imath\hat{H}t/\hbar}\hat{B}e^{\imath\hat{H}t/\hbar}$ is the time propagated operator in the Heisenberg picture. $C_{\hat{A}\hat{B}}$ is a complex quantity and the equivalent detailed balance condition is $C_{\hat{A}\hat{B}}(t) = C^*_{B\hat{A}}(-t)$. Another common form of the quantum TCF is the Kubo-transformed time correlation function [154], defined as

$$K_{\hat{A}\hat{B}}(t) = \frac{1}{\beta\mathcal{Z}}\int_0^\beta d\lambda\, Tr\left[e^{-(\beta-\lambda)\hat{\mathcal{H}}}\hat{A}e^{-\lambda\hat{\mathcal{H}}}e^{\imath\hat{\mathcal{H}}t/\hbar}\hat{B}e^{-\imath\hat{\mathcal{H}}t/\hbar}\right] \tag{2.39}$$

This version seems more cumbersome, but it is real rather then complex, and the detailed balance condition is simply given by $K_{\hat{A}\hat{B}}(t) = K_{\hat{B}\hat{A}}(-t)$. It is related to the standard TCF by the relation

$$\mathcal{F}\{C_{\hat{A}\hat{B}}(t)\}(\omega) = \frac{\beta\hbar\omega}{1-e^{-\beta\hbar\omega}}\mathcal{F}\{K_{\hat{A}\hat{B}}(t)\}(\omega) \tag{2.40}$$

and they are both related to the classical TCFs in the limit of high temperature. Considering the dynamics of the ring polymer and its effective Hamiltonian (2.36), the RPMD approximation of the Kubo-transformed time correlation function [125] of two observables A and B is:

$$K^{(P)}_{AB}(t) \simeq \frac{1}{Z^{(P)}(2\pi\hbar)^P}\int dx_1\ldots d_P\int dp_1\ldots dp_P \\ e^{-\beta H^{(P)}_{cl}(\{x_k,p_k\})}A^{(P)}(0)B^{(P)}(t) \tag{2.41}$$

where $A^{(P)}(0) = \frac{1}{P}\sum_{k=1}^P A(x_k(0))$ and $B^{(P)}(t) = \frac{1}{P}\sum_{k=1}^P B(x_k(t))$ [2], and $Z^{(P)}$ given by (2.35). This expression is exact for time equal to zero, and for the harmonic potential for correlation functions of the form $K_{Ax}(t)$ and $K_{xB}(t)$, where x is the position of the quantum particle.

The RPMD method has been also used for computing properties at times $t > 0$ with satisfactory results in some applications [33, 111, 112], even though some limitations have also been identified, such as the spurious peaks in the RPMD spectra [115]. In order to tackle this last problem, a thermostatted version of RPMD method ((T)RPMD) [153] was

[2] We removed the operator sign from the observables A and B as they are now purely classical expectation values obtained in the classical isomorphism, where the exact equality is obtained only in the limit of infinite beads, i.e. $\langle\hat{A}\rangle = \lim_{P\to\infty}\langle A\rangle_P$, where $\langle A\rangle_P = \frac{1}{(2\pi\hbar)^P}\frac{1}{Z^{(0)}}\int d\mathbf{p}\int d\mathbf{x}\, e^{-\beta_P H^{(P)}_{cl}(\mathbf{x},\mathbf{p})}\, A^{(P)}(\mathbf{x},\mathbf{p})$.

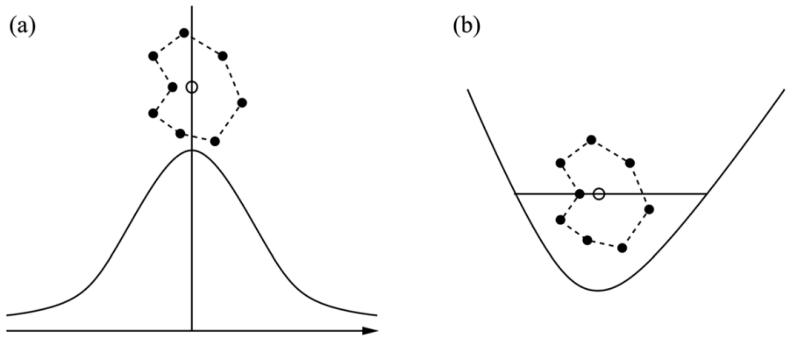

Figure 2.5: Qualitative representation of the tunneling (a) and zero-point energy (b) in the RPMD method (from [112]). The centroid is represented by an empty circle.

introduced. The main idea is to attach a Langevin thermostat on the internal modes of the centroid (and possibly on the centroid itself). All results valid for RPMD method have been shown to be valid also for (T)RPMD, keeping in mind the dependence of dynamical properties on the friction parameter γ of the Langevin thermostat. Moreover, the bath allows the correct and faster thermalization of the ring-polymer modes. In this work, we make mostly use of this last version of the RPMD method.

2.4.4 Nuclear quantum effects in RPMD

As pictured in Figure 2.4, the ring-polymer description allows a description the delocalization of the quantum particle [112]. Indeed, we can define the gyration radius of the ring-polymer of a free particle

$$\Delta q = \sqrt{\langle \frac{1}{N} \sum_{k=1}^{N} (x_k - \bar{q})^2 \rangle} \tag{2.42}$$

where the position of the centroid of the polymer is defined as

$$\bar{q} = \frac{1}{N} \sum_{k=1}^{N} x_k$$

For $N \to \infty$, the gyration radius has the following limit for a free particle:

$$\Delta q = \sqrt{\frac{\beta \hbar^2}{12m} \left(1 - \frac{1}{N^2}\right)} \to \frac{\hbar}{\sqrt{12 m k_B T}} \tag{2.43}$$

which is related to de Broglie thermal wavelength (1.1). Nuclear Quantum Effects (NQEs), in particular zero-point energy and tunneling, have a intuitive representation in the RPMD formalism, as shown in Figure 2.5. Indeed, a classical particle at low temperature is at its equilibrium position, while a quantum particle has zero-point quantum fluctuations. This affects both static properties (in which case the effect of the ZPE is captured exactly by RPMD) and dynamical ones (in which case RPMD is approximate).

Moreover, in presence of a potential energy barrier $V(x)$, a classical particle cannot overcome it unless it has an energy equal or higher than the top of the barrier V_{max}. The Canonical probability to find the classical particle at the top of the barrier is $e^{-\beta V_{max}}$. Instead, a quantum particle can tunnel through a potential barrier with exponentially low but finite probability depending on the width of the potential. A ring-polymer reproduces qualitatively this quantum effect. Indeed, in the low temperature limit, the polymer tends to cross the barrier progressively, one bead at a time, so that the average energy over the beads remains lower than V_{max}, whereas at high temperature, the polymer remains more compact because the spring constants are stiff, so that it passes the barrier altogether and the classical result is recovered. Therefore, the polymer can cross the barrier even if the mean energy (averaged over the different beads) is lower than the barrier height.

2.4.5 The RPMD estimators of energy and pressure

The main macroscopic quantities of a system, such as energy and pressure, have in certain cases a different expression in the PI/RPMD formalism. Here we report the main estimators for potential and kinetic energy, and pressure, and we refer to [124] for their derivation and discussion. Bear in mind that any ensemble average in the PIMD formalism implies the fixed number of replicas P used in the numerical simulation, i.e. $\langle \dots \rangle = \langle \dots \rangle_P$.

Considering the effective Hamiltonian (2.36) for one 1D particle, and the ring-polymer partition function (2.35), the average potential energy estimator is

$$\langle V \rangle = \langle \sum_{k=1}^{P} \frac{1}{P} V(x_k) \rangle \tag{2.44}$$

and the standard kinetic energy estimator is

$$\langle K_{prim} \rangle = \langle \sum_{k=1}^{P} \frac{p_k^2}{2m} - \frac{1}{2} m\omega_P^2 \sum_{k=1}^{P} (x_{k-1} - x_k)^2 \rangle \tag{2.45}$$

also known as primitive estimator. However, since the fluctuations for the primitive kinetic energy estimator grow with P [155], another estimator is introduced, called the virial estimator of the kinetic energy

$$\langle K_{vir} \rangle = \langle \frac{1}{2P} \sum_{k=1}^{P} x_k \frac{\partial V}{\partial x_k} \rangle \tag{2.46}$$

Finally, as the former is not translationally invariant [156], the centroid-virial estimator is introduced

$$\langle K_{Cvir} \rangle = \langle \frac{1}{2\beta} + \frac{1}{2P} \sum_{k=1}^{P} (x_k - \bar{x}) \frac{\partial V}{\partial x_k} \rangle \tag{2.47}$$

where $\bar{x}$ is the ring-polymer centroid position.

For the average pressure, several estimators can be introduced, such as

$$\langle P \rangle = \langle \frac{1}{V} \left(2K_{prim} - \frac{1}{P} \sum_{k=1}^{P} x_k \frac{\partial V}{\partial x_k} \right) \rangle \tag{2.48}$$

where V is the total volume of the simulation box. Pressure estimator is used in the extension of the RPMD method for the constant pressure ensemble (N, P, T) [157].

2.4.6 Integration of the equations of motion in RPMD

The BAOAB integration scheme used in the (T)RPMD is analogous to the classical Langevin scheme of Figure 2.3, with few important modifications. Firstly, in order to decouple the beads oscillations in the equations of motion (2.37), we use the transformation from the beads representation $\{x_1, \ldots, x_P\}$ to the normal modes representation $\{q_0, \ldots, q_{P-1}\}$

$$\begin{cases} \tilde{p}_j = \sum_{k=1}^{P} p_k C_{jk} \\ \tilde{q}_j = \sum_{k=1}^{P} x_k C_{jk} \end{cases}$$

The coefficients C_{jk} are the elements of the transformation matrix $\hat{C}$, which transforms, for a constant potential, the beads into the normal modes, i.e. the eigenmodes of the dynamical matrix for the free ring-polymer. Their expression can be found in reference [158]. With this transformation, the ring-polymer Hamiltonial (2.36) has the form

$$H_{cl}^{(P)}(\{\tilde{q}_j, \tilde{p}_j\}) = \sum_{j=0}^{P-1} \left(\frac{\tilde{p}_j^2}{2m} + \frac{1}{2} m \tilde{\omega}_j^2 (\tilde{q}_j)^2 \right) + \frac{1}{P} \sum_{k=1}^{P} V \left(\sum_{j=0}^{P-1} C_k j q_j \right)$$

where $\tilde{\omega}_j = 2\omega_P sin(\pi j / P)$. Note that the potential V cannot be simply decomposed on the normal modes, which means that, in order to compute it, we need to transform back to the beads coordinates.

The BAOAB integration scheme is thus applied on all normal modes coordinates in the same sequence as the classical case. Figure 2.6 shows the pseudo-code for the (T)RPMD integration method for a single particle in 1D. The generalization to N particles in 2D or 3D is straightforward. Notice that RPMD simulations involve a significant increase of the computational cost, roughly proportional to the number of beads P with respect to a classical MD simulation.

2.5 Quantum Thermal Bath

One quantum MD alternative not based on the path-integral formalism is the Quantum Thermal Bath [159], similar to the Quantum thermostat implemented by Ceriotti et al. [160, 161]. The main idea of the QTB consists in mimicking the quantum delocalization of a light nucleus with a stochastic process. It is based on the generalized Langevin equation

$$\begin{cases} \frac{d\mathbf{r}_i}{dt} = \frac{\mathbf{p}_i(t)}{m_i} \\ \frac{d\mathbf{p}_i}{dt} = -\nabla_{\mathbf{r}_i} U(\mathbf{r}) - \int_0^\infty \Gamma(\tau)\, \mathbf{p}_i(t-\tau)\, d\tau + \mathbf{R}(t) \end{cases} \tag{2.49}$$

where the momentum $\mathbf{p}_i$ is convoluted with the memory function $\Gamma(\tau)$, used to obtain a generalized frictional force. If the memory kernel $\Gamma(\tau)$ is chosen as $\Gamma(\tau) = \gamma\, \delta(\tau)$, where

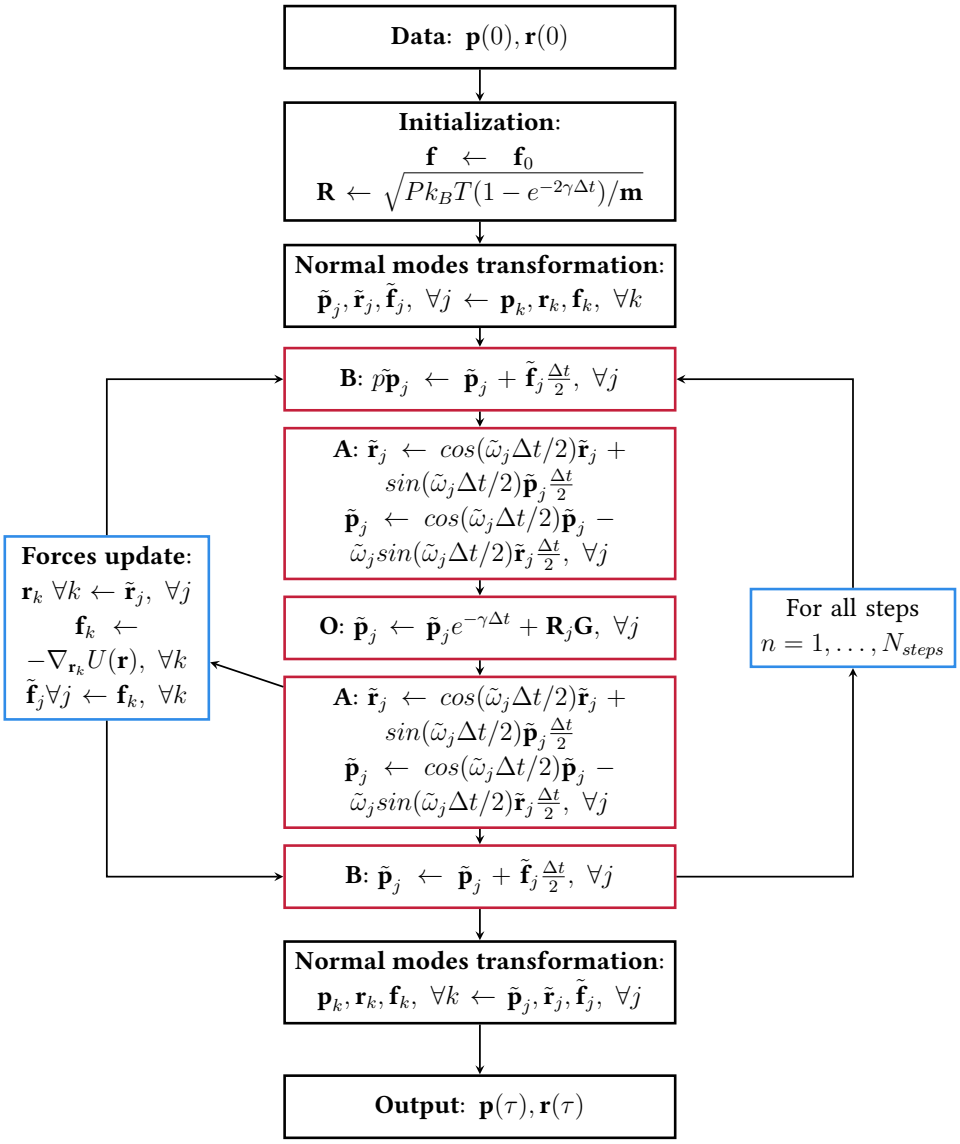

Figure 2.6: Flowchart of the Langevin thermostated RPMD with BAOAB integration scheme, where $\mathbf{g} \sim \mathcal{N}(0,1)$

$\delta(\tau)$ is the Dirac delta function and γ the friction parameter, then the stochastic process loses memory immediately of itself (i.e. is a Markov process [162]) and we recover the conditions (2.16) [3].

As for the classical Langevin thermostat, a random force $\mathbf{R}(t)$ is also added, which now makes explicit the quantum nature of the particle via its power spectral density. Indeed, the bath now is a quantum version of the Langevin thermal bath:the random force $\mathbf{R}(t)$ is not a white noise, but a colored 'quantum' noise. The main advantages of the QTB are the reduced computational costs, comparable to classical MD, and the use of a clear classical picture, in which the concept of particle's trajectories in real time is well defined and can be easily simulated with well known MD techniques.

As before, we consider a 1D system, which can be easily generalized to more dimensions and N particles. The main difference from the classical case is the implementation of the random force $R(t)$, which now is a random process with $\langle R(t)\rangle = 0$ and the power spectral density defined as

$$C_{RR}(\omega) = 2m\gamma\theta(\omega, T) \tag{2.50}$$

For $\theta(\omega, T) = k_B T$, where k_B is the Boltzmann constant, the classical Langevin power spectral density is recovered (2.16). Here instead, the quantum distribution of energy $\theta(\omega, T)$ is given by the following formula:

$$\theta(\omega, T) = \hbar\omega \left(\frac{1}{2} + \frac{1}{e^{\frac{\hbar\omega}{k_B T}} - 1} \right) \tag{2.51}$$

where $\hbar$ is the reduced Plank constant. This expression corresponds to the average energy of an harmonic oscillator of frequency ω at thermal equilibrium. Thus, the idea of the QTB is thus to thermalize each vibration mode of the quantum system, not with the classical distribution of energy - given by the Equipartition theorem 1 - but with the quantum energy distribution $\theta(\omega, T)$. In particular, the first term $\frac{\hbar\omega}{2}$ corresponds to the zero-point energy and ensures that, even at very low T, the system does not freeze but instead continues to fluctuate with an average probability distribution that mimics the delocalization of the quantum ground state. For the case of the harmonic oscillator, this method is exact by construction, given small enough values of the friction parameter γ.

The QTB equations can be integrated by the BAOAB algorithm already employed for classical Langevin thermostat. The only difference is in the step O of the velocity rescaling (2.19) and in particular in the expression of the random force $R(t)$, which is now correlated in time. For the numerical details of the method we refer to the work of Brieuc et al. [116] and Mangaud et al. [117]. The flowchart of the QTB method is the same of the classical Langevin method of Figure 2.3, with the only difference of using the colored noise in the step O. Notice that the colored noise is correlated in time, and cannot be computed at each step; rather it is generated at the beginning of the simulation for the whole trajectory,

[3] The relation between the frictional force and the random force in the Langevin equation is related a much more general result by Kubo [154], which takes the name of Fluctuation-Dissipation theorem (FDT) (see Appendix B for more details). It states that the response of a system to an external disturbance is related to the internal fluctuations of the system in absence of the disturbance. Time-correlation functions can express and characterize internal fluctuations - or their fluctuations spectra - and they are linked in general to quantities such as admittance or impedance.

which might occupy much of the memory available. Hence, in practice, this procedure is done only for a segment of simulation of N_{steps}. The total time of the simulation is then $\tau = N_{seg} \times N_{steps}\Delta t$.

The QTB method has been used in several applications with satisfactory results. We can mention for instance the structural properties of MgO [159], the isotope effect in LiH *versus* LiD [163], the phase transition of AlOOH under pressure [164], and vibrational spectra in polyatomic molecules [165]. However, as explained in the next Section, the method suffers of an intrinsic problem, Zero-Point Energy Leakage (ZPEL), which made it fail in specific applications [166–169]

2.6 Adaptive Quantum Thermal Bath

2.6.1 Zero-Point Energy Leakage

Although the QTB gives exact results in the simulation of NQEs in harmonic systems [3, 6, 163] in presence of anharmonicity it does not always give satisfactory results, due to the so-called Zero-Point Energy Leakage (ZPEL) [116]. Indeed, the quantum bath is coupled with Hamilton's equations for the system via the parameter γ. The quantum bath aims at thermalizing each vibrational mode of the quantum system at the correct harmonic energy density $\theta(\omega, T)$, given by (2.51). However, for anharmonic systems, the modes are coupled. This means that, even though all modes are thermalized with $\theta(\omega, T)$, the energy of high frequency modes is transfered to the low frequency ones, as the classical equations of motions tend to the Equipartition theorem (2.14). As a results, the effective energy density distribution will be lower than $\theta(\omega, T)$ for high frequency modes and higher than $\theta(\omega, T)$ for low frequency modes.

The first approach to tackle the ZPEL is to use higher values of the friction γ, which has been shown to reduce - but not fully eliminate - the drawback, at the cost of a stronger influence on the dynamics by the bath [116]. A second, more sophisticated and precise method used to correct the ZPEL takes the name of Adaptive Quantum Thermal Bath (adQTB). The main idea to quantify the error given by the ZPEL is to measure the violation of the quantum Fluctuation Dissipation Theorem [117].

The Fluctuation-Dissipation theorem is a general result of the Linear Response theory [154, 170], valid for both classical and quantum systems. For a full derivation of the Linear Response Theory we refer to [124]. In our one-dimensional quantum case, given the position and velocity operators $\hat{x}$ and $\hat{v}$, a way to express the Fluctuation-Dissipation theorem is

$$\mathrm{Re}\left[\chi_{\hat{v}\hat{x}}(\omega)\right] = \frac{\omega}{2\imath\theta(\omega,T)} \int_{-\infty}^{+\infty} \langle \hat{x}(0)\hat{v}(t)\rangle e^{-\imath\omega t} dt = \frac{C_{\hat{v}\hat{v}}(\omega)}{2\theta(\omega,T)} \tag{2.52}$$

where $C_{\hat{v}\hat{v}}(\omega)$ is the Fourier transform of the velocity-velocity time correlation function, $\theta(\omega, T)$ is the quantum thermal energy (2.51); finally, the $\chi_{\hat{v}\hat{x}}(\omega)$ is the linear generalized susceptibility - defined in full generality in [154] - which, in this case, characterizes the velocity response $\Delta v(\omega)$ to a small perturbation force in the frequency domain $\Delta v(\omega) = \chi_{\hat{v}\hat{x}}(\omega)\Delta R(\omega)$. For a general discussion of the generalized susceptibility and the

FDT we refer to [117, 171]. Eq. (2.52) is valid for every frequency and it is exact for quantum operators which evolve with the correct quantum dynamics. However, in the QTB we are using classical equations of motion and classical variables as observables, instead of quantum operators. Thus, this relation is not exact anymore and we can measure the difference of the two quantities in order to correct the ZPEL.

In the case of the Langevin QTB random force $R(t)$, the generalized susceptibility can be written in terms of the velocity-random force time correlation spectrum and random force autocorrelation spectrum [117] as

$$\mathrm{Re}\left[\chi_{vx}(\omega)\right] \simeq \frac{\mathrm{Re}\left[C_{vR}(\omega)\right]}{C_{RR}(\omega)} \tag{2.53}$$

This yields to the following version of the FDT

$$m\gamma C_{vv}(\omega) = \mathrm{Re}\left[C_{vR}(\omega)\right] \tag{2.54}$$

The physical interpretation of Eq. (2.54) is the following: $\mathrm{Re}\left[\chi_{vx}(\omega)\right]$ corresponds to the spectrum of the power injected into the system by the random force $R(t)$, while $m\gamma C_{vv}(\omega)$ the power dissipated by the friction force. Any deviation from Eq. (2.54) is due to the energy that is transferred from a frequency to another one. Therefore, Eq. (2.54) provides a quantitative measure of the ZPEL. Indeed, Based on the fact that the components of the random force $R(t)$ at distinct frequencies are not correlated, the quantum Fluctuation-Dissipation theorem is fulfilled for each degree of freedom.This is also true for simulations, provided $\Delta\omega = \frac{2\pi}{N_{steps}\Delta t}$ be small i.e. for long enough simulations.

2.6.2 Adaptation routine of adQTB

The main idea of the adQTB [117] is to use in the expression of the power spectral density the random force a function of the frequencies $\gamma(\omega)$ and adapt on the fly the dynamics in such way that it compensates the error given by the ZPEL on the energy distribution, using (2.54). In the original work of Mangaud et al. [117] it is called adQTB-r, but in this work we refer to it as simply adQTB method. Note that it can be the kernel $\Gamma(\tau)$ appearing in the frictional term of the GLE (2.49) to be alternatively adapted, leading to a completely equivalent version of the method. However, this second version, which takes the name of adQTB-f, it was not used in the current work.

The adaptation routine starts by defining a power spectral density for the random force $R(t)$ in the following way

$$C_{RR}(\omega) = 2m\gamma(\omega)\theta(\omega, T) \tag{2.55}$$

such that (2.54) takes the form:

$$C_{vR}(\omega) = m\gamma(\omega)C_{vv}(\omega) \tag{2.56}$$

and we can compute the difference

$$\Delta_{FDT}(\omega) = \mathrm{Re}\left[C_{vR}(\omega)\right] - m\gamma(\omega)C_{vv}(\omega) \tag{2.57}$$

From this quantity we have a estimation of the ZPEL for each frequency, hence we can correct it by adapting the $\gamma(\omega)$ in a way such that it increases at high ωs and decreases at low ωs. Once C_{vv}, C_{vR} and the difference (2.57) are computed, the main goal is to adapt $\gamma(\omega)$ such that $\Delta_{FDT} \simeq 0, \forall \omega < \omega_{cut}$. In order to correct for the ZPEL in a systematic way, we have an equation for the friction function for every frequency:

$$\frac{d\gamma(\omega)}{dt} = \gamma A_\gamma \frac{\Delta_{FDT}(\omega)}{||\Delta_{FDT}(\omega)||} \tag{2.58}$$

where γ is the friction parameter, A_γ is the 'velocity' of adaptation (homogeneous to an inverse time) and $||\Delta_{FDT}(\omega)||$ is the norm

$$||\Delta_{FDT}(\omega)|| = \sqrt{\sum_{\omega<\omega_{cut}} \Delta^2_{FDT}(\omega)} \tag{2.59}$$

The adaptation process of the function $\gamma(\omega)$ is not done over a single time step Δt but over a full segment $N_{steps}\Delta t$We obtain therefore

$$\gamma^{(n+1)}(\omega) = \gamma^{(n)}(\omega) + \gamma A_\gamma \frac{\Delta_{FDT}(\omega)}{||\Delta_{FDT}(\omega)||}(N_{steps}\Delta t) \tag{2.60}$$

where the index n indicates the segment of the simulation ($n = 1, \ldots, N_{seg}$). The initial value of the friction function $\gamma^{(0)}(\omega) = \gamma_0$ is a free parameter of the method. Note that the adaptation process is done in the adQTB algorithm on a finite time segment. This means that the quantities estimated to compute $\Delta_{FDT}(\omega)$ are in principle statistical averages, but they are subject to statistical fluctuations. Hence, larger values of the parameter A_γ leads to a faster convergence, but $\Delta_{FDT}(\omega)$ can be estimated less precisely, which can have repercussions on the dynamics.

The adaptive quantum thermal bath method has been tested and use on several model systems with satisfactory results, and on Ne_{13} clusters where it was able to stop the spurious melting due to the ZPEL of the QTB method [117, 169]. Moreover, it was used to compute accurately radial distribution functions and vibrational spectra in liquid water [118]. However, it was never tested to compute transport coefficients, which is one of the goal of the this work and the results are exposed in Chapter 3.

2.7 Path-integral Quantum Thermal Bath

The final method presented in this Chapter is an hybrid version of the PI/RPMD method and the QTB method. As mentioned Section 2.4, in order to obtain a faster convergence with respect to the number of beads for the PI/RPMD method, Ceriotti et al. [151] introduced the idea of using a generalized Langevin equation. Lately, Brieuc et al. [77] formulated a procedure which combine the PI method with the quantum thermal bath to reach the same goal. A first version of the Path Integral Quantum Thermal Bath (PIQTB) it was applied to various anharmonic systems, with faster convergence than the standard RPMD method in terms of number of beads. In this Section, however, we propose an alternative and simpler derivation of the method, firstly derived by Thomas Plé during his PhD, which allows to avoid few numerical passages.

The main idea of PIQTB is to use the QTB formulation of power spectral density of the random force and adapt it to the PI case. Therefore, we obtain a colored noise Langevin whose spectrum depends on the number of beads. Up to now, we encountered several times the power spectral density for the Langevin random force, written in three ways:

- Classical and RPMD methods: $C_{RR}(\omega) = 2m\gamma k_B T$
- QTB method: $C_{RR}(\omega) = 2m\gamma\theta(\omega, T)$
- adQTB method: $C_{RR}(\omega) = 2m\gamma(\omega)\theta(\omega, T)$

All these definitions of the random force can be put under the general form

$$C_{RR}(\omega) = 2m\gamma k_B T\kappa(\omega, T) \tag{2.61}$$

where $\kappa(\omega, T)$ is the spectral thermal energy distribution function. All previous methods have a different expression of this function:

- Classical and PIQTB methods: $\kappa(\omega, T) = 1$
- QTB method: $\kappa(\omega, T) = \frac{\theta(\omega,T)}{k_B T}$
- adQTB method: $\kappa(\omega, T) = \frac{\gamma(\omega)\theta(\omega,T)}{\gamma k_B T}$

Now, the PIQTB method needs a new expression of $\kappa(\omega, T)$ depending on the number of beads P, which reduces to the QTB case when $P = 1$, and reduces to the standard RPMD case ($\kappa(\omega, T) = 1$) when $P \to \infty$.

Following the original derivation of Brieuc et al. [77], in order to find the expression for the function $\kappa(\omega, T)$ for the PIQTB, we consider the harmonic oscillator case of potential $V(x) = \frac{1}{2}m\omega^2 x^2$. Then, the mean squared fluctuations of the position x at temperature T is given by

$$(\langle x^2\rangle)^{h.o.} = \frac{\theta(\omega, T)}{m\omega^2} = \frac{\hbar}{2m\omega}\coth\left(\frac{\beta\hbar\omega}{2}\right) \tag{2.62}$$

where $\beta = 1/k_B T$. In the PIMD method (Section 2.4) we made use of the transformation from the P beads representation of coordinates $\{x_1, \ldots, x_P\}$ to the normal modes representation $\{q_0, \ldots, q_{P-1}\}$. In the particular case of the external potential being harmonic, the expression for the eigenfrequencies of the system can be written analytically as

$$\omega_j^2 = \omega^2 + \frac{4P^2}{\beta^2\hbar^2}\sin^2\left(\frac{j\pi}{P}\right) \tag{2.63}$$

The relation between the beads coordinates and the normal modes coordinates is given by the (discrete) Fourier transform

$$x_k = \frac{1}{\sqrt{P}}\sum_{j=0}^{P-1} q_j e^{2\pi ikj/P}$$

Then, we can write the mean squared fluctuations of the position of a single bead as

$$\langle x_k^2 \rangle = \frac{1}{P} \sum_{j=0}^{P-1} \langle q_j^2 \rangle \tag{2.64}$$

Also, for the harmonic potential we can solve analytically the equation of motion of each normal mode, and its position fluctuations is

$$\langle q_j^2 \rangle = \frac{\kappa_j(\omega_j, T)}{m\omega_j^2} \tag{2.65}$$

Therefore, using Eq. (2.62) and (2.64), the following expression should hold for the harmonic case of PIQTB:

$$\frac{1}{P} \sum_{j=0}^{P-1} \frac{\kappa_j(\omega_j, T)}{m\omega_j^2} = \frac{\theta(\omega, T)}{m\omega^2} \tag{2.66}$$

Thus, our goal is to find the expressions for $\kappa_j(\omega_j, T)$ of each normal mode, in order for Eq. (2.66) to hold true. In doing so, and by using their expression for the power spectral density of the random force (2.61), we ensure the correct positions fluctuations in the harmonic case, and consequently the correct average potential energy

$$\langle V \rangle = \frac{1}{P} \sum_{k=1}^{P} V(x_k) = \frac{\theta(\omega, T)}{2}$$

Introducing the following quantities

$$\begin{cases} u = \frac{\beta\hbar\omega}{2} \ (a) \\ h(u) = u \coth(u) \ (b) \\ u_j^2 = \left(\frac{\beta\hbar\omega_j}{2}\right) = u^2 + P^2 \sin^2\left(\frac{j\pi}{P}\right) = u^2 + \tilde{u}_j^2 \ (c) \\ H_j(\omega_j) = \frac{\beta}{P}\kappa_j(\omega_j, T) \ (d) \end{cases} \tag{2.67}$$

and explicitly separating the contribution of the polymer centroid mode $j = 0$, we rewrite Eq. (2.66) as follow

$$\sum_{j=0}^{P-1} H_j(\omega_j) \left(\frac{u}{u_j}\right)^2 = h(u) \tag{2.68}$$

The goal now is to find the expressions for all $H_j(\omega_j)$.

At this point, an important difference is drawn between the original method by Brieuc et al. [77] and the following derivation. Starting from the former, the choice made was to treat all normal modes in the same way, and uses the natural formulation of having the same spectrum $H_j(\omega_j) = H(\omega_j)$ for all modes $j = 0, \ldots, P$. Then, the function H is found numerically via a self-consistent iterative technique inspired by [150], which is not described in this work. Note that, for the PIQTB, momenta contains part of the quantum fluctuations, i.e.

$$\langle \frac{p_k^2}{2m} \rangle \geq \frac{K_B T}{2}$$

Hence, the centroid virial estimator for the kinetic energy (2.46) should be modified. Alternatively, following the idea of Ceriotti et al. [150], the mode of the centroid $j = 0$ can be treated classically, i.e. by imposing $\kappa(\omega_0, T) = k_B T$. Consequently, Eq. (2.68) becomes

$$\sum_{j=1}^{P-1} H(\omega_j) \left(\frac{u}{u_j}\right)^2 = h(u) - 1 \tag{2.69}$$

and the centroid virial estimator for the kinetic energy can be used safely.

The second solution of the PIQTB, which is reported in the following sections, lies on a different choice for the functions $H_j(\omega_j)$: each normal mode have a different spectrum, such that they all match at the shifted frequency of each mode (i.e. $H_j(\omega_j) = H(\omega)$). In this way, the method does not need a iterative solution of Eq. (2.68), but the functions $H_j(\omega)$ can be computed directly by rewriting Eq. (2.68) as

$$H(\omega) \left[1 + \sum_{j=1}^{P-1} \left(\frac{u^2}{u_j^2}\right)^2\right] = h(u) \tag{2.70}$$

where we used the fact that $H_i = H_j$, $\forall i, j$. If we explicit the expression for u_j^2 (2.67)-(c), we obtain the following expression for the power spectral density applied to the ring-polymer modes

$$H_j(\omega) = \frac{h(\sqrt{u^2 - \tilde{u}_j^2})}{1 + \sum_{j'=1}^{P-1} \frac{u^2 - \tilde{u}_j^2}{u^2 - \tilde{u}_j^2 + \tilde{u}_{j'}^2}} \tag{2.71}$$

for all frequencies ω greater than $\tilde{\omega}_j$.

As previously stated, the normal mode $j = 0$, corresponding to the centroid can be treated differently from the others, in order to use the central virial estimator for the kinetic energy (2.46). Moreover, in our case, we prefer this option because we are interested in dynamical observables (in particular the diffusion coefficient), which in the PIMD method are obtained from centroid properties. Hence, we choose the following expression for our target functions

$$\begin{cases} H_0(\omega) = 1 \\ H_j = H, \ \forall j > 0 \end{cases} \tag{2.72}$$

Then, we can rewrite the solution of Eq. (2.68) as

$$H_j(\omega) = \frac{h(\sqrt{u^2 - \tilde{u}_j^2}) - 1}{\sum_{j'=1}^{P-1} \frac{u^2 - \tilde{u}_j^2}{u^2 - \tilde{u}_j^2 + \tilde{u}_{j'}^2}} \tag{2.73}$$

for all modes other than the centroid $j = 0$, and all frequencies ω greater than $o\tilde{m}ega_j$. Once the expression for the functions $\kappa(\omega, T)$ is obtained for all frequencies of all normal modes j, the power spectral density of the PIQTB noise can be computed and applied in the step O of the BAOAB integration scheme.

2.8 Conclusion: where the methods are used in this work

In this Chapter, we described the computational details of the molecular dynamics methods used in this work. All of them have in common the initial assumption of Born-Oppenheimer approximation, a trajectory-based picture of the particle dynamics, and the use of Langevin equation to ensure sampling from the Canonical ensemble [76] - (N, V, T) when the Langevin thermostat is used, (N, P, T) when both Langevin thermostat and barostat are used. Two class of methods are called 'quantum', as they include Nuclear Quantum Effects on the dynamics, with different degrees of approximation. The first class are based on the Path Integral formalism (see Section 2.4), the second class use a quantum thermostat (see Sections 2.5 and 2.6). An hybrid method between the two classes is described in Section 2.7.

These methods are tested and used in the following Chapters in this order:

- Chapter 3: the classical Langevin method (ClMD) and all quantum methods, namely (T)RPMD, QTB, adQTB and PIQTB, are assessed and compared on a model problem of diffusion of a quantum particle in a solid:
- Chapter 4: the simulations of ammonia hydrate systems are performed mainly with classical Langevin method. However, some results obtained as well via adQTB and (T)RPMD methods.

Appendix

A Liouville operator formalism

Given the phase-space trajectory $(\vec{x}(t), \vec{p}(t))$ in phase space, we can introduce the phase-space density density $\rho(\vec{x}(t), \vec{p}(t), t)$. Therefore, the evolution of the system is given by the time evolution of the generalized density [124]

$$\frac{d\rho}{dt} = \frac{\partial \rho}{\partial t} + \sum_{i=1}^{N} \left[\frac{\partial \rho}{\partial p_i} \frac{dp_i}{dt} + \frac{\partial \rho}{\partial x_i} \frac{dx_i}{dt} \right]$$

Theorem 2 (Liouville's theorem) *Under Hamilton's equations,*

$$\frac{d\rho}{dt} = 0$$

Another way to express Liouville's theorem is to state the incompressibility of the flux in the phase space i.e. the volume occupied by the system in the phase space does not change in time. Therefore, we can write Liouville equation

$$\frac{\partial \rho}{\partial t} = -\imath \hat{\mathscr{L}} \rho \tag{2.74}$$

where $\hat{\mathscr{L}}$ is Liouville operator, defined as follows:

$$\imath \hat{\mathscr{L}} = \sum_{i=1}^{N} \left[\frac{\partial H}{\partial p_i} \frac{\partial}{\partial x_i} - \frac{\partial H}{\partial x_i} \frac{\partial}{\partial p_i} \right] \tag{2.75}$$

Hence, the solution of the (2.74) for a small time interval Δt

$$\rho(t + \Delta t) = e^{-\imath \hat{\mathscr{L}} \Delta t} \rho(t) \tag{2.76}$$

We can also write Liouville operator in the following way, in order to highlight explicitly the contribution coming from the positions and the contribution of the momenta

$$\imath \hat{\mathscr{L}} = \imath (\hat{\mathscr{L}}_x + \hat{\mathscr{L}}_p) = \sum_{i=1}^{N} \left[\frac{p_i}{m_i} \frac{\partial}{\partial x_i} + f_i \frac{\partial}{\partial p_i} \right]$$

The effects of the two contributions on the density of the system during the integration are the following:

- $\hat{\mathscr{L}}_x$: taken this part individually, we obtain $\rho(t + \Delta t) = \rho(\vec{p}, \vec{x} + \frac{\vec{p}}{m} \Delta t, t)$, which is a general translation of all positions;
- $\hat{\mathscr{L}}_p$: taken this part individually, we obtain $\rho(t + \Delta t) = \rho(\vec{p} + \vec{f} \Delta t, \vec{x}, t)$, which is a general translation of all momenta.

However, the combined effect is not trivial and we need to rely on an approximation to split the two contributions and integrate separately positions and momenta. We consider the general operators/matrices $n \times n$ A, B and a real parameter λ. We state the Lie-Trotter product formula [143]

$$e^{\lambda(A+B)} = \lim_{N\to\infty} \left(e^{\lambda A/N} e^{\lambda B/N}\right)^N \tag{2.77}$$

This formula is generalized by the Baker–Campbell–Hausdorff formula for non commutative operators [144]. Then, if we consider the following splitting:

$$e^{\lambda(A+B)} \simeq e^{\lambda A} e^{\lambda B}$$

It is easy to demonstrate that it would lead to an error $\mathcal{O}(\lambda^2)$ i.e. of the second order in λ. In order to obtain an error $\mathcal{O}(\lambda^3)$, we use the following symmetric splitting:

$$e^{\lambda(A+B)} \simeq e^{\lambda B/2} e^{\lambda A} e^{\lambda B/2}$$

which in terms of Liouville operator becomes

$$e^{\imath\hat{\mathscr{L}}\Delta t} \simeq e^{\imath\hat{\mathscr{L}}_B \Delta t/2} e^{\imath\hat{\mathscr{L}}_A \Delta t} e^{\imath\hat{\mathscr{L}}_B \Delta t/2} \tag{2.78}$$

Therefore, it is possible to integrate the equations of motion with an error of the order of Δt^3, which is negligible if the integration time step is small enough. The latter integration scheme that is applied is the Velocity-Verlet algorithm [172]. The BAOAB method developed by Leimkhuler et al. [133–135] constitutes a generalization of this formalism to the case of Langevin dynamics.

B Harmonic Analysis of Stationary Stochastic Processes

Let us suppose $s(t)$ is a stationary stochastic process i.e. its probability distribution does not change in time [170]. For any signal $s(t)$ in a limited temporal window, it is possible to compute its energy spectral density and the power spectral density i.e. the energy spectral density per unit time. The spectrum of a physical phenomena contains interesting information about its properties and it is particularly useful in the study of stochastic processes. Consider a signal $s(t)$, its total energy E is given by

$$E = \int_{-\infty}^{+\infty} dt\ |s(t)|^2 \tag{2.79}$$

for which we can define the energy spectral density (ESD) as

$$\hat{S}(\omega) = |s(\omega)|^2 \tag{2.80}$$

where we defined $s(\omega)$ as the Fourier transform $\mathcal{F}\{s(t)\}$ in the following way:

$$s(\omega) = \int_{-\infty}^{+\infty} dt\ s(t) e^{-2\pi\imath\omega t}$$

The same definitions are valid in the case of the total power of a signal

$$P = \lim_{T\to\infty} \frac{1}{T} \int_0^T dt\ |s(t)|^2 \tag{2.81}$$

The Fourier transform of $s(t)$ now is defined as

$$s(\omega) = \frac{1}{T}\int_0^T dt\; s(t)e^{-\imath\omega t}$$

and the power spectral density (PSD) as

$$\hat{S}(\omega) = \lim_{T\to\infty} \mathbb{E}\left[|s(\omega)|^2\right] \tag{2.82}$$

where $\mathbb{E}$ is the expected value, which can be written explicitly in the following way, for $s(t)$ complex in general

$$\mathbb{E}\left[|s(\omega)|^2\right] = \mathbb{E}\left[\frac{1}{T}\int_0^T dt\; s^*(t)e^{\imath\omega t}\int_0^T dt'\; s(t')e^{-\imath\omega t'}\right] = \\ \frac{1}{T}\int_0^T dt\; \frac{1}{T}\int_0^T dt'\; \mathbb{E}\left[s^*(t)s(t')\right]e^{\imath\omega(t-t')} \tag{2.83}$$

We consider the definition of the PSD (2.82) and we take the limit with $T \to \infty$. In this way, we obtain is the Wiener–Khinchin theorem

Theorem 3 (Wiener–Khinchin) *For an absolutely integrable $C_{ss}(t)$, the PSD is given by:*

$$\hat{S}(\omega) = \int_{-\infty}^{+\infty} C_{ss}(t)e^{-\imath\omega t}dt = C_{ss}(\omega) = \mathcal{F}\{C_{ss}(t)\} \tag{2.84}$$

where the expected value $\mathbb{E}\left[s^*(t)s(t')\right]$ is expressed as a TCF with $\Delta t = (t - t')$

$$\mathbb{E}\left[s^*(t)s(t')\right] = \langle s^*(t)s(t+\Delta t)\rangle = C_{ss}(\Delta t)$$

Chapter 3

Nuclear Quantum Effects on hydrogen diffusion: a model study

3.1 Diffusion in solids . . . 47
3.1.1 Brownian motion and the Langevin equation . . . 47
3.1.2 Particle in an external potential . . . 49
3.2 Exactly solvable model . . . 50
3.2.1 Sum-over-states method . . . 50
3.2.2 Free particle . . . 51
3.2.3 Particle in a fixed periodic lattice . . . 53
3.3 Hydrogen diffusion in a 2D lattice . . . 54
3.3.1 Model systems . . . 55
3.3.2 Simulation setup of MD-based methods . . . 57
3.3.3 Diffusion coefficient in a fixed lattice: quantum vs. classical 58
3.3.4 Quantum Thermal Bath: a critical analysis . . . 61
3.3.5 Path-Integral Quantum Thermal Bath: a possible compromise? . . . 66
3.4 Isotope effect . . . 69
3.5 Diffusion in flexible lattice . . . 71
3.6 Conclusions . . . 71
Appendix . . . 73
A Quantum diffusion coefficient calculations . . . 73
B Diffusion coefficient tables . . . 74
C Diffusion events and friction dependence . . . 74
D Zero-point-energy leakage correction . . . 77

In this Chapter, we compare different molecular dynamics methods on the problem of the diffusion of a particle in a solid. We focus in particular on the diffusion of hydrogen and deuterium, and we aim at assess and comparing the results of the methods in a model system

of 2D material. The use of an analytical model allows us to tune the parameters and achieve the desired testing conditions for the different methods. Moreover, it allows us to develop an exact solution for the diffusion coefficient of the particle in a fixed periodic potential. Our ultimate goal is to probe the advantages and limits of quantum thermal baths (both standard and adaptive versions) for the study of diffusion, compared to the accurate, yet approximated and expensive ring-polymer methods. Unfortunately, we show that quantum thermal baths are not suited to compute diffusion coefficient, and we explain the reasons behind this finding. Furthermore, we test the use of a colored bath to improve the convergence of the ring-polymer method in terms of number of replicas, again with negative results for diffusion.

3.1 Diffusion in solids

The main fundamental problem of quantum dynamics is the impossibility of resolution of the time-dependent Schrödinger equation for large systems, due to its exponential scaling with the number of degrees of freedom. This is not only valid for electrons, but also for nuclei, even if we are not interested in the exchange and quantum coherence properties. In the Introduction, we have shown that NQEs of light nuclei are fundamental phenomena in a vast amount of complex systems. Despite the fact that much progress has been done, the computation of time-dependent properties of the nuclei remains a very important theoretical challenge. Many techniques and methods are being developed in recent years [76]. However, currently, these methods are all approximations and there is not a unified quantum theory for non-static systems. Only two limit cases can be shown to be exactly captured by most of approximated methods: the classical (high temperature) limit and the case of system with harmonic potential. Outside these limiting cases, precise criteria for comparing different approximate methods are lacking. The discussion of the full extent of simulation methods to compute dynamical properties is outside the scope of this work. Here, we will focus on trajectory-based methods as they provide computationally efficient approximations for treating light nuclei as quantum particle in complex environments.

In this Chapter, we consider hydrogen as light nucleus and the aim is to illustrate and study new methods that allow the simulation of its diffusion properties in solids. Although its mass is much heavier than the electron mass ($m_H = 1836 m_e$), the hydrogen atom has a De Broglie wavelength at room temperature of the order of the Å. For a generic solid material, we then expect that the quantum delocalization of the hydrogen has a major impact on the properties of the system and the NQEs cannot be neglected [173], and more particularly zero-point motion which allows the hydrogen to diffuse even in a very low temperature regime. Tunneling, another typical quantum phenomena, can also influence hydrogen diffusion.

Before tackling more specifically the problem of H diffusion in solids, we examine a paradigmatic example of a diffusive process: the Brownian motion. Notice that, in this simplified case, the diffusing particle does not interact with any external potential.

3.1.1 Brownian motion and the Langevin equation

The Brownian motion [132] is the random motion of a small particle in a viscous medium. Its experimental observation found a first theoretical explanation by Einstein [174], which was later confirmed by Perrin in 1909 [175]. Einstein firstly described the problem in terms of a diffusion equation for the Brownian particle: he considered a one dimensional system, in which he defined a continuous probability density for the Brownian particles $\rho(x,t)$, depending on both the position x and the time t, and he introduced the diffusion coefficient D_x. Then, the diffusion equation for the particle's density is written as

$$\frac{\partial \rho(x,t)}{\partial t} = D_x \frac{\partial^2 \rho(x,t)}{\partial x^2} \tag{3.1}$$

The formal solution of this equations gives a normal density distribution of the form $\rho(x,t) \propto e^{-\frac{x^2}{4Dt}}$. Hence, the first two moments of the distribution are derived: the mean displacement is vanishing, resulting in the absence of a drift in the motion of the Brownian particle; on the contrary, the variance - or mean-squared displacement $\langle (x(t) - x(0))^2 \rangle$ - is non-vanishing

$$\langle x^2 \rangle \sim 2D_x t \tag{3.2}$$

where we considered the initial position $x(0) = 0$. In all previous formulas we also denoted the diffusion constant with a subscript x to indicate that Einstein's result is valid in the position space. Einstein's main result is that the displacement of a Brownian particle is proportional to the squared root of time. This means that the Brownian particle follows a random walk in its diffusive motion [176]. Furthermore, based on Eq. (3.2), Einstein derived an expression for the diffusion coefficient directly from the definition of the mean-squared displacement

$$D_x = \lim_{t\to\infty} \frac{1}{t2d} \langle |\mathbf{r}(t) - \mathbf{r}(0)|^2 \rangle \tag{3.3}$$

where $\mathbf{r}(t)$ is the particle position at the generic time t, and d is the dimensionality of the system. The average $\langle \dots \rangle$ is taken over the ensemble - in our case, Canonical ensemble - at thermal equilibrium. Introducing the friction parameter γ of the fluid and using the Equipartition theorem (1), Einstein obtains the relation

$$D_x = \frac{k_B T}{m\gamma} \tag{3.4}$$

Eq. (3.4), known as the Einstein's relation for the diffusion coefficient, relates directly the friction parameter γ of the fluid to the main transport coefficient of diffusion. Eq. (3.4) is an example of Fluctuation-Dissipation relation [154], as it links the dissipation parameter γ to the displacement fluctuations expressed by the diffusion coefficient (3.3). The theory of Brownian motion is one of the simplest approximate ways to treat a diffusive system in which fluctuations play a major role in the dynamics.

Einstein's result (3.4) can be written in a equivalent way in terms of the velocity-velocity time correlation function (TCF) $C_{\mathbf{vv}}(t)$ [124]

$$D_x = \lim_{T\to\infty} \frac{1}{Td} \int_0^T dt_1 \int_0^t dt_2 \, \langle \mathbf{v}(t_1)\mathbf{v}(t_2) \rangle = \frac{1}{d} \int_0^\infty dt \, \langle \mathbf{v}(0)\mathbf{v}(t) \rangle = \frac{1}{d} \int_0^\infty dt C_{\mathbf{vv}}(t) \tag{3.5}$$

where T is the total (simulation) time and d is the dimensionality of the system. We can also introduce the Fourier transform of the velocity autocorrelation function

$$\tilde{C}_{\mathbf{vv}}(\omega) = \frac{1}{2\pi} \int_{-\infty}^{+\infty} dt \, e^{-i\omega t} \, C_{\mathbf{vv}}(t) \tag{3.6}$$

which takes also the name of density of vibrational states, the power spectrum or spectral density, as it encodes the information about the vibrational modes of the system. The diffusion coefficient can be computed equivalently as

$$D_x = \frac{1}{d} \lim_{\omega\to 0} \tilde{C}_{\mathbf{vv}}(\omega) \tag{3.7}$$

where d is the dimensionality of the system.

The Langevin equation was introduced as an approach to model Brownian motion [132]. It builds a microscopic and stochastic dynamics by the addition of two terms to the equations of motion for a free particle: a frictional force of friction coefficient γ, and a random force. The former models the systematic effect of the viscous medium in which the Brownian particle moves. The random force aims at modeling the random collisions that the Brownian particle has with the surrounding particles of the medium. Thus, the Langevin equation has the following form:

$$m\frac{d^2x}{dt^2} = -\gamma m\frac{dx}{dt} + m\xi(t) \tag{3.8}$$

for a 1D particle of mass m. The force $m\xi(t)$ is a white noise random variable, for which the two following properties hold:

$$\begin{cases} \langle \xi(t) \rangle = 0 \\ \langle \xi(t_1)\xi(t_2) \rangle = 2D\delta(t_2 - t_1) \end{cases} \tag{3.9}$$

The physical reason behind this stochastic process introduced by Langevin is to model the random collisions in the viscous medium. These collisions result in no net drift for the particle, hence the first property. Moreover, after a punctual collision in time, the second property makes the system lose memory of its condition before the collision, in such a way that the random force time correlation function vanish. By solving the system of equations (**??**) and using the Equipartition theorem (1), we find the expression for the diffusion coefficient in the velocity space

$$D_v = \frac{\gamma k_B T}{m} \tag{3.10}$$

and in the position space

$$D_x \simeq \frac{\sigma_x^2}{2t} = \frac{D}{\gamma^2} = \frac{k_B T}{m\gamma}$$

which is equivalent to the Einstein's expression (3.4). From this point onward, we refer to the diffusion coefficient in the position space with the symbol D.

3.1.2 Particle in an external potential

We introduce now the presence of the lattice in our problem, which translates in adding an external potential $U(\mathbf{r}_1, \ldots, \mathbf{r}_{N+1})$ depending in general on all particle positions. Notice that, within the Born-Oppenheimer approximation, this potential energy surface (PES) can be an analytical expression, as in this Chapter, or from a force field as in Chapter 4, or computed via *ab initio* methods. We assume the N to be the number of atoms of the lattice, and a single diffusing particle. The classical Hamiltonian of the problem is then

$$\mathcal{H} = \sum_{i=1}^{N+1}\left(\frac{|\mathbf{p}_i|^2}{2m_i}\right) + U(\mathbf{r}_1, \ldots, \mathbf{r}_{N+1}) \tag{3.11}$$

where $\mathbf{p}_i$ is the momentum of the particle i. The Langevin equation for the particle i is

$$m\frac{d^2\mathbf{r}_i}{dt^2} = -\gamma m\frac{d\mathbf{r}_i}{dt} + m\xi(t) + \mathbf{F}_i(t) \tag{3.12}$$

where we added to (3.8) the external force $\mathbf{F}_i(t)$ computed from the potential U at time t. The diffusion coefficient can be computed in the same manner via Eq. (3.3), (3.5) or (3.7) equivalently.

In the classical case, we can assume that the potential for the diffusing particle is a series of (N) wells, separated by potential energy barrier ΔU, which can be also called activation energy E_a. We can then introduce the empirical law that relates the diffusion coefficient to the activation energy E_a and the temperature at which the system is thermalized

$$D(T) = D_0 e^{-\beta E_a} \tag{3.13}$$

which takes the name of Arrhenius law [177, 178]. Note that this law is valid in more general cases, for which the activation energy is not equivalent to the potential energy barrier ΔU. The pre-exponential D_0 is in principle also temperature dependent [179], but it is generally considered constant as its variation with T is slower then the exponential term. The Arrhenius law therefore simply describes the diffusion process as a series of jumps over the free energy barrier at a given temperature T. Two regimes are possible: for $k_B T >> E_a$, the thermal energy of the particle always activate the diffusion process and $D(T)$ tends to the limit of a free particle; on the contrary, for $k_B T << E_a$, the diffusion is exponentially damped. In this regime, the diffusion process is a rare event, and the particle spends most of the time around the equilibrium position at the bottom of the well, and performs fast and sudden jumps from one well to the other. This is exactly the regime we are focusing on in this Chapter.

The quantum version of the problem under exam has exactly the form of the classical problem, with the hamiltonian operator being

$$\hat{\mathcal{H}} = \sum_{i=1}^{N+1} \frac{|\hat{\mathbf{p}}_i|^2}{2m_i} + U(\hat{\mathbf{r}}_1, \ldots, \hat{\mathbf{r}}_{N+1}) \tag{3.14}$$

where $\hat{\mathbf{p}}_i$ and $\hat{\mathbf{r}}_i$ are now the momentum and position operators respectively of the ith atom and m_i is its atomic mass. Definitions of quantum TCFs (standard (2.38) or Kubo-tranformed (2.39)) differs from the classical version (2.13). However, as we are interested in the diffusion coefficient, for all of them the Eq. (3.7), i.e. the limit of $\omega \to 0$ of the power spectral density, is the same.

3.2 Exactly solvable model

3.2.1 Sum-over-states method

In full generality, our ideal solution of the quantum problem described in the previous Section would consist in solving the time-dependent Schrödinger equation (2.7), which becomes quickly an impossible task for realistic systems due to the curse of dimensionality. However, for the simplified problem of a single hydrogen atom in a fixed two-dimensional lattice some further efforts can be done in this direction.

Our goal is computing the diffusion coefficient from the evaluation of the velocity auto-correlation function. By definition, its explicit expression for a quantum particle of mass m

and momentum operator $\hat{\mathbf{p}}$ has the form

$$C_{\hat{\mathbf{v}}\hat{\mathbf{v}}}(t) = Tr\left[\frac{e^{-\beta\hat{\mathcal{H}}}}{\hat{\mathcal{Z}}} e^{-i\frac{\hat{\mathcal{H}}t}{\hbar}} \frac{\hat{\mathbf{p}}}{m} e^{i\frac{\hat{\mathcal{H}}t}{\hbar}} \frac{\hat{\mathbf{p}}}{m}\right] \tag{3.15}$$

where $\hat{\mathcal{H}}$ is the Hamiltonian operator of the system, $\hat{\mathcal{Z}}$ is the quantum partition function, $\hat{\mathbf{p}}$ is the momentum operator, m is the mass of the particle, $\hbar$ is the reduced Planck constant, and $\beta = 1/k_B T$ with k_B the Boltzmann constant and T the temperature.

If we assume to have a solution of the Schrödinger equation (2.7) for the quantum particle in terms of the eigenstates $\{|\phi_n\rangle\}$ and eigenvalues $\{\mathcal{E}_n\} = \{\hbar\omega_n\}$ of $\hat{\mathcal{H}}$, the trace in Eq. (3.15) can be recast as

$$\begin{aligned} C_{\hat{\mathbf{v}}\hat{\mathbf{v}}}(t) &= \sum_n \frac{e^{-\beta\mathcal{E}_n}}{\hat{\mathcal{Z}}} e^{-i\omega_n t} \langle\phi_n| \frac{\hat{\mathbf{p}}}{m} e^{+\frac{i\hat{\mathcal{H}}t}{\hbar}} \frac{\hat{\mathbf{p}}}{m} |\phi_n\rangle \\ &= \sum_{n,l} \frac{e^{-\beta\mathcal{E}_n}}{\hat{\mathcal{Z}}} e^{-i(\omega_l-\omega_n)t} \frac{|\langle\phi_n| \hat{\mathbf{p}} |\phi_l\rangle|^2}{m^2} \end{aligned} \tag{3.16}$$

where we used the completeness relation $\sum_l |\phi_l\rangle \langle\phi_l| = \mathbb{1}$. In Equation 3.16 it will be crucial to evaluate the matrix elements, $\langle\phi_n| \hat{\mathbf{p}} |\phi_l\rangle$. To this end, we will first consider the simple case of a free particle and then we move on to a particle in a fixed periodic lattice.

3.2.2 Free particle

Although the diffusion of a free particle is not particularly insightful, the calculation of the velocity TCF (3.15) is particularly instructive to elucidate our approach, which will be then extended to a particle in a periodic lattice. In absence of external force, the Hamiltonian has the simple form

$$\hat{\mathcal{H}} = \frac{\hat{\mathbf{p}}^2}{2m} \tag{3.17}$$

We introduce the basis of plane waves, which are eigenstates of this simple Hamiltonian:

$$|\phi_{\mathbf{k}}\rangle = \frac{1}{\sqrt{2\pi V}} e^{i\mathbf{k}\cdot\mathbf{r}} \tag{3.18}$$

where $\mathbf{k}$ is the wave-vector in reciprocal space, V is the volume, and $\mathbf{r}$ is the position of the particle. We can thus write the general matrix element element appearing in Eq. (3.16) as

$$\langle\phi_{\mathbf{k}'}| \hat{\mathbf{p}} |\phi_{\mathbf{k}}\rangle = \hbar\mathbf{k}\delta(\mathbf{k}-\mathbf{k}') \tag{3.19}$$

and Equation 3.16, after integration of the resulting Gaussian integral, now becomes

$$C_{\hat{\mathbf{v}}\hat{\mathbf{v}}}(t) = \frac{k_B T}{m} \tag{3.20}$$

Interestingly now the velocity autocorrelation function is time-independent, as it should be for a free particle. We can thus obtain the Fourier transform as

$$\tilde{C}_{\hat{\mathbf{v}}\hat{\mathbf{v}}}(\omega) = \int dt C_{\hat{\mathbf{v}}\hat{\mathbf{v}}}(t) e^{i\omega t} = \frac{2\pi k_B T}{m} \delta(\omega) \tag{3.21}$$

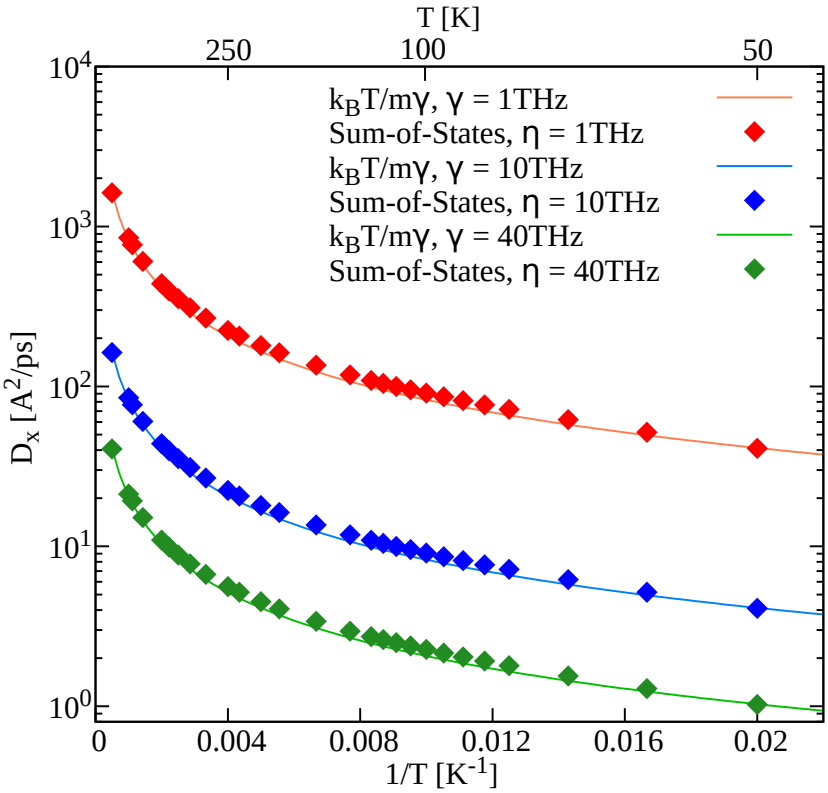

Figure 3.1: Sum-over-state solution for the diffusion coefficient of a free quantum particle (diamond points) compared to Eq. (3.4) (solid line) for different values of $\eta = \gamma$.

The expression is, up to this point, exact. To obtain an expression which can be dealt with numerically, we now substitute the delta function of Equation 3.21 with a Cauchy distribution centered at $\omega_0 = 0$ with a parameter η, which controls the width of the distribution, and has the dimensions of a inverse time. Thus, Equation 3.21 can be re-written as

$$\tilde{C}_{\hat{v}\hat{v}}(\omega) \simeq \frac{2\pi k_B T}{m} \frac{\eta/\pi}{\omega^2 + \eta^2} \tag{3.22}$$

Thanks to this substitution, we can compute the diffusion coefficient as the zero-frequency component of the Fourier transform of the velocity autocorrelation function

$$D_x(T) = \frac{1}{2}\tilde{C}_{vv}(\omega = 0) = \frac{k_B T}{m\eta} \tag{3.23}$$

hence, the introduction of the Cauchy distribution in (3.21) and the parameter η avoids to find a infinite diffusion coefficient for the entirely free particle. Moreover, Eq. (3.23) can be compared with the classical well-known expression of the diffusion coefficient in the presence of a friction characterized by coefficient γ (as in the Langevin equation (3.12)).

$$D_x^{Cl}(T) = \frac{k_B T}{m\gamma} \tag{3.24}$$

The parameter η has the same dimension of γ, and we can give it the physical interpretation of the friction of the Brownian motion. Figure 3.1 shows the Sum-over-States (SoS) diffusion

coefficients as function of inverse temperature $1/T$, computed for different values of η, compared to classical formula (3.24) for a Brownian particle with friction parameter $\gamma = \eta$. As expected, classical and quantum solutions coincide, which verifies Eq. (3.23) for a free particle, and benchmark the code used to compute the SoS diffusion coefficients.

3.2.3 Particle in a fixed periodic lattice

We now introduce the presence of the two-dimensional lattice into the problem. As a first step, the heavy atoms of the lattice are considered fixed in their equilibrium positions $\mathbf{R}_{ij}^{(0)} = i\mathbf{a} + j\mathbf{b}$, where $\mathbf{a}$ and $\mathbf{b}$ are the lattice vectors, hence preserving the lattice symmetry. The interaction potential appearing in Eq. (3.14) between the hydrogen particle and the lattice have now the general form

$$U(\mathbf{r}; \{\mathbf{R}_{ij}^{(0)}\}) = \sum_j U(\mathbf{r} - \mathbf{R}_{ij}^{(0)}) \tag{3.25}$$

where the position operator $\mathbf{r}$ of the hydrogen particle is the only variable and the $\{\mathbf{R}_{ij}^{(0)} = i\mathbf{a} + j\mathbf{b}\}$ are fixed. The time-independent Schrödinger equation for the problem in the position representation is therefore

$$\hat{\mathcal{H}}\psi_{\mathbf{k}n}(\mathbf{r}) = \left(\frac{\hat{\mathbf{p}}^2}{2m} + U(\mathbf{r}; \{\mathbf{R}_{ij}^{(0)}\})\right)\psi_{\mathbf{k}n}(\mathbf{r}) = \mathcal{E}_{\mathbf{k}n}\psi_{\mathbf{k}n}(\mathbf{r}) \tag{3.26}$$

where $\mathcal{E}_{\mathbf{k}n}$ are the eigenvalues and $\psi_{\mathbf{k}n}(\mathbf{r})$ the eigenfunctions of the Hamiltonian $\hat{\mathcal{H}}$. The index $\mathbf{k}$ is again the wave-vector and the index n is the band number. As solutions of (3.26) we introduce the Bloch functions

$$\psi_{\mathbf{k}n}(\mathbf{r}) = e^{+i\mathbf{k}\cdot\mathbf{r}}u_{\mathbf{k}n}(\mathbf{r}) \tag{3.27}$$

The functions $u_{\mathbf{k}n}$ have the same periodicity of the lattice, i.e. $u_{\mathbf{k}n}(\mathbf{r}+\mathbf{R}_{ij}^{(0)}) = u_{\mathbf{k}n}(\mathbf{r})$, $\forall i, j$, for which is valid the Bloch theorem

Theorem 4 (Bloch Theorem)

$$\psi_{\boldsymbol{k}n}(\boldsymbol{r} + \boldsymbol{R}_{ij}^{(0)}) = e^{+i\boldsymbol{k}\cdot\boldsymbol{R}_{ij}^{(0)}}\psi_{\boldsymbol{k}n}(\boldsymbol{r})$$

As for the free particle, our goal is to compute the diffusion coefficient from the velocity autocorrelation function. Therefore, we evaluate the matrix elements of Eq. (3.16) as

$$\begin{aligned}\langle\psi_{n'\mathbf{k}'}|\,\hat{\mathbf{p}}\,|\psi_{n\mathbf{k}}\rangle &= \int d\mathbf{r}\; e^{-i\mathbf{k}'\cdot\mathbf{r}}u^*_{\mathbf{k}'n'}(\mathbf{r})\;\hat{\mathbf{p}}e^{+i\mathbf{k}\cdot\mathbf{r}}u_{\mathbf{k}n}(\mathbf{r}) = \\ &= \int d\mathbf{r}\; e^{i(\mathbf{k}-\mathbf{k}')\cdot\mathbf{r}}u^*_{\mathbf{k}'n'}(\mathbf{r})\,(\hbar\mathbf{k} - i\hbar\nabla_{\mathbf{r}})\,u_{\mathbf{k}n}(\mathbf{r})\end{aligned}$$

The expression is further simplified, noting that any position of the particle can be related to the lattice vectors as $\mathbf{r} = i\mathbf{a} + j\mathbf{b} + \tilde{\mathbf{r}}$. By exploiting the periodicity of $u_{\mathbf{k}n}(\mathbf{r})$, we obtain

$$\begin{aligned}\langle \psi_{n'\mathbf{k}'} | \, \hat{\mathbf{p}} \, | \psi_{n\mathbf{k}} \rangle = \sum_{ij} e^{i(\mathbf{k}-\mathbf{k}')\cdot\mathbf{R}_{ij}^{(0)}} \int d\tilde{\mathbf{r}} \; e^{i(\mathbf{k}-\mathbf{k}')\cdot\tilde{\mathbf{r}}} u^*_{\mathbf{k}'n'}(\tilde{\mathbf{r}}) \left(\hbar\mathbf{k} - i\hbar\nabla_{\tilde{\mathbf{r}}}\right) u_{\mathbf{k}n}(\tilde{\mathbf{r}}) = \\ = \delta^{\mathbf{k}'}_{\mathbf{k}} \int d\tilde{\mathbf{r}} \; e^{i(\mathbf{k}-\mathbf{k}')\cdot\tilde{\mathbf{r}}} u^*_{\mathbf{k}'n'}(\tilde{\mathbf{r}}) \left(\hbar\mathbf{k} - i\hbar\nabla_{\tilde{\mathbf{r}}}\right) u_{\mathbf{k}n}(\tilde{\mathbf{r}}) = \\ = \langle u_{n'\mathbf{k}} | \left(\hbar\mathbf{k} - i\hbar\nabla_{\tilde{\mathbf{r}}}\right) | u_{n\mathbf{k}} \rangle\end{aligned}$$

where we introduced a discretization of the wave-vectors $\mathbf{k}$ through the Born-von Karman periodic boundary conditions, and make use of the Kronecker function $\delta^{\mathbf{k}'}_{\mathbf{k}}$. In the last term, we also recognize the velocity operator of the Bloch particle, which can be written in terms of the derivatives of the eigenvalues of the Hamiltonian $\{\mathcal{E}_{n\mathbf{k}}\}$ with respect to the $\mathbf{k}$ vector in the reciprocal space, as

$$\langle u_{n\mathbf{k}} | \, \hat{\mathbf{v}} \, | u_{n\mathbf{k}} \rangle = \langle u_{n\mathbf{k}} | \left(\hbar\mathbf{k} - i\hbar\nabla_{\tilde{\mathbf{r}}}\right) | u_{n\mathbf{k}} \rangle = \frac{1}{\hbar}\nabla_{\mathbf{k}}\mathcal{E}_{nk} \tag{3.28}$$

Notice that in Eq. (3.28) we consider only the index $n = n'$, as we are interested in the zero-frequency limit $\omega = 0$ for the diffusion coefficient.

Thus, Eq. (3.16) takes the following form for a Bloch particle in a fixed periodic lattice

$$C_{\hat{\mathbf{v}}\hat{\mathbf{v}}}(t) = \sum_{n,l,\mathbf{k}} \frac{e^{-\beta\mathcal{E}_{n\mathbf{k}}}}{\hat{\mathcal{Z}}} e^{-i(\omega_{l\mathbf{k}} - \omega_{n\mathbf{k}})t} \frac{1}{\hbar^2} \left(\nabla_{\mathbf{k}}\mathcal{E}_{nk}\right)^2 \tag{3.29}$$

Its Fourier transform is expressed as

$$\widetilde{C}_{\hat{v}\hat{v}}(\omega) = \sum_{n,l,k} \frac{e^{-\beta\mathcal{E}_{nk}}}{\hat{\mathcal{Z}}} \delta(\omega_{l\mathbf{k}} - \omega_{n\mathbf{k}}) \frac{1}{\hbar^2} \left(\nabla_{\mathbf{k}}\mathcal{E}_{nk}\right)^2 \tag{3.30}$$

Until this point, the derivation is exact. In Eq. (3.30) we use the same substitution of the Dirac delta $\delta(\omega)$ with the Cauchy distribution of parameter η, as explained in the free particle solution, which leads to the final expression

$$D_{SoS}(T, \eta) = \frac{1}{\eta} \sum_{n,\mathbf{k}} \frac{e^{-\beta\mathcal{E}_{n\mathbf{k}}}}{\hat{\mathcal{Z}}} \frac{1}{\hbar^2} \left(\nabla_{\mathbf{k}}\mathcal{E}_{nk}\right)^2 \tag{3.31}$$

We have shown that, apart from the free parameter η, by solving the eigenvalue problem given by Eq. (3.26), in a periodic fixed lattice, the fully quantum diffusion coefficient of a quantum particle can be computed. Implementation details of the Sum-over-State method are given in Appendix A.

3.3 Hydrogen diffusion in a 2D lattice

In the following Section, after the description of the model used, we present and discuss the results of different MD methods. In particular, we compare the diffusion coefficients as a function of temperature $D(T)$ and we discuss the advantages and limits of each methods, with the help of the Sum-over-States method just described in the previous Section.

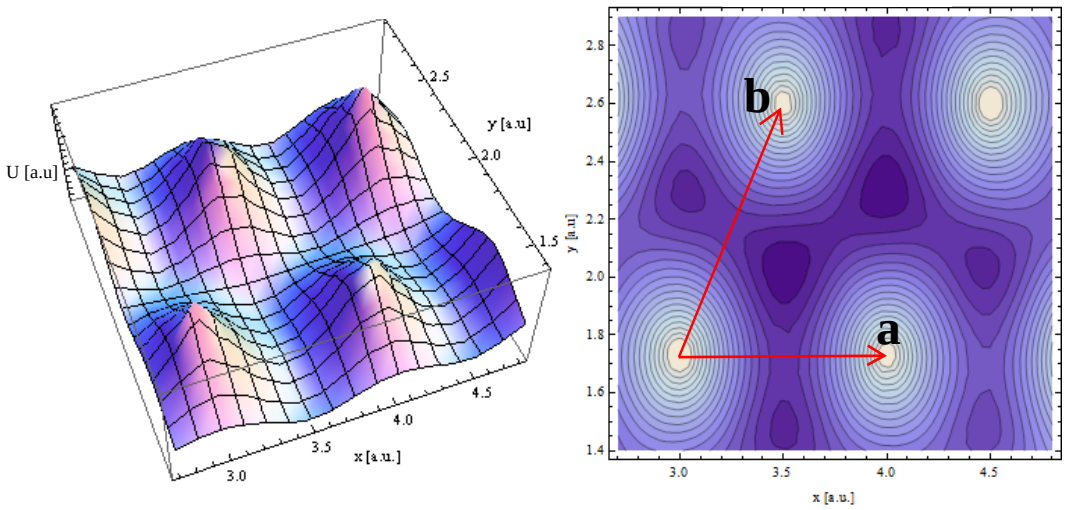

Figure 3.2: Portion of model potential energy surface in 3D (left) and contour plot (right), where also the lattice vectors (3.32) are represented.

3.3.1 Model systems

The model system to study diffusion is formed by the following elements. We consider a particle bearing the same mass of the H (or D) atom (m_H = 1.00784 amu and m_D = 2 m_H, respectively), moving in a bi-dimensional (2D) lattice. The time-independent Schrödinger equation for the problem has the form of Eq. (3.26). The lattice can be fixed, with the form of (3.25) or flexible.

The lattice system is a triangular lattice defined by means of two lattice vectors, **a** and **b**:

$$\mathbf{a} = a_{latt} \begin{pmatrix} 1 \\ 0 \end{pmatrix} ; \mathbf{b} = a_{latt} \begin{pmatrix} 1/2 \\ \sqrt{3}/2 \end{pmatrix} \tag{3.32}$$

where a_{latt} is the lattice constant. The triangular geometry is less effected to shear displacement, hence more stable than for instance a squared geometry. The lattice interacts with the moving H/D particle via an analytical potential with the simple form

$$V(d_1, \ldots, d_N) = \sum_{i=1}^{N} V_0 e^{-\frac{d_i}{\Delta}} \tag{3.33}$$

where i runs on the N atoms of the lattice, V_0 and Δ are two parameters of the potential and d_i is the distance if the light atom with each element of the lattice. Note that since we are in a 2D system the distance is $d_{iH} = \sqrt{(x_i - x_H)^2 + (y_i - y_H)^2}$. Figure 3.2 shows a portion of the potential energy surface (PES) created by the analytical model (3.33), in three dimensions (on the left) and as a contour plot (on the right), where also the lattice vectors (3.32) are represented. The highest peak of the are in correspondence on the equilibrium position of the lattice atoms $\{\mathbf{R}_{ij}^{(0)} = i\mathbf{a}+j\mathbf{b}\}$, surrounded by six wells. The typical dynamics of the diffusing particle consists in long periods of oscillations in a single lattice well, and sudden jumps between one well to another one. Figure 3.3 panel A shows the schematic representation of the 2D system: the blue dots are the positions of the heavy atoms forming

7

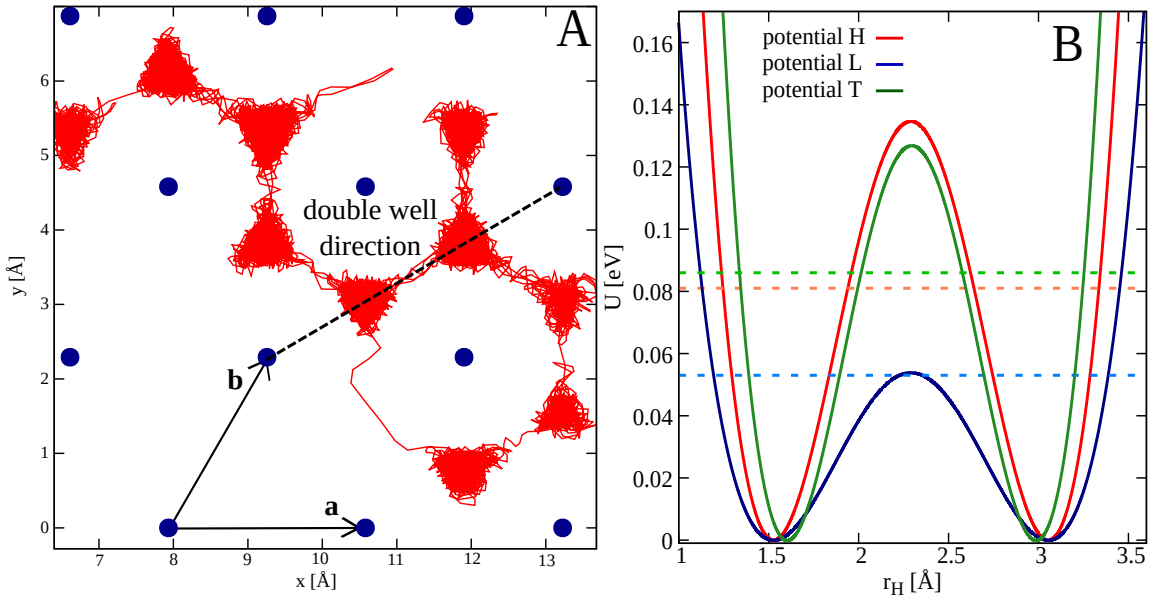

Figure 3.3: *Panel A*: simplified picture of the 2D system. Blue dots are the heavy atoms positions according to lattice vectors **a** and **b**, red line is one prototypical trajectory of the diffusing H/D atom. The lattice vectors (3.32) are represented, as well as the direction (dashed line) along which we find a double well potential. *Panel B*: double well potentials L, H and T with the respective ZPE values, along the direction of the dashed line in panel A.

the lattice according to the vectors **a** and **b**; the red line represents an example of the trajectory of the H/D atom.

This simple interaction potential provides a 2D lattice in which the light particle moves, as shown in Figure 3.2 and 3.3 panel A. Along the diagonal direction (dashed line on Figure 3.3 panel A) between two wells, we obtain a profile of the interaction potential, which corresponds to a one-dimensional double well, as reported in Figure 3.3 panel B. The interaction is determined by the potential height is proportional to the parameter V_0, while the width of the barrier is related to the parameter Δ and to the lattice constant, a_{latt}. By solving the corresponding Schrödinger equation, it is possible to compute the zero point energy (ZPE), which is reported on Figure 3.3 panel B as dashed line for the H mass. We thus tuned the three parameters, V_0, Δ and a_{latt}, obtaining three representative cases:

1. H-potential: in which the barrier is much higher than the ZPE;
2. T-potential: which has a slightly smaller and thinner barrier compared to the H-potential, and about the same ZPE;
3. L-potential: in which now the barrier is lowered by about a half of H- and T-potentials, such that ZPE is on the same level of the barrier height.

Table 3.1 reports the parameters of the three model potential given by Eq. (3.33), as well as the lattice constants, and the corresponding values of the barrier hight ΔU. It reports

Table 3.1: Parameters of the model potential (3.33), lattice constant, values of barrier hight, zero point energy (ZPE) and oscillation frequency at the bottom of the well for the three particle - lattice potential interactions.

Name	V_0 [eV]	Δ [Å^{-1}]	a_{latt} [Å]	ΔU [meV]	ZPE [meV]	ν_0 [ps^{-1}]
High (H)	6.8	2.46	2.65	135	81	20
Low (L)	6.8	1.13	2.65	53	52	6
Tunnel (T)	7.5	1.61	2.40	127	87	21

also the ZPE values, computed from the solution of Eq. (3.26), and the typical frequency of oscillation at the bottom of the well ν_0, obtain from a harmonic fit. Note that the harmonic approximation of the frequency for the potentials H and T is in good agreement with the ZPE $E_0 = h\nu_0$ (where h is the Planck constant), whereas the approximation fails for the potential L.

In the case of flexible lattice, the interaction between the N atoms of the lattice is a Morse potential

$$V(\mathbf{R}_1, \ldots, \mathbf{R}_N) = \sum_{i=1}^{N-1} \sum_{j=i+1}^{N} D \left(1 - e^{-\alpha(|\mathbf{R}_i - \mathbf{R}_j| - d_0)}\right)^2 \tag{3.34}$$

with parameters $D = 1.36$eV, $\alpha = 0.529$Å and $d_0 = 2.645$Å. The lattice particles bear the mass of Pb atom (m_{Pb} = 164 m_H). Interactions are computed for all atoms within a cutoff radius of $r_{cutoff} = 13.23$Å.

3.3.2 Simulation setup of MD-based methods

We performed different molecular dynamics simulations, using the methods described in Chapter 2: classical Langevin MD (ClMD), Quantum Thermal Bath (QTB), Adaptive Quantum Thermal Bath (adQTB), thermostatted ring polymer ((T)RPMD) and PIQTB. All these methods were applied to the rigid lattice case, while only ClMD, QTB and (T)RPMD were also selected, after analyzing the results obtained for the rigid lattice, for the flexible lattice case. Simulations were done at different temperatures in the range [1K,900K]. Simulation times are of the order of tens of nanoseconds for each trajectory, and about 20 trajectories were collected for each temperature.

In ClMD, QTB and (T)RPMD simulations we used 10THz as value of the main friction parameter γ. We tested the dependence of the friction parameter on the diffusion coefficient, finding little effects in the range between 1THz to 40THz. Higher friction values led to an overdamped diffusion regimes, while values smaller than 1THz required very long thermalization period before the actual trajectory, with little differences in the final results. Appendix C reports the comparisons for different values of friction γ. In the case of the adQTB method, for each model potential, an initial adaptation of the frictional function $\gamma(\omega)$ was performed and tested for different values of initial γ_0 and adaptation velocity A_γ, from the initial value of $\gamma_0 = 10$ps^{-1}. The adaptation is stopped when the function $\gamma(\omega)$

converges in time, i.e. only small variations can be observed. Bear in mind that this function is being adapted on the fly throughout the whole length of the simulation.

(T)RPMD simulations were done using a variable number of beads for each temperatures, in order to speed up the calculations for the trajectories at high temperature. A convergence study of the average kinetic and potential energies with the number of beads is done to ensure the stability of each result. Simple RPMD have been also tested, finding little differences with the main version of the method.

3.3.3 Diffusion coefficient in a fixed lattice: quantum vs. classical

The diffusion coefficient was computed via the velocity autocorrelation function - as in Eq. (3.7) - from the trajectories of the hydrogen atom at different temperatures. Figure 3.4 reports the results for all methods under study, except for PIQTB, in the three model potentials, H, L and T in panel A, B and C respectively. The numerical values of the diffusion coefficients are reported in Appendix B.

For each case, an Arrhenius law (3.13) is fitted on the classical results, in order to obtain an estimation of the classical activation barrier. The values for the barrier E_a are 137meV, 55meV and 128meV, for the H, L and T potentials respectively, which are close to the values of the potential energy barriers ΔU reported in Table 3.1. As expected, the classical results have a linear dependence on the inverse temperature in logarithmic scale, and the diffusion coefficient tends to zero, as small thermal fluctuations do not allow the particle to overcome the potential energy barrier and jump in the neighboring well. Therefore, the hydrogen atom remains confined in the well and oscillates around its equilibrium positions located at the bottom of the well. Via the computation of the mean-squared displacement Δr^2, we checked systematically if the number of jumps is high enough to obtain a proper diffusion regime. In the cases when no or very few jumps are performed within the simulation time, the diffusion coefficient is not computed. For further details, we refer to Appendix C.

The Sum-over-State method is used to estimate the accuracy of the MD methods including NQEs. As discussed previously, the η parameter appearing in Eq. (3.31), in the limit of free particle, can be associated to the friction γ in the Langevin equation (see Eq. (3.23)). However, in order to fix its numerical value in the lattice case, we thus choose η such as to obtain the same classical diffusion coefficient curve in the limit of high-temperature, when we expect that quantum and classical diffusion should coincide (see Appendix A for more details). For the three potential under study, shown in Figure 3.4, the chosen values of η are 31.5ps^{-1}, 26.0ps^{-1} and 35.0ps^{-1}, for the H, L and T potentials respectively. They are of the same order of magnitude than the typical oscillation frequencies of the hydrogen atom.

At this point, for all three potential, the quantum diffusion coincides with the classical one at high temperature, and it diverges from it more and more as temperature decreases, reaching a plateau. This is the signature of quantum effects (ZPE and tunneling), which allows the hydrogen to diffuse at any temperature, as long as the barrier is not infinitely high. Panels A and B of Figure 3.4 demonstrates this effect, as the ZPE of the potential L is much closer to the top of the barrier than the ZPE of the potential L (see Figure 3.3 for the direct comparison between potentials). Consequently, the saturation of the diffusion

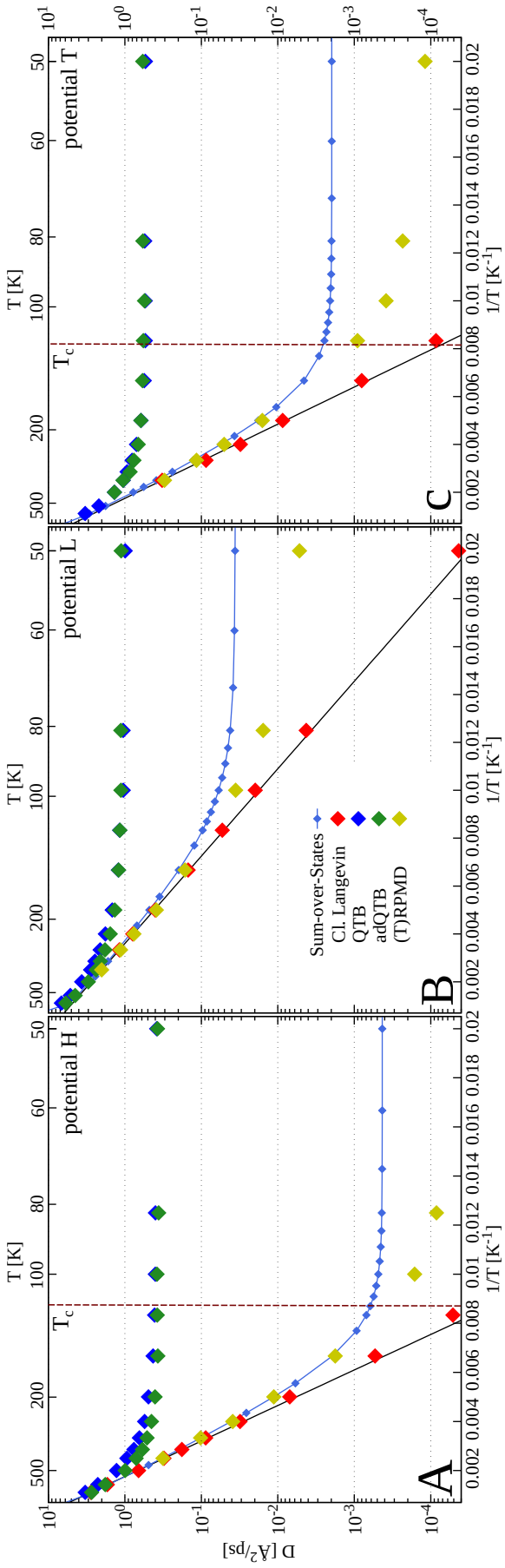

Figure 3.4: Diffusion coefficients obtained via classical Langevin (red), QTB (blue), adQTB (green) and (T)RPMD (yellow), compared the Sum-over-State solution; all three model potential are depicted: H (panel A), potential L (panel B) and potential T (panel C). Error bars are within point dimensions.

Table 3.2: Values of barrier hight from Arrhenius fit, zero point energy (ZPE), η parameter and istanton T_c for the three H/D-lattice potential interactions.

Name	ΔU [meV]	ZPE [meV]	η [ps^{-1}]	T_c [K]
High (H)	135	81	31.5	115
Low (L)	53	52	26.0	28
Tunnel (T)	127	87	35.0	123

coefficient from the SoS method in potential L appears at two orders of magnitude above the saturation in potential H. Moreover, the tunneling effect could also play a role. Indeed, comparing the panels A and C of Figure 3.4, almost one order of magnitude increment in the diffusion coefficient saturation is observed when the potential T is used, due to a thinner and lower barrier.

If we now compare the quantum MD methods with the Sum-over-States solution, across all three potentials, the QTB method consistently overestimates the diffusion coefficient at almost every temperature regimes, except for very high temperatures at which it tends to the classical Arrhenius regime; the adQTB appears to not be able to correct this effect. On the contrary, the (T)RPMD captures both general trends, i.e. classical Arrhenius at high-T and quantum saturation at low-T; it underestimate the SoS results of about one order of magnitude at 50K, being closer to the classical limits.

On the panels for the potential H and T, we also report as well the transition temperature T_c from the swallow tunneling regime to the deep tunneling regime [112, 180]. The critical temperature for the potential L is out of scale, but its numerical value can be found in Table 3.2. In the shallow tunneling regime, the diffusion process takes place through the tip of the barrier, which can be approximated as a parabolic barrier around the maximum $\bar{x}$, i.e. $V(x) \simeq V(\bar{x}) - \frac{1}{2}m\omega_b(x-\bar{x})^2$. The frequency ω_b is linked to the normal mode frequency of the centroid oscillating around the top of the barrier, as $\omega_0 = i\omega_b$. From them, the critical temperature is obtained with the formula

$$T_c = \frac{\hbar\omega_b}{2\pi k_B} \tag{3.35}$$

where $\hbar$ is the Planck constant and k_B is the Boltzmann constant. The three critical temperatures are 115K, 28K and 123K for the model potentials H, L and T respectively. Thus, we notice that, for the model potential L, all simulations lie well above T_c, where mostly ZPE effects are espected to affect the diffusion rate, whereas the results for the other two model potentials are split between the shallow tunneling regime and the deep-tunneling regime. Hence, we could assume that the main contribution to the diffusion is given by the zero-point energy in potential L. For the other two potentials instead, both quantum effects give a contribution to the diffusion. Also, (T)RPMD is related to the (ImF version of) instanton theory, which shows that passage rates through a symmetric barrier is underestimate [181] in the ring-polymer approximation.

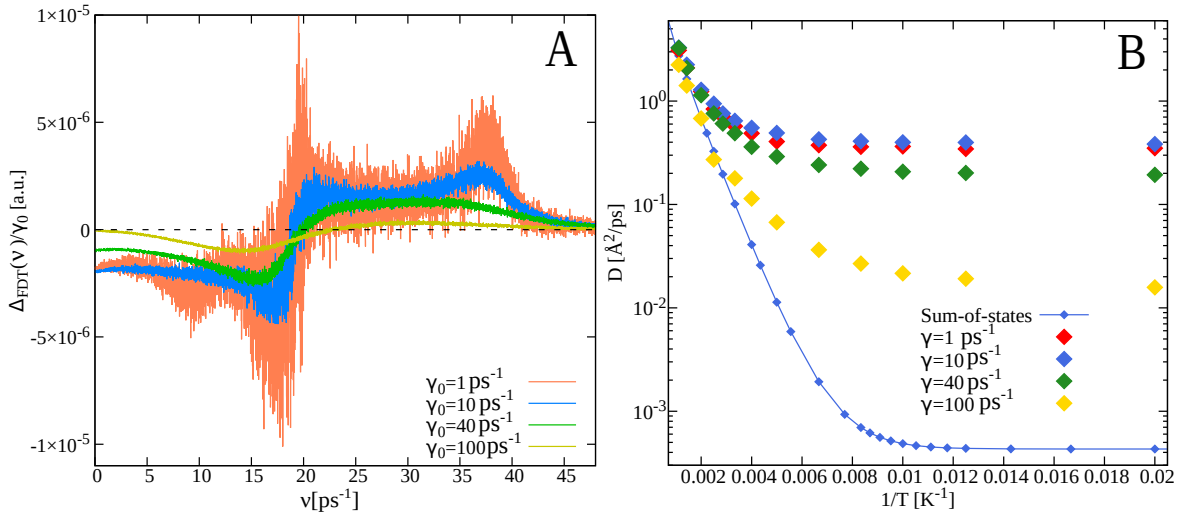

Figure 3.5: *Panel A*: average FDT evaluation from Eq. (2.54) as a function of the frequencies ν for different values of friction parameter γ; *panel B*: diffusion coefficients as function of the inverse temperature for different values of friction parameter γ, compared with the SoS results, in the model potential H.

3.3.4 Quantum Thermal Bath: a critical analysis

In the following Section, we concentrate on the QTB method. We observed in Figure 3.4 that the QTB method consistently overestimates the diffusion coefficients at almost every temperature, except very high.

The first effect we focus on is the zero-point energy leakage (ZPEL), which, as explained in Section 2.5, is the major drawback for the use of the standard QTB method. Panel A of Figure 3.5 shows the measure of the Fluctuation-Correlation Theorem (2.54) (difference between the power spectrum injected in the system by the random force and the one dissipated by the friction force), for different values of the friction γ and fixed temperature of 1K, for a hydrogen atom in the model potential H. In a system without ZPEL, the difference between the two terms shoud be null. Instead, for all frictions, $\Delta_{FDT} \geq 0$ for the high frequency modes (i.e. above the typical oscillation frequency of the system), and $\Delta_{FDT} \leq 0$ for low frequency modes. The thermostat is able to attenuate this effect: if a larger value of the friction γ is applied, the ZPEL is reduced [116]. However, using high values of friction parameter ($\gamma \gg \nu_0$) has an effect on the dynamics of the system, and the value of the diffusion coefficient could be affected by it. Indeed, as shown in the panel B of Figure 3.5, the diffusion coefficient depends on the friction parameter. If the values of γ are much higher than the typical frequencies of the system, the dynamics is overdamped and the diffusion decreases. This effect is observed also in classical and (T)RPMD simulations. We need therefore a method which specifically disentangle the specific effect of the ZPEL from the effect of γ on the dynamics.

As explained in Section 2.6, the main goal of the adaptive QTB method is the compensation on the fly of the ZPEL when the quantum bath is coupled to the equations of motion. It has been shown that the adQTB successfully corrects the ZPEL and allows the computation

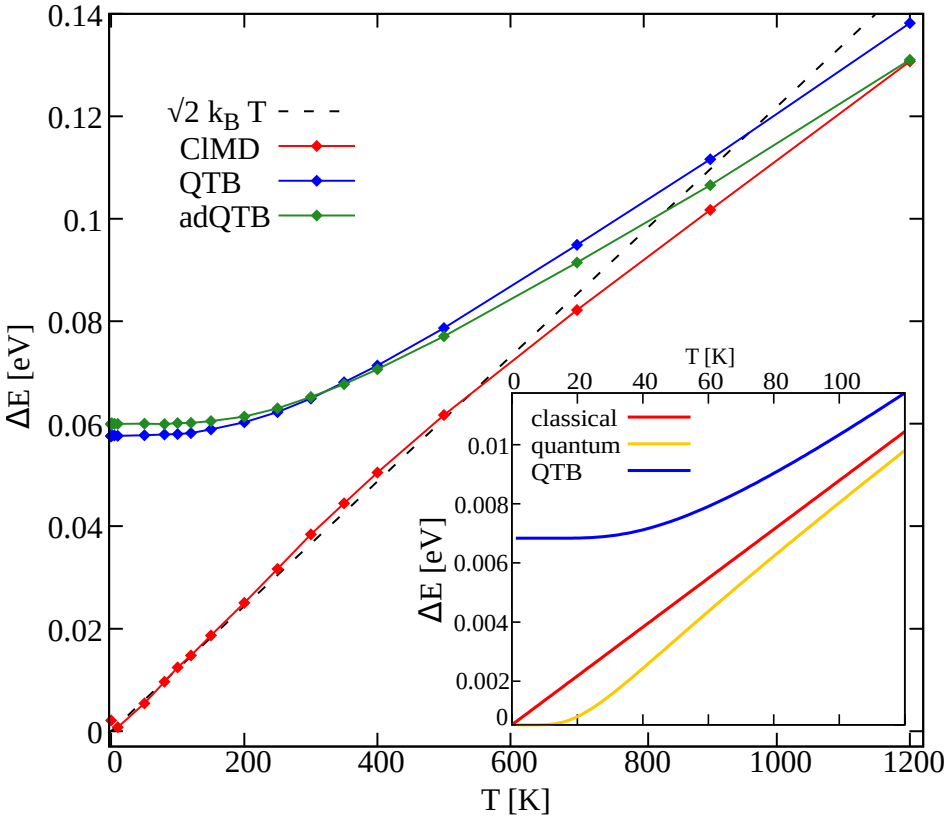

Figure 3.6: Average energy fluctuations as function of temperature for ClMD, QTB and adQTB methods, for the model potential H; in the small panel, the energy fluctuations of a one-dimensional harmonic oscillator for the classical, exact quantum and QTB method as function of temperature.

of properties including NQEs in much shorter simulation time compared to the (T)RPMD method [118]. However, in the case of the diffusion coefficient, we observed in Figures **??** and **??** that the adQTB results are still very close to the QTB diffusion coefficient curves [1]. This fact, coupled with the observation of the important differences between QTB results at different γ and the SoS curve in Figure 3.5, raises the question if the limit of quantum bath regarding diffusion is more fundamental.

In order to answer to this question, we recall the original purpose of the quantum thermal bath method. Dammak et al. [159] developed the method based on the generalized Langevin equation in order to have a dissipative force to thermalize the system and a colored noise (with power spectral density proportional to $\theta(\omega, T)$ (2.51)) to mimic the delocalization of the quantum particle. The method reproduces exactly the mean energy of a quantum harmonic oscillator as a function of temperature. However, in the problem of diffusion over a barrier, anharmonic effects prevail and we should consider the energy fluctuations $\Delta E = \sqrt{\langle E^2 \rangle - \langle E \rangle^2}$, which are the main responsible for the particle to overcome the barrier.

[1] For more details on the compensation of the ZPEL and the dependence of adQTB results on the initial friction parameter γ_0 see Appendix D.

Figure 3.6 shows the average energy fluctuations as function of temperature for the ClMD, QTB and adQTB methods, for the model potential H (for all method, the friction parameter is fixed at 10ps^{-1}). The expected classical value $\Delta E = \sqrt{2}k_BT$ for a two-dimensional harmonic oscillator is also shown for comparison. Classical simulations reproduce this result up to 600K, when energy fluctuations are much higher than the potential barrier and the anharmonicity effect starts to visible. On the contrary, both QTB and adQTB method deviates from the classical result, in particular at low temperature, where the values of ΔE saturate due to the presence of the zero-point energy.

This result is expected for both methods. Indeed, if we consider a classical (one-dimensional) harmonic oscillator of frequency ω, we can derive the energy fluctuations as derivative

$$(\Delta E^2)_{cl} = \frac{\partial}{\partial\beta}\log(\mathcal{Z}) = \frac{1}{\beta^2} \tag{3.36}$$

where β is the inverse temperature $1/k_BT$ and $\mathcal{Z}$ is the classical partition function. On the other hand, if we consider the same quantum problem, the quantum energy fluctuations read

$$(\Delta E^2)_q = \frac{\partial}{\partial\beta}\log\left(\hat{Z}\right) = \frac{(\hbar\omega/2)^2}{\sinh^2(\beta\hbar\omega/2)} \tag{3.37}$$

where $\hat{\mathcal{Z}}$ is the quantum partition function and $\hbar\omega/2$ is the zero point energy of the system. Finally, the energy fluctuations of the QTB method are $\Delta E = \theta(\omega, T)$ as in Eq. (??) [159]. The inside panel of Figure 3.6 compares the three expressions as function of temperature, for a given frequency of ω =20ps^{-1}. It is clear that the QTB drastically overestimates the energy fluctuations at low temperature, compared to both classical and quantum expressions.

Another way to express the previous result is showing how the different methods sample the barrier at fixed temperature. In particular, we are interested in regimes close to the crossover temperature T_c between the shallow tunneling and deep tunneling regime. To clarify our intent, we first introduce, in the canonical ensemble, the Helmholtz free energy

$$F(T) = -k_BTlog(Q) \tag{3.38}$$

where Q is the canonical partition function

$$Q \propto \int d^Nr\ e^{-\beta U(r_1,\ldots,r_N)} \tag{3.39}$$

here we assumed the potential energy to be independent on the momenta of the system. Often, as in our case, we are interested in the computation of the free energy as function of a certain collective variable ξ that characterize a certain process of interest between two states. In this case, we can define the probability distribution of the system along the collective variable as

$$Q(\xi) = \frac{\int d^Nr\ \delta(\xi(r_1,\ldots,r_N) - \xi)e^{-\beta U(r_1,\ldots,r_N)}}{\int d^Nr\ e^{-\beta U(r_1,\ldots,r_N)}} \tag{3.40}$$

which, according to Eq. (3.38) lead to the free energy $F(\xi, T) = -k_BTlog(Q(\xi))$, also called mean force potential (MFP). Notice that the collective variable ξ could be a geometrical

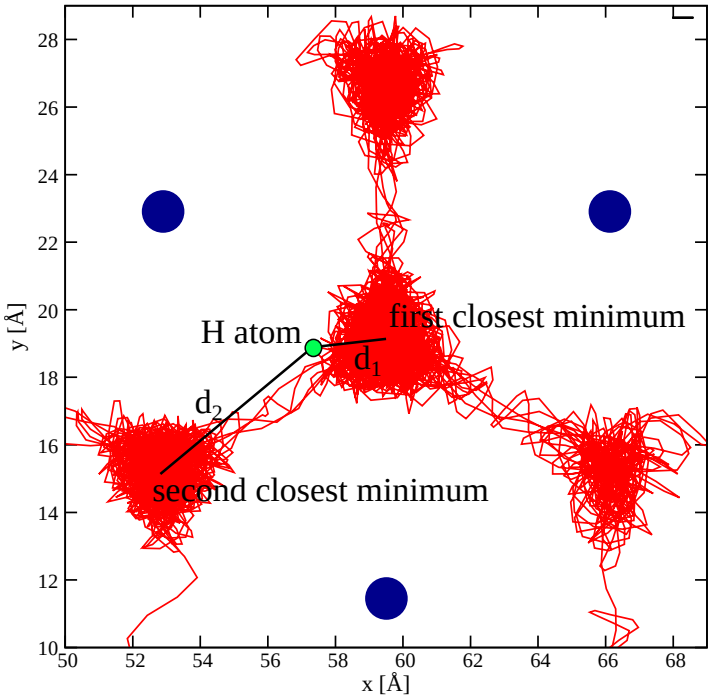

Figure 3.7: Graphic representation of the collective variable $\xi(r) = \left|\vec{d}_2(r) - \vec{d}_1(r)\right|$ given a possible trajectory of the diffusing particle (in red) in the lattice (positions of the fixed lattice atoms in blue).

coordinate or a more general function of the system positions $r_1, \ldots, r_N$. As we are interest in the barrier between the two well, which separates the particle before and after a jump, in our work we define the collective variable as

$$\xi(r) = \left|\vec{d}_2(r) - \vec{d}_1(r)\right| \tag{3.41}$$

where d_1 is the distance of the H/D particle from the closest minimum and d_2 is the distance from the second closest minimum. Figure 3.7 shows a graphic representation of the collective variable (3.41) given a possible trajectory of the diffusing particle (in red) in the lattice (positions of the fixed lattice atoms in blue). Then, the MFP can be computed from MD simulation for long enough simulation times, with all our methods, from the trajectory of the hydrogen particle. In particular, Eq. (3.40) can be computed as

$$Q(\xi) = \lim_{t\to\infty} \frac{1}{t} \int_0^t \rho(\xi(t')) \tag{3.42}$$

where the density ρ is the number of occurrences of ξ in a infinitesimal interval. For a finite time simulation, Eq. (3.42) is approximated by an histogram $h(\xi)$.

Figure 3.8 compares the free energy barrier as function of the reaction coordinate (3.41), for the two model potentials H and T, at fixed temperature of 100K. Simulation times are of the order of 500ps.

At this temperature, it is clear that the classical particle cannot reach the top of the barrier and perform a jump within the simulation time, which would count as a first diffusion event. On the contrary, both quantum methods are able to activate the diffusion process and

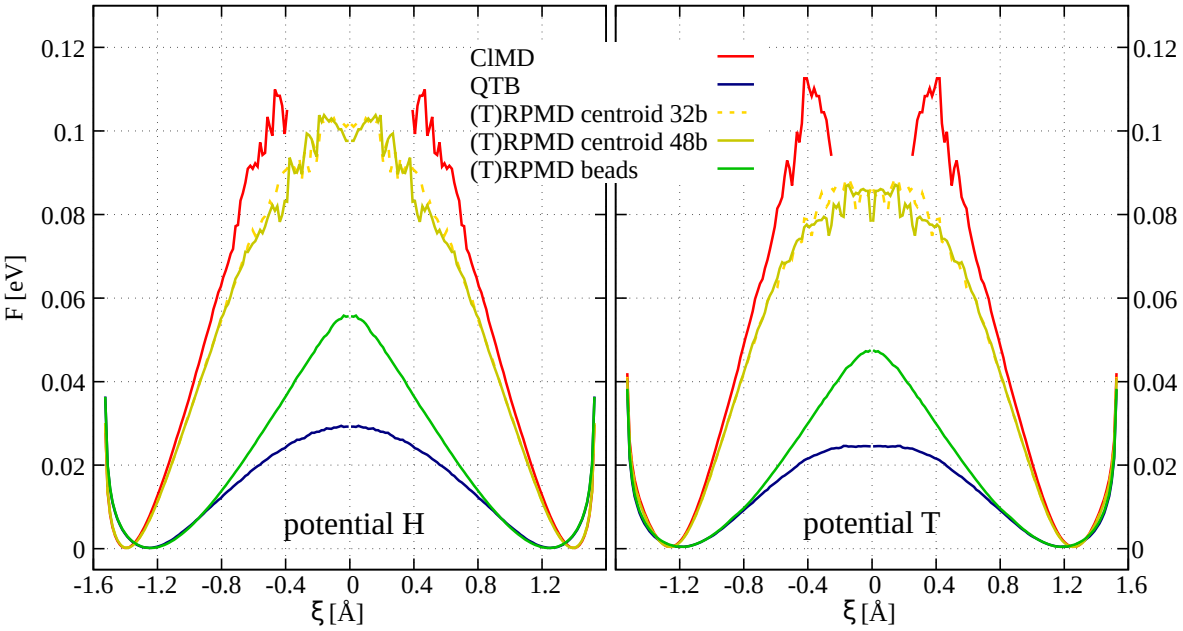

Figure 3.8: Free energy barrier as function of the collective variable (3.41) for the model potential H and L at fixed temperature of 100K. The plots are symmetrized for visualization purposes.

explore the top of the barrier within the simulation time, even though longer trajectories would be necessary to obtain smoother profiles. Starting with the (T)RPMD, we plot both the centroid distribution for 32 and 48 beads, and the beads distribution. As expected, the beads distribution is much lower than the centroid, which instead appears to be close to the classical barrier for most of the curve, except for the top. Indeed, the centroid can perform jumps from one well to the other at lower temperature. Moreover, for the model potential T, the centroid barrier is lower compared to the potential H barrier of about 20meV (whereas the difference between the potential barriers is about 8meV). As for the beads distribution, it has a much smaller height and a different shape, both for the top of the barrier and for the two wells. On the other hand, the QTB methods has a free energy barrier much smaller than the (T)RPMD centroid barrier, and comparable to the beads distribution around the wells. All these results are consistent with the diffusion coefficient values plotted in Figure 3.4.

Therefore, we can conclude that the QTB method is specifically designed to include the harmonic ZPE contribution in the average energy, but it does incorrectly reproduce the quantum energy fluctuations. It is now evident the reason why the QTB method overestimates the diffusion process, and the adQTB does not differs from the original method in this regard. An analogous result was found in QTB simulation fragmentation rate constants and activation energies [182].

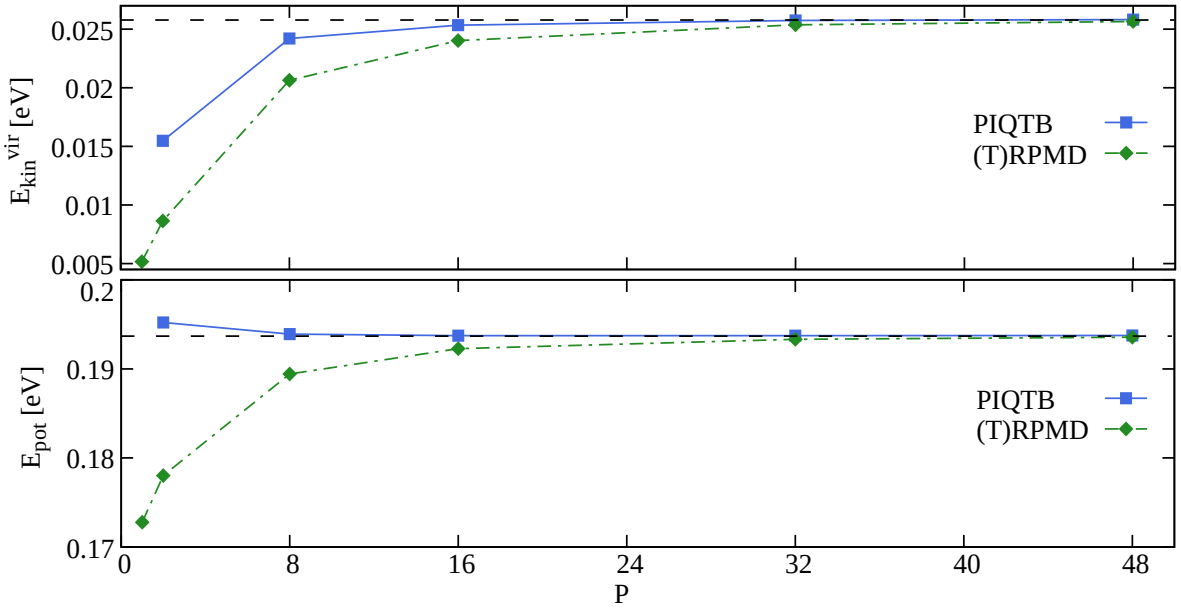

Figure 3.9: Average central virial kinetic energy (Eq. 2.47) and potential energy (Eq. 2.44) estimators as function of the number of beads P, in the L model potential at 60K, for the RPMD/(T)RPMD and PIQTB methods. Error bars are within point dimensions.

3.3.5 Path-Integral Quantum Thermal Bath: a possible compromise?

In previous Section, we compared the diffusion coefficients obtained via the QTB and the (T)RPMD methods, discovering that the former method overestimate diffusion at almost every temperature, while the latter does capture well the overall trend at both high and low temperature. However, the (T)RPMD simulations have a computational cost roughly P times higher than classical or QTB trajectories, where P is the number of replicas of the system. Therefore, we aim at designing a way to increment the efficiency of the method and accelerate its convergence in terms of number of beads.

In this Section, we analyze the performances of the hybrid method PI/RPQTB, specifically the version of PI/RPQTB with the classical centroid (see Section 2.7 for more details). Our choice is due to the fact that we are interested in computing dynamical properties, such as the diffusion coefficient, from the centroid trajectory $(\mathbf{r}_c, \mathbf{p}_c)$. In Figure 3.9, we show the convergence of estimators of the potential (2.44) and centroid virial kinetic (2.47) energy estimators, and in Figure 3.10 the diffusion coefficient, as a function of the number of beads. For the following results, the model potential selected is the low-barrier potential (L) and the temperature is fixed at 60K for all trajectories. [2]

Both kinetic and potential energy estimators converges faster as function of the number of beads for the PIQTB method. In particular, the difference between the values at $P = 8$ and at $P = 48$ are about 6% and 0.1%, for the kinetic energy and potential energy respectively. If we repeat the same comparison for the (T)RPMD we find 20% and 2% differences. This fact is well expected, since the design of the PIQTB method is exactly to improve

[2] The friction parameter γ is fixed at 10ps^{-1}. We tested the effect of the friction on the properties, finding little differences in the convergence in a range between 0.1ps^{-1} to 40ps^{-1}.

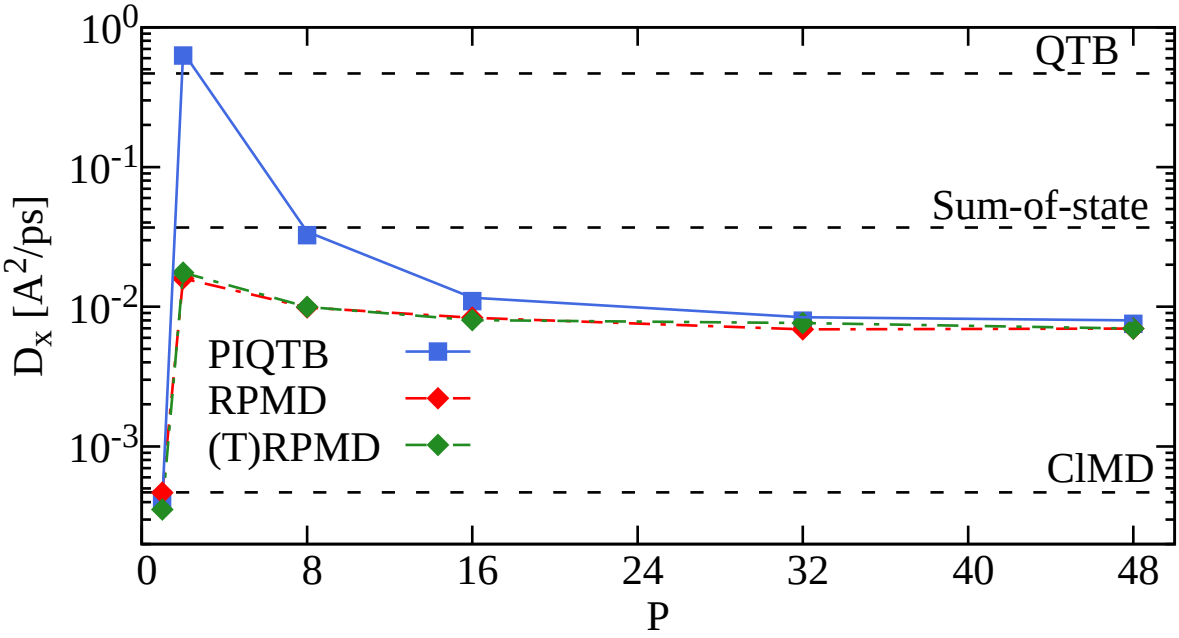

Figure 3.10: Diffusion coefficient as function of the number of beads P, in the L model potential at 60K and $\gamma = 10$THz, for the RPMD/(T)RPMD and PIQTB methods. Error bars are within point dimensions.

convergence of the energy estimators via the use of a colored thermal bath instead of the classical bath of the standard RPMD method.

The diffusion coefficient, however, reveals a different convergence behavior as the number of beads P is increased. Figure 3.10 shows the convergence with P of the diffusion coefficient, in the L model potential at 60K and γ =10ps^{-1}, for the RPMD/(T)RPMD and PIQTB methods. First of all, in the limit of $P = 1$, all methods reproduce the classical diffusion coefficient. This result is trivial for the RPMD method, and it is expected for the PIQTB method as the classical centroid variant of the method is used. The values of $D(P = 2)$ reveal the first differences between the methods. In particular, the PIQTB value is comparable to the QTB limit at the same temperature, which is consistent with the action of the quantum thermal bath on the beads. As P increases, the PIQTB method converges towards the (T)RPMD values. Contrary to the energy estimators, the diffusion coefficient of (T)RPMD method converges faster as function of the number of beads compared to the PIQTB. Indeed, comparing again the values at $P = 8$ and $P = 48$, we obtain 300% difference for the PIQTB method, and 42% for the (T)RPMD method. Notice that, for both method, the convergence for $P > 1$ is monotonous from above, which means that the diffusion coefficient is higher for low number of beads. In particular, for $P = 2$, both values are close to the solution of the Sum-over-States method. This result, however, is an artifact of the methods.

To complete the previous analysis, we add to the picture the sampling of the energy barrier made by the two different methods (PIQTB and (T)RPMD) as function of the number of replicas P. We use the same collective variable (3.41), and we compute the histogram of the mean force potential (3.42).

Figure 3.11 shows the free energy barrier as function of the reaction coordinate (3.41),

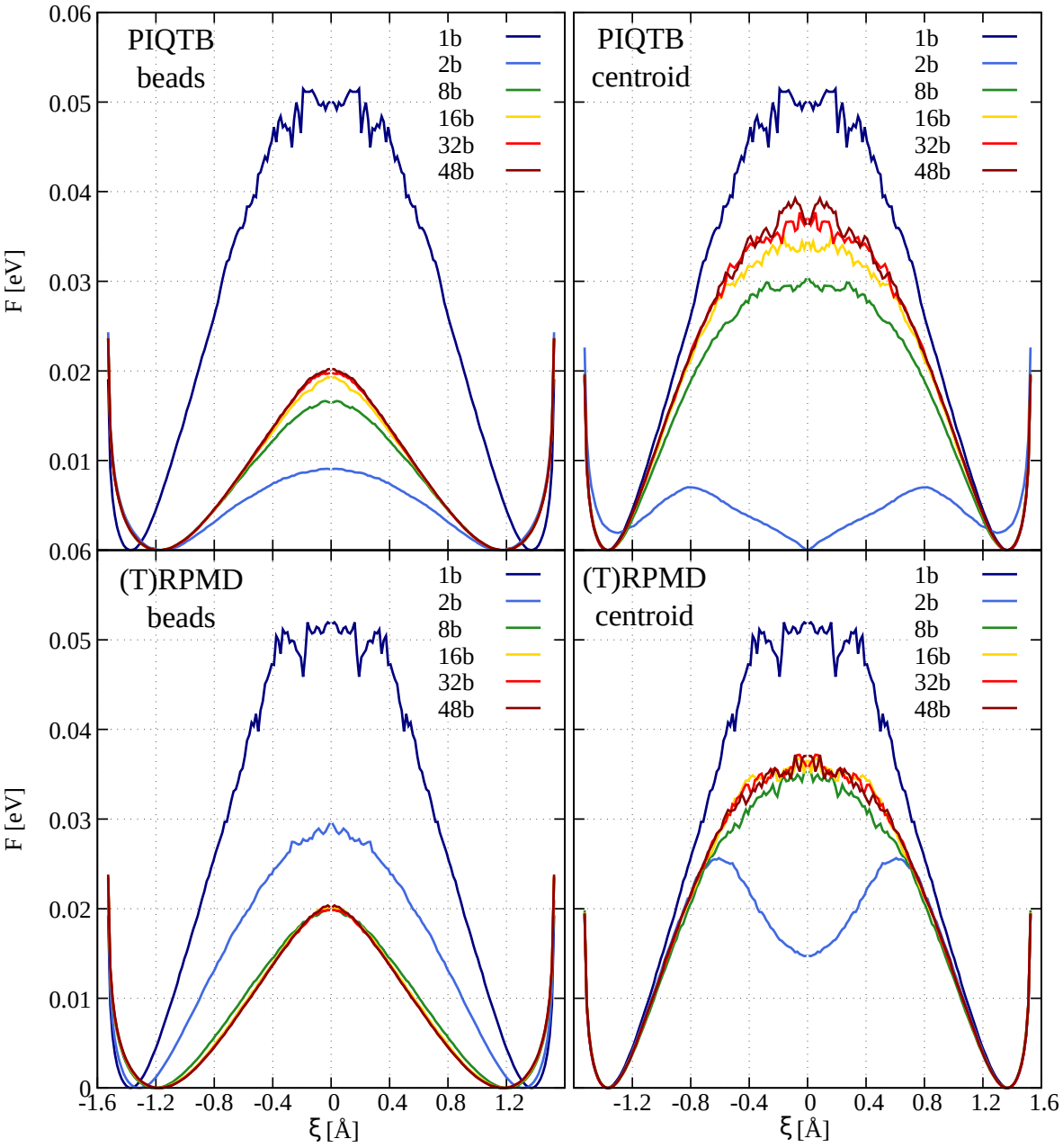

Figure 3.11: Free energy barrier as function of the collective variable (3.41) for the PIQTB (panel A and B) and (T)RPMD (panel C and D) methods with different number of beads P; the model potential is the L potential and the temperature is fixed at 60K. The plots are symmetrized for visualization purposes.

for the PIQTB (panel A and B) and (T)RPMD (panel C and D) methods with different number of beads P; the model potential is the L potential and the temperature is fixed at 60K. For $P = 1$, the classical limit is recovered for all methods. The barrier height is around 50meV, which is comparable with the potential energy barrier of the model potential L (see Table 3.1). Starting with the beads distribution, for both methods the same barrier is recovered; however, the convergence in terms of number of beads is faster for the (T)RPMD method, as it reaches convergence for $P = 8$ both for the centroid and the beads distribution. Notice that the convergence is reached from above in the case of the (T)RPMD beads, whereas it is recovered from below in the PIQTB beads. For both methods, instead, the centroid distribution converges from below. Therefore, the (T)RPMD method is closer to the classical result for low number of beads, whereas the PIQTB tends to the QTB result in the same limit.

This fact is particularly evident for the centroid distributions. Starting with the (T)RPMD method, the result at $P = 2$ has a minimum in the center of the barrier and two maxima around it. Indeed, the two beads which form the polymer are either both concentrated in one of the well, or they find themselves separated. In this last case, the resulting effect is a centroid position in the center of the barrier. This effect is also the explanation of why the diffusion coefficient are higher for low number of beads (see Figure 3.10) and it disappear as soon as the number of beads is large enough. A similar situation is observed for the PIQTB method, with the difference that the beads are thermalized with the quantum bath, which flattens drastically the height of the barrier. A grater number of beads makes the centroid distribution tend to the same form as the (T)RPMD one, as expected since the colored noise then tends to the white noise of standard RPMD.

To summarize, the PIQTB method is still valid for including NQEs in the nuclei dynamics, and it has a computational advantage for macroscopic observables, such as the energy of the system. On the other hand, the diffusion coefficient does not converge faster in terms of beads compared to standard ring-polymer methods. If we take into consideration the overall picture, the (T)RPMD method remains the most reliable method to compute the diffusion of a quantum particle. However, the low computational costs of quantum thermal baths methods (both standard and adaptive) does not rule them completely out from a computation point of view. They can be safely used to compute equilibrium observables including zero-point energy effects [118], but they need to be carefully used in the computation of transport properties.

We have now concluded the main comparison between the two class of methods, namely the quantum bath methods and the ring-polymer methods. In the following Sections we focus on two main physical effects expected for the diffusion of a light particle in a solid: the isotope effect due to the exchange of hydrogen with deuterium, and the phonon assisted hopping in a flexible lattice. For the next Section only classical Langevin, QTB and (T)RPMD methods are used.

3.4 Isotope effect

An experimental marker of the importance of NQEs is the isotope effect, i.e. the isotopic exchange of hydrogen with deuterium. Indeed, most isotope effects cannot be captured

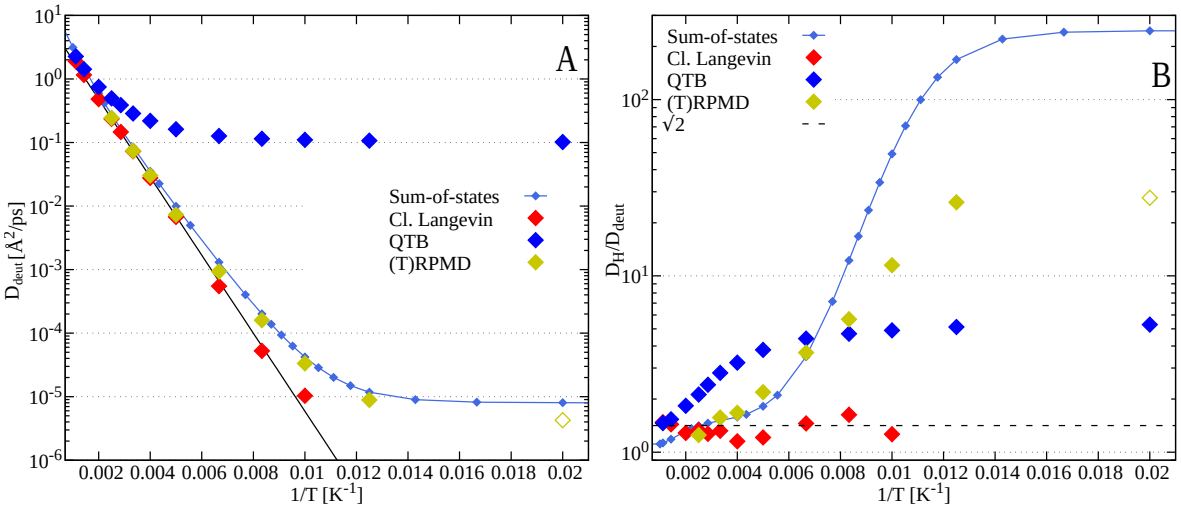

Figure 3.12: *Panel A*: diffusion coefficient of deuterium atom as function of inverse temperature in the model potential T; *panel B*: ratio of hydrogen and deuterium diffusion coefficient as function of inverse temperature. Error bars are within point dimensions.

within a classical description of the nuclei and they have a major impact on dynamical, elastic and thermal properties in condensed matter [183]. For example, it changes vibrational spectra of lithium hydrade when it is deuterated (LiH $\rightarrow$ LiD) [163]; it varies the transition temperature in potassium hydroxide (KOH) [184] or completely hinder a quantum phase transition in sodium hydroxide (NaOH) [185]. Isotope effect is also relevant in the measure of the diffusion coefficient in metals [29]; therefore, we tested the difference between the different methods on the diffusion coefficient of deuterium atom in the 2D fixed lattice.

We characterize the isotope effect with our model, in the case of the model potential T. Figure 3.12 panel A reports the diffusion coefficients obtained via classical Langevin, QTB and (T)RPMD methods as function of the inverse temperature. Simulation time were incremented , in order to obtain the convergence needed in terms of number of diffusing events, in particular for the simulations with deuterium, which are expected to have a lower number of jumps per unit time compared to hydrogen. The parameter η of the Sum-over-State method is 15ps^{-1}, and it was again chosen in order to match the classical curve between 250K and 500K. Classical Arrhenius fit gives a barrier height of $\Delta U = 134\text{meV}$, which is slightly higher than the barrier obtained from the hydrogen results. The QTB method overestimate the diffusion coefficient, as for the hydrogen atom. On the contrary, the (T)RPMD diffusion coefficients captures correctly the trend of the SoS results; however, at low temperatures (below 80K) the number of diffusing events is not enough to justify the convergence of the method and longer simulation times are needed [3].

In order to highlight the isotope effect, panel B of Figure 3.12 shows a further comparison between the methods, by picturing the ratio between the diffusion coefficient of hydrogen and deuterium D_H/D_{deut} as function of the inverse temperature. Classical simulations give the expected result, which is the factor $\sqrt{2}$ between the masses of the two isotopes.

[3] We indicate this result with a empty dot in Figure 3.12.

All other methods converge to this limit at high temperature, with the exception of the SoS method that, given the choice of η, reproduces the classical results between 250K and 500K. At higher temperature, the SoS results slowly transition towards the free particle limit, where the diffusion coefficient depends strongly on the parameter η (see Eq. (3.23)).The low temperature limit, on the other hand, highlights important differences between the methods. While the classical results remains around the mass difference ratio $\sqrt{2}$, as no nuclear quantum effects are present, all quantum methods diverge from it, and saturate as the zero-point energy contribution becomes dominant at low temperature. However, the QTB has a behavior clearly different from what expected by the SoS method, while (T)RPMD results almost coincide with the reference until temperatures of 120K. Below this limit, a saturation is observed, due also partially to the low number of events registered within the simulation time, in particular for the point at 50K of (T)RPMD.

To sum up, all quantum methods used are able to detect the isotope effect on the diffusion coefficient. Moreover, while QTB is once again overestimating the diffusion, the (T)RPMD method seems to work better for deuterium, getting closer to the expected result of the SoS method until temperatures of about 100K, within the given simulation time.

3.5 Diffusion in flexible lattice

As explained in Section 3.2, the Sum of State method was derived in the particular case of a perfect symmetric lattice, for which the Bloch theorem 4 is valid. In the more physical problem of a moving lattice, i.e. each atom of the lattice is allowed to oscillate around its equilibrium position, the symmetry is broken and the Eq. (3.31) is not valid anymore. Nevertheless, we compared the diffusion coefficient via each method (except the PIQTB) in the case of the flexible lattice. The main goal is to assess the presence and the intensity of the phenomenon of phonon assisted hopping [34, 186], according to which the diffusion process is enhanced by the collective oscillations of the lattice.

Figure 3.13 shows the diffusion coefficients obtained via classical Langevin, QTB, and (T)RPMD methods, for the model potential L (panel A) and T (panel B). Simulation times are of the order of the ns and about 10 trajectories were collected for each temperature. Classical results are fitted with the Arrhenius law (3.13), which gives the barrier height of $\Delta U = 56$meV and $\Delta U = 105$meV. Note that only the latter is lower than the respective fixed barrier, which suggest that the effect of the phonons is perceived by the classical diffusing particle only for high potential energy barriers. Finally, diffusion coefficients obtained with both quantum methods (QTB and (T)RPMD) are enhanced by the oscillations of the lattice atoms, which confirms the phonon assisted hopping effect.

3.6 Conclusions

In this Chapter, we compared two main families of molecular dynamics methods - quantum bath and ring-polymer -, as well as their hybrid version, on the problem of the diffusion of a light atom in a solid, in order to assess the intensity of nuclear quantum effects on a

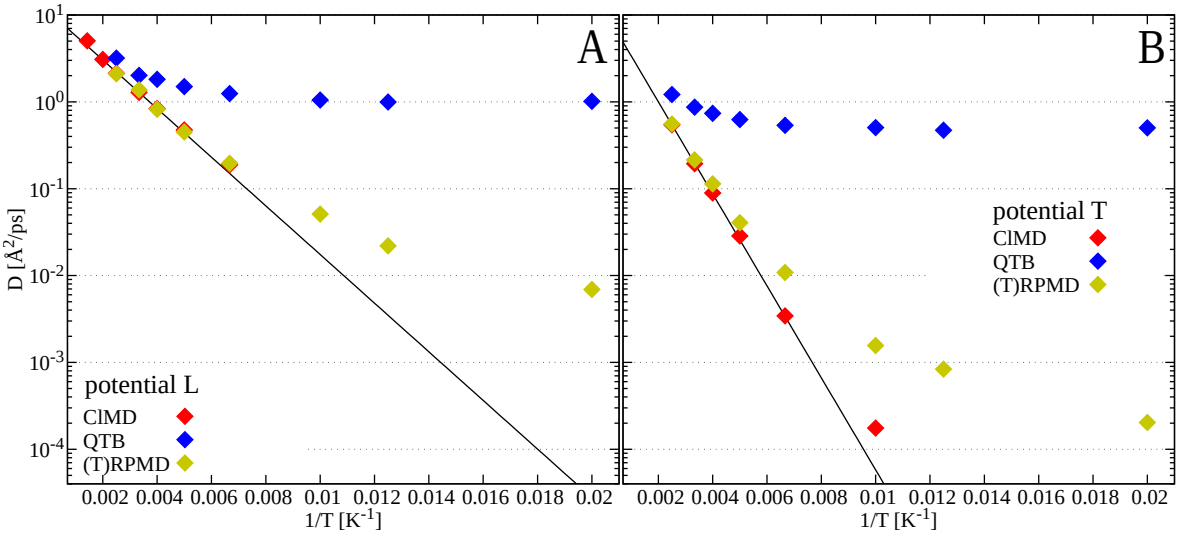

Figure 3.13: Diffusion coefficients obtained via classical Langevin (red), QTB (blue), and (T)RPMD (yellow), in the flexible version of the potential L (panel A) and potential T (panel B). Error bars are within point dimensions.

transport process and assess the accuracy of each method.

We conclude that the latter is the most accurate method for numerically evaluate the diffusion coefficient, despite its computational cost. We explain the failure of the quantum thermal bath methods in terms of incorrect energy fluctuations. Finally, we studied an hybrid version of ring-polymer method which uses the quantum thermal bath to accelerate the convergence in terms of the number of beads. Although better performances are observed for energy estimators, the method does not present advantages for the computation of the diffusion coefficient.

Appendix

A Quantum diffusion coefficient calculations

To obtain the quantum diffusion coefficient as in Equation (3.31), one has to solve firstly the 2D time-independent Schrödinger equation of the system. We have thus obtained eigenvalues and eigenvectors using the general potential $U(\hat{r};\{R_j^{(0)}\}) = \sum_j U(\hat{r} - R_j^{(0)})$ [4]. The Bloch theorem 4 was used to find the solution of the problem.

In particular, using the lattice vectors defined previously (see Equation (3.32)), we can define the reciprocal lattice vector

$$\mathbf{G} = p\mathbf{a}^* + q\mathbf{b}^* \tag{3.43}$$

and writing the potential and the Bloch functions in the reciprocal space as:

$$V(\mathbf{r}) = \sum_{p,q} v_{p,q} e^{2\pi i(p\mathbf{a}^* + q\mathbf{b}^*)\cdot\mathbf{r}} \tag{3.44}$$

$$u_{\mathbf{k}}(\mathbf{r}) = \sum_{p,q} u_{\mathbf{k},p,q} e^{2\pi i(p\mathbf{a}^* + q\mathbf{b}^*)\cdot\mathbf{r}} \tag{3.45}$$

The time independent Schrödinger equation now reads:

$$\frac{\hbar^2}{2m}(p\mathbf{a}^* + q\mathbf{b}^* + \mathbf{k})^2 u_{\mathbf{k}pq} + \sum_{p',q'} v_{p'-p,q'-q} u_{\mathbf{k},p',q'} = \mathcal{E}_{\mathbf{k}} u_{\mathbf{k},p,q} \tag{3.46}$$

Here the indices p, q are taken in the $[-n_p, n_p]$ range where n_p is the order of Fourier truncation: this is the first parameter for the numerical solution of the problem. Exact solution requires a large truncation number, which however slow down the computation. The indices p', q' denote a different reciprocal lattice vector $\mathbf{G}'$ and we used the property:

$$\int d\mathbf{r} e^{i(\mathbf{G}-\mathbf{G}')\cdot\mathbf{r}} = \delta(\mathbf{G} - \mathbf{G}') \tag{3.47}$$

For the numerical diagonalization, the indexes p, q can be further labeled through a single index $l = p + n_p + 1 + (q + n_p)(2n_p + 1)$, with $l \in [1, (2n_p + 1)^2]$. We have now obtained, for each $\mathbf{k}$ in the Brillouin zone, a set of equations in the coefficients $u_{\mathbf{k},p,q}$, which form our eigenproblem. The number of vectors in the Brillouin zone considered, n_k, is the second convergence parameter of the sum-of-states method. The diagonal elements of the matrix $\hat{\mathcal{H}}$ are: $\frac{\hbar^2}{2m}(p\mathbf{a}^* + q\mathbf{b}^* + \mathbf{k})^2 + v_{0,0}$, while the off diagonal elements are $v_{p-p',q-q'}$.

Figure 3.14 shows the lowest eigenstates for the H potential. We can clearly distinguish in state 1 and 2 the two wells of the triangular lattice shown in Figure 3.2. Notice that, even for the lower possible state, the probability to find the quantum particle is not null in both wells.

Numerical diagonalization was done using the Fortran LAPACK library to obtain the eigenvalues of the Hamiltonian. Then, the derivatives $\nabla_{\mathbf{k}}\mathcal{E}_{\mathbf{k}}$ are obtained via a finite difference method and we have summed all of them according to Equation (3.31). The convergence of the solution in terms of n_k and n_p has been verified, choosing as final values

[4] In practice, this potential has the form specified by Eq. (3.33)

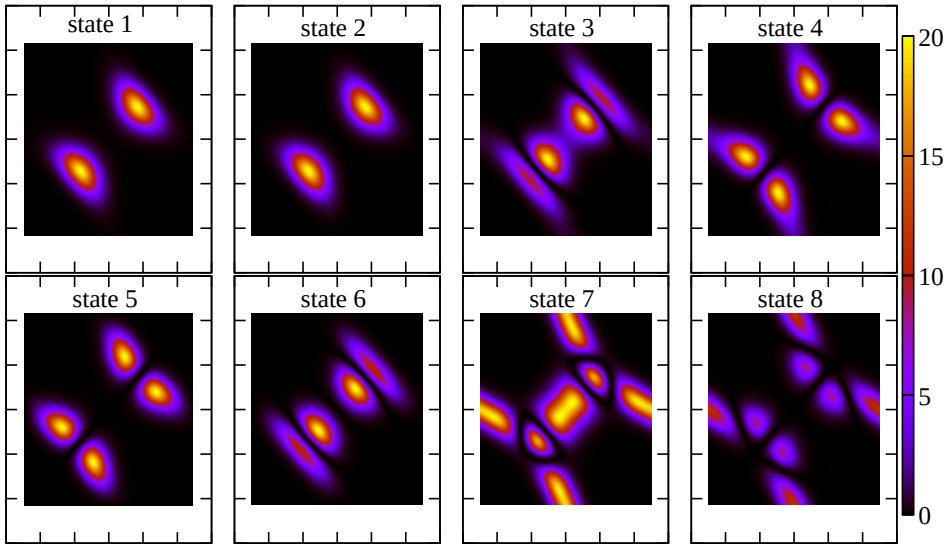

Figure 3.14: Lowest eigenstates for the H potential.

$n_k = 20$ and $n_p = 40$. Finally, to obtain the diffusion coefficient there is a free parameter to evaluate in Equation (3.31), η. This was graphically determined in order to obtain at high temperatures (where classical and quantum dynamics converge) the same results as in classical simulations. Figure 3.15 shows the classical results in the range between 250K and 900K, compared to the rescaled SoS method.

B Diffusion coefficient tables

We report here the numerical values of the diffusion coefficients obtained via the different methods and showed in the Figures of Chapter 3.

C Diffusion events and friction dependence

The diffusion coefficients obtained from the velocity auto-correlation function (3.7) in the classical method show an anomalous dependence on the simulation time. Indeed, for thermal energy much smaller than the activation barrier (see Arrhenius law (3.13)), the diffusion process happens via sudden and rare jumps from one potential well to the other. Consequently, the simulation time to describe this process grows exponentially.

Figure 3.16 shows the mean-squared displacement $\langle (x(t) - x(0))^2 \rangle$ of the hydrogen particle as function of time, for different temperatures and simulation times, in the case of the model potential H. The mean-squared displacement is related to the diffusion coefficient by Einstein equation (3.2), and it is particularly useful in this situation, because it provides a direct of observation of the jumps of the hydrogen atom between one well to the other. When simulation times are inferior to 10^4ps, only few jumps are observed at 100K, while lower temperatures do not show any diffusion. Only in the panel D, for times of the order of 10^5ps, the number of jumps is high enough to obtain a diffusion curve at 100K. Notice

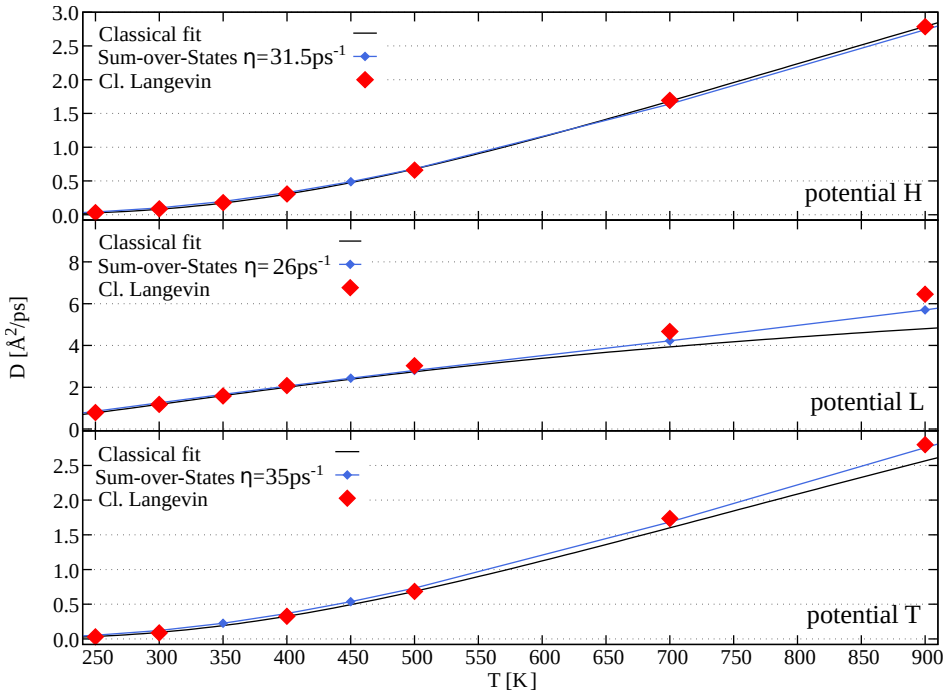

Figure 3.15: Graphic determination of the η parameter of Eq. (3.31) compared to the classical high temperature results, for each model potential.

Table 3.3: Diffusion coefficient values as function of temperature in the model potential H for all methods.

Diffusion coefficient $[\text{Å}^2/ps]$				
$T[K]$	ClMD	QTB	adQTB	(T)RPMD
50	–	3.84E-01	3.74E-01	–
80	–	3.99E-01	3.61E-01	8.44E-05
100	–	4.00E-01	3.80E-01	1.62E-04
120	5.13E-05	4.09E-01	3.77E-01	–
150	5.35E-04	4.27E-01	3.70E-01	1.77E-03
200	6.99E-03	4.92E-01	4.02E-01	1.13E-02
250	3.12E-02	5.51E-01	4.48E-01	3.89E-02
300	8.78E-02	6.45E-01	5.12E-01	1.02E-01
350	1.80E-01	7.60E-01	5.89E-01	–
400	3.08E-01	9.43E-01	7.11E-01	3.17E-01
500	6.62E-01	1.29E+00	9.93E-01	–
700	1.69E+00	2.25E+00	1.81E+00	–
900	2.79E+00	3.30E+00	2.72E+00	–

Table 3.4: Diffusion coefficient values as function of temperature in the model potential L for all methods.

Diffusion coefficient [$Å^2/ps$]				
$T[K]$	ClMD	QTB	adQTB	(T)RPMD
50	4.32E-05	0.99	1.12	0.01
70	–	–	–	0.01
80	4.26E-03	1.05	1.13	0.02
100	1.97E-02	1.05	1.13	0.04
120	5.33E-02	1.17	1.16	–
150	1.48E-01	1.22	1.21	0.16
200	4.00E-01	1.46	1.35	0.39
250	7.89E-01	1.80	1.55	0.76
300	1.18E+00	2.11	1.82	1.14
350	1.58E+00	2.46	2.09	–
400	2.08E+00	2.80	2.37	2.01
500	3.03E+00	3.67	3.00	–
700	4.67E+00	5.17	4.46	–
900	6.46E+00	6.75	5.92	–

Table 3.5: Diffusion coefficient values as function of temperature in the model potential T for all methods.

Diffusion coefficient [$Å^2/ps$]				
$T[K]$	ClMD	QTB	adQTB	(T)RPMD
50	–	0.54	0.58	1.18E-04
80	–	0.55	0.58	2.33E-04
100	–	0.54	0.55	3.84E-04
120	8.54E-05	0.54	0.57	9.06E-04
150	7.99E-04	0.56	0.59	–
200	8.64E-03	0.62	0.62	1.60E-02
250	3.08E-02	0.70	0.67	5.04E-02
300	8.70E-02	0.81	0.76	1.16E-01
350	–	0.94	0.85	–
400	3.25E-01	1.05	1.06	3.04E-01
500	6.84E-01	1.37	1.37	–
700	1.74E+00	2.18	–	–
900	2.80E+00	3.30	–	–

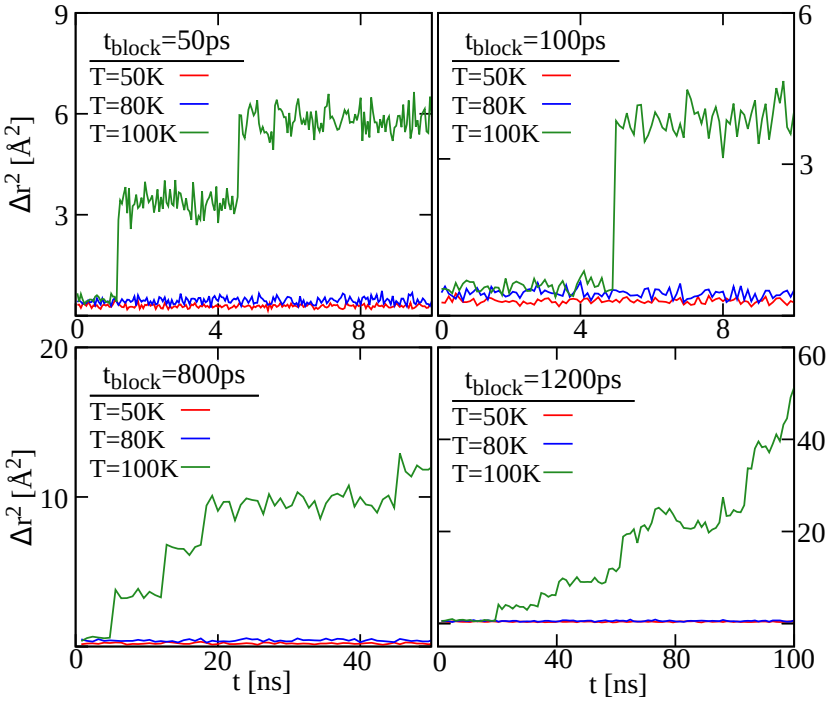

Figure 3.16: Mean squared displacement of hydrogen particle as a function of time, at 50K, 80K and 100K, in the fixed potential H, for different simulation time block lengths.

that a smooth curve would require an average over many trajectories.

Figure 3.17 shows the dependence of the diffusion coefficient on the friction parameter γ (classical simulations), for three temperatures in the three different potentials.

D Zero-point-energy leakage correction

The adaptive QTB method is design to correct the zero-point-energy leakage on the fly for each mode of the system. In order to do it, it evaluates a version of the fluctuation-dissipation theorem (FDT) given by Eq. (2.54). In Figure 3.18 we show the difference between the

$$\frac{Re\left[C_{vR}(\nu)\right]}{\gamma} - mC_{vv}(\nu)$$

which measures the of the FDT during the simulation. Both QTB and adQTB results are compared, for two of the model potentials, at different temperatures.

It is clear that, for all modes above the typical oscillation frequency ν_0 of the hydrogen particle (see Table 3.1), the leakage is corrected and the difference (2.54) is zero. However, for frequencies below ν_0, the leakage still persists, and it affects in particular the mode at zero frequency, from which we compute the diffusion coefficient.

As a result, the diffusion coefficients obtained via adQTB method are still depending on the value of the initial friction parameter γ_0 (starting point of Eq. (2.60)), as shown in Figure 3.19.

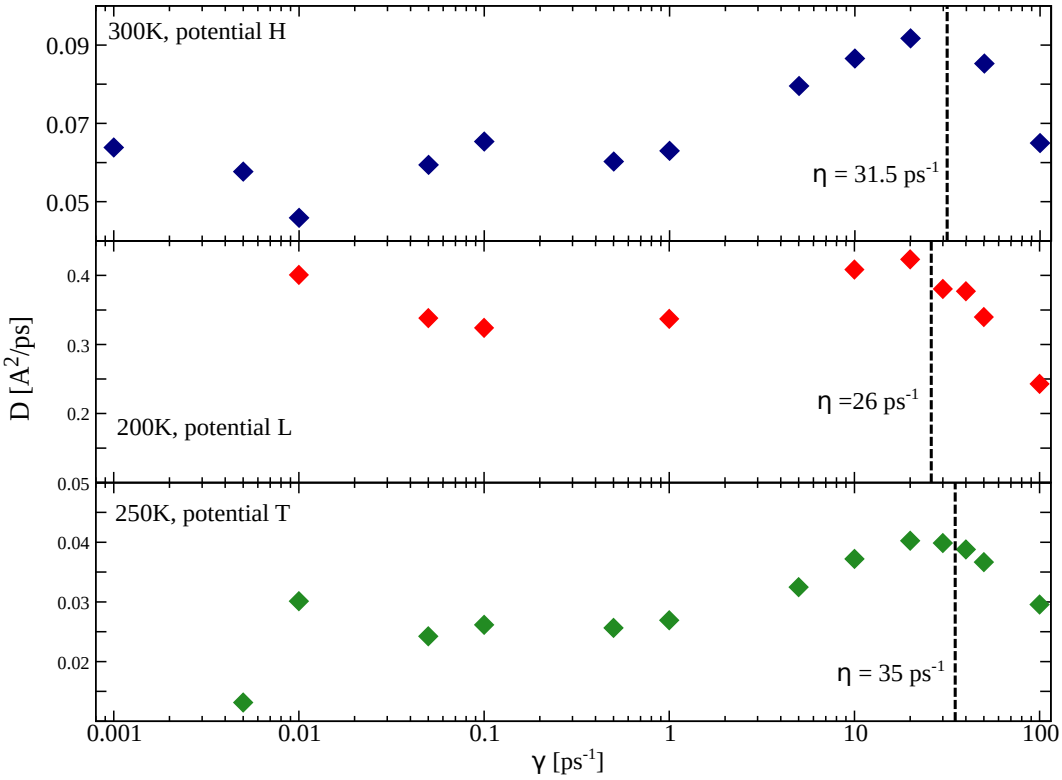

Figure 3.17: Diffusion coefficients dependence on friction γ, for three different temperatures and model potentials.

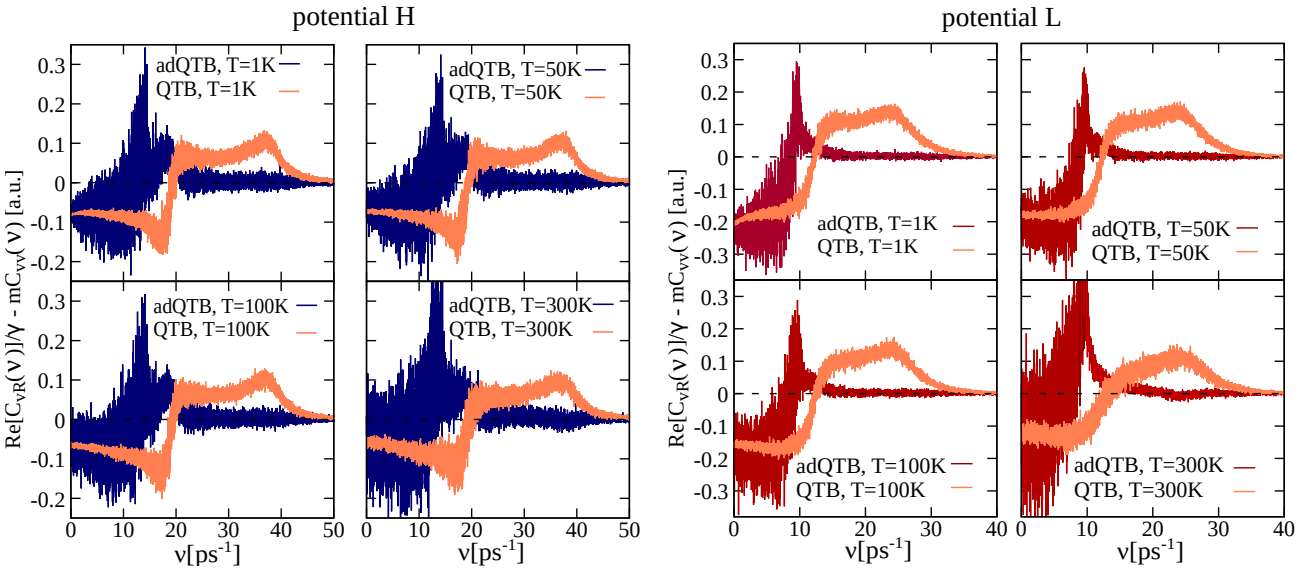

Figure 3.18: Comparison of QTB and adQTB fluctuation-dissipation theorem at different temperatures, in the H model potential (panel A) and L model potential (panel B).

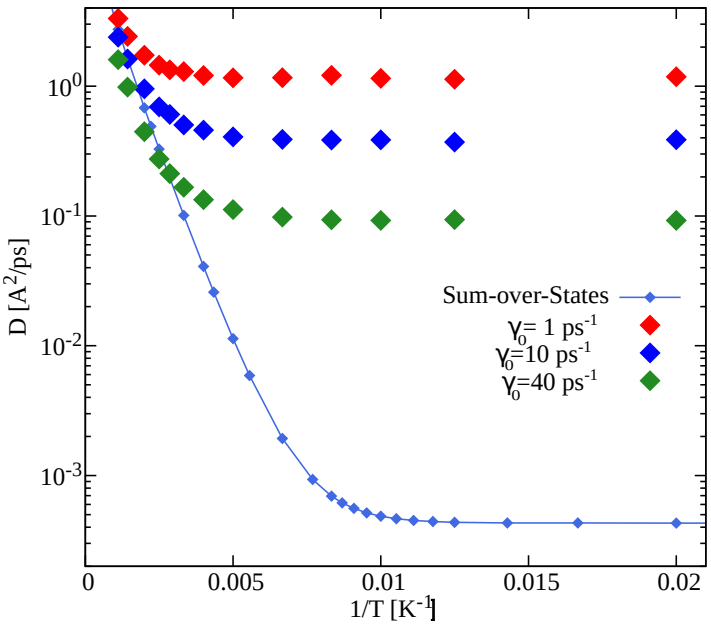

Figure 3.19: Diffusion coefficients obtained via adQTB method in the model potential H, as a function of the inverse temperature, for different values of the initial frequency γ_0.

Chapter 4

Plastic phase of Ammonia Hemi-Hydrate

4.1 Molecular dynamics simulations setup . . . 83
4.1.1 Description of the input AHH-II structure . . . 83
4.1.2 Computational details of MD-based methods . . . 85
4.2 Thermodynamics . . . 87
4.2.1 Establishing the phase transition . . . 87
4.2.2 Structural properties: structure factors and pair distribution functions . . . 90
4.2.3 Evolution of the hydrogen bond network . . . 98
4.2.4 Discussion of thermodynamics results . . . 102
4.3 Dynamical characterization of the AHH plastic phase . . . 103
4.3.1 Hydrogen bonds lifetimes . . . 103
4.3.2 Molecule dipoles rotations . . . 106
4.3.3 Hydrogen rotations and molecular diffusion . . . 108
4.3.4 Formation of the disordered molecular alloy . . . 112
4.4 Addition of Nuclear Quantum Effects . . . 116
4.4.1 Intermediate ordered structure of AHH-II . . . 118
4.5 General conclusions . . . 122
Appendix I . . . 124
A Metastability and simulation times . . . 124
B Comparison between quantum MD methods . . . 127
Appendix II: simulations beyond P=6GPa . . . 129
C Compression at 300K . . . 131
D Compression at 500K . . . 132
E Cooling at 18GPa and decompressing at 300K . . . 135
F Tables . . . 137

In this Chapter, we present the main results obtained from molecular dynamics simulations on Ammonia Hemi-Hydrates (AHH) at high pressure. We determine equilibrium and dynam-

ical properties, and compare them to the experimental data on AHH of Andriambariarijaona et al. [44, 73]. Our findings can be summarized as follow:

- *observation of a phase transition between the (monoclinic) crystal phase AHH-II to the plastic solid phase of AHH-pbcc, at P-T values coherent with the experiments;*
- *observation of a phase transition between the plastic solid phase of AHH-pbcc to the liquid phase, at P-T values coherent with the experiments;*
- *dynamical characterization of the plastic behavior of the AHH-pbcc phase;*
- *complete microscopical explanation of the transition mechanism, focusing in particular on the formation of the disordered molecular alloy (DMA) feature of AHH-pbcc. The name given to the microscopical process is orientational-disorder-driven site disorder (ODDSD), whose combine molecular diffusion and a precise crystalline alloy structure and it is due to the directionality of water and ammonia hydrogen bonds.*

As for the numerical methods, we use a force field approach for the electronic potential (within the Born-Oppenheimer approximation), and mostly classical Langevin molecular dynamics (ClMD) method as the main simulation tool. For some properties, we also include the nuclear quantum effects (NQEs) via two of the methods described in Chapter 2, namely the Adaptive Quantum Thermal Bath (adQTB) [117] and the thermostatted Ring-Polymer Molecular Dynamics ((T)RPMD) [112].

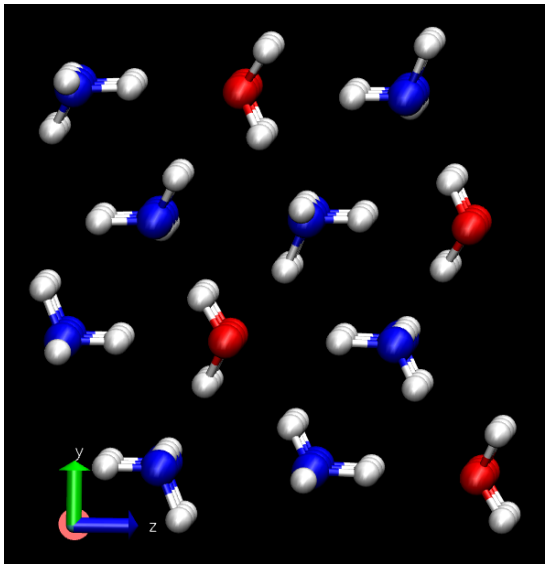

(a) Water and ammonia sequences along the $(1,0,0)$ direction.

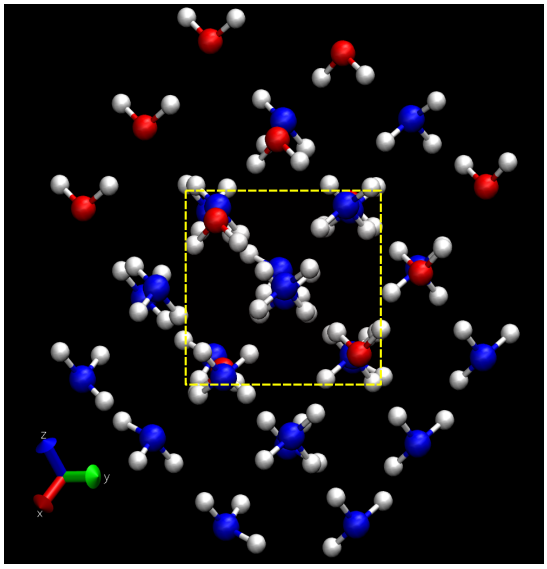

(b) Same structure projected along the $(1,1,1)$ direction.

Figure 4.1: Low temperature AHH-II phase structure [54] replicated 3 times over direction (1,0,0). The yellow square in panel (b) is a guide for the eye to help identify how the structure can be related to a *bcc* structure (though it is deformed with respect to the perfect cubic structure).

4.1 Molecular dynamics simulations setup

In the Introduction of this thesis, we described the state-of-the-art on ammonia hydrate systems, focusing in particular on the latest updates on ammonia hemi-hydrates (AHH) in the P-T range of [300K-700K] and [2GPa-26GPa] [44, 73]. The following Sections describe the starting point of our theoretical investigation, namely the phase AHH-II [54], and the details of the numerical simulations we performed.

4.1.1 Description of the input AHH-II structure

The crystalline structure of AHH-II was determined at 3.6GPa and room temperature by Wilson et al. [54] via neutron scattering diffraction. The elementary cell of AHH-II has a monoclinic structure, with a β angle of $94.4°$. The symmetry space-group is $P2_1/c$. Figure 4.1 shows the elementary structure of AHH-II replicated three times along the direction of the vector $\hat{x} = (1,0,0)$. As depicted in Figure 4.1a, the ammonia and water molecules are ordered in homogeneous stacks along the $\hat{x}$ axis. AHH-II is therefore characterized by a precise chemical order in this crystal structure. Moreover, we can notice that each water molecule (oxygen atoms in red) is surrounded by an hexagon of ammonia molecule (nitrogen atoms in blue). The hexagon shape suggests the presence of a deformed *bcc* cell. The $(1,0,0)$ direction would be the ternary axis of the *bcc* structure.

Figure 4.1b shows the AHH-II structure along the $(1,1,1)$ direction, along which the

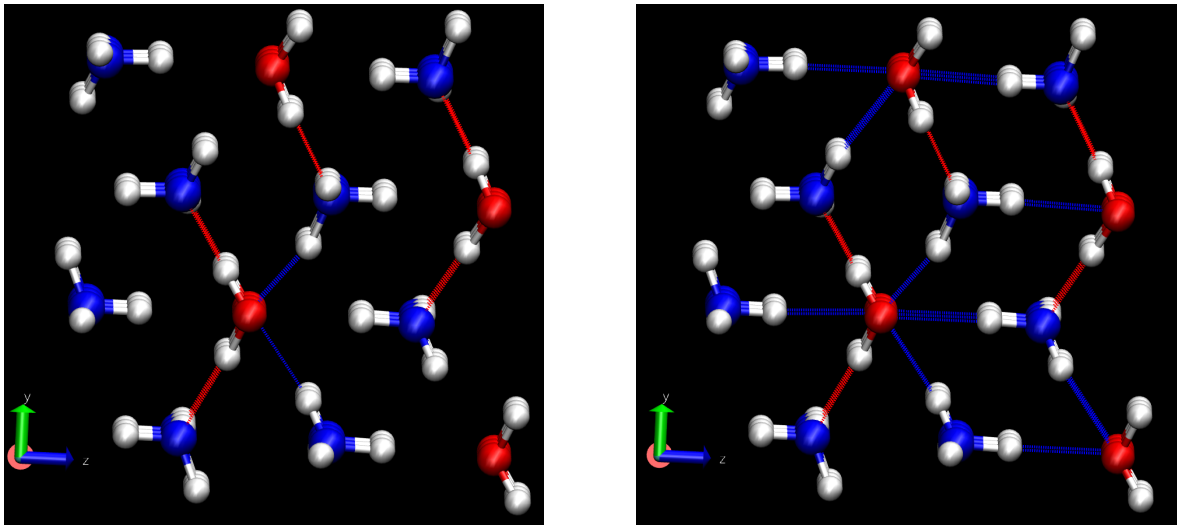

(a) Cutoff radius of 3.1Å.

(b) Cutoff radius of 3.5Å.

Figure 4.2: Hydrogen bonds in the low temperature structure [54] at different cutoff radius and cutoff angle of 30°. In Figure (b) there are also present ammonia homonuclear H-bonds in the direction $(1, 0, 0)$. Red lines indicate an oxygen donor, blue lines a nitrogen donor.

alternance of ammonia and water molecules follows the stoichiometric formula, i.e. two molecules of ammonia and one of water. We want to draw the attention to the yellow square drawn at the center of the image. This represents the projection on the $(1, 1, 1)$ direction of what would be a *bcc* cell. On one of the diagonals of this cube, i.e. the $(1, 0, 0)$ direction, water molecules occupy what in a standard *bcc* lattice would be the first neighbor position, at a distance of $\sqrt{3}a/2 = 2.4$Å, where $a = 3.39$Å is the lattice parameter of the elementary *bcc* cell. However, as it is already clear in the picture, the cubes are deformed in a the monoclinic structure, and the distance between water molecules is larger (of a additional 0.2Å on average) than the first neighbor distance.

We proceed now to the analysis of the H-bond pattern in this structure. Figure 4.2 shows the hydrogen bonds in the low temperature structure with different cut-off distances: 3.1Å in panel 4.2a and 3.5Å in panel 4.2b. Starting with the former, two main types of hydrogen bond appear: the OH$\cdots$N bond (red lines), with typical distances inferior to 3Å, and NH$\cdots$O, with typical distances around 3.1Å(blue lines). When the cutoff radius is extended to the standard 3.5Å criterion [187], other hydrogen bonds become visible, along the direction of the vector $\hat{z} = (0, 0, 1)$. In total, each water molecule receives four bonds from the surrounding ammonia molecules, while it gives two bonds to two ammonia molecules. Two of them, which were partially appearing also with a smaller cut-off, are established on the directions $(-1, 1, 1)$ and $(1, -1, 0)$; the other two hydrogen bonds come from the second neighbors ammonia molecules along the $(1, 0, 0)$ direction. Moreover, notice that, not visible in the picture from this prospect, each ammonia molecule has a homo-molecular bond with its neighbors, along direction of the vector $\hat{x}$, with typical distances around 3.2Å. As a final remark, we notice that the hydrogen bond network of the structure of AHH-II is very anisotropic: the energetically stronger hydrogen bonds (with the water as donor) have a component in the direction $\hat{y}$; on the contrary, the directions $\hat{x}$ and $\hat{z}$ only contains weaker hydrogen bonds with the ammonia as donor. For more details on the respective strength of

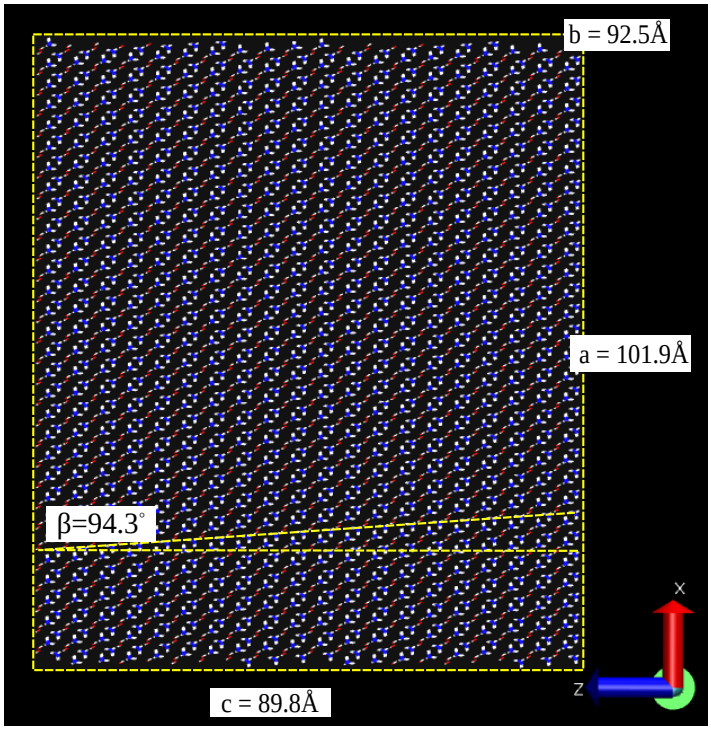

Figure 4.3: Optimized AHH-II structure shown along the direction $(0, 1, 0)$ direction in order to visualize the β angle within the monoclinic box. Three box dimensions (a, b, c) are also reported.

water and ammonia hydrogen bonds we refer to [16].

The starting configuration for the simulations is constructed from the AHH-II experimental structure determined by Wilson et al. [54]. The unit cell has been replicated 10 times along $\hat{y}$ and $\hat{z}$ directions, and 30 times along $\hat{x}$ directions. Lattice parameters were slightly modified in order have a integer number of atoms on all directions. The final simulation box counts 12k water molecules, 24k ammonia molecules, for a total of 132k atoms. Periodic boundaries conditions are applied. As final result, we obtain an orthorhombic simulation box of overall parameters shown in Figure 4.3, with the desired angle β in the bulk, due to the periodic conditions, visible in the x-z plane. The structure was then optimized via the TinkerHP structure optimization program to ensure a stable starting configuration for the molecular dynamics simulations.

4.1.2 Computational details of MD-based methods

All Molecular Dynamics (MD) simulations described in this Chapter have been performed via the TinkerHP package for GPU architecture [97, 188]. The code is able to handle large numbers of molecules and it includes a variety of Force Field (FF) potentials. Moreover, it can perform simulations with MD methods including NQEs, such as thermostatted Ring-Polymer molecular dynamics ((T)RPMD) and Adaptive Quantum Thermal Bath (adQTB) [76]. These methods had been tested with success in previous works on liquid water [84, 118, 119], using the same version of the TinkerHP code. Thanks to the direct interaction

with the developers in Jean-Philip Piquemal's group at LCT (in particular Thomas Plé), we were able to add some specific features, such as the anisotropic barostat for NPT simulations [139, 157], which were crucial for our theoretical investigation. Shorter simulations were also performed with LAMMPS code [189] using an equivalent setup, in order to assess the effect of the orthorhombic barostat.

TinkerHP includes a large variety of force fields potentials, shaped in particular for biological molecules. For ammonia molecules, the FF used for the following simulations is the Optimized Potentials for Liquid Simulations All Atoms (OPLS-AA) [88, 94] included in the TinkerHP package. Referring to the notation of Eq. (2.9) and Eq. (2.10), the parameters k_r, k_θ, ϵ_{ij} and σ_{ij} used can be found in [99]. For water molecules, we used the Simple Point-Charge flexible (SPC/fw) [95], with parameters (k_r, k_θ, ϵ_{ij} and σ_{ij}) from Paesani et al. [96]. As a preliminary check, a 2ns long, NPT simulation on liquid water was performed at 298K and 1atm pressure. The simulation box containing 4000 water molecules is used to safely avoid finite size effects. The average density obtained is ρ =1.0056±0.004g/cm^3, which is comparable to the value reported by Paesani et al. [96] and slightly overestimate the experimental result [190]. Moreover, we compute the self diffusion coefficient from a linear fit of the MSD (Eq. (3.3)), obtaining D =0.227Å/ps, comparable once again with the experimental result and compatible with the value of Paesani et al. [96]. Notice that the SPC/Fw model has also its quantum equivalent, namely the q-SPC/Fw, which would allow to use safely the methods to include nuclear quantum effects. Indeed, the parameters in SPC/Fw as in other force fields were fitted in order to best reproduce experimental results when used in MD simulations with classical nuclei. Therefore the force field parameters implicitly account for NQEs and they should be refitted in order to be used with explicit NQE methods such as adQTB and (T)RPMD.

TinkerHP includes also polarizables force fields, such as AMOEBA (Atomic Multipole Optimized Energetics for Biomolecular Applications). The AMOEBA force field coupled with Langevin-based MD methods has given remarkably accurate results on liquid water [118] and it has been recently adapted to deal with NQEs (q-AMOEBA [119]). However, while being fitted with high precision for water molecules at ambient pressure, preliminary testing of the AMOEBA force field on ammonia hydrates were unsatisfactory. In particular, both classical and quantum MD simulations of the AHH system at high pressure encountered unexpected force estimation failures when temperature was raised above the 500K and 300K thresholds respectively. Thus, we concluded that the AMOEBA force field, as it is fitted for ambient conditions, cannot be used in the high-pressure/high-temperature range and was therefore impossible to use for this study.

Classical molecular dynamics simulations are performed in the NVT and NPT ensemble using the Langevin thermostat [134] and the anisotropic Langevin barostat [139, 157] (see Section 2.3 for more details). If not specified, the system-bath coupling constant γ_{therm} is 20ps^{-1}. The barostat has also a coupling constant γ_{bar} = 20ps^{-1} and a piston mass in a range between 10^6[a.u] and 10^7[a.u] (where a.u. stands for the arbitrary units of TinkerHP), chosen to guarantee a fast equilibration of the box parameters. A BAOAB [135] with double integration time scheme is used. Simulation times are specified and discussed in Appendix A. As stated before, two main methods are used for the inclusion of NQEs in the simulations: adQTB and (T)RPMD. The methods are described in Sections 2.6 and 2.4.3 respectively. For

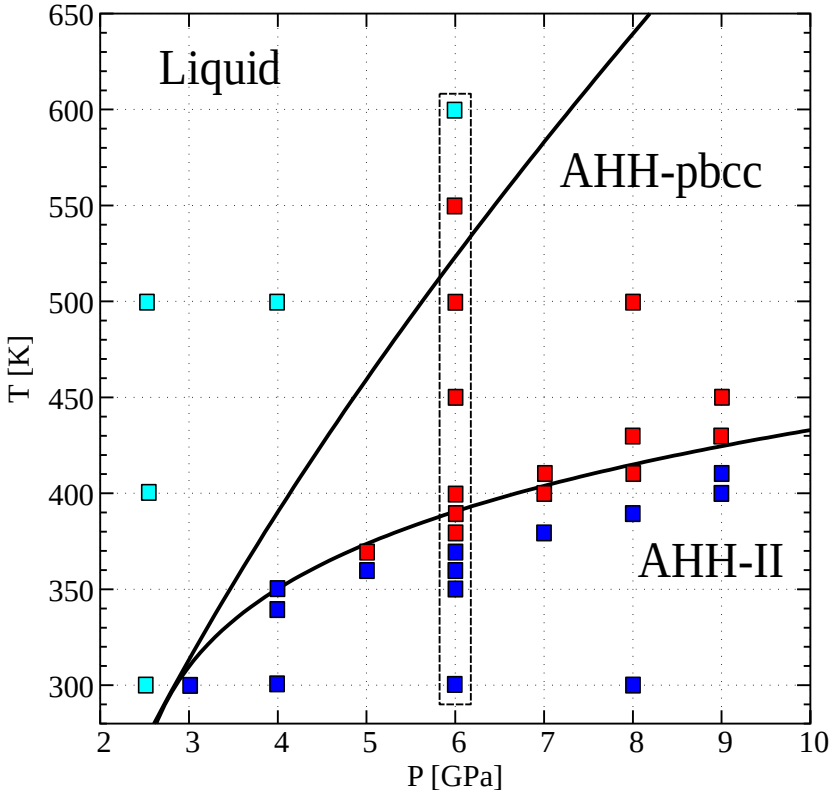

Figure 4.4: Simulation points drawn on the experimental phase diagram by Andriambariarijaona et al. [44, 73]. Blue points for phase AHH-II, red points for phase AHH-pbcc, light-blue points for liquid.

the adQTB, the initial γ_0 is fixed to 20ps^{-1} and the functions $\gamma(\omega)$ are adapted for a period of 1ns before the start of the simulations, and then on the fly during the whole trajectory. Computation times are of the same order of magnitude as for the classical Langevin method. On the other hand, the number of beads used for (T)RPMD methods is P=32. Computation times are of the order of 1ns, due to the higher computational cost.

4.2 Thermodynamics

4.2.1 Establishing the phase transition

The main goal of the theoretical investigation presented in this Chapter is the study of the crystal-plastic phase transition, highlighted by Andriambariarijaona et al. [44, 73], when the AHH-II phase [54] at 300K is heated to higher temperatures.

Figure 4.4 shows the points obtained from classical NPT simulations drawn on the experimental phase diagram from Andriambariarijaona et al. [44, 73]. The three phases are labeled by the following colors: blue points for phase AHH-II, red points for phase AHH-pbcc, light-blue points for liquid. The starting configuration for the simulations is the AHH-II system at 300K and 6GPa. Keeping the pressure stable at 6GPa via the Langevin barostat,

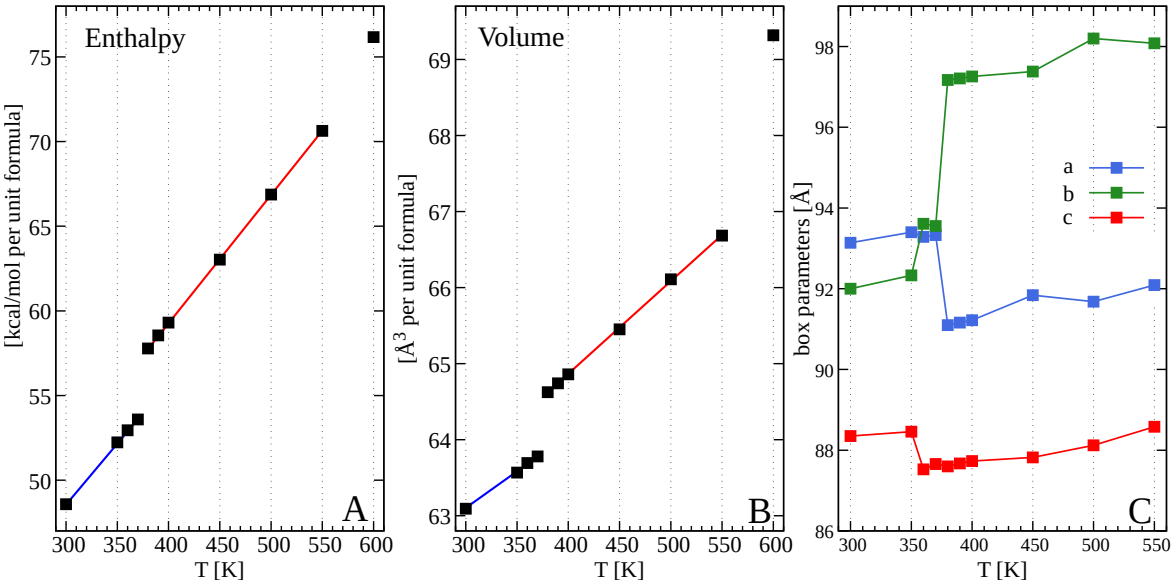

Figure 4.5: Average values of enthalpy (panel A), volume (panel B) and three box parameters (panel C) as function of temperature, at fixed pressure of 6GPa. The colored lines linking the dots in the enthalpy and volume picture indicate the solid phase: blue for the AHH-II solid, red for the AHH-pbcc solid. Error bars are within the point dimensions.

we heat the system until the liquid phase, found at 600K. Then, the system has been then cooled to explore the reversibility of the transitions. Notice that all results presented in this Section are at thermodynamic equilibrium. Simulation times are different for each trajectory: their choice is discussed in Appendix A.

In addition to the simulations at fixed pressure of 6GPa, Figure 4.4 shows also simulation points at different values of pressure, in approximate correspondence with the experimental transition line drawn by Andriambariarijaona et al. [44, 73] between AHH-II and AHH-pbcc [1]. Each point was characterized to be in one of the two phases under study, in order to establish the differences between the simulations and the experimental phase diagram. Overall, our simulations underestimate the experimental transition line with a margin of about 20K. Each point was assigned to each phase based on the direct observation of the configurations' evolution and the monitoring of the behavior of major thermodynamic observables, such as the total energy, the lattice parameters and stresses, along the simulation. In Section 4.4.1, we clarify in details these criteria.

From this point onward, the main analysis is carried out on the results obtained at fixed pressure of 6GPa. Figure 4.5 shows the average values of enthalpy (panel A), volume (panel B) and box parameters (panel C) as a function of temperature. In all three pictures,

[1]The experimental trantion lines are obtained with a fit of the measured pressures and temperatures via the Simon's law [191]:

$$T_t = T_0 \left[\left(\frac{P_t - P_0}{a} \right)^{1/b} + 1 \right] \tag{4.1}$$

where (P_t, T_t) are the transition points, (P_0, T_0) are the lowest points measured, and a and b are free parameters of the fit.

Table 4.1: Comparison of volume and lattice parameter between experiments (from Andriambariarijaona et al. [44, 73]) and simulations at 300K and 6.9GPa. In parenthesis, the percentage error between the simulation and the experimental value.

Experimental results from [44] (pag. 115).					
$T[K]$	$P[kbar]$	$V[\text{Å}^3/mol]$	a[Å]	b[Å]	c[Å]
300	69	21.232(3)	3.243	9.040	8.713
Simulation results					
$T_{in}[K]$	$P_{in}[katm]$	$\langle V\rangle_t[\text{Å}^3/mol]$	$\langle a\rangle_t/30$[Å]	$\langle b\rangle_t/10$[Å]	$\langle c\rangle_t/10$[Å]
300	69	20.618(4) (-2.9%)	3.079 (-5.1%)	9.165 (1.4%)	8.700 (-0.2%)

a sharp discontinuity in the curves is highlighted between 370K and 380K. Therefore, our claim is that, at fixed pressure of 6GPa, a first order transition occurs at a temperature T_c between 370K and 380K, which is about 20K lower than the experimental result at the same pressure. Moreover, the average enthalpy and volume experience another sudden increase between 550K and 600K, when the solid melts into the liquid phase. The full transition line has not yet been explored in details, but the values at fixed pressure of 6GPa indicates a overestimation of the fusion line of about 50K.

For the average volume, we observe two volume discontinuities: $\Delta V/V = 1.4\%$ between 370K and 380K, and $\Delta V/V = 4\%$ at the melting transition. The value reported by experimental observations, between 400K and 433K at 8.5GPa, is $\Delta V_{exp}/V = 0.6\%$ [44, 73], which is ascribed to the solid-solid phase transition between the AHH-II phase and the high temperature phase. Furthermore, Wilson et al. [70] report a volume jump between the AHH-II and what they called generically the DMA phase of 1-3%.

From the values of volume and temperature, we computed the coefficient of thermal volume expansion $\alpha = 1/V(\Delta V/\Delta T)$. We obtain two values, below and above the transition, i.e below 370K and above 380K at 6GPa, which are $\alpha_{<T_c}$ =1.5×10^{-4}K^{-1} and $\alpha_{>T_c}$ =2×10^{-4}K^{-1}. These values are of an order of magnitude larger than that reported by Andriambariarijaona et al. [44, 73]. This result might be due to the orthorhombic constraint of the simulation box and we plan to verify these discrepancies by the use of the Lammps code, which allows to relax the angular constraints.

As explained in Section 4.1.2, the barostat applied to the system is anisotropic, in order to separately adapt each box parameters, here denoted with the letters *a*, *b* and *c*, for the crystal unitary directions $(1,0,0)$, $(0,1,0)$, and $(0,0,1)$ respectively. Following their evolution as temperature increases (Figure 4.5 panel C), the *b* parameter presents a positive sudden increase between 370K and 380K, roughly $\Delta b/b$ =3.9%. A smaller but sudden increase, of $\Delta b/b$ =1.4%, is observed between 350K and 360K as well. On the contrary, the box parameter *a* shows a sudden decrease between 370K and 380K, of about $\Delta a/a$ = -2.4%. Below this temperature, the *a* parameter is constant, and above it slightly increases. Finally, the *c* parameters only shows a relatively smaller decrease between 350K and 360K, of about $\Delta c/c$ =-1.1%. No other sudden changes are observed at higher temperature, but only a smooth increase with temperature. The physical interpretation behind the drastic change of the box parameters at T_c comes from the changes in the anisotropic hydrogen bond network, and it will be clear at the end of this Section.

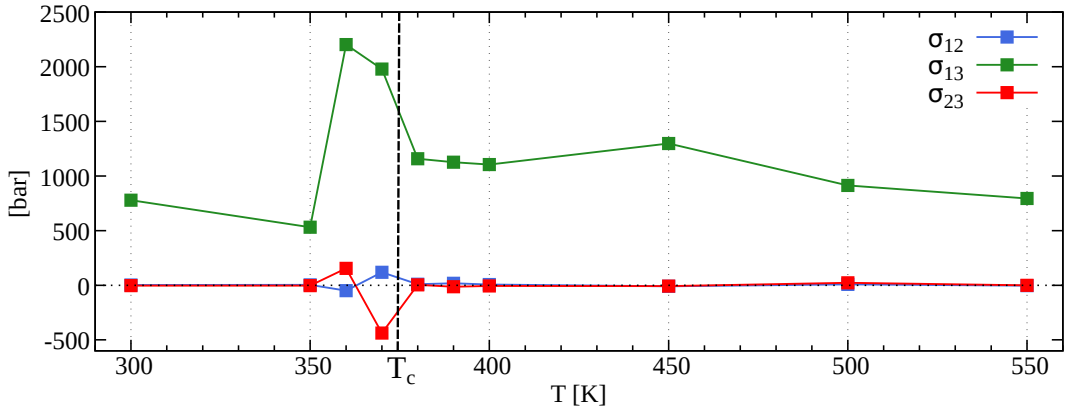

Figure 4.6: Average off-diagonal stress matrix components as a function of temperature, at fixed pressure of 6GPa.

Table 4.1 reports the box parameters for the AHH-II structure at 300K and 6.9GPa, from the work of Andriambariarijaona et al. [44, 73], as well as the results of our simulations at the same T-P conditions.The relative volume difference between the simulation value and the experimental result is about 3%. The differences of the box parameters a, b, c are 5%, 1% and 0.1% respectively.

Finally, we discuss the values of the average stresses, from which the total pressure is computed. For the indexes, the Voigt notation is used. The diagonal components are all stable around the values of input pressure, due to the action of the Langevin barostat. Off-diagonal stresses, shown in Figure 4.6, even though they are in general much than the diagonal components, they are not equal to zero for all temperatures. In particular, the σ_{13} component, which correspond to the angle β between the $\hat{x}$ and $\hat{z}$ directions, has values of the order of the kbar, hence about three order of magnitude grater than the other two components. We can conclude that the orthorhombic box poses still some constraints on the structure at both low and high temperature. Calculations with the Lammps code, which allows the use a full anisotropic barostat, are being performed at the moment, in order to verify the link between the stress components and the orthorhombic box used for the simulations.

In conclusion, from the observation of macroscopic observables, we localized a solid-solid phase transition, with transition temperature T_c between 370K and 380K at 6GPa. Another phase transition, from solid to liquid, is observed between 550K and 600K. Both results are in agreement with the experimental phase diagram of AHH by Andriambariarijaona et al. [44, 73]. We continue now to characterize the solid-solid phase transition from the study of the structural properties.

4.2.2 Structural properties: structure factors and pair distribution functions

In this Section, we describe the structural properties computed in the solid AHH as function of temperature, at fixed pressure of 6GPa (see Figure 4.4). In particular, we compute the

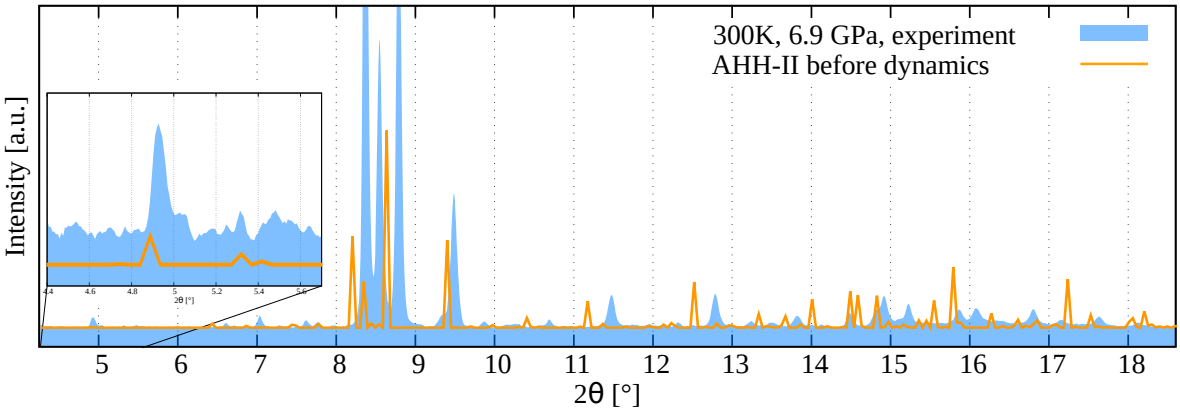

Figure 4.7: Structure factor of the initial configuration (an approximation of the structure of Wilson et al. [54]) compared with experimental X-ray diffraction pattern of AHH-II phase from Andriambariarijaona et al. [44, 73].

structure factors at different temperatures and compare them with the X-ray diffraction patterns measured by Andriambariarijaona et al. [44, 73]. Moreover, we present the radial distribution functions (RDF), and the angular distribution functions (ADF) of molecular dipoles and OH and NH distances.

Structure factor

As explained in Section 4.1.1, the expected structure of the low temperature phase is the AHH-II monoclinic structure of space group $P2_1/c$ found by Wilson et al. [54]. The heating of this phase produces a symmetrization of the structure into a *bcc* lattice. using the following formula

$$S(\vec{\mathbf{q}}) = \frac{1}{N}\left|\sum_j f_j e^{-i\vec{q}\cdot\vec{R}_j}\right|^2 \tag{4.2}$$

where f_j is the form factor of oxygen or nitrogen atoms. Hydrogen atoms were not included in the computation, since the hydrogen X-ray form factor is small compared to the two other chemical species. The estimated numerical resolution is $\Delta\theta = 0.05°$.

As an initial check, the structure factor is computed on the initial configuration described in Section 4.1.1. In Figure 4.7 we compare the result with the experimental X-ray diffraction pattern of phase AHH-II of Andriambariarijaona et al. [44, 73]. The box parameters of the simulation box are $a = 101.9$Å, $b = 92.5$Åand $c = 89.8$Å, which are different from the experimental dimensions. This explain the mismatch on the positions of the peak. However, many similarities between the two curves can be drawn. Starting from low angles, the peak around 5° is well reproduced, as well as the peak around 9.5°. Most importantly, the simulation reproduce the main feature of the AHH-II phase observed from the experimental results, which is the triplet of peaks between 8° and 9°. Finally, for higher angles a multitude of peaks is present and correspondences can be drawn with the experimental result, with a position mismatch of about 0.3°.

Figure 4.8 show the comparison between the X-ray diffraction results from Andriambariar-

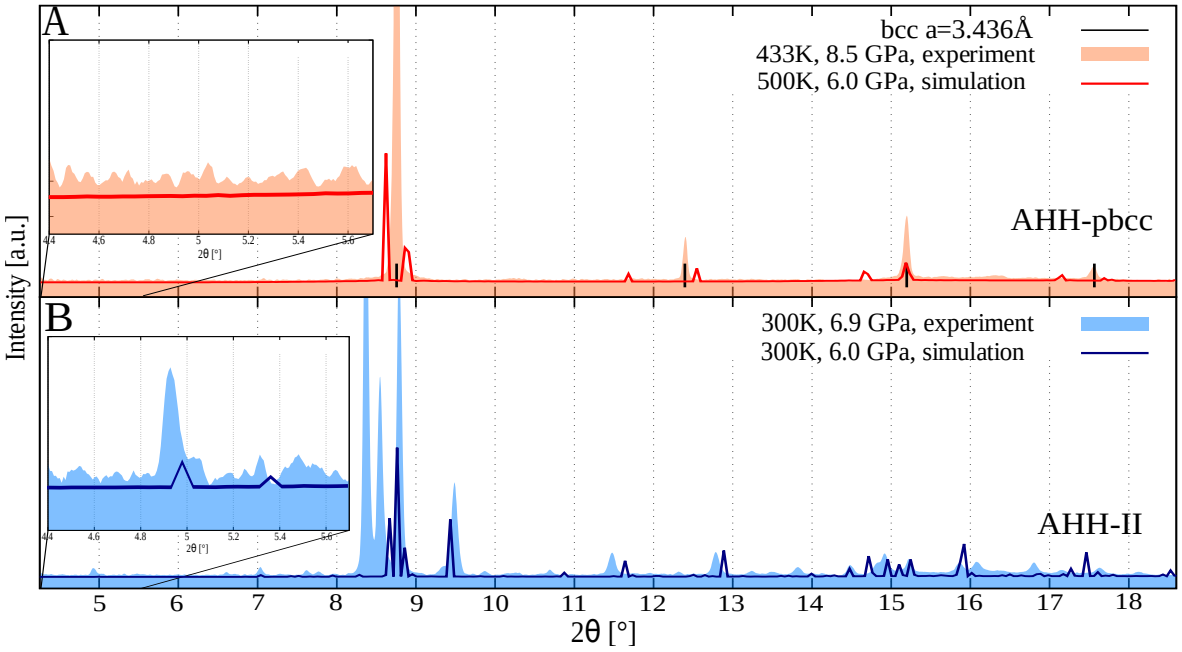

Figure 4.8: Average structure factors (solid lines) compared with experimental X-ray diffraction results [44, 73] at the two main temperature regimes: low temperature in blue (panel B), high temperature in red (panel A).

ijaona et al. [44, 73], compared with the results of the NPT simulations. In order to highlight the difference between the two main phases under study, only two main curves are compared: the 300K curve (Figure 4.8 panel B) for the low temperature phase AHH-II, and the 500K curve (Figure 4.8 panel A) for the high-temperature structure of AHH-pbcc. Both results show remarkable consistence with the experimental results. Several discrepancies, however, call for further comments.

Starting with the structure factor of AHH-II at 300K and 6GPa, the triplet of peaks between 8° and 9° is visible, but much more condensed than the experiment. The main features at 5°, 9.5° are still well visible, as well as the peaks at higher angles, which are now closer to the experimental positions due to the adaptation of the box parameters during the simulation. On the other hand, the simulation diffractogram at high temperature (Figure 4.8 panel A) is in good agreement with the experimental one. In particular, low angles peaks are completely absent, and the only visible features (peaks at 9°, 12.5° and 15°) correspond to the *bcc* structure of lattice parameter 3.436Å reported by the experiment. However, the splitting of the peaks indicates the presence of a quasi-*bcc* rather than a perfect *bcc*. Preliminary tests mad with Lammps code suggest that this result is due to the orthorhombic simulation box used for the Tinker simulations. Indeed, when the constraint on the angles is relaxed, the diffractogram obtained evolves quickly to a perfect *bcc*.

In conclusion, structure factors clearly indicate a overall change in the bulk structure of AHH ice along the 6GPa isobaric line, as temperature rises. As explained in Section 4.1.1, the AHH-II structure has a monoclinic structure, which can be seen also as a deformed *bcc* structure visible on directions such as $(1, 1, 1)$ and its analogous (see Figure 4.1). The phase at high temperature has now a global (quasi)-*bcc* structure, as predicted by the experiments.

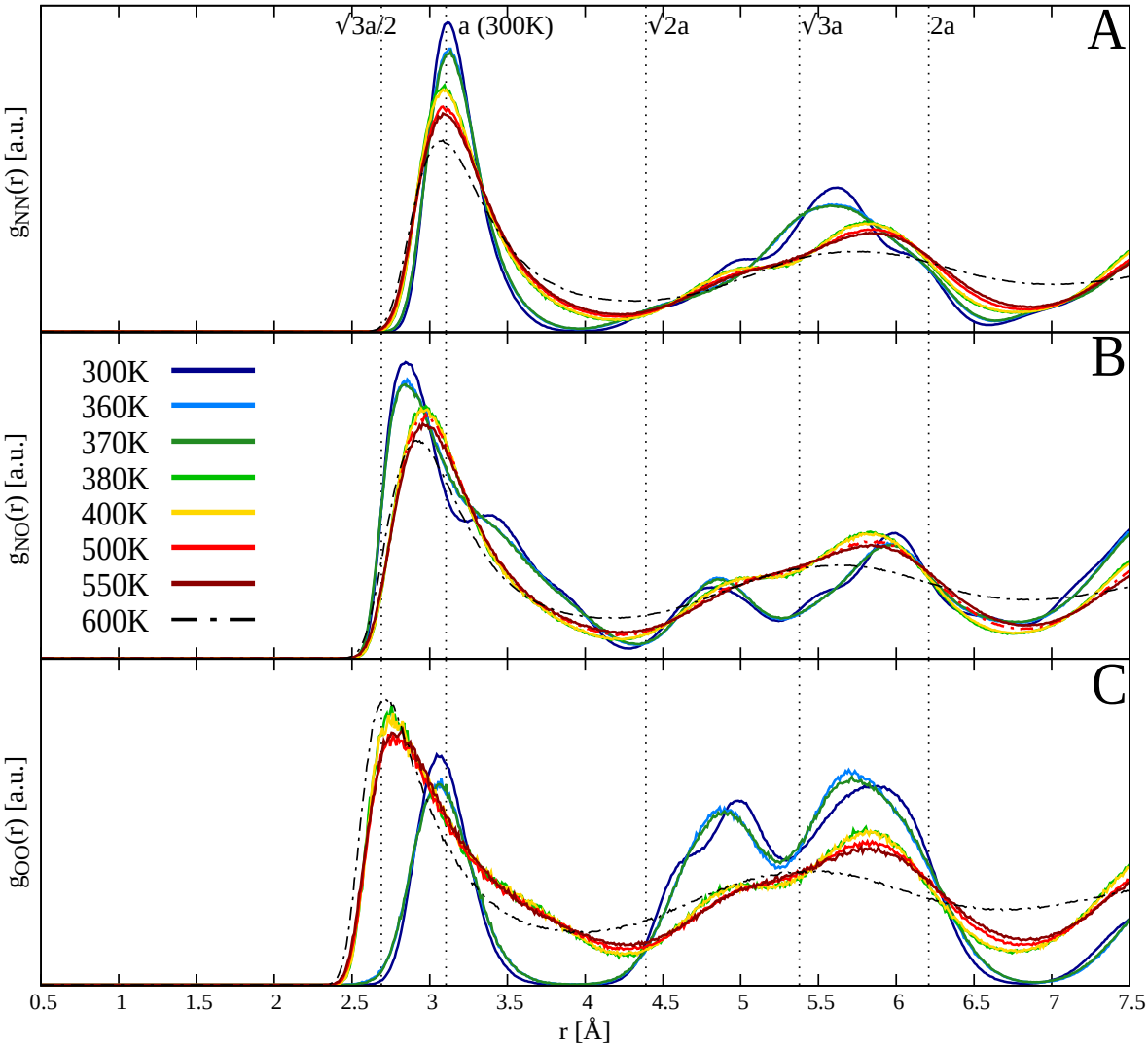

Figure 4.9: Average radial distribution functions of NN, NO and OO distances as function of increasing temperature (fixed pressure of 6GPa).

The transformation of the monoclinic (deformed *bcc*) into *bcc* is crucial in the reading of the following results, namely radial and angular distribution functions, and the hydrogen bonds network.

Radial distribution functions

After having analyzed the structure factors along the 6GPa isobaric line, we analyze the radial distribution functions (RDF) $g_{NN}(r)$, $g_{NO}(r)$, and $g_{OO}(r)$ between the N and O species (Figure 4.9), and $g_{NH}(r)$ and $g_{OH}(r)$ involving H atoms (Figure 4.10). On each graph, the box parameter $a(300K) = 3.105$Å is depicted, obtained from the first box parameter at 300K (see Table 4.8 in Appendix F) divided by a factor 30, which is the number of times the structure given by Wilson et al. [54] was replicated along the direction $(1, 0, 0)$.

In panel A of Figure 4.9, $g_{NN}(r)$ is depicted as a function of temperature. The position

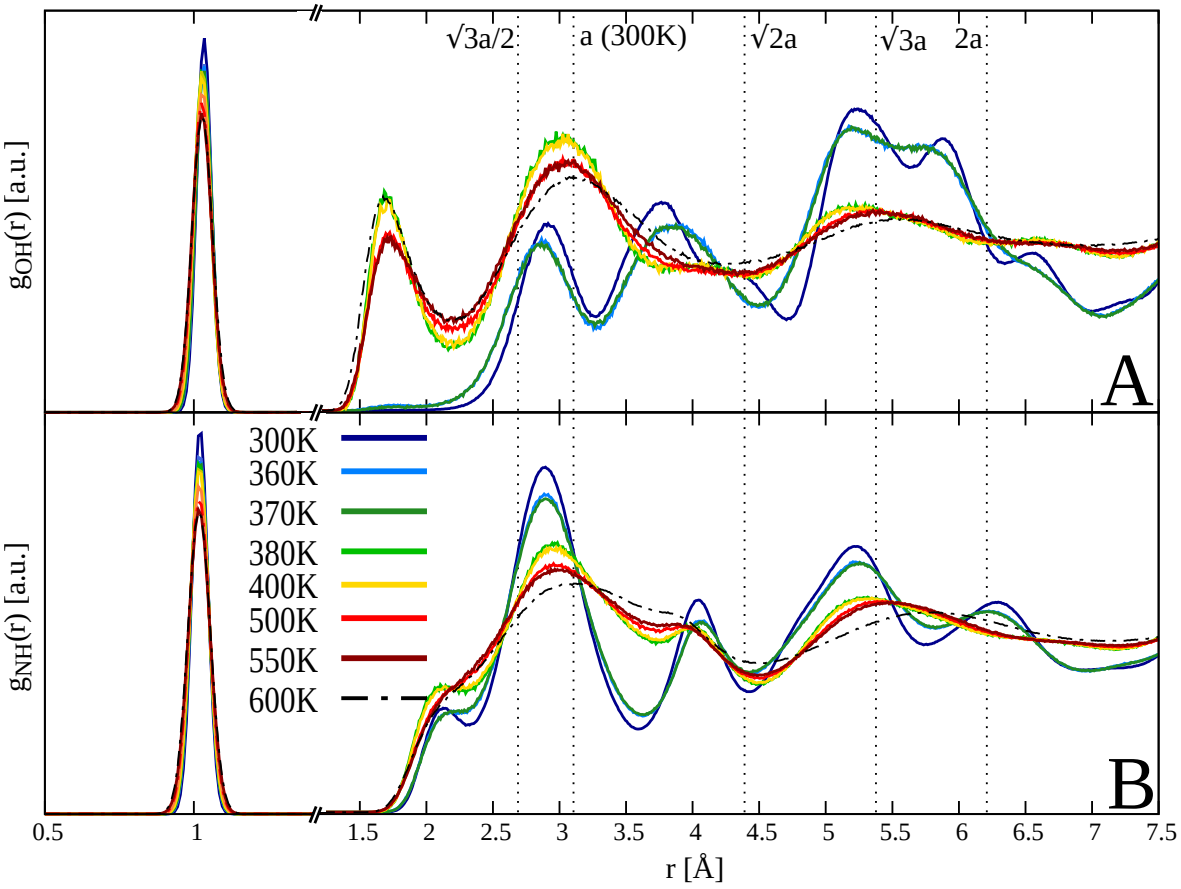

Figure 4.10: Average radial distribution functions of OH and NH distances as function of increasing temperature (fixed pressure of 6GPa).

of the first peak remains almost unchanged along the entirety of the 6GPa line, around the distance $a(300K)$. On the other hand, there is a marked change for both $g_{NO}(r)$ and $g_{OO}(r)$ (panel B and C of Figure 4.9) around 370K-380K: the first peak of $g_{NO}(r)$ displaces from 2.8Å ($T \leq$370K) to 3Å ($T \geq$380K). At the same time , the first peak of $g_{OO}(r)$, which is around a for $T \leq$370K, moves to shorter distances ($\sim$2.7Å) at 380K and above. This is a sign of molecular displacements of water molecules due to the formation of water homonuclear hydrogen bonds, which were completely absent in the low temperature AHH-II crystal.

We comment now the RDF involving the hydrogen atoms, pictured in Figure 4.10. The panel A shows the the change of $g_{OH}(r)$ with temperature. The increase of temperature creates and progressively populates a new peak at 1.7Å, which is completely absent in the structure at low temperature. Noticeably, this peak appears at 380K. Also the peak structure at higher distances is substantially modified, with the creation of a broad peak centered at distance a, at the place of two peaks in the low temperature phase. The $g_{NH}(r)$ (panel B of Figure 4.10) also reveals the progressive flattening of the very well marked peaks present at low temperature.

In conclusion, RDFs reveal that the changes from AHH-II at low temperature to the solid phase at high temperature strongly impact the structure due to the reordering of the water molecules. It is shown by the appearance of a short distance peak in $g_{OH}(r)$, and the

Table 4.2: Miller indexes of crystal directions and corresponding spherical angles according to the ISO convention.

Crystal direction	θ [°]	ϕ [°]
($\pm$1,0,0)	90	0 or 180
(0,$\pm$1,0)	90	$\pm$90
(0,0,$\pm$1)	0 or 180	undefined
(1,1,0)	0	45
(1,0,1)	45	0
(0,1,1)	45	90
(1,1,1)	55	45

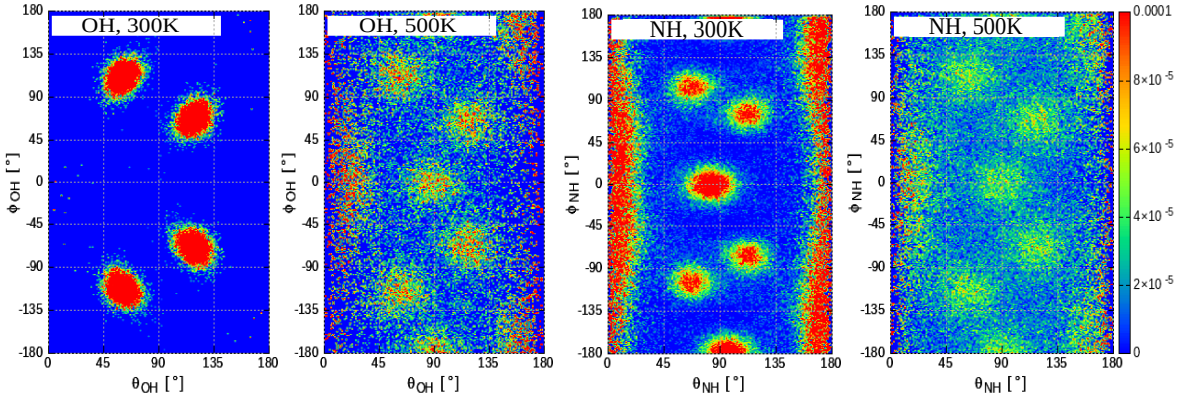

Figure 4.11: Average angular distribution $P(\theta, \phi)$ of intramolecular OH and NH vectors at different temperatures and pressure of 6GPa.

displacement of the first peak of $g_{OO}(r)$ towards shorter distances, as temperature rises. Indeed, the RDFs clearly show that OH$\cdots$O bonds are forming, which necessarily involve rotations of the molecules On the other hand, the RDFs of ammonia molecules seem to be mostly unaffected by temperature.

Angular distributions of intramolecular OH and NH vectors

The RDFs reveal precious insights on the contribution of each molecule in the overall modification of the structure observed via the structure factors. However, as plastic phases are expected to present some form of rotational disorder, we introduce the angular distributions functions (ADFs) $P(\theta, \phi)$. They are computed as histograms over all polar angles (θ, ϕ), once the Cartesian coordinates are transformed in spherical ones, around the heavy atom of the molecule (N for NH_3 and O for H_2O). Table 4.2 lists the main crystal directions and the respective values of the spherical angles θ and ϕ, which follow the ISO convention. In general, we are interested in two types of rotational disorder: the rotation of molecular dipole, as signature of a full reorientation of the dipole axis, and the rotation of hydrogen atoms, which could reveal reorientation of the hydrogen bonds around the dipole axis.

Figure 4.11 shows the two-dimensional ADF of the intra-molecular covalent OH and

NH bonds respectively, at two different temperatures at 6GPa. The cutoff radius used is 1.5Å, in order to consider only the contribution of intermolecular hydrogen atoms. The angular distributions for the two molecular species present an increasing level of disorder as temperature rises, from 300K to 500K. However, a qualitative difference is observed between OH and NH bonds. Indeed, for the OH distribution, only four, very well distinguishable directions are visible at 300K and 6GPa. They are close to the direction $(0, 1, 1)$ and its equivalents, which correspond to the hydrogen bonds established by water with the surrounding ammonia molecules (see Figure 4.1a). As temperature rises, other preferential directions appear, for a total of eight. They correspond to the eight corners of the cube surrounding a water molecule at the center, which indeed suggests the presence of a *bcc* structure. Note that although still visible, the peaks are blurred, indicating hops between different H-bonds.

On the other hand, at 300K, the NH angular distribution shows the main peaks at $(\theta, \phi) = (90°, 0°/180°)$, corresponding to the hydrogen bonds between ammonia molecules along the direction $(\pm 1, 0, 0)$; the four peaks already visible in the OH distribution correspond to ammonia-water hydrogen bonds in the direction $(0, 1, 1)$ and its equivalents; finally, two last ammonia-water hydrogen bonds are in the direction $(0, 0, \pm 1)$. The peaks are much more blurred compared to the OH distribution, indicating a higher level of orientational disorder. The same is true for the phase at at 500K: the disorder is almost complete. However, the positions of the peaks are the same of the ones in the distribution of OH vectors, which again suggests the possibility of ammonia to form hydrogen bonds with atoms surrounding it on a cube.

In conclusion, the hydrogen atoms of both water and ammonia molecules tend to assume different but fixed orientations, in agreement with the structure of AHH-II at low temperature; however, the hydrogen atoms of ammonia molecules already show an higher degree of rotation than the water counterpart. High temperature enhances rotations for both molecules and cancels the differences in the preferred directions for the two molecular species. Therefore, at 500K, each molecule has eight others surrounding it on the vertex of a cube, which would correspond to an average *bcc* structure.

Angular distributions of molecular dipoles

We consider now the ADFs of molecular dipoles, in order to study the rotations of the entire molecule as a function of temperature. Figure 4.12 shows the angular distribution of water and ammonia molecular dipoles, respectively, for several increasing temperatures. The liquid phase at 600K is included for comparison. This distribution functions gives a qualitative picture of the orientational disorder of dipoles in the different temperature regimes. It is clear that the structure of AHH-II ice is rigid, with molecules well fixed in specific orientations. Water molecules (panel A, 300K) are oriented in such way that their dipoles lie on the x-z plane, as ϕ is around 0° or 180°. Ammonia dipoles (panel B) are also oriented in four preferred directions at 300K, corresponding also to the orientation of the OH bonds in that phase. Notice that a small degree of disorder is visible after a long simulation, when very few molecules had the time to rotate to another preferred configuration. However, the overall structure remains rigid within the simulation time.

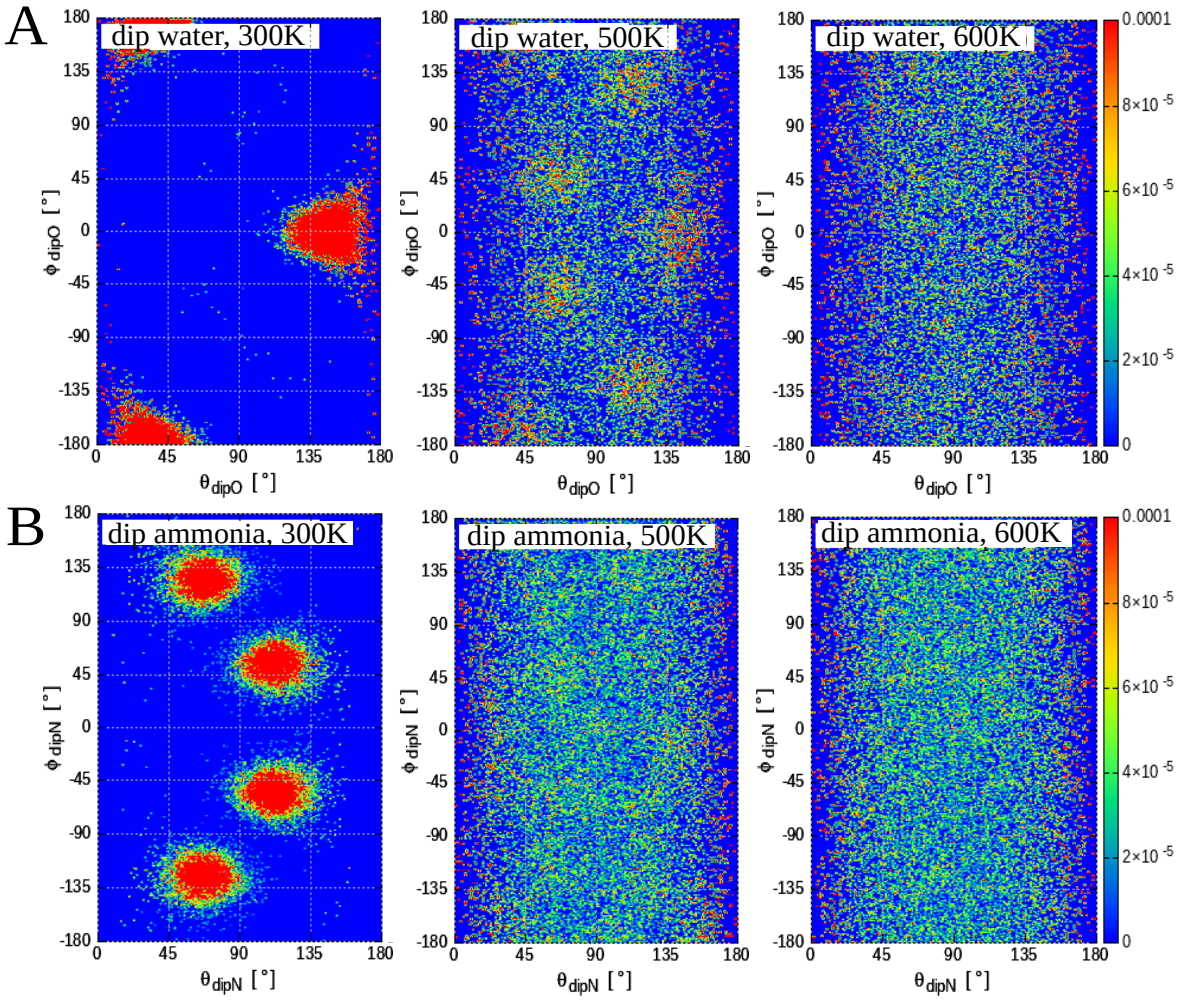

Figure 4.12: Average angular distribution $P(\theta, \phi)$ of water and ammonia dipoles at different temperatures and fixed pressure of 6GPa.

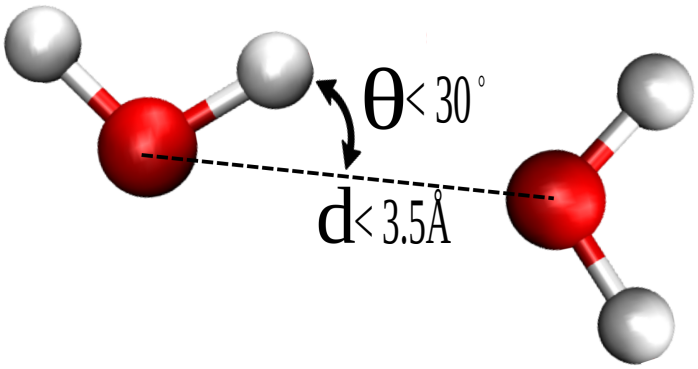

Figure 4.13: Water dimer with acceptor-donor distance d and the angle θ between donor-acceptor distance highlighted. The hydrogen bond is established according to the criterion of [187].

As temperature rises, new preferred directions appear in the water dipoles distribution. They corresponds to the faces of the *bcc* cell in the AHH-pbcc structure, on directions $(1, 1, 1)$ and its analogous. Moreover, a general orientational disorder is clearly visible, in particular for ammonia molecules, which distribution at 500K is almost comparable to the liquid phase. This is an important difference with respect to the distribution of OH and NH distances. Indeed, both dipoles distributions are much more sensitive to the phase transition under study, whereas the sign of a qualitative change at the transition are well visible for the OH distribution, but less pronounced for the NH distribution. Moreover, ammonia molecules appear to rotate around their dipole axis at every temperature above 300K, while water molecules maintain rigidly both their dipoles and the OH covalent bonds below 370K.

To conclude, we addressed the orientations of both OH and NH intermolecular vectors (Figures 4.11), and the water and ammonia dipole orientations (Figures 4.12) via angular distribution functions $P(\theta, \phi)$. We highlighted how two kinds of orientational disorder, the former around the dipole axis, the latter of full molecule rotations, increase with temperature. There is a marked change in the molecules' dynamics above and below the transition: both water and ammonia orientational distributions change from a distribution corresponding to a rigid structure, to a phase of full molecular reorientations, where the blurred preferred directions are coherent with a *bcc* lattice.

4.2.3 Evolution of the hydrogen bond network

Finally, we discuss the evolution of the hydrogen bond network (HBN) with temperature at P =6GPa. Indeed, as explained in the Introduction of this thesis, the competition between different types of hydrogen bonds and the degree of connectivity of the HBN play a crucial role in the structures of AHH ice.

Four types of hydrogen bonds are studied, two of which involve homo-nuclear species, namely NH$\cdots$N and OH$\cdots$O, and two hetero-nuclear bonds, namely NH$\cdots$O and OH$\cdots$N. For all of them, we computed the mixed distribution $P(d, \theta)$ of donor-acceptor distance d,

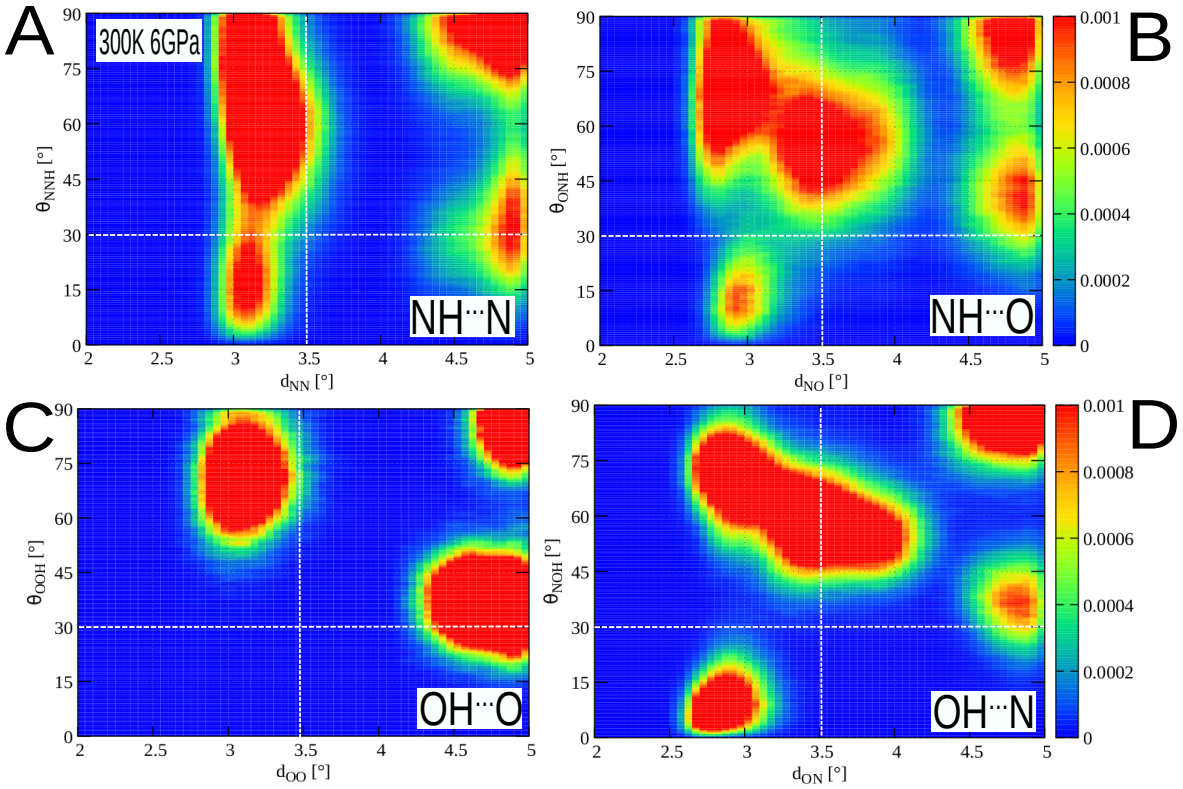

Figure 4.14: Mixed radial-angular distributions $P(d, \theta)$ at 300K for four types of hydrogen bonds, as specified in the lower right corner of each panel.

and the angle θ between donor-acceptor distance d and the donor-hydrogen distance, as shown in Figure 4.13. Notice that we distinguish between the hydrogen atoms linked to water molecules and hydrogen atoms linked to ammonia molecules.

Figures 4.14 and 4.15 show the mixed radial-angular distribution $P(d, \theta)$ at two different temperatures (300K and 500K respectively).Since the hydrogen bond is directional, we are interested in bonds with angles θ smaller than 30°, and $d \leq 3.5$Å, accordingly with the Luzar-Chandler criterion [187]. From Figures 4.14, we observe a well defined portion of the distribution within the limits of the CL criterion, which makes it use consistent. Moreover, starting from panel A of Figure 4.14, H-bonds between ammonia molecules involve distances $d \in [2.9\text{Å}, 3.5\text{Å}]$, and the distribution is almost independent of θ. On the contrary, all other three distributions show a dependence on the θ angle. If we consider only the part of the distribution limited by d_{max} =3.5Å and θ_{max} =30°, NH$\cdots$O bonds (panel B), a distinct but broad peak is present at 2.9Å and 15°, which is significative of directional hydrogen bonds. The distribution of OH$\cdots$N bonds in panel D shows a maximum at $d \simeq 2.8$Å and $\theta \simeq 10°$ that is very marked at 300K, while blurred at 500K. Finally, we remark the absence of OH$\cdots$O bonds at low temperature, consistent with the crystal AHH-II phase.

The picture at high temperature (Figure 4.15) is completely different. As expected, thermal agitation smooths most of the peaks in all distributions. Noticeably, for OH$\cdots$N bonds in panel D, the important peak is still visible but it lost most of its intensity. Moreover,

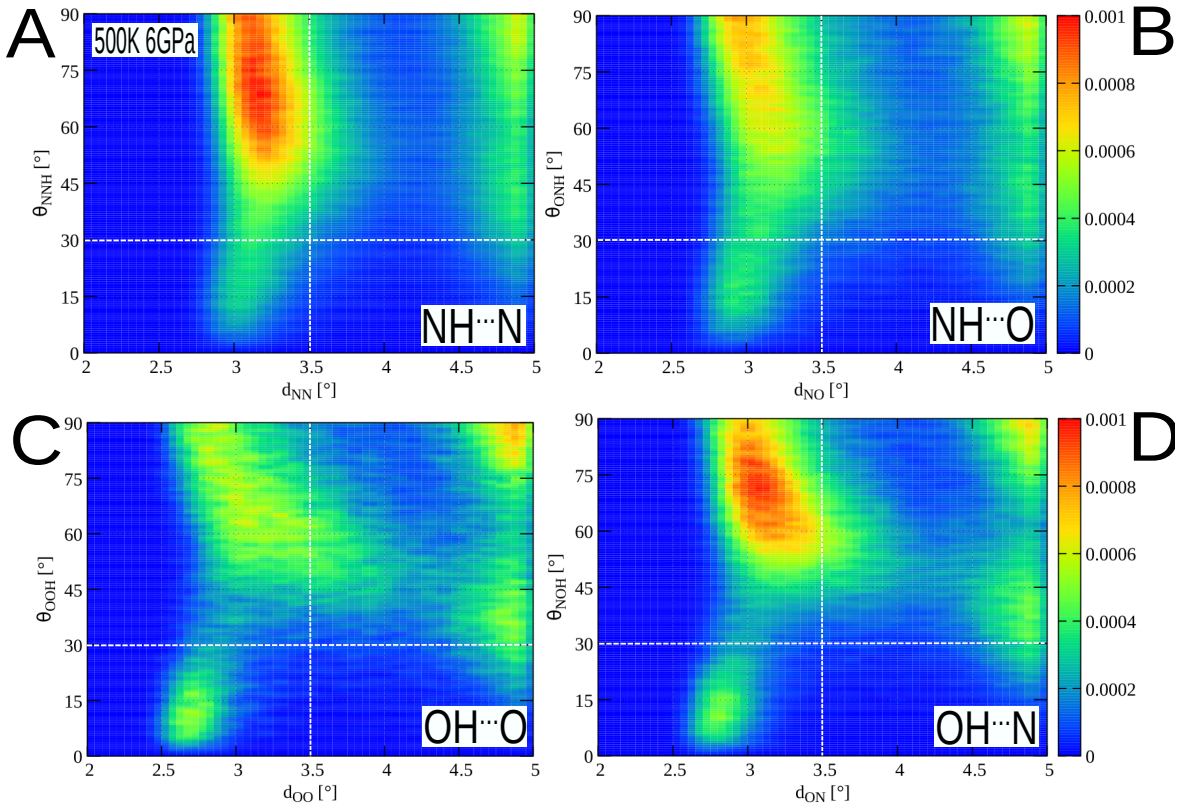

Figure 4.15: Mixed radial-angular distributions $P(d, \theta)$ at 500K for four types of hydrogen bonds, as specified in the lower right corner of each panel.

Table 4.3: Normalized number of hydrogen bonds at different temperatures, with $r_{cut} = 3.5$Å and $\theta_{cut} = 30°$. The normalized number is obtained by dividing the total number of bonds by the total number of donors per type. The first line (pale yellow) is the reference number of H-bonds of AHH-II according to the structure of Wilson et al. [54].

$T_{in}[K]$	$n_{OH...O}$	$n_{NH...N}$	$n_{NH...O}$	$n_{OH...N}$
–	0	1	2	2
300	0.00(0)	1.07	1.81	1.99
350	0.01	1.11	1.68	1.97
360	0.02	1.11	1.69	1.96
370	0.02	1.12	1.66	1.96
380	0.64	1.61	0.96	1.20
390	0.63	1.59	0.97	1.20
400	0.64	1.59	0.95	1.18
500	0.59	1.47	0.93	1.16
600	0.66	1.34	0.81	1.05

all distributions have now the same shape, with a low intensity peak around 15°, also for OH$\cdots$O bonds, whereas they were completely absent at low temperature. The remarkable difference dwells in the internuclear distance: water as donor corresponds to peaks between 2.6Å and 3Å, whereas nitrogen donor originates bonds with distance well centered around 3Å.

Having shown that the criteria for the existence of H-bonds corresponds to a well defined region of the (d, θ) distribution, we discuss now the average number of hydrogen bonds, counted as a simple sum of existing bonds between all respective triplets of donor-hydrogen-acceptor atoms of the system. Table 4.3 reports the normalized number of hydrogen bond per trajectory. This normalized number is obtained by dividing the total number of bonds by the number of donors for each type. Thus, the total number of NH$\cdots$X bonds is divided by the number of ammonia molecules (where X could be either N or O atom), and the OH$\cdots$X bonds by the total number of water molecules.

The first line of Table 4.3) shows the normalized number of hydrogen bonds in the structure of Wilson et al. [54], which we consider our reference structure of AHH-II. Each ammonia molecule forms a homo-molecular bond in the direction $(1, 0, 0)$, and two bonds (one as a donor, one as an acceptor) with the neighboring water molecules (see as well Figure 4.2b). On the other hand, each water molecule donates two bonds to its ammonia neighbors. At the same time, it accepts four hydrogen bonds from the neighboring ammonia molecules. No OH$\cdots$O exists in this structure.

This same picture stands at 300K and 6GPa: the number of OH$\cdots$O bonds is zero, while two OH$\cdots$N bonds are present, with almost the same proportions as the ones expected in this crystal phase. Crucially, the number of OH$\cdots$N bonds is stable. As temperature increases, this picture is modified. The number of bond types suddenly increases or decreases between 370K and 380K. Starting with the number of hydrogen bonds between water molecules, it jumps from zero to over 50% at 380K. At the same time, the number

of OH$\cdots$N bonds decreases by 40% at the transition temperature. Concerning the ammonia molecules, the number of NH$\cdots$N bonds increases by 30% and the number of NH$\cdots$O bonds decreases by 40% at the transition. All these values remain almost constant in the high temperature phase, until the melting of the system.

In conclusion, the overall hydrogen bond network undergoes a consistent and qualitative change at the phase transition, with the breaking of strong hydrogen bonds with water as donor to the ammonia, and the formations of water homonuclear hydrogen bonds. Overall, the numbers of H-bonds obtained at 500K are coherent with a disordered *bcc* phase, where we have $2/3$ of probability to find on each vertex of the cube a nitrogen atom, and $1/3$ an oxygen atom, taking into account the respective strengths.[2]Further network topology analysis of the HBN could be performed on the AHH structure, as done by Toffano et al. in the case of pure water ice VII [66].

4.2.4 Discussion of thermodynamics results

From the results exposed in the previous Sections we can draw some important conclusions on the existence and the nature of the phase transition in AHH along the 6GPa isobaric line. First, the AHH-II structure of Wilson et al. [54] is found to be stable between 300K and 370K. Confirmation of its presence is given by the structure factors compared to the experimental results (see Figures 4.7 and 4.8). The stability of the AHH-II crystal is mainly due to the hydrogen bonds that oxygen donors establish with nitrogen acceptors. This fact is coherent with the RDFs (see Figure 4.9 panel C), where no water molecules are first nearest neighbors. The stability of this type of bond, namely OH$\cdots$N is confirmed by the ADF of OH distances (Figure 4.11) and water dipole ADF (Figure 4.12 panel A). Indeed, no orientational disorder is observed in the low temperature phase for water.

As temperature rises, we found a clear, abrupt transition in all the structural quantities, between 370K and 380K. Discontinuities are observed in the average enthalpy, box parameters and volume (Figure 4.5). The structure factor reveals a change from the monoclinic structure of AHH-II to a (quasi)-*bcc* at high temperature. New peaks are formed at short distances in the $g_{OO}(r)$ and $g_{OH}(r)$ (Figures 4.9 and 4.10), which point at the existence of neighboring water molecule in the new structure. This fact is coherent with the sudden increase of the number of OH$\cdots$O bonds (see Table 4.3), which highlights the formation of hydrogen bonds between water molecules in the new structure. Moreover, at the transition temperature, the number of OH$\cdots$N suddenly decreases, coherently with the beginning of the rotation of water molecules. Henceforth, we suggest that the main driving mechanism for the phase transition to occur is given by the breaking of the OH$\cdots$N bonds, which are the strongest H-bonds in the system [16]. The evolution of the box parameter with temperature is coherent with this interpretation, as the parameter b suddenly increases when the OH$\cdots$N are broken, whereas the parameter a decreases as new OH$\cdots$O bonds are formed in this direction. Finally new peaks appears in all ADFs of covalent bond distances and dipoles corresponding to faces and corners of *bcc* cell, coupled with a general and persis-

[2]The stronger hydrogen bonds in the structure are the ones with water as donor, and the weakest is NH$\cdots$O [16, 192].

tent orientational disorder of molecules.

To summaries, our current results not only confirm the presence of a solid-solid phase transition for AHH ices, but they suggest the following properties:

- the high temperature phase could be classified as plastic, because of its orientational disorder, which appears suddenly above the transition temperature;
- the high temperature phase has a *bcc* structure, which may be the result of the evolution of the HBN with temperature;
- the normalized number of hydrogen bonds has a trend towards the expected limit for a DMA phase at high temperature.

Although encouraging, our results are still incomplete. Indeed, we lack the explanation on the following points:

- we characterize the plasticity of the AHH at high temperature only through static observables, without analyzing the dynamics;
- the static picture lacks a quantification of the interplay between the evolution of the hydrogen bond network and the orientational disorder observed;
- the mechanism of of appearance of site disorder leading to the DMA phase at high temperature is not yet clear.

In the following Section, we address these remaining issues.

4.3 Dynamical characterization of the AHH plastic phase

In the previous Section 4.2 we discussed the static picture of the phase transition between the AHH-II ice to the high temperature phase, in particular at fixed pressure of 6GPa. Our results foresee a transition temperature T_c between 370K and 380K, above which we observe a *bcc* structure and high orientational disorder for both water and ammonia molecules. Moreover, the hydrogen bond network changes significantly above T_c. In this Section, we investigate the dynamical properties which are inherent to the plastic phase, using the trajectories at different temperatures and fixed pressure $P = 6$GPa. They provide a more precise picture on the transition process occurring at interface between the two phases and specify the plasticity of phase AHH-pbcc.

4.3.1 Hydrogen bonds lifetimes

In Section 4.2.3, we have highlighted the difference between the low and high temperature hydrogen bond networks. In particular, we suggest how the breaking of OH$\cdots$N hydrogen bonds of the AHH-II phase might be the driving mechanism for the phase transition to

Table 4.4: Hydrogen bonds lifetimes τ, as obtained by fitting via a simple decay exponential vs. T. The typical error bar is on the last digit in brackets.

$T[K]$	$\tau_{OH...O}$ [ps]	$\tau_{NH...N}$ [ps]	$\tau_{NH...O}$ [ps]	$\tau_{OH...N}$ [ps]
300	–	11.9(1)	18.3(4)	159.1(4)
350	–	7.4(0)	11.3(8)	65.7(8)
360	–	6.6(4)	7.5(1)	49.4(2)
370	–	5.9(9)	7.2(3)	43.9(3)
380	2.3(7)	3.7(9)	4.0(4)	11.5(5)
390	1.9(7)	2.9(0)	3.2(2)	7.2(1)
400	1.8(6)	2.0(8)	2.3(0)	3.8(2)
500	1.2(7)	0.8(3)	0.9(7)	0.9(3)
600	0.8(4)	0.5(8)	0.6(7)	0.7(0)

occur. In this Section, we study the kinetics of the hydrogen bonds network, with the goal of determine the lifetimes of each bond type as a function of temperature.

Figure 4.16 shows the time decay of the normalized number of hydrogen bonds at different temperatures. [3] The curves start form the values reported in Table 4.3, which are the normalized number of H-bonds. The decay is obtained with the following method: at each time step, we count the number of hydrogen bonds fulfilling the existence criterion given by Luzar and Chandler [187]. If a bond does not fulfill the criterion at time t', the bond is considered as broken and it will not figure in the count anymore at larger $t > t'$. As temperature increases, the decay of hydrogen bonds in which nitrogen is the donor becomes more pronounced, without a clear distinction between the low temperature and the high temperature regime. On the contrary, a clear transition is visible when oxygen is the donor in the bond. In panel B, for the OH$\cdots$N bonds, the high temperature curves show a much slower decay for temperatures below the transition, whereas at 380K the decay becomes faster. Moreover, the OH$\cdots$O bonds (panel D) are completely absent at low temperature. Their number suddenly increases at 380K and it decays exponentially as a function of time for all temperatures above T_c.

Table 4.4 reports the hydrogen bonds lifetimes obtained from the fit of the curves in Figure 4.16 via a simple decay exponential. Notice that the values at low temperature for the OH$\cdots$O are absent in AHH-II phase. Figure 4.17 is the plot of the bonds lifetimes as function of temperature. In general, all H-bond lifetimes decrease with temperature. However, a main distinction occur between the H-bonds either with water or ammonia donor. At low temperature, NH$\cdots$X bonds break more easily, leading to lifetimes of the order of 10ps; OH$\cdots$N, on the contrary, establish much stronger hydrogen bonds with lifetimes of order of hundreds of ps. This difference of lifetimes between water and ammonia donors is coherent with the relative strength of the H-bonds.As temperature rises above T_c, all bonds lifetimes reduce to the order the ps, which indicates that the AHH-pbcc phase is characterized by short living H-bonds, whose lifetimes do not depend anymore on the donor/acceptor type.

[3] These results are obtained from 200ps long NVT simulations, performed after full NPT equilibration at 6GPa (simulation times in Table 4.7). Volume is kept constant in order to avoid artificial modifications of the distances between the atoms via the barostat.

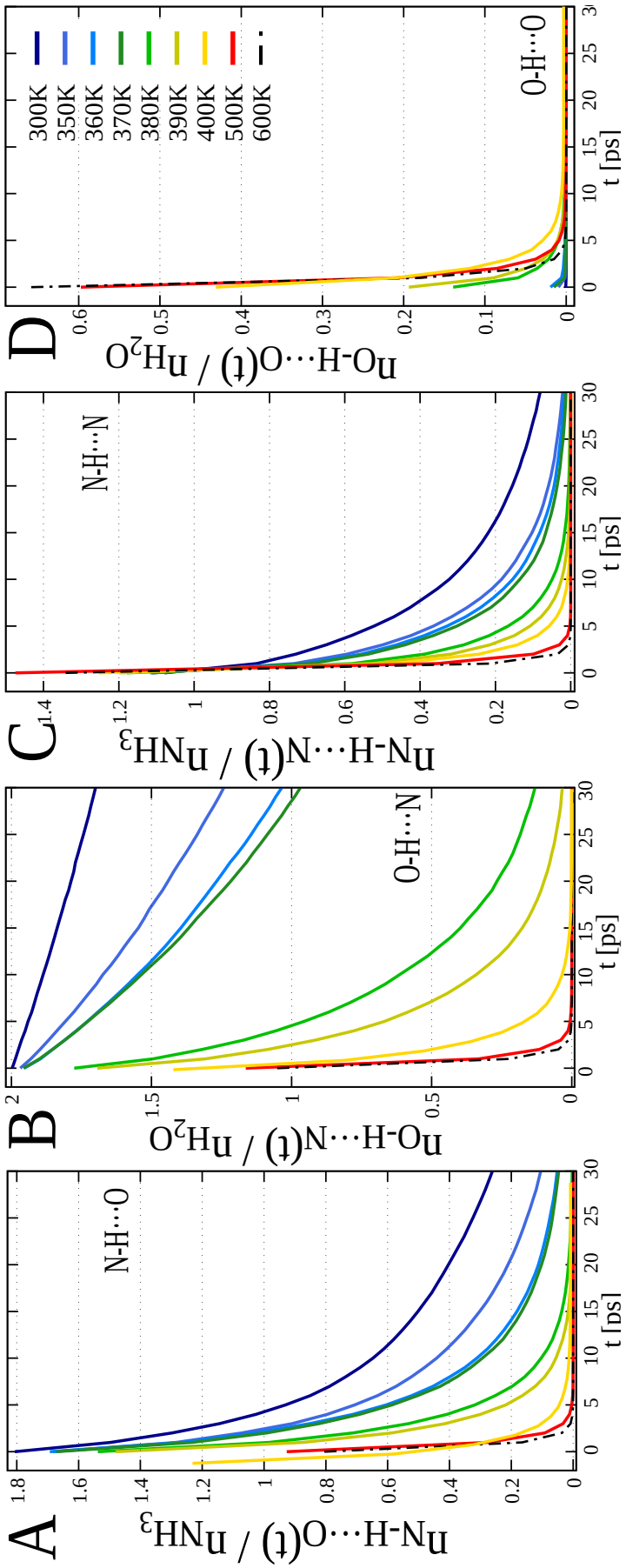

Figure 4.16: Hydrogen bond number $n_{XH...Y}(t)$ as function of time. Cutoff parameters: radius 3.5Å, angle 30°.

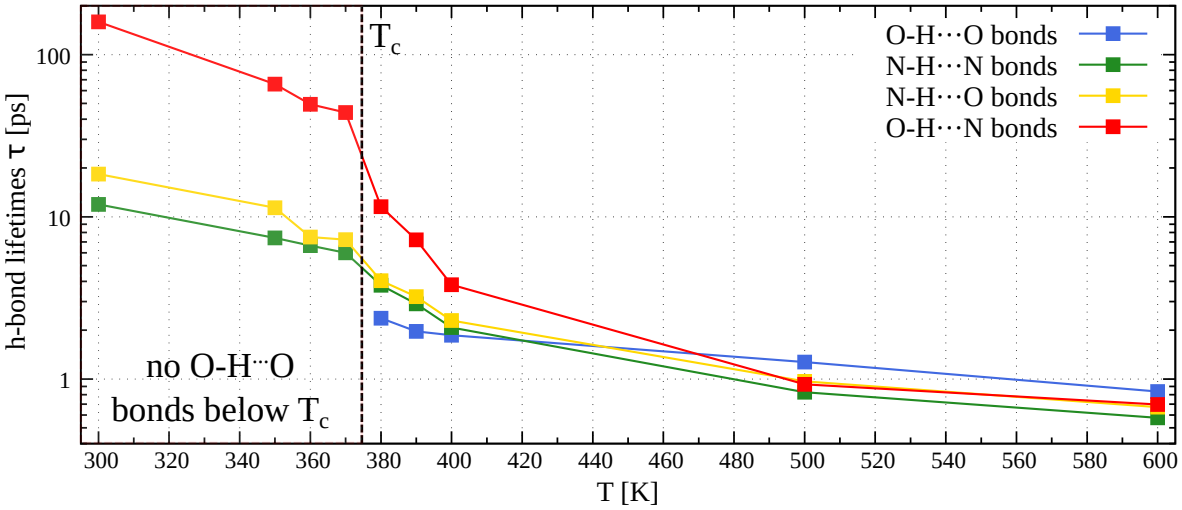

Figure 4.17: Hydrogen bond lifetimes τ [ps] from Table 4.4. The fit is a single decreasing exponential.

In the next Sections, we explore how the breaking dynamics of the hydrogen bonds observed translates in a general orientational disorder of the high temperature phase, creating the plastic behavior suggested by the experiments and the analogous phenomena observed for other ammonia hydrates (AMH [57]).

4.3.2 Molecule dipoles rotations

We analyze now the dynamics of the orientational disorder of ammonia and water molecules as a function of temperature, at $P = 6$GPa. Here, we firstly focus on the orientation of the molecular dipoles. The ADFs shown in Figure 4.12 indicate a qualitative picture of the disorder of the dipoles as function of temperature. We are now interested in studying the evolution of the dipole orientations as a function of time for each temperature. The orientational disorder of hydrogen atoms pictured in Figure 4.11 is addressed from a dynamical point of view in the next Section 4.3.3.

Starting with the orientation of molecules as a whole, we make use of the dipoles orientation time correlation function of Eq. (4.3), inspired by analogous studies on pure hot dense ammonia ices [38] to characterize the plasticity of solid phases

$$\langle u^2(t)\rangle = \frac{1}{N}\sum_{i=1}^{N} \vec{\mathbf{u}}_i(t)\cdot\vec{\mathbf{u}}_i(0) \tag{4.3}$$

where $\vec{u}_i(t)$ is the dipole unitary vector for the i water or ammonia molecule. This function $\langle u^2(t)\rangle = 1$ if the dipoles are perfectly correlated and decreases towards zero as rotational movement de-correlates the dipoles in time. [4]

[4] In order to keep the volume constant, 200ps long NVT simulations were performed, after full NPT equilibration (simulation times in Table 4.7). Specific tests found no significant dependence on the thermostat friction parameter.

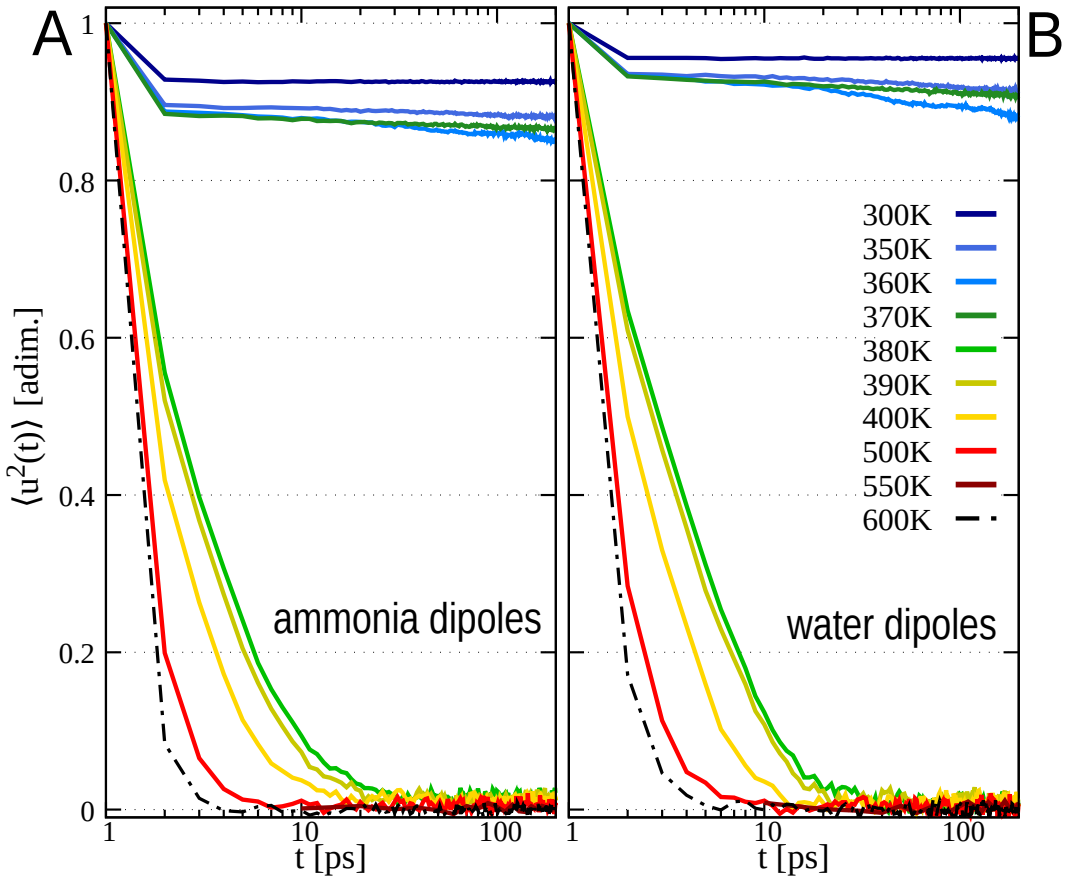

Figure 4.18: Dipoles time-correlations functions (Eq. (4.3)) for different, increasing temperatures, for ammonia molecules (panel A) and water molecules (panel B).

Table 4.5: Dipoles de-correlation times and saturation constants at different, increasing temperatures at $P = 6$GPa.

$T_{in}[K]$	τ^{H_2O} [ps]	τ^{NH_3} [ps]	$C(T)^{H_2O}$	$C(T)^{NH_3}$
300	1000.1	1348.4	0.955	0.926
350	69.9	58.2	0.913	0.881
360	77.5	74.2	0.873	0.844
370	50.9	46.6	0.908	0.866
380	4.7	3.9	0.009	0.017
390	4.2	3.4	0.011	0.015
400	2.5	2.3	0.009	0.013
500	1.1	0.9	0.003	0.005
550	0.4	1.4	0.001	0.001
600	0.8	0.5	0.000	0.000

Figure 4.18 reports the dipole time (de-)correlation functions, for both ammonia (panel A) and water (panel B) molecules. The liquid phase (black dashed line) sets a lower bound to the other curves, representing the limit of fastest possible de-correlation, obtained in few ps. The high temperature (500K, red curve) phase presents a correlation decay analogous to the liquid, with a transient period depending on temperature, for both molecules. The dipole de-correlation shows a clear transition of regimes between 370K and 380K. Indeed, at low temperature, after an initial transient due to the thermal motion, $\langle u^2(t)\rangle \simeq 0.9$ on timescales of hundreds of ps. In contrast, above 370K, $\langle u^2(t)\rangle$ decreases suddenly after few ps, with a slope which becomes steeper as temperature increases.

The de-correlation curves have been fitted by a simple exponential function of the form $Be^{-t/\tau}+C(T)$. Table 4.5 reports the de-correlation times $\tau(T)$ and the saturation constants $C(T)$. They are shown in Figure 4.19. Notice that the first point of all curves was not included in the fit. The reason lies in the separation between the full rotation of the molecule and the fast initial de-correlation due to thermal movement around the equilibrium position. The latter is clearly visible in Figure 4.18 for all curves at low temperature; temperatures above the transition do not clearly differentiate the two periods. As a result, it is clear from Figure 4.19 that the typical rotation times of molecules at low temperature are few order of magnitude longer than the rotation times at high temperature. A clear transition is visible between 370K and 380K, where the times decrease by a factor 40. The same abrupt transition is visible for the saturation constant $C(T)$, when becomes almost null at the transition. In conclusion, the low temperature phase might include molecular rotations on time scales of the ns or longer, whereas the high temperature phase shows full molecular reorientation on the ps timescale.

4.3.3 Hydrogen rotations and molecular diffusion

In the previous Section, we characterized the plastic nature of phase AHH-pbcc from the drastic change in the rotational correlation between molecular dipoles at the transition

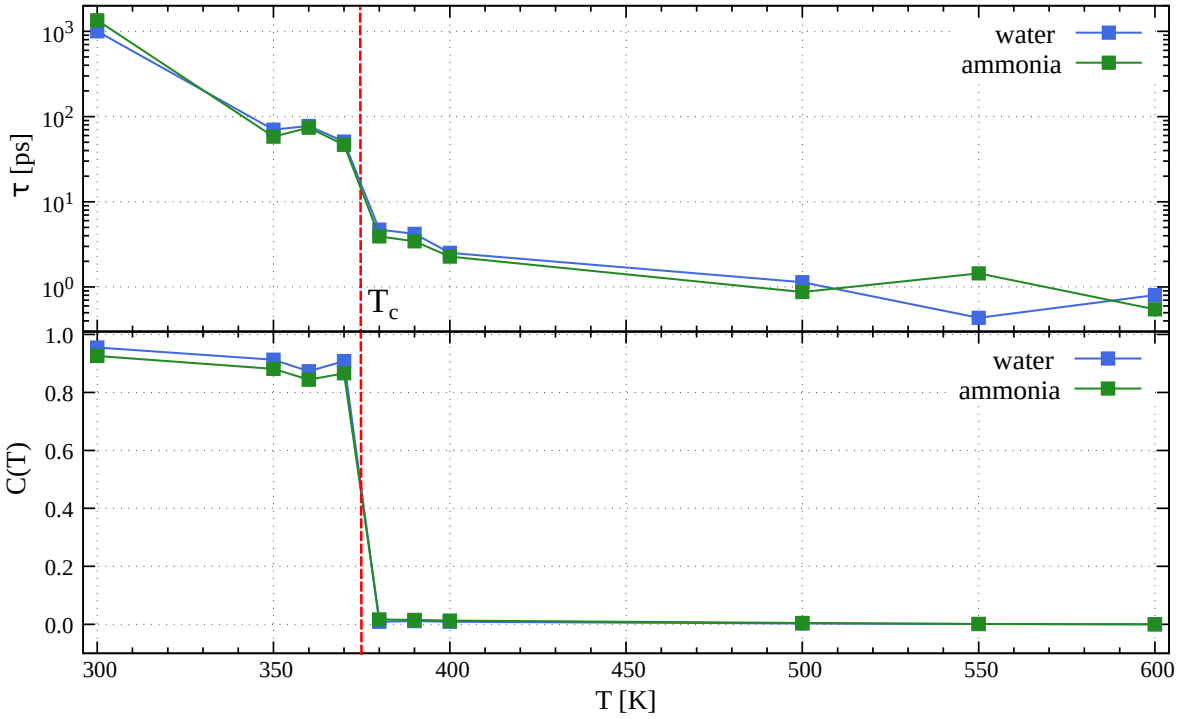

Figure 4.19: Characteristic (de)correlation times τ (panel A) and saturation constants $C(T)$ (panel B) from the fit of the dipole orientation correlation function (Eq. (4.3) as function of temperature.

temperature, i.e. between 370K and 380K. We focus now on the rotation of the hydrogen atoms around the molecules from a dynamical point of view.

Figure 4.20 shows the mean squared displacement (MSD) of hydrogen atoms in ammonia (panel A) or water (panel B) molecules, as a function of time, for temperatures between 300K and 400K. Starting with panel A, after a sharp increase in the first ps (or 10ps) of simulation, all curves between 300K and 370K saturate at ~ 2Å^2. This movement corresponds approximately to the distance the hydrogen atom attached to the molecule of ammonia would cover during the rotation from one preferred orientation to the other (which are depicted in Figure 4.11). Notice that the plateau is reached after a characteristic time which depends on T (at most 200ps for the 300K curve). This result reflect the fact that hydrogen bonds with nitrogen donor mostly break after times of the orders of tens of ps, also in the low-T phase (see Figure 4.16). The curve at 380K also saturates, but at values slightly above 2Å^2. Finally, the 390K curve, after an initial saturation at the same level of 380K, exhibits a change of regime, becoming linear with time. The same linearity with time is clearer for the 400K curve. At these temperatures above the critical one T_c, full molecular diffusion occurs.

On the other hand, hydrogen atoms belonging to water molecules show a more heterogeneous behavior. For all temperatures below the transition, i.e between 300K and 370K, the saturation is not sudden (of the order of a few tents of ps), but it requires much longer times. At 300K, water molecules are almost fixed in their rotational motion, coherently with what observed in Section 4.2.2. At higher temperature, few rotations occurs but the typical times to reach some saturation values -around 1.5Å - are of the order of the ns.

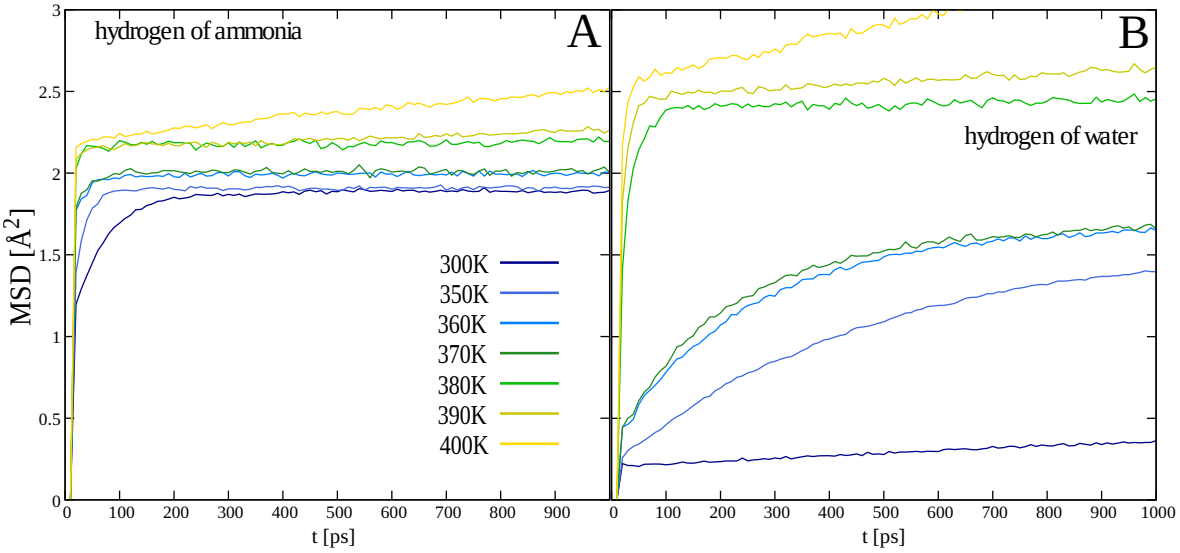

Figure 4.20: Mean squared displacement (MSD) of hydrogen atoms belonging to ammonia molecules (panel A) or water molecule (panel B) as function of time.

Again, for temperatures above 380K, a linear regime starts to appear. In conclusion, hydrogen rotations for ammonia molecules are present at all temperatures, whereas hydrogen atoms belonging to water molecules rotate, with slower characteristic times. They both show however a significant change of behavior at the transition.

Having analyzed both types of molecular rotations are analyzed, we can draw some conclusions. A limited degree of orientational disorder of hydrogen atoms is observed in both phases (see Figure 4.20), mostly due to rotations around the dipole axis; however, hydrogen atoms attached to water molecules rotates on time scales much larger than hydrogen atoms of ammonia molecules. This is coherent with the existence of strong OH$\cdots$N bonds. Furthermore, both molecular dipoles are sensitive to the phase transition occurring between 370K and 380K (see Figure 4.18). Full molecular rotations occurs on scales of few ps at high temperature, completely analogous with the liquid phase. This phenomenon is not observed at low temperature. Therefore, we can confirm the plastic character of the high temperature phase.

Finally, we complete the picture with the diffusion at all temperatures, between 300K and 600K. Figure 4.21 reports the mean squared displacement of ammonia and water molecules as function of temperature. [5]

From Figure 4.21, we observe no diffusion process below 380K, within the simulation times. On the contrary, at temperatures above 380K, molecular diffusion is observed, with T-dependent diffusion coefficient. [6] Table 4.6 reports the diffusion coefficient values of water

[5]The results are obtained from 1ns NPT trajectories performed starting from the final configuration obtained from the main trajectory. As explained in Section 2.3, larger values of the friction parameter might have an over-damping effect on the diffusion. Therefore, we checked the convergence for decreasing values of γ. The final value chosen for the friction is $\gamma = 0.1$THz, and the mass of the piston was increased by a factor 10, in order to ensure the pressure stability. Atomic positions are saved every 10ps.

[6]Notice that, for the temperatures between 380K and 400K, the diffusion is studied on the trajectories

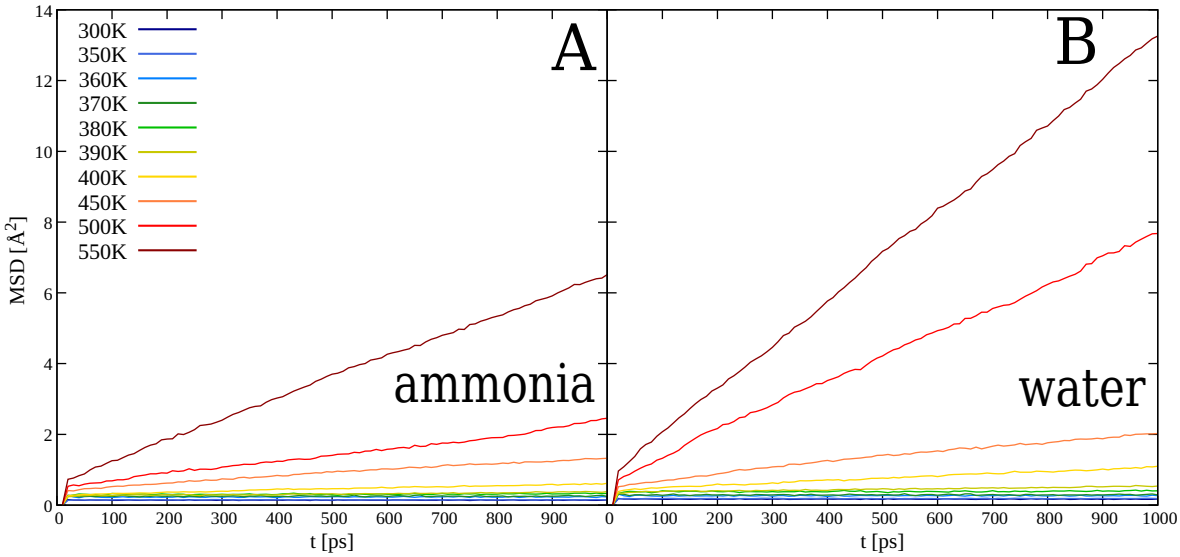

Figure 4.21: Mean squared displacement (MSD) of nitrogen atoms (panel A) and oxygen atoms (panel B) as function of time.

Table 4.6: Molecular diffusion coefficients at increasing temperatures.

$T_{in}[K]$	D_{H_2O} $[10^{-5}cm^2/s]$	D_{NH_3} $[10^{-5}cm^2/s]$
380	0.0002(8)	0.0001(8)
390	0.0003(6)	0.0002(2)
400	0.0007(1)	0.0004(5)
450	0.00240(7)	0.00148(8)
500	0.01148(2)	0.00300(9)
550	0.02081(1)	0.00974(1)
600	2.85087	2.35581

and ammonia molecules at different temperatures. They are obtained from a linear fit of the MSD curves shown in Figure 4.21. Quantitatively, we observe that the diffusion coefficient of water is higher than the diffusion coefficient of ammonia across all temperatures between 380K and 550K.

Above the transition temperature, the diffusion coefficients follow an Arrhenius regime, until the transition to the liquid phase between 550K and 600K, where a steep increase of almost three orders of magnitude is observed. The points between 390K and 550K are fitted with the Arrhenius law (3.13). To conclude, the high temperature plastic phase present a consistent molecular diffusion of both water and ammonia molecules. The diffusion coefficient for $T \leq$550K is at least two orders of magnitude lower than the liquid AHH at 600K and 6GPa.

At the moment, there are no experimental data on the diffusion in AHH, for both liquid and plastic solid phases. However, Zhang et al. [57] measured the diffusion coefficient of liquid AMH. We performed some simulations of liquid AHH in analogous T-P conditions,

obtained by a cooling from the 550K final configuration (see Appendix A for more details).

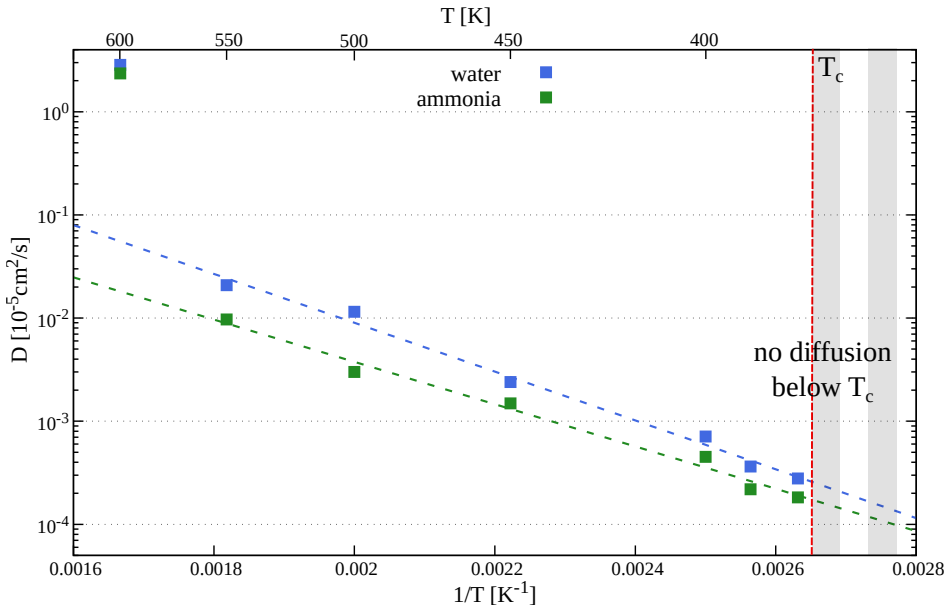

Figure 4.22: Arrhenius plot and fit (3.13) of classical diffusion coefficients from Table 4.6.

finding the same order of magnitude of the experimental values (see Table 4.10 in Appendix F).

4.3.4 Formation of the disordered molecular alloy

We have now gathered all the elements in order to describe the microscopic dynamics underlying the plastic phase transition in AHH. As an example, we consider the trajectory at 400K and 6GPa. Indeed, at this temperature, the diffusion process described in Section 4.3.3 is slow enough to be able to isolate single diffusing events within the global system, and observe the microscopic dynamics of single atoms. [7]

Figure 4.23 shows a portion of the system in the y-z plane. The hydrogen atoms have been hidden for clarity, since for the moment we are only interested in highlighting the motion of the heavy atoms O and N, and a few representation events towards the creation of DMA phase. The panel on the top right of Figure 4.23 shows the first event of molecular diffusion observed: an ammonia molecule transits from one column of its peers to a column of water. This first event triggers other neighboring diffusion events around it, which are visible in the lower panels of the Figure 4.23. First, the hole left by the ammonia molecule is replaced by another molecule coming from a neighboring line; then, an water molecule fills the hole left by the ammonia.

In order to understand how the first diffusion event occurs, the same sequence is depicted in the x-z plane in Figure 4.24. Once again, hydrogen atoms have been hidden, all but the ones directly involved in the process. The initial configuration, visible in the panel A of Figure 4.24, shows the column of water molecules along $\hat{x}$, surrounded by the columns of ammonia molecules. Water molecules are regularly spaced, and no hydrogen bonds

[7] The time-step between the saving of each configuration is 0.1ps.

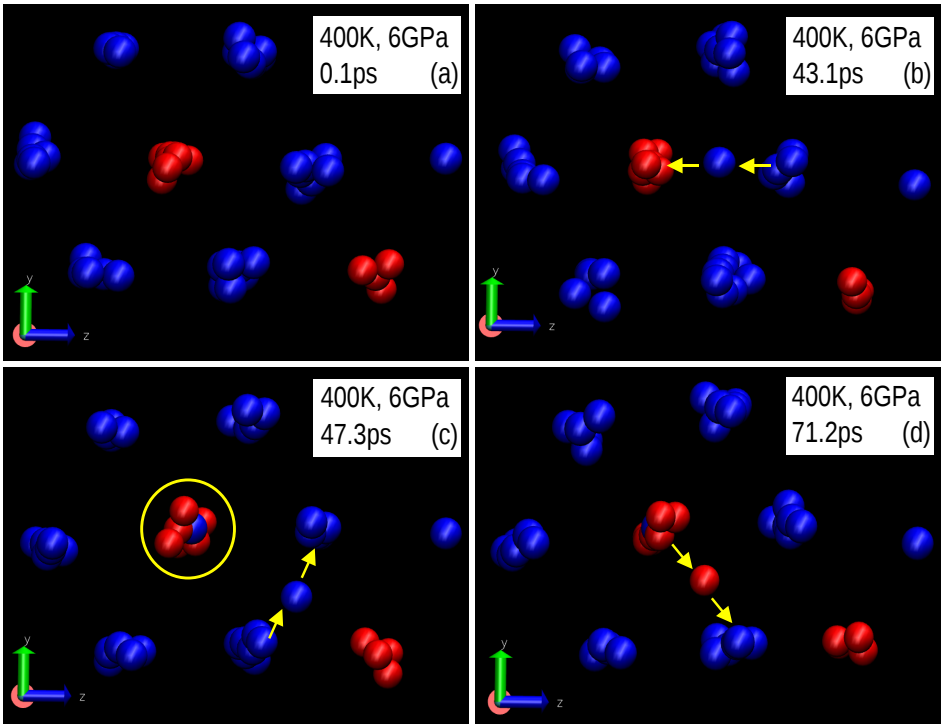

Figure 4.23: Portion of AHH system at 400K, 6GPa in the x-y plane. Oxygen (in red) and nitrogen (in blue) are all visible, whereas hydrogen atoms have been hidden for clarity.

are formed between them. This situation changes after few ps (panel B of Figure 4.24), when water molecules have formed OH$\cdots$O bonds between them, shortening their distance. Even though these bonds are broken after few tens of ps, during their lifetimes they deform the cystal and create a void space (highlighted in the panel C of Figure 4.24), which remains stable on a few ps timescale. We do not exclude that temporary hydrogen bonds formed with neighboring ammonia molecules may play an additional role in the stability of the 'defect' created in the water column. Panel C also shows the subsequent occupation of the 'defect' in the water column by a neighboring ammonia molecule, for which we included the hydrogen atoms in order to highlight it. Finally, in panel D, the same molecule has occupied the 'defect' and it is now part of the water column, leaving a vacancy behind it. As already stated, this event is the first of several different diffusion events, which eventually leads to the disorder molecular alloy of phase AHH-pbcc.

Hitherto, the diffusion process has been described in terms of migrations of molecules and vacancy creation, regardless of the crystal structure. We draw now the attention to the last Figure 4.25, which illustrates how the diffusion process occurs on the *bcc* sites and modifies the original structure of AHH-II into the average *bcc* structure of the plastic phase. The configuration in Figure 4.25 is visualized in a intermediary orientation. The yellow squares highlight the space where the *bcc* cell appears at the end of the simulation. Again, hydrogen atoms have been hidden for clarity, except those whose molecules are directly involved in the process we want to clarify.

At the beginning of the simulation (panel (a)) the chemical order in AHH-II is still visible: water molecules occupies two corners and the central position of the pseudo-*bcc* cell

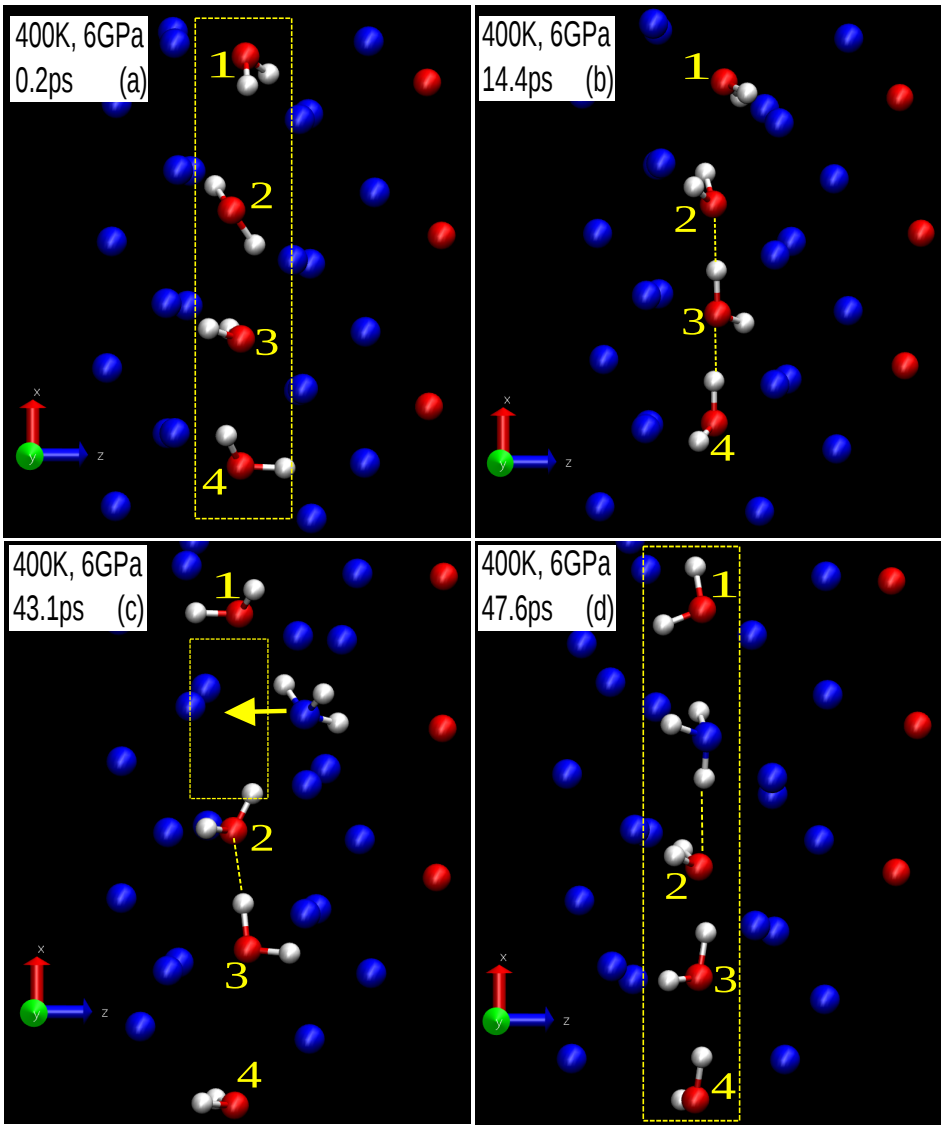

Figure 4.24: Portion of AHH system at 400K, 6GPa in the plane x-z. Oxygen (in red) and nitrogen (in blue) are all visible, whereas hydrogen atoms (in white) have been hidden for clarity.

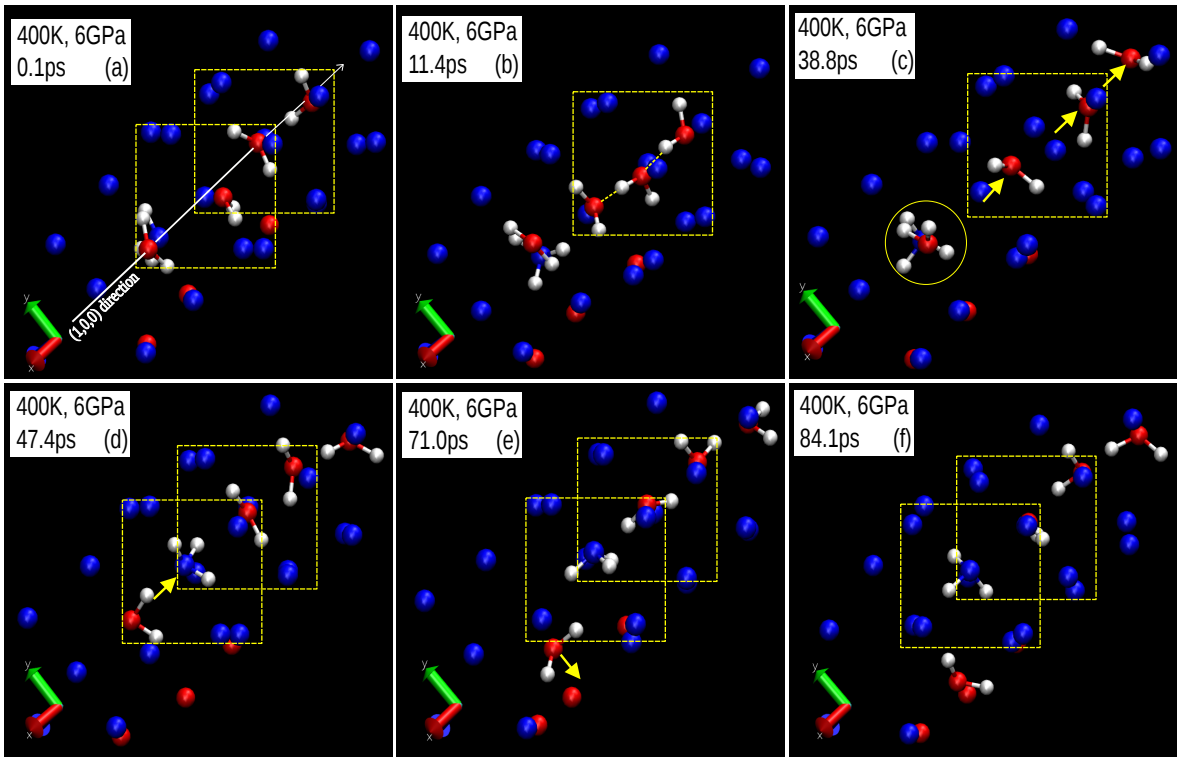

Figure 4.25: Portion of AHH system at 400K, 6GPa in a intermediary orientation. Oxygen (in red) and nitrogen (in blue) are all visible, whereas hydrogen atoms (in white) have been hidden for clarity.

along the $(1, 0, 0)$ direction (highlighted in white), but the absence of OH$\cdots$O and the preferred orientation of strong OH$\cdots$N bonds globally deform the cells towards the monoclinic structure of AHH-II. As the process just described starts (creation of OH$\cdots$O bonds, creation of void defects in the sequence along $\hat{x}$ of water molecules and the insertion of an ammonia molecule) the local structure is modified in few tens of ps (panel B). At this point, panel (c) of Figure 4.25 shows how the diffusion process takes place through displacements between the *bcc* sites: water molecules are caught in their migration from a *bcc* site to an other along the $(1, 0, 0)$ direction. After few ps, in panel (d), the ammonia molecule leaves its site to occupy the vacancy left previously by the neighboring water molecule. Then panel (e) shows also another water molecule migrating towards another vacancy, and its place is later occupied by an ammonia molecule. The final result, visible in panel (f) of Figure 4.25, is a local configuration in which the substitutional disorder took over the original structure. The chemical order is lost, and on the sites of the *bcc* cells there is a disordered distribution of ammonia and water molecules: the DMA phases is formed.

Before drawing the final conclusions on the crystal-plastic phase transition occurring in AHH under pressure, we study the same system with the inclusion of nuclear quantum effects (NQEs) in the dynamics. The next Section collects and exposes some results with NQEs and it compares them to the current findings, establishing if important changes occur and need to be further investigated.

4.4 Addition of Nuclear Quantum Effects

Ammonia hydrates are hydrogen-rich system, whose properties are mainly determined by the hydrogen bond interactions. We are therefore interested in adding the nuclear quantum effects (NQEs) to our system, in order to determine whether the quantum delocalization of hydrogen might change the features of the solid phases of AHH. Indeed, in general NQEs have the effect of strengthening the strong hydrogen bonds and weaken the weaker ones [17]. Although at different T-P regimes, we know for instance from previous studies at higher temperature and pressures [39] that a proton transfer mechanism and superionicity are possible in ammonia hydrides.

We mainly use the Adaptive Quantum Thermal Bath (adQTB) [117], in reason of its low computational cost and its successful results on previous studies on liquid water [118]. However, due to the fact that not all dynamical properties are well described by the adQTB method (see Chapter 3 on diffusion), we use also the thermostatted Ring-Polymer Molecular Dynamic ((T)RPMD) [112] method as a benchmark for our quantum results. From the starting configuration of AHH-II at 300K and 6GPa, the system has been progressively heated at fixed pressure, until 600K, where the liquid phase was observed in the classical phase diagram.

Figure 4.26 shows the values of the average volume as function of temperature and fixed pressure of 6GPa, obtained via the different methods. In panel A, we show the curve obtained using the classical Langevin method for the dynamics, and both classical and quantum versions of the flexible SPC force field by Paesani et al. [96]. Notice that the classical SPC/fw potential is fitted to optimize water properties taking into account NQEs, whereas

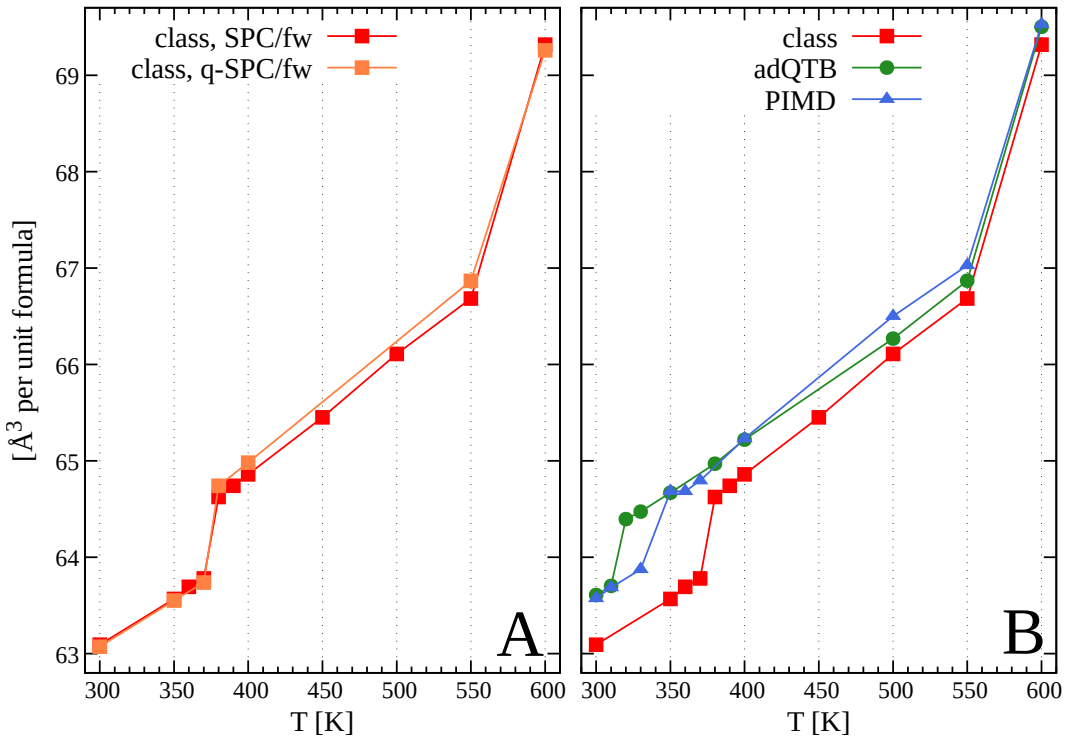

Figure 4.26: Average volume values obtained via different methods as function of temperature and fixed pressure of 6GPa. Error bars are within the point dimensions.

the q-SPC/fw potential is fitted on experimental and theoretical results without the NQEs corrections. In this way, we ensure the fact that NQEs are not counted twice in the simulations, one implicitly in the potential energy surface, and the other by using dynamical methods such as adQTB or (T)RPMD. As no important differences were observed, we can safely assume that any discrepancy observed between the classical and quantum MD simulations wound not be due to the use of the q-SPC/fw force field rather than SPC/fw.

Panel B of Figure 4.26 shows the difference in the volume evolution with temperature between the different methods, at fixed pressure of 6GPa. As already stated, the classical transition between the AHH-II phase and the AHH-pbcc phase is observed between 370K and 380K. The data collected from the simulations performed using the adQTB method reveal the same transition between 320K and 330K, with a expansion of $\Delta V/V = 1.1\%$. The coefficient thermal expansion below and above the transition are $\alpha_{<T_c} = 1.510^{-4}\text{K}^{-1}$ and $\alpha_{>T_c} = 2.210^{-4}\text{K}^{-1}$ respectively. The transition towards the liquid phase instead is unaltered with respect with the classical simulations. Finally, the simulations with the (T)RPMD method shows a global agreement with the adQTB results, with the exception of the transition temperature, which is observed between 330K and 350K. However, longer simulation times might be required to confirm this result.

To conclude, the adQTB lowers the transition between AHH-II and AHH-pbcc by about 60K at 6GPa. Other pressures might present a different value, but they have not yet been tested. Moreover, the average volume and direct observations of the simulation system reveals a crystalline structure of AHH-II at 300K different from what was previously observed at the same temperature with classical simulation. In the next Section, we propose

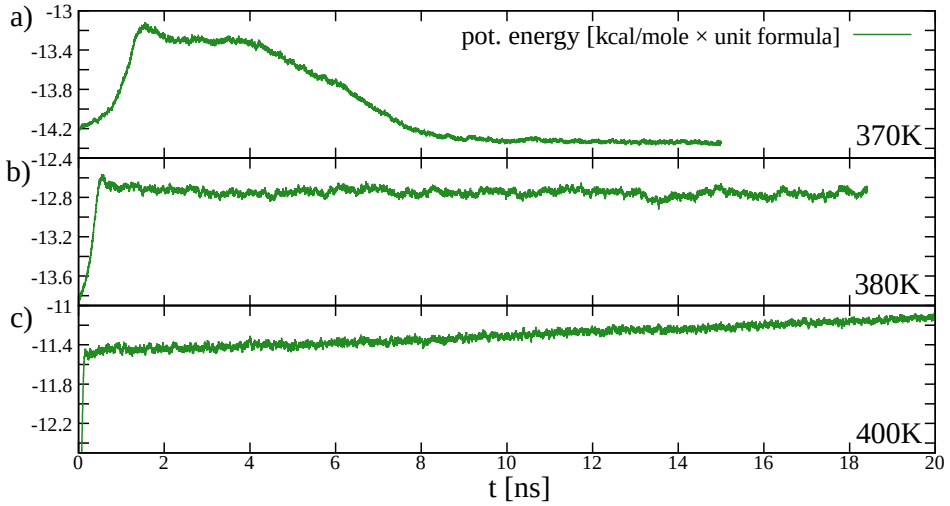

Figure 4.27: Evolution of potential energy values for the classical 370K, 380K and 400K trajectories at 6GPa.

an explanation of this apparent change of structure of AHH-II when zero-point energy contribution is included. For the solid-liquid transition, no important differences are observed when NQEs are added via adQTB. (T)RPMD results globally confirm these findings. Appendix B reports further comparison of the two methods (adQTB and (T)RPMD) using RDFs.

4.4.1 Intermediate ordered structure of AHH-II

In the previous Section, we showed how NQEs added via adQTB lowers the transition temperature between AHH-II and AHH-pbcc. Moreover, the AHH-II structure found at 300K and 6GPa is slightly different from what we observed in the classical simulations. The main feature of this intermediate ordered structure is the presence of different orientations of the water molecules compared to the AHH-II structure of Wilson et al. [54] (see Appendix B for a direct comparison of ADFs). However, this very same intermediate structure is not completely odd, as it was found also in the classical simulations between 360K and 370K. In the following Section, we describe the process of formation of this structure, its main characteristics, and how it helped in the exact determination of the transition line between the AHH-II and AHH-pbcc, shown in Figure 4.4.

Figure 4.27 shows the evolution of the potential energy for the 370K, 380K and 400K trajectories at fixed pressure of 6GPa. The thermostat is the classical Langevin. Starting from the top panel (370K), the potential energy increases significantly in few ps, and then decreases slowly towards a lower stable state. This peculiar behavior is the trace of the structure reorganization that we explain as follow. The nature of this reorganization is explained as follow. In Figure 4.28, the evolution of potential energy at 370K is compared with the evolution of the angular distribution of water dipoles. At the very beginning of the trajectory, the structure is mainly comparable to the AHH-II (see Figure 4.12, 300K panel), but after few tens of ps, the molecules break their hydrogen bonds and start to rotate, finding

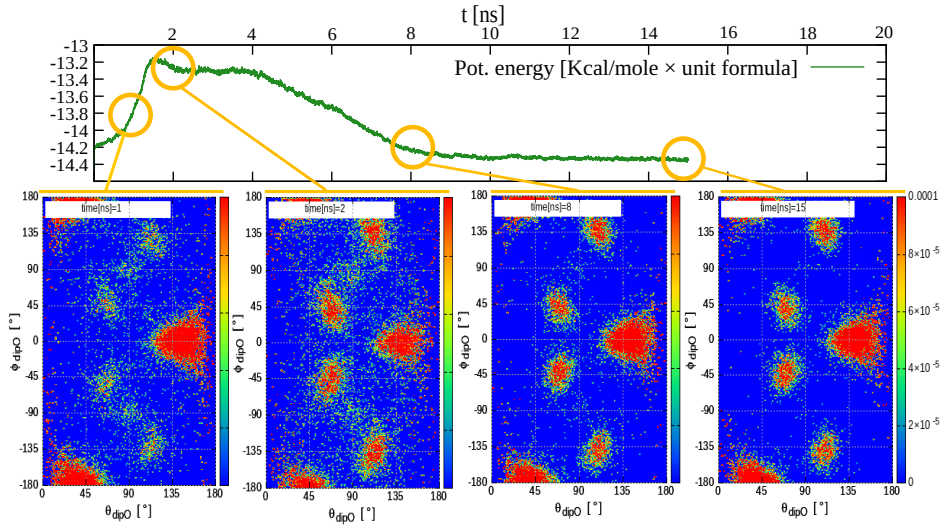

Figure 4.28: Evolution of water dipole angular distribution $P(\theta, \phi)$ along the trajectory at 370K and 6GPa, coupled with the evolution of the potential energy. Themostat is classical Langevin.

new favorable positions. After few ps of relative disorder, the water molecules slowly reorder towards both the original positions, or to four new angular positions, reestablishing the same number of hydrogen bonds present before the disorder (see Table 4.3).

A completely different phenomenon occurs at 380K (central panel of Figure 4.27): once initially the orientational disorder is formed, it does not decrease, and it is completely analogous a what is observed at higher temperature. The 390K trajectory (which is not depicted for simplicity) has the same behavior. Indeed, at these temperatures, the molecules cannot reform stable hydrogen bonds with long lifetimes and they are constantly turning. This phenomenon, already highlighted, is the global orientational disorder which characterizes the high temperature phase. Finally, at 400K, the evolution of the potential energy not only shows a rapid increase at the beginning of the simulation, but it undergoes a slow but steady increase for the whole duration of the simulation. This is the trace of the slow - compared to molecular reorientation - diffusion process, occurring on the scale of tents of ns at this temperature. Direct observations of the 390K trajectory shows also some local events of diffusion, but the global observables are not yet affected within the simulation time. The 380K trajectory does not present clear diffusion events within the simulation time.

This sharp change in behavior of the total energy, as well as other macroscopic observables as function of time, such as density or stresses, clearly divide the AHH-II phase from the AHH-pbcc phase. The same results are observed along the full transition line depicted in Figure 4.4.

In order to determine if the new structure observed at 370K is a possible intermediate phase of AHH between the AHH-II and AHH-pbcc phase, we computed its structure factor, which is compared to the experimental results in Figure 4.29 panel A. The new structure at 370K (green curve) seems to be hardly distinguishable from the AHH-II results at 300K (blue curve), except by the respective positions of the peaks which is due to the difference of lattice parameters. Thus, we conclude that, even though a local reorganization of the

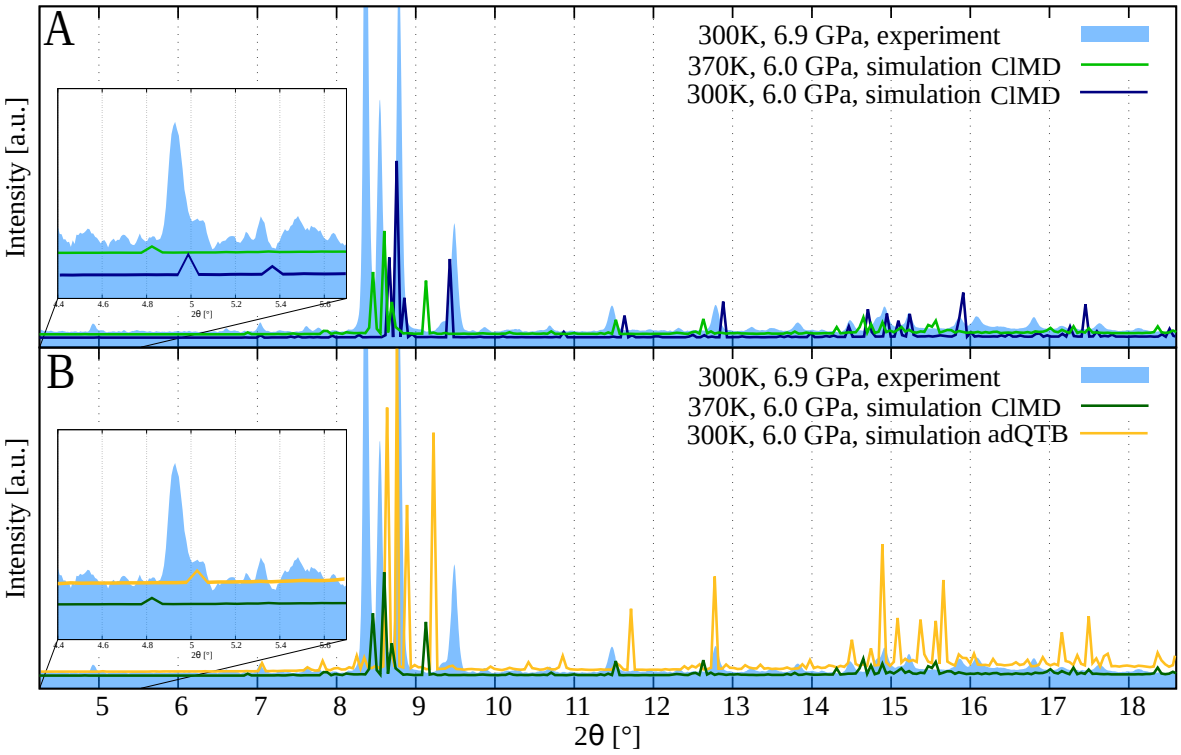

Figure 4.29: *Panel A*: classical structure factors compared with experimental X-ray diffraction results [44, 73], at 300K (blue) and 370K (green). *Panel B*: in yellow, the average structure factor obtained at 300K and 6GPa from adQTB trajectory, compared to the 370K classical result (dark-green) and the experimental result.

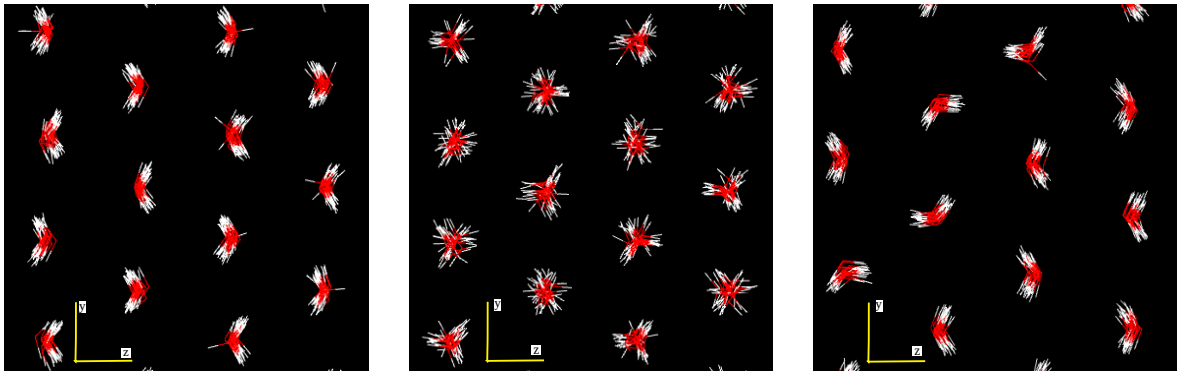

(a) Snapshot of the structure of AHH at 300K (only water molecules) after 10ps dynamics.

(b) Snapshot of the structure of AHH at 380K (only water molecules) after 10ps dynamics.

(c) Snapshot of the structure of AHH at 370K (only water molecules) after 15ps dynamics.

Figure 4.30: Water molecules orientations in AHH system in the y-z plane. The ammonia molecules are hidden in the picture for clarity.

structure had been observed, this does not correspond to a new phase, but rather to an equivalent crystal structure of AHH-II. Indeed, not only the pseudo-*bcc* structure is still in place (see Figure 4.30c), but also the strongest OH$\cdots$N bonds are re-established. In panel B of the same Figure, we show also the structure factor obtained via adQTB at 300K (yellow curve), compared to the classical 370K curve (dark-green). Also in this case, we can recognize the same main features in both cases, namely the triplets of peaks between 8.5° and 9°, the peak at 9.2°, the low angle peak, and many of the features at high angles.Therefore, we confirm once again the similarity between the classical 370K configuration of AHH-II and the adQTB 300K one.

As a conclusion, in Figure 4.30 we show three different configurations of solid AHH at 6GPa, at 300K (panel A), 380K (panel B) and 370K (panel C). Only water molecules are visible, as the ammonia molecules have been hidden for clarity. As explained in Section 4.1.1, in the direction $(1, 0, 0)$, the water molecules form lines without any alternance with ammonia molecules. This is true for all three configurations represented here, as no diffusion is occurred. Panel A shows the typical orientations of water molecules in AHH-II from Wilson et. al [54], coherent with the initial structure depicted in Figure 4.1a. At 380K (panel B) the structure clearly shows the orientational disorder of molecules, which is the driving mechanism of the formation of AHH-pbcc. In panel C, however, we show the structure of water molecules at 370K, after the reorganization process explained in this Section. New preferred orientations are formed, but all of them are fixed, with stable hydrogen bonds in place.

As final remark, we state that the low temperature phase (300K-310K) observed via the adQTB method is similar to that obtained in classical simulations at 360K and 370K. Therefore, as we argued above, it still corresponds to the AHH-II phase, while the phase transition only occurs at 320K. The molecule reorganization is enhanced by the addition of the zero-point energy and therefore occurs at lower temperatures compared to the classical simulation.

4.5 General conclusions

In this Chapter, we have exposed the results obtained via classical molecular dynamics simulations of AHH crystal at different temperatures and pressures, focusing in particular on the evolution at fixed $P = 6$GPa. The starting configuration lies in the AHH-II phase [54] at 300K. The system has been heated and cooled in order to explore a portion of the phase diagram, and then compare our results to the experimental work of Andriambariarijaona et al. [44, 73]. We analyzed the transition between the monoclinic crystal AHH-II to plastic *bcc* phase at higher temperature. In particular, once the structural change is established in Section 4.2.2, then we discussed the hydrogen bond structure (Section 4.2.3) and dynamics (Section 4.3.1) as temperature rises; we established the link with the orientational disorder of molecules (Section 4.3.2); and finally we added the molecular diffusion which trasform the AHH-II solid in a DMA phase (Section 4.3.3).

Furthermore, in Section 4.4, we added the NQEs to our simulations via the adQTB and (T)RPMD methods, and checked the similarities and differences with the classical simulations.

The following conclusions are drawn in this Chapter:

- the phase transition between the AHH-II crystal and the AHH-pbcc phase is due to the breaking of strong hydrogen bonds and the establishing of a lasting rotational disorder of molecules. The AHH-II phase is characterized by a precise chemical order, and the stability of the structure is due to the competition of strong and weak hydrogen bonds. On the other hand, the plasticity of the high-T phase is characterize by absence of orientational correlations between molecules on timescales larger than few ps, the short-living hydrogen bonds which cannot be differentiated by donor/acceptor type;

- the *bcc* structure established at high-T is the direct consequence of the smoothing of the differences between ammonia and water geometries and hydrogen bond strengths. Indeed, as molecular rotations are well established above T_c, the monoclinic structure is transformed in a higher symmetrical cubic structure;

- above T_c, the formation and breaking of (short living) hydrogen bonds deforms locally the molecular configurations, allowing molecules to escape their original position and diffuse. However, the diffusion process is not free, but it involves motions from one *bcc* site to another, preventing the solid from melting. This process, called Orientational-Disorder-Driven Site Disorder (ODDSD), allows the formation of the disordered molecular alloy (DMA) in the phase AHH-pbcc. Moreover, it reintroduces[8] the diffusion in the conception of plastic as purely rotational disordered state, by adding a diffusion process in the solid phase. The coexistence of the two elements is due to the directionality of hydrogen bonds (rather than the isotropic Van der Waals interactions), which allows to locally deform the molecular environment,

[8] As explained in the Introduction, self-diffusion coefficients were measured for various plastic crystals via radiotracer techniques [58].

but at the same time maintain the compressive order of the structure. The novelty is the formation of the alloy of AHH, due to the presence of two molecular species.

- finally, the addition of NQEs does not change the overall picture obtained via classical molecular dynamics simulations. The descriptions of the phases is the same, as well as the melting of the AHH-pbcc crystal. The only difference is a change of the crystal-plastic transition temperatures T_c at lower temperatures, which might be explained by the fact that NQEs increase the probability of breaking the hydrogen bonds and enhance molecular rotations. Proton transfer mechanism might be needed to establish the correct transition temperature.

Table 4.7: Simulation times for heated and cooled trajectories at given temperatures and fixed pressure of 6GPa. The starting configuration for the heating process is the last configuration at the temperature below, the contrary for the cooling process.

T_{in}[K]	t_{sim}[ns] heating from 300K	t_{sim}[ns] cooled from 550K
300	10	5
350	15	5
360	37	–
370	15	–
380	18.5	5
390	33	5
400	30	10
450	10	–
500	10	10
550	19.2	—
600	10	–

Appendix I

A Metastability and simulation times

All results presented in Chapter 4 are obtained once the system is at thermodynamical equilibrium. However, the convergence of the result is not uniform, rather the simulation times and the initial configurations of each trajectory depend on the temperature at which we want to simulate the system. In this Section, we explain how we obtained the equilibrium results for each trajectory at fixed pressure of 6GPa, and we discuss the different simulation times required.

Figure 4.4 in Section 4.2.1 shows the simulation points in the P-T phase diagram. Initially, the starting configuration of AHH-II at 300K and 6GPa was heated up to 600K, performing a trajectory every 50K and the simulation time was set to 10ns. The solid-liquid transition was located between 550K and 600K. The melting process at 600K happens on the scale of a few ns, and all macroscopic observables converged to a stable value. The same was observed for 550K: after a thermalization period of about 100ps, the AHH-pbcc phase is stable for final simulation times of 20ns.

However, for temperatures around to the transitions, between 350K to 450K, trajectories showed some changes in the overall structure, as well as the appearance of orientational disorder and molecular diffusion, but the transition process from AHH-II to AHH-pbcc appeared to be still far from convergence. At this point, the transition between the solids was located between 350K and 400K, but longer trajectories and more simulations were needed. From the final configuration at 350K, we heated the solid through steps of 10K up to 400K, in order to locate more precisely the transition. Moreover, we extended the simulation time for the other temperatures. Final simulation times for each trajectory are shown in Table 4.7. Also, from the final configuration at 6GPa and 550K, we started the

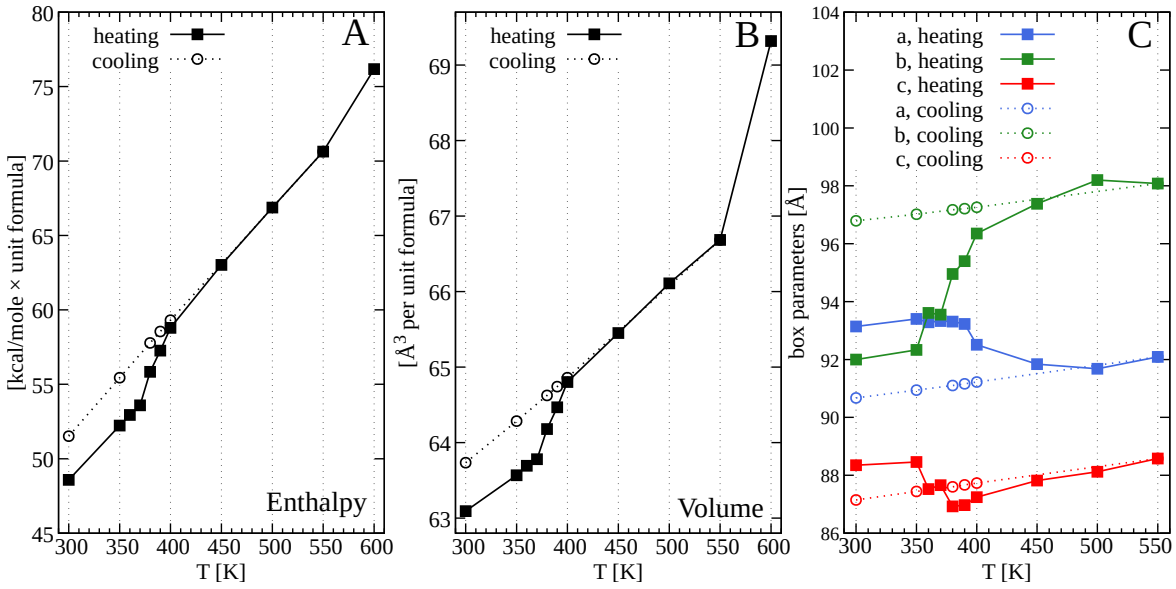

Figure 4.31: Average values of enthalpy (panel A), volume (panel B) and three box parameters (panel C) as function of temperature, at constant pressure of 6GPa. The 300K configuration is the starting point of for each simulation labeled 'heating'; the 550K configuration for for each simulation labeled 'cooling'. Error bars are within the point dimensions.

cooling process to 300K, in order to determine the reversibility of the transition. Table 4.7 reports the simulation times for the cooled trajectories as well.

Figure 4.31 shows the average values of enthalpy (panel A), volume (panel B) and box parameters (panel C), for both heating and cooling processes at 6GPa. From this data, the transition between AHH-II and AHH-pbcc is already visible, as well as the melting point, although the transition temperature is still unclear. Moreover, the parameters' evolution appears to be smooth with temperature, rather then experience a sudden discontinuity. We can also clearly see the absence of reversibility of the transition on the ns scale: once the disordered molecular alloy (DMA) phase is established at high temperature, it is preserved upon cooling. Particularly interesting is the behavior of the box parameters (panel C): in the cooling process the three parameters a, b and c have the same dependence on temperature, which suggest the preservation of an almost *bcc* structure in the bulk at lower temperatures.

This static picture cannot give more information on the transition temperature T_c and the equilibrium values. However, some insights can be gained from the evolution of the average enthalpy and volume with time. As explained in Section 4.4.1, the trajectories at the temperatures close to the transition, i.e. between 360K and 390K, show an interesting behavior as a functions of time. If we plot the average values of the enthalpy and volume for different times, as depicted in Figure 4.32, we clearly observe some trends in the convergence.

Starting with enthalpy (panel A), the values for temperatures below or equal to 370K tends to increase with time at the beginning, then they decrease and converge to a steady value indicated with the black squares. At this point, equilibration is assumed, as the re-

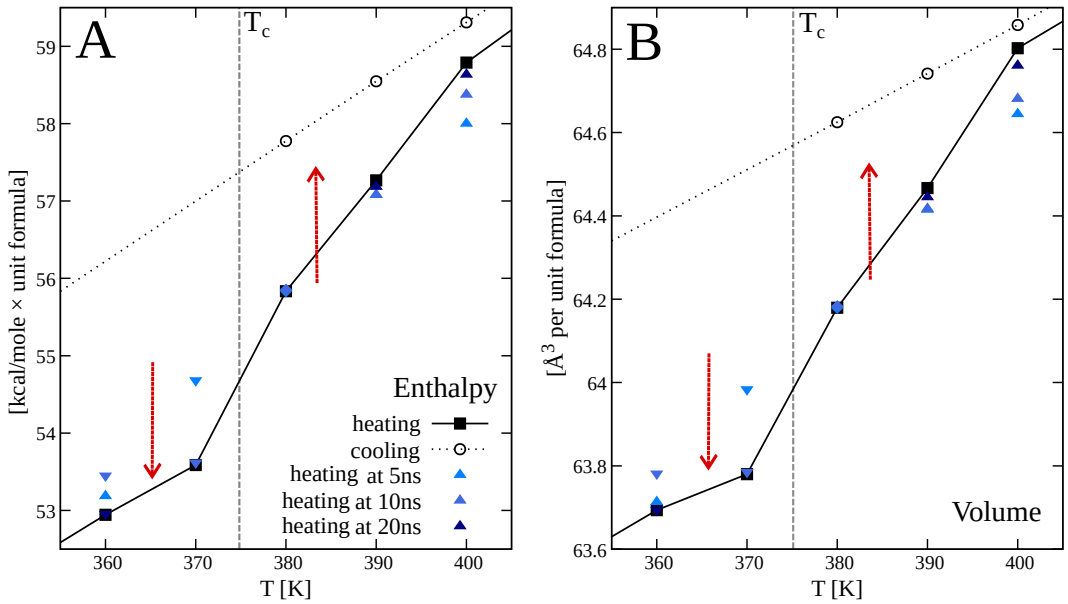

Figure 4.32: Convergence for enthalpy (a) and volume (b) in the transition range 360K-400K. ▲ points indicates a tendency to increase, ▼ points indicates the opposite tendency. ◆ point marks a stable value.

ordering process explained in Section 4.4.1 came to an end. Above the transition temperature, both 390K and 400K average enthalpy values increase steadily with time. At this temperature, the molecular diffusion process leads towards the high-temperature DMA phase, but it would take longer times to fully converge. The reason is due to the molecular diffusion process forming the site disorder, whose speeds depends on temperature (see diffusion coefficients in Section 4.3.3). For this reason, we assume that the final values of enthalpy are the ones obtained by cooling the system from the 550K configuration. Finally, we notice that the values of the trajectory at 380K are stables. However, as explained in the main Chapter, the phase transformation is due to the orientational disorder of the molecules, which, after having broken the stable hydrogen bonds, they are free to rotate. At this temperature, the orientational disorder is stable (see Figure 4.27 panel B), but the probability to initiate the diffusion is very low and it would require exponentially longer simulation times to be observed directly. We therefore assume that also at 380K the convergence values comes from the cooled trajectory. All these informations are the same in the case of volume (panel B).

To conclude, simulation times were adapted for each trajectory as different dynamical processes occur at different temperatures, in particular molecular diffusion above T_c. The results of Chapter 4 are at equilibrium, obtained from heated trajectories below and well above the transition ($T \geq 450$K), and from the cooled trajectories for temperatures $T_c \in [380\text{K}, 400\text{K}]$. The criterion chosen to assign a phase for the points at higher or lower pressure in the phase diagram is the following: starting from the AHH-II configuration at 300K, temperature is increased and we checked the persistent presence of orientational disorder for times superior to 10ns. If the disorder is stable, the point is assigned to the AHH-pbcc phase and the equilibrium values are obtained from a cooled simulation from a very high temperature simulation. If instead the disorder diminish with time, the point in

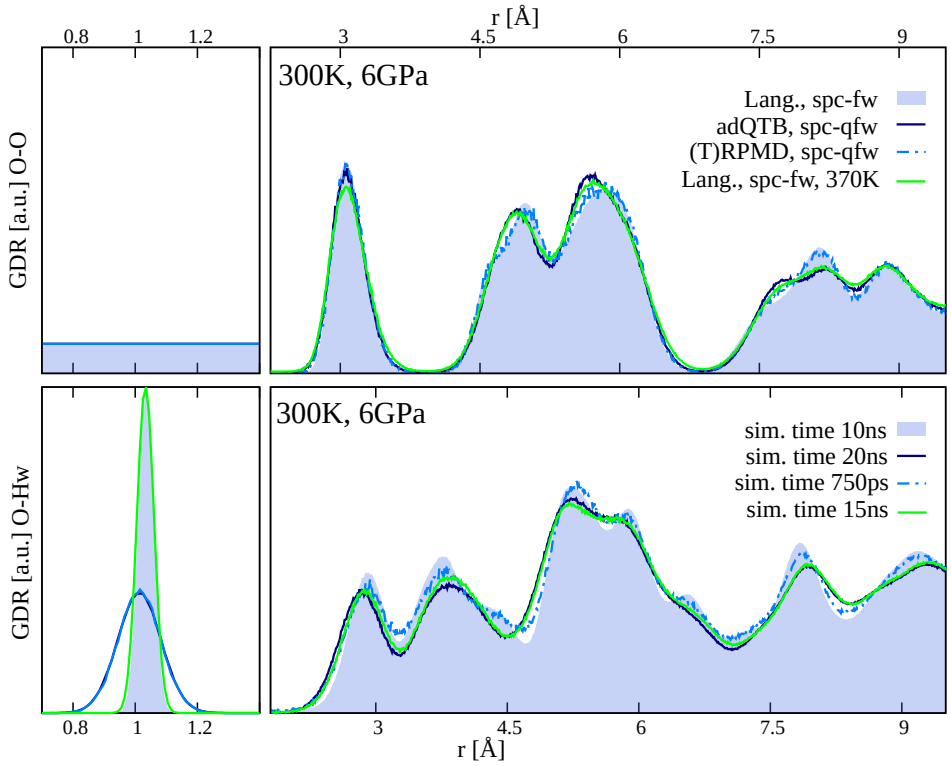

Figure 4.33: Average radial distribution functions of OO and OH (where H belongs to water molecules) distances at 300K and fixed pressure of 6GPa, with different methods.

the phase diagram is assigned to the AHH-II phase.

B Comparison between quantum MD methods

In Section 4.4 we compared few results obtained via classical Langevin MD and the quantum methods adQTB and (T)RPMD. Here we report some other direct comparisons between the two methods and we comment on the accuracy of the respective results.

Figures 4.33 and 4.34 reports the RDFs of OO and OH distances (where H belongs to water molecules), obtained via different methods at 300K and 500K respectively. In the former, also the classical 370K result is depicted. The main difference between the classical and the quantum methods is visible on the $g_{OH}(r)$ distribution at small distances. Indeed, the hydrogen atom is well localized at the intramolecular distance of 1Å from the oxygen atom in the classical method, while its position is delocalized (and slightly shifted) for both quantum methods.

As explained in Section 4.4.1, the 300K configuration of AHH-II obtained via adQTB method is comparable to the 370K configuration obtained via classical Langevin molecular dynamics. The RDFs confirm this result. On the contrary, the (T)RPMD result strongly resembles the classical result (both at 300K). The main difference between the two is the simulation time: only 750ps long trajectory is used, against the 10ns of adQTB trajectory. We therefore expect that the (T)RPMD results would converge towards the adQTB curve

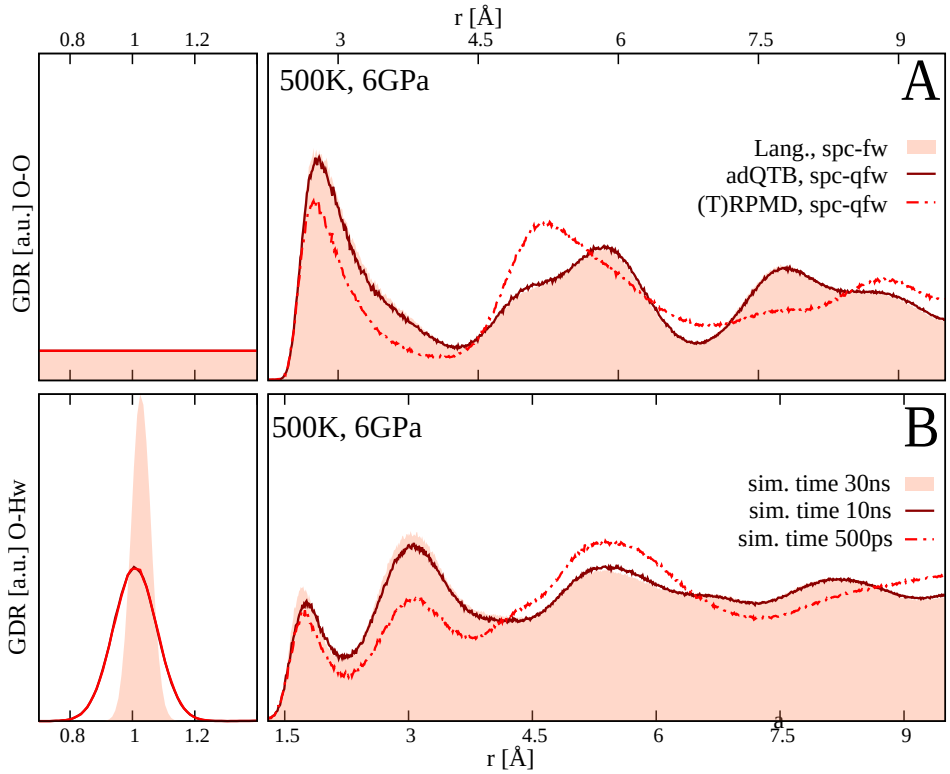

Figure 4.34: Average radial distribution functions of OO and OH (where H belongs to water molecules) distances at 300K and fixed pressure of 6GPa, with different methods.

at longer simulation times.

This result is even more visible at high temperature (500K), depicted in Figure 4.34. Classical and adQTB results almost perfectly coincide, with the exception of the hydrogen distribution at intra-molecular distances. On the contrary, the (T)RPMD result needs more simulation time to converge to the AHH-pbcc phase: the times of formation of the DMA structure are of the order of few or tenths of ns (depending on the temperature), which is much longer than the 500ps of (T)RPMD trajectory.

Finally, we depict the same result with the ADF of water dipoles in Figure 4.35. The distribution of 370K classical trajectory is very close to the one of the adQTB 300K trajectory, while the 300K classical result resembles the 300K (T)RPMD result. Once again, the main difference lies in the simulation times: the (T)RPMD method would require a longer trajectory to converge towards the adQTB result, which is computationally costly.

To conclude, the adQTB method is an efficient computation tool to include zero-point energy contribution and it gives satisfactory results in the computation of static properties, such as RDFs. Note also that we make use of a force field with an harmonic potential form for the bond stretching and bending, and the QTB/adQTB methods are designed to include the exact energetic contribution of the quantum harmonic oscillator (see discussion in Chapter **??**, Section 3.3.4).

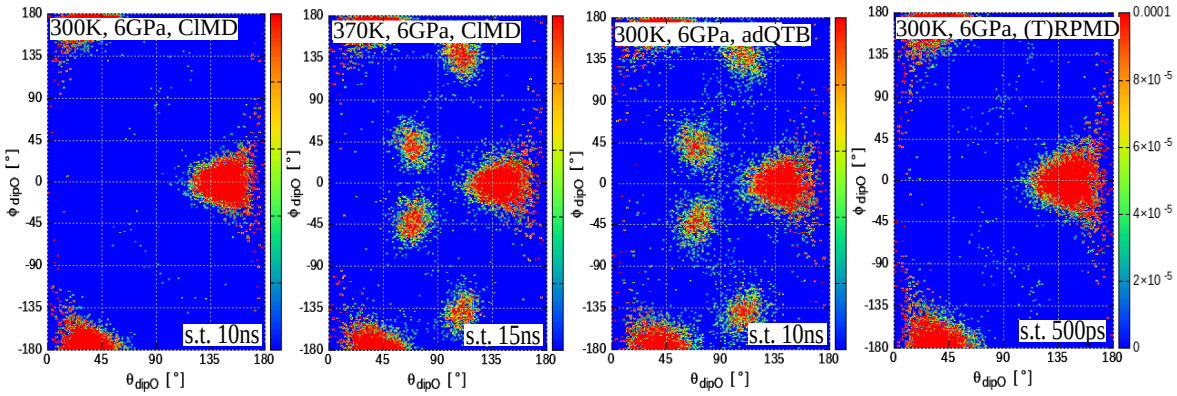

Figure 4.35: Average angular distribution $P(\theta, \phi)$ of water dipole at 300K/370K and fixed pressure of 6GPa, from different MD methods.

Appendix II: simulations beyond P=6GPa

In the following Section we expose the results obtained beyond the exploration of the 6GPa isobaric line. Figure 4.4 already reported many simulation points at along the phase transition line between the AHH-II and AHH-pbcc phases, as well as some points in the liquid phase. However, the work of Andriambariarijaona et al. [44, 73] reports two others interesting phases (see Figure **??**): the phase AHH-qbcc, obtained by compression of the AHH-pbcc phase, which eventually becomes the AHH-DIMA phase; moreover, they highlight a intermediary region between AHH-II and AHH-DIMA phase at ambient temperature, where AHH-qbcc is thought to be metastable. Our theoretical investigations of these phase has the purpose to preliminary explore the classical properties of these phases. Bear in mind that the main limitation we might encounter is the absence of the ionization process and proton diffusion, due to the nature of the non-reactive force field used.

Figure 4.36 shows the simulation points on the full experimental phase diagram traced by Andriambariarijaona et al. [44, 73]. The points already shown in Figure 4.4 are not reported to simplify the picture. Four main direction of exploration were followed:

- 300K isotherm: from the initial structure of AHH-II at 300K and 6GPa, the pressure was decreased until 2GPa and increased until 26GPa;
- 500K isotherm: after the study of the evolution of AHH crystal with temperature at fixed pressure of 6GPa, the result obtained at 500K is progressively compressed until 18GPa, at constant temperature;
- 18GPa isobar: from the configuration obtained at 500K and 18GPa, the temperature was gradually decreased until 300K, at fixed pressure;
- inverse 300K isotherm: from the structure obtained at 300K and 18GPa from the previous thermodynamic transformations, the pressure was gradually released until the original starting point of 300K and 6GPa.

The following sections reports the structural results obtained along these directions.

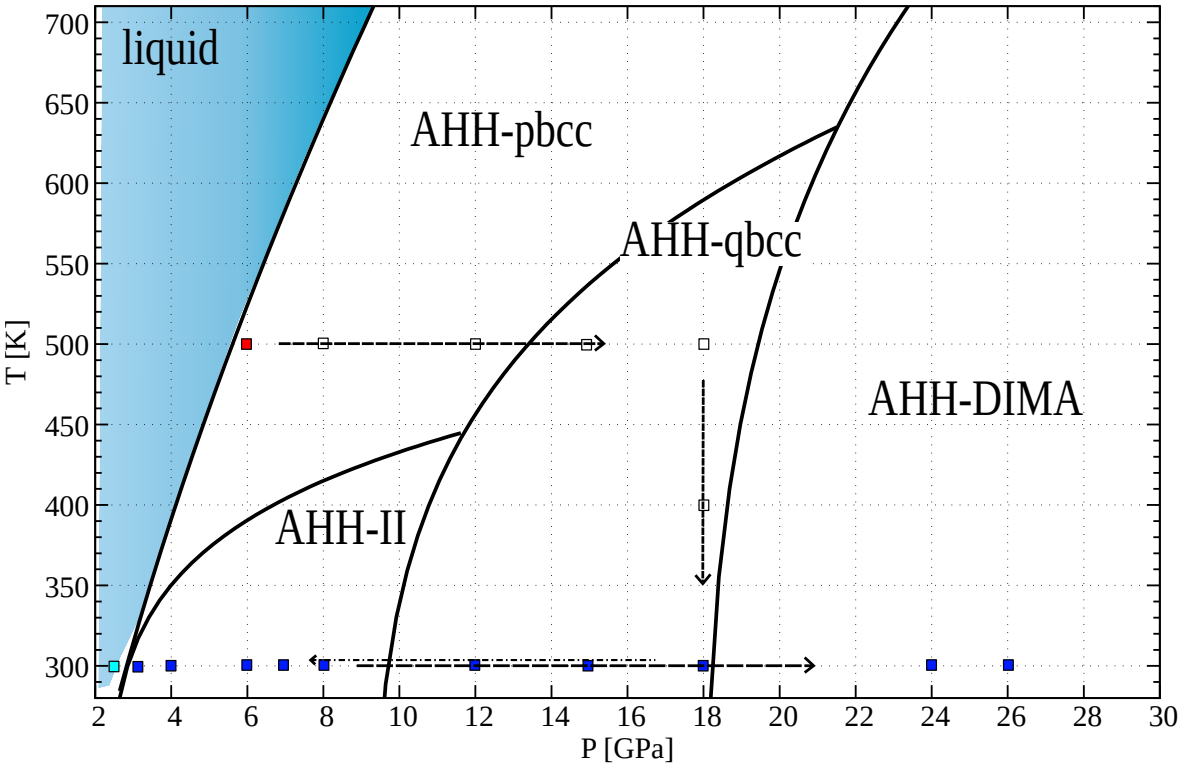

Figure 4.36: Simulation points drawn on the experimental phase diagram of Andriambariarijaona et al. [44, 73]. The colors stand: blue for AHH-II, red for AHH-pbcc, white for unassigned.

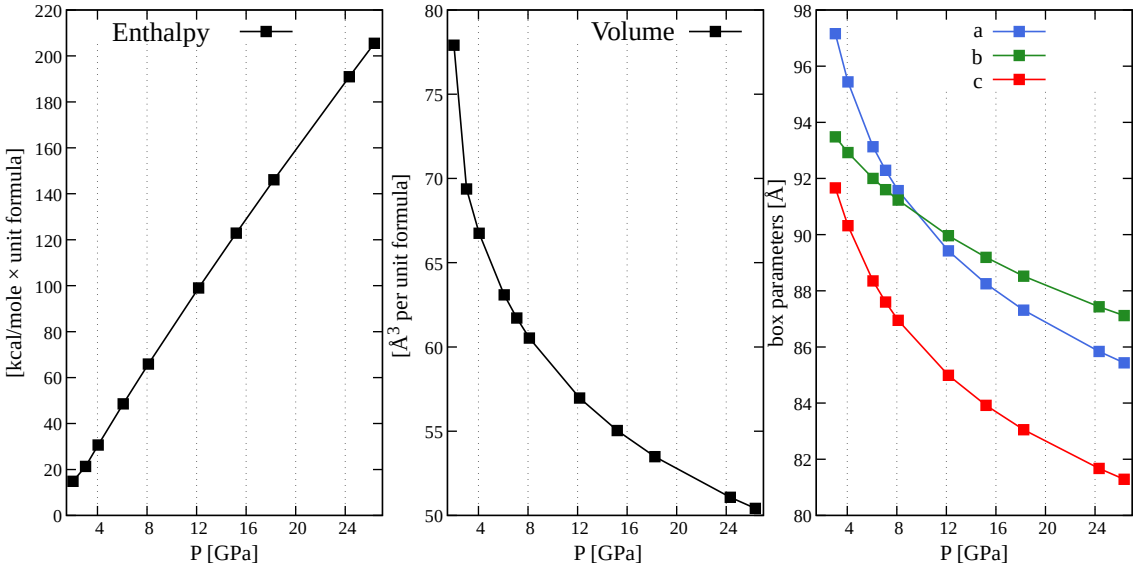

Figure 4.37: Average values of enthalpy (panel A), volume (panel B) and three box parameters (panel C) as function of pressure, at constant temperature of 300K. Error bars are within the point dimensions.

C Compression at 300K

For the 300K isothermal line, the structure of AHH-II described in Section 4.1 is used as starting configuration. It has been progressively compressed up to 26GPa. In addition, the structure has been progressively decompressed until 2GPa in order to confirm the presence of the liquid phase at low pressures (as shown in Figure 4.4). As for the previous study of the phase transition along the 6GPa line, we report the values of enthalpy, box parameters and volume as function of pressure in Figures 4.37 panel A, B and C respectively. The enthalpy of the systems increases linearly with pressure from 3GPa to 24GPa. For the simulation at 2GPa, direct observations of the system established the melting of the AHH-II structure at these pressures, and fixed the transition pressure between 2GPa and 3GPa. This result is in agreement with the experimental melting line reported in Figure 4.36 from the work of Andriambariarijaona et al. [44, 73]. Indeed they report a melting pressure of 2.7GPa at 300K, while Wilson et al. [54] report the solidification of the liquid and the formation of AHH-II crystal at 3.6(4)GPa. No other macroscopic change is observed along the 300K isothermal line. The same absence of discontinuity is observed for the values of the box parameters. However, around 10GPa, the a parameter, i.e. the box dimension along direction $(1, 0, 0)$, crosses the b parameters, i.e. the box dimension along $(0, 1, 0)$ direction. All parameters depend on the inverse of the pressure. From the box parameter, the average volume is computed. Its values are shown in Figure 4.37 panel B as functions of pressure. The only discontinuous change is visible between 2GPa and 3GPa, where we locate the solid-liquid transition. For the rest of the curve, volume decreases depending on the inverse pressure. No other transitions are observed.

Between all the other results, we show in Figure 4.38 the angular distribution of water dipoles as function of the increasing pressure and fixed temperature of 300K. Clearly, no orientational disorder is present at any point along the compression, and molecules are fixed

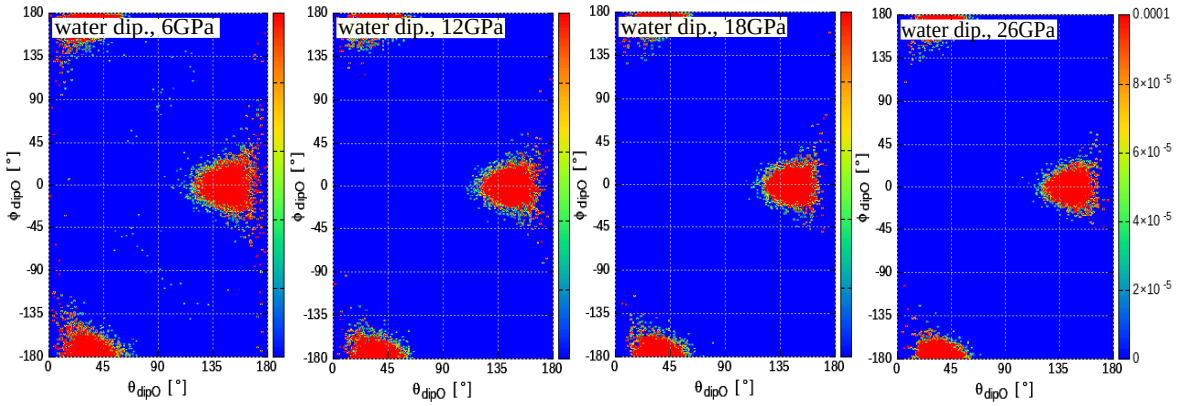

Figure 4.38: Average angular distribution $P(\theta, \phi)$ of water and ammonia dipoles at different pressures and temperature of 300K.

in their original orientation of the AHH-II structure. RDFs and structure factor results are coherent with this finding.

To conclude, no solid-solid phase transition is observed along the 300K isothermal line by progressive compression of the AHH-II structure at 6GPa and 300K. This fact is in clear contradiction with all experimental studies: Wilson et al. [70] report a solid-solid phase transition at 26.5GPa; Ma et al. [71] they report a first phase transition at 19GPa and a second phase transition at 25GPa; finally, Andriambariarijaona et al. [44, 73] report the gradual transition between AHH-II and DIMA phase between 10GPa to 34GPa, without volume discontinuity. However, this result was expected, due to the nature of the non reactive force field used for this study. Indeed, all previous experiments agree in characterizing the new phase as partially ionic. Therefore, the study of this phase transition require a reactive force field or a different method, such as *ab initio* (DFT/DFTB) molecular dynamics.

D Compression at 500K

The study at fixed temperature shown in the previous Section C was repeated for the temperature of 500K. Figure 4.36 reports the simulation points along this direction. The configuration obtained at 500K and 6GPa is taken as a starting point. It has been progressively compressed until 18GPa. The values of enthalpy, box parameters and volume are shown in Figure 4.39.

Starting with enthalpy, its values obtained at 500K are reported, as well as the ones obtained along the 300K isothermal line, and the values along the 6GPa isobaric line. The two latter curves are reported as a reference to visualize the procedure followed for this study. The values along the 500K isothermal line do not present discontinuities, with the exception of the point at 2.5GPa and 4GPa, where the liquid phase is observed. The slope of the curve is approximately the same of what obtained along the 300K isothermal line. Concerning the box dimensions (panel C), however, discontinuities are observed between 8 and 12GPa. Contrary to the behavior of the box parameters at low temperature, only the b parameters decreases smoothly with pressure. Indeed, parameter a remains constant between

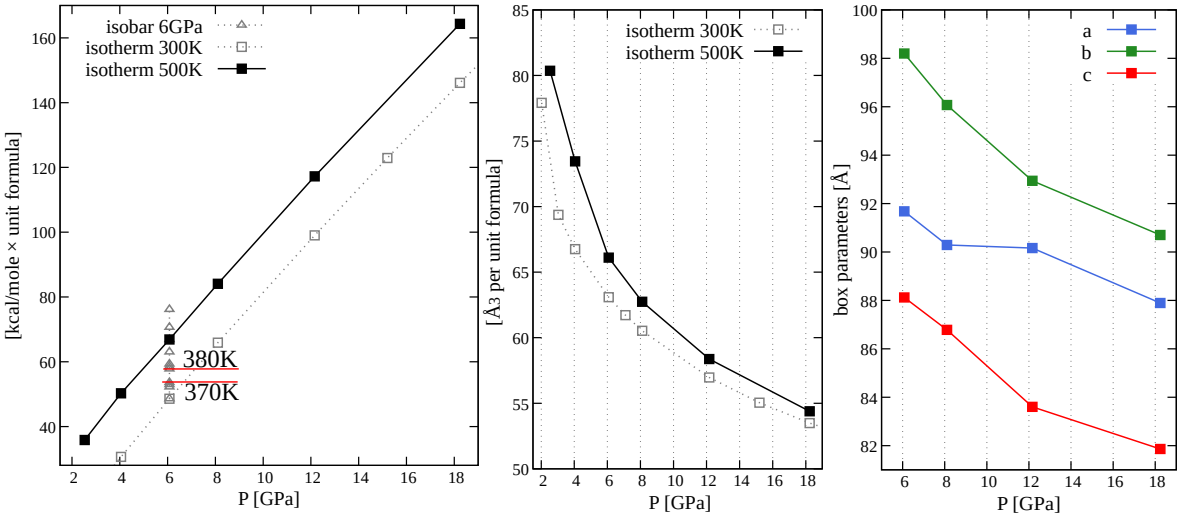

Figure 4.39: Average values of enthalpy (panel A), volume (panel B) and three box parameters (panel C) as function of pressure, at constant temperature of 300K. Error bars are within the point dimensions.

8GPa and 12GPa, while parameter c has a sudden jump, of about $\Delta c/c$ =3.7%. Finally, the average volume (panel B) decreases smoothly with the inverse of pressure. In conclusion, average enthalpy and volume along the 500K isothermal line decrease smoothly with pressure. Traces of possible transition are only detected in the box parameters, between 8GPa and 12GPa.

Figure 4.40 shows the comparison of the experimental X-ray diffraction pattern at 12.7GPa and 468K with the simulation result at similar P-T conditions. Even though the simulation detects the doubling of the main peaks (at 9°) due to the quasi-*bcc* structure, most of the structure factor is flat, missing some main features of the experiment. The evolution of the structure factor with higher pressure does not add any peak. Based on this result, we cannot safely assume to have observed the proper AHH-qbcc structure, but rather a quasi-*bcc* probably due to the orthorhombic simulation box. Ongoing Lammps simulations with a monoclinic box would clarify the effect of the constraints and hopefully reproduce the correct transition from a perfect *bcc* to a quasi-*bcc* only due to the reordering of molecules in a new phase.

Figure 4.41 shows the molecular dipoles ADFs for water (panel A) and ammonia (panel B), for three main pressures at fixed temperature of 500K. As the pressure in increased, the AHH-pbcc structure found at 6GPa shows some degree of re-ordering, with the appearance of privileged directions. In the case of water, they are recognizable as the faces of the *bcc* cell; for the ammonia molecules, some new directions appears but the degree of orientational disorder is still to high to clearly distinguish some fixed direction and assign their orientations.

To sum up, our results are inconclusive on the presence of a phase transition and on the nature of this new structure. A certain degree of reorganization is observed by the dipoles ADFs (Figure 4.41) but further investigations are necessary. In particular, three conditions might lead to more striking findings: firstly, longer simulation times are needed

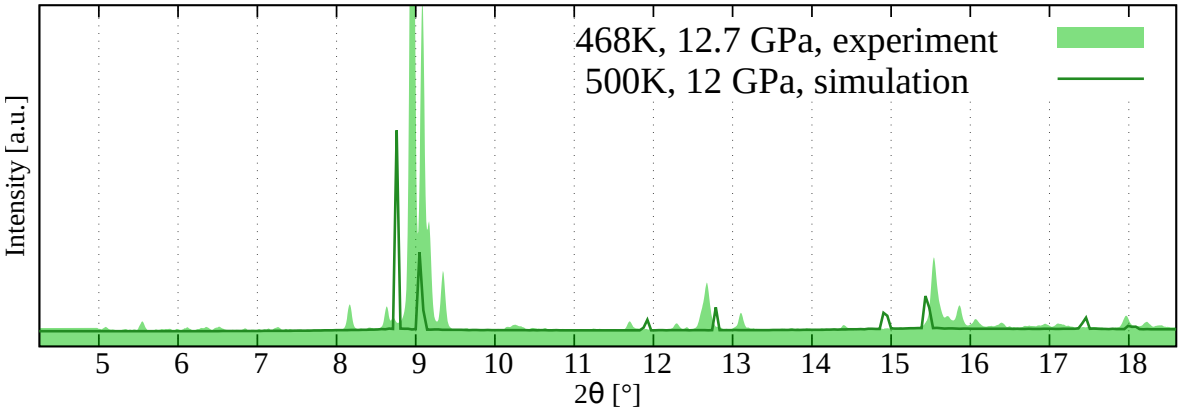

Figure 4.40: Classical structure factors compared with experimental X-ray diffraction results [44], at 300K (blue) and 370K (green). In yellow, the average structure factor obtained at 300K and 6GPa from adQTB trajectory.

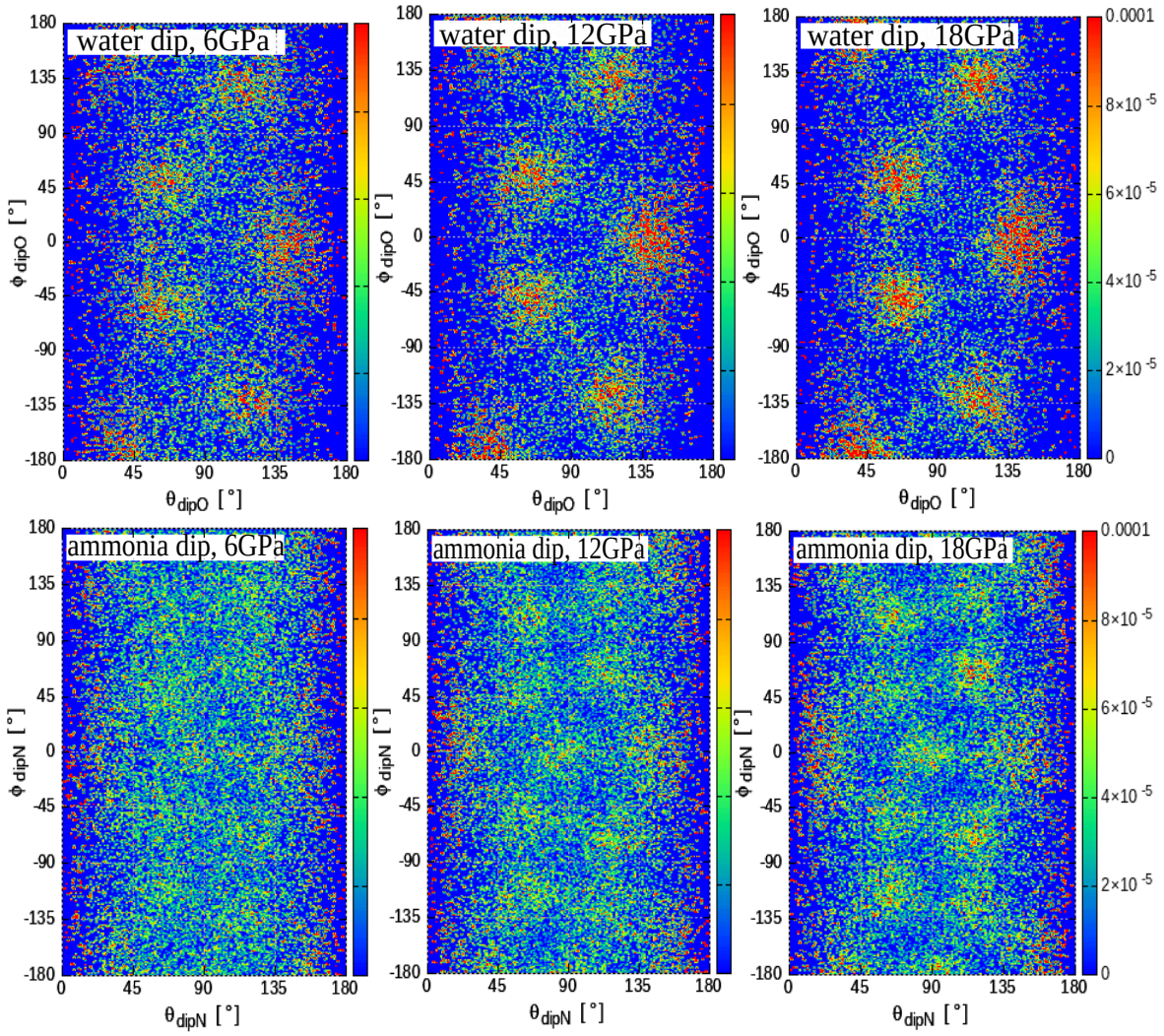

Figure 4.41: Average angular distribution $P(\theta, \phi)$ of water and ammonia dipoles at different pressures and temperature of 500K.

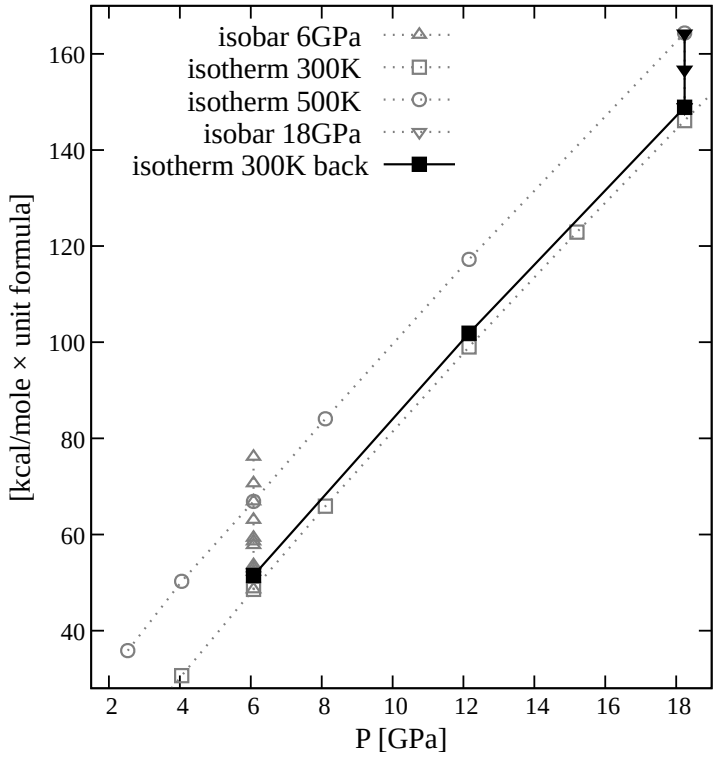

Figure 4.42: Average enthalpy values as function of temperature along the 300K isothermal line after the thermodynamic cycle, made along the 300K and the 500K isothermal lines, and the 6GPa and 18GPa isobaric line. Error bars are within the point dimensions.

to ensure the reordering process; second, different thermodynamic path could be followed, which might enhence the transition to occur; finally, as higher percentages of dissociated chemical species are observed in AHH-pbcc and eventually in DIMA phase, the use of a reactive force field or *ab initio* methods is needed.

E Cooling at 18GPa and decompressing at 300K

Other two lines have been explored on the phase diagram of AHH (see Figure **??**). First, the 18GPa line, along which the structure obtained at 500K has been cooled until 300K. The second is the same 300K isothermal line, with the main difference that, as starting configuration, we use the AHH structure obtained after three thermodynamic transformations: heating at 6GPa, compression at 500K, cooling at 18GPa.

Starting with the 18GPa isobaric line, the structure obtained at 500K under compression of 18GPa is used as starting configuration. It has been progressively cooled until 300K. The average enthalpy evolution, represented in Figure 4.42, is smooth with temperature and reaches values above the previous simulations when the 300K configuration of AHH-II was compressed. This is the macroscopic sign that the original structure of AHH-II is never recovered.

Figure 4.43 shows the dipole angular distribution of the ammonia and water molecules

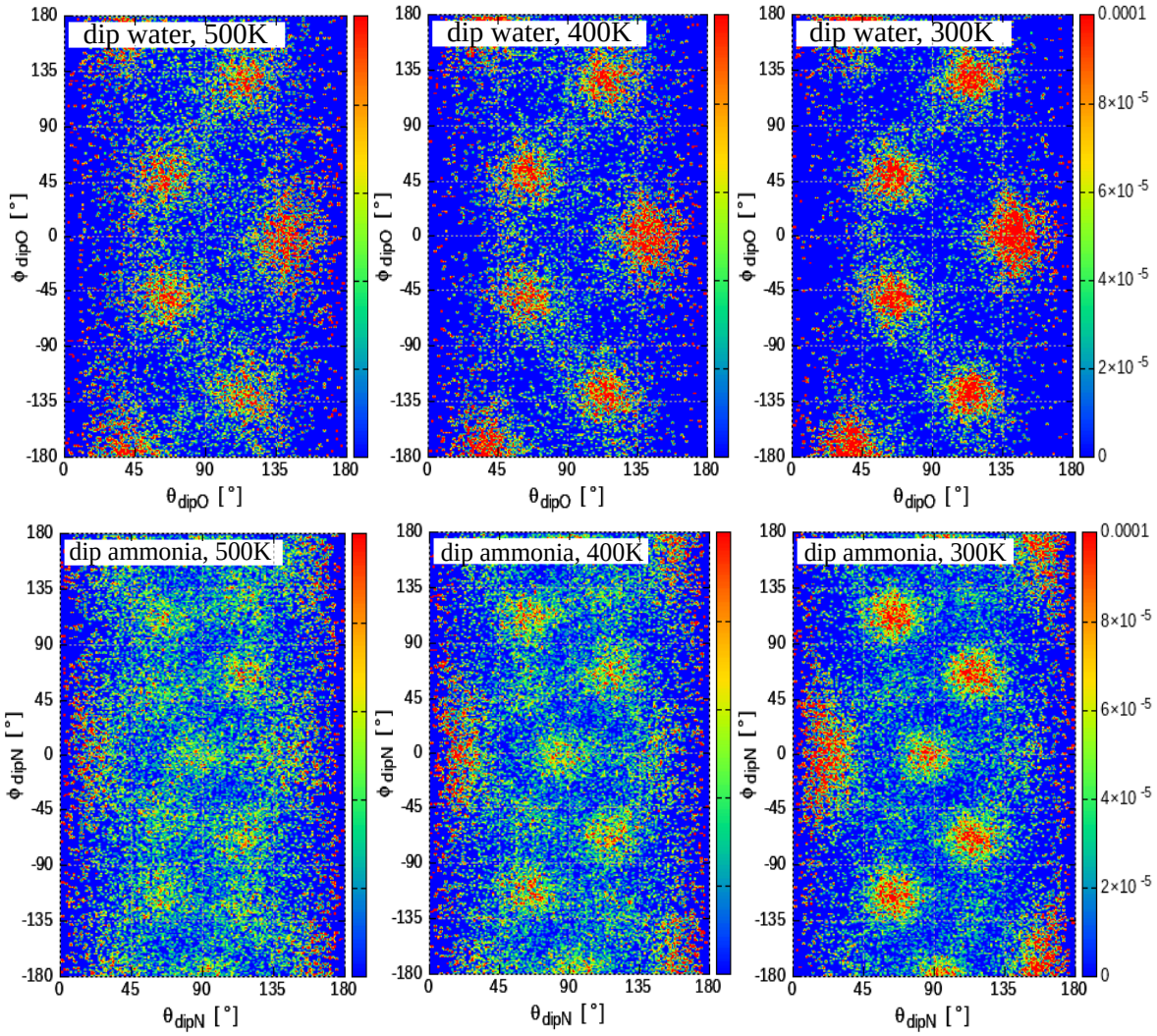

Figure 4.43: Average angular distribution $P(\theta, \phi)$ of water and ammonia dipoles at different temperatures and pressure of 18GPa.

Table 4.8: Time-averaged volume, box dimensions and enthalpy for different input temperature (input pressure of 6GPa), using classical Langevin thermostat and barostat.

$T_{in}[K]$	$\langle V\rangle_t[nm^3]$	$\langle a\rangle_t$[Å]	$\langle b\rangle_t$[Å]	$\langle c\rangle_t$[Å]	$\langle H\rangle_t[kcal/mol \times u.f.]$
300	757.1	93.14	92.00	88.35	48.58
350	762.8	93.40	92.33	88.46	52.23
360	764.3	93.29	93.61	87.53	52.95
370	765.1	93.33	93.55	87.66	53.98
380	775.5	91.10	97.17	87.60	57.78
390	776.9	91.16	97.21	87.67	58.54
400	778.3	91.22	97.26	87.73	59.31
450	785.4	91.84	97.38	87.82	63.02
500	793.3	91.68	98.20	88.12	66.80
550	800.2	92.09	98.10	88.58	70.63
600	831.8	–	–	–	76.17

as function of decreasing temperature, at the fixed pressure of $P = 18$GPa. As temperature is decreased, the general disorder of dipoles observed at high temperature decreases, and the preferred directions, already spotted at 500K, are enhanced. Therefore, a new crystal structure is formed, with new preferred orientations of both ammonia and water dipoles. Notice that the water orientations point at the faces of the *bcc* cube, whereas the ammonia dipoles point at the eight corners of the cube. The same ADFs are observed when pressure is released until 6GPa.

Even though the results presented are at a very preliminary state, the qualitative behavior of the simulations on the thermodynamic cycle matches the conclusion of Andriambariarijaona et al. [44, 73]. Indeed, once the AHH-qbcc phase is formed at high temperature, it does not transform into AHH-II once temperature is decreased. Moreover, in the region between 10GPa and 19GPa, AHH-II and AHH-DIMA are metastable phases of AHH-qbcc, for temperatures inferior to 450K.

F Tables

We report here the Tables with the equilibrium values of volume, box dimensions and enthalpy for each (N, P, T) simulation shown in Chapter 4 and Appendix B.

We report also the diffusion coefficients obtained in liquid AHH for different temperatures and pressures (Table 4.10).

Table 4.9: Time-averaged stresses for different input temperature (input pressure of 60katm), using classical Langevin thermostat and barostat.

$T_{input}[K]$	$\langle\sigma_{12}\rangle_t$[bar]	$\langle\sigma_{13}\rangle_t$[bar]	$\langle\sigma_{23}\rangle_t$[bar]
300	1.77	767.91	-3.37
350	3.60	524.32	-3.85
360	-34.41	2193.18	114.30
370	117.27	1952.90	-431.84
380	-3.43	2916.61	7.19
390	0.18	2748.71	-3.53
400	-4.62	1992.11	14.83
450	-7.72	1269.40	-6.59
500	-26.81	883.65	6.26
550	-5.15	781.51	-5.08
600	-3.92	2.79	-1.05

Table 4.10: Diffusion coefficients of liquid AHH at different pressures and temperatures.

$P_{in}[katm]$	$T_{in}[K]$	$D_{\mathrm{H_2O}}$ [10^{-5}cm^2/s]	$D_{\mathrm{NH_3}}$ [10^{-5}cm^2/s]
2	300	0.839(6)	0.787(6)
2.5	400	2.656	2.325
2.5	500	5.597	4.891

Table 4.11: Time-averaged volume, box dimensions and enthalpy for different input pressure (input temperature of 300K), using classical Langevin thermostat and barostat.

$P_{in}[katm]$	$\langle V\rangle_t[nm^3]$	$\langle a\rangle_t$[Å]	$\langle b\rangle_t$[Å]	$\langle c\rangle_t$[Å]	$\langle H\rangle_t[kcal/mol \times u.f.]$
20	934.9	–	–	–	14.84
30	832.5	97.16	93.48	91.66	30.63
40	801.0	95.44	92.92	90.32	56.36
60	757.1	93.14	92.00	88.35	48.58
80	726.3	91.57	91.23	86.95	65.88
120	683.6	89.42	89.96	84.99	99.02
150	660.5	88.25	89.19	83.92	122.90
180	641.9	87.31	88.52	83.05	146.11
240	612.9	85.84	87.43	81.67	190.96
260	605.0	85.43	87.12	81.29	205.53

Table 4.12: Time-averaged volume, box dimensions and enthalpy for different input pressure (input temperature of 500K), using classical Langevin thermostat and barostat.

$P_{in}[katm]$	$\langle V\rangle_t[nm^3]$	$\langle a\rangle_t$[Å]	$\langle b\rangle_t$[Å]	$\langle c\rangle_t$[Å]	$\langle H\rangle_t[kcal/mol \times u.f.]$
25	964.3	–	–	–	35.85
40	881.3	–	–	–	50.24
60	793.3	91.68	98.20	88.12	66.80
80	752.8	90.29	96.08	86.78	84.09
120	702.0	88.20	93.86	84.79	117.23
180	654.5	86.18	91.61	82.89	164.34

Table 4.13: Time-averaged volume, box dimensions and enthalpy for different input temperatures (input pressure of 18GPa), using classical Langevin thermostat and barostat.

$T_{in}[K]$	$\langle V\rangle_t[nm^3]$	$\langle a\rangle_t$[Å]	$\langle b\rangle_t$[Å]	$\langle c\rangle_t$[Å]	$\langle H\rangle_t[kcal/mol \times u.f.]$
500	654.5	86.18	91.61	82.89	164.34
400	649.3	85.95	91.41	82.65	156.74
300	643.99	85.71	91.19	82.50	148.88

Table 4.14: Time-averaged volume, box dimensions and enthalpy for different input pressures (input temperature of 300K), using classical Langevin thermostat and barostat.

$P_{in}[katm]$	$\langle V\rangle_t[nm^3]$	$\langle a\rangle_t$[Å]	$\langle b\rangle_t$[Å]	$\langle c\rangle_t$[Å]	$\langle H\rangle_t[kcal/mol \times u.f.]$
180	643.99	85.71	91.19	82.50	148.88
120	687.05	87.57	93.26	84.13	101.86
60	764.9	90.72	96.84	87.06	51.46

Conclusions and prospectives

In this work, we addressed the problem of dynamical properties of molecular model systems, from a numerical simulation perspective. Our approachis based on using molecular dynamics techniques to obtain statistical and dynamical informations from the system trajectory. In order to include nuclear quantum effects, we tested a class of methods which use a quantum bath, inspired from the Langevin approach to sample the canonical ensemble, to mimic the delocalization of nuclei.

The Chapter 3 focused on the problem of quantum diffusion. An analytical model system is used to assess the different quantum molecular dynamics methods on the problem. We solve the Schrödinger equation for one particle in a 2D fixed periodical lattice and compute the diffusion coefficient from the velocity autocorrelation function. Thanks to this reference, we can compare the classical Langevin method, the quantum thermal bath methods (standard and adaptive) and the ring-polymer approximation of the path-integral molecular dynamics. We conclude that the latter is the most accurate method for numerically evaluating the diffusion coefficient, despite its computational cost. We explain the failure of the quantum thermal bath methods in terms of incorrect energy fluctuations. Finally, we studied an hybrid version of ring-polymer method which uses the quantum thermal bath to accelerate the convergence in terms of the number of beads. Although better performances are observed for energy estimators, the method does not present advantages for the computation of the diffusion coefficient.

The Chapter 4 presents the theoretical investigation of the crystal-plastic phase transition in ammonia hemi-hydrate (AHH) under high pressure. We have accurately reproduced the transition in accordance with experimental results. The AHH-II monoclinic crystal, whose stability is mostly due the strong hydrogen bonds formed between oxygen donors and nitrogen acceptor, transforms to a (quasi)-*bcc* phase at high temperature, which eventually melts. The AHH-pbcc phase has a plastic character: hydrogen bonds are short living, experiencing fast formations and breaking on the scale of ps; hence, molecules orientations are not fixed but they rotate, establishing the standard plastic character of the phase. In addition, we were able to show that the plastic phase present also molecular diffusion, with water and ammonia molecules changing their original position and passing from one *bcc* site to the other. The net result of this process is the formation of the disordered molecular alloy predicted by the experiments. The AHH-pbcc phase experiences therefore the so called Orientational-Disorder-Driven Site Disorder (ODDSD), which remarkably combine molecular diffusion and a precise crystalline structure. Although that the presence of self-diffusion in plastic phases was already observed [58], the novelty of ODDSD is the formation of the alloy due to the coexistence of two molecular species. Moreover, the main role is played by the hydrogen bonds rather then the isotropic Van der Waals forces.

Finally, we point at few possible further developments, between the many questions still open on the ammonia hydrate systems, and solid phases with analogous properties. The problem of proton hopping as a function of pressure must be addressed, in order to describe ionic and molecular phases such as AHH-DIMA [70, 73, 74], fully deprotoneted phase [75] or superionic AHH [39]. Theoretical investigations can be carried out via the

accurate but expensive techniques of *ab initio* molecular dynamics, possibly usign (T)RPMD method for the nuclear effects. However, as we hope to have shown in this work, the force fields approach offers not only approximated, yet rich enough results to understand phase transition dynamics, but it allows the efficient simulation of millions of atoms for times up to the order of μs. Therefore, the solution may lie in the development of reactive and/or machine learning force fields for water and ammonia mixture, which would offer the possibility to study not only the AHH system, but also the other hydrates phase diagrams.

Bibliography

[1] T. E. Markland and M. Ceriotti. "Nuclear quantum effects enter the mainstream". In: *Nat. Rev. Chem.* 2.3 (2018). URL: https://doi.org/10.1038/s41570-017-0109 (cit. on p. 2).

[2] I. R. Sims. "Tunnelling in space". In: *Nat. Comm.* 5.9 (2013), pp. 734–736. URL: http://www.nature.com/articles/nchem.1736 (cit. on p. 2).

[3] Y. Bronstein et al. "Quantum-driven phase transition in ice described via an efficient Langevin approach". In: *Phys. Rev. B* 89.21 (2014), p. 214101. URL: https://link.aps.org/doi/10.1103/PhysRevB.89.214101 (cit. on pp. 2, 35).

[4] M. Ceriotti et al. "Nuclear Quantum Effects in Water and Aqueous Systems: Experiment, Theory, and Current Challenges". In: *Chem. Rev.* 116.13 (2016), pp. 7529–7550. URL: https://pubs.acs.org/doi/10.1021/acs.chemrev.5b00674 (cit. on p. 2).

[5] K. M. Hickson et al. "Quantum Tunneling Enhancement of the C + H_2O and C + D_2O Reactions at Low Temperature". In: *J. Phys. Chem. Lett.* 7.18 (2016), pp. 3641–3646. URL: https://pubs.acs.org/doi/10.1021/acs.jpclett.6b01637 (cit. on p. 2).

[6] Y. Bronstein et al. "Quantum versus classical protons in pure and salty ice under pressure". In: *Phys. Rev. B* 93.2 (2016), p. 024104. URL: https://link.aps.org/doi/10.1103/PhysRevB.93.024104 (cit. on pp. 2, 35).

[7] L. Zhang, W. L. Zhong, and W. Kleemann. "A study of the quantum effect in BaTiO3". In: *Phys. Lett. A* 276.1-4 (2000), pp. 162–166. URL: https://linkinghub.elsevier.com/retrieve/pii/S0375960100006320 (cit. on p. 2).

[8] M. Benoit, D. Marx, and M. Parrinello. "Tunnelling and zero-point motion in high-pressure ice". In: *Nature* 392.6673 (1998), pp. 258–261. URL: http://www.nature.com/articles/32609 (cit. on p. 2).

[9] X. Jia et al. "Magnetic Fields of the Satellites of Jupiter and Saturn". In: *Space Sci. Rev.* 152.1-4 (2010), pp. 271–305. URL: http://link.springer.com/10.1007/s11214-009-9507-8 (cit. on p. 2).

[10] D. Kang et al. "Nuclear quantum dynamics in dense hydrogen". In: *Sci. Rep.* 4.1 (2015), p. 5484. URL: http://www.nature.com/articles/srep05484 (cit. on p. 2).

[11] J. Teixeira. "The double identity of ice X". In: *Nature* 392.6673 (1998), pp. 232–233. URL: http://www.nature.com/articles/32542 (cit. on p. 2).

[12] T. Steiner. "The Hydrogen Bond in the Solid State". In: *Angew. Chem. Int. Ed.* 41.1 (2002), pp. 48–76. URL: https://doi.org/10.1002/1521-3773(20020104)41:1%3C48::aid-anie48%3E3.0.co;2-u (cit. on pp. 3, 17).

[13] S. Schaack et al. "Quantum driven proton diffusion in brucite-like minerals under high pressure". In: *Sci. Rep.* 10.1 (2020), p. 8123. URL: http://www.nature.com/articles/s41598-020-64813-8 (cit. on pp. 3, 4).

[14] C. Fonseca Guerra et al. "Hydrogen Bonding in DNA Base Pairs: Reconciliation of Theory and Experiment". In: *J. Am. Chem. Soc.* 122.17 (2000), pp. 4117–4128. URL: https://doi.org/10.1021/ja993262d (cit. on p. 3).

[15] G.A. Jeffrey. *An Introduction to Hydrogen Bonding*. 1997. URL: https://books.google.fr/books?id=ZRAFifo37QsC (cit. on p. 3).

[16] J. Řezáč and P. Hobza. "Describing Noncovalent Interactions beyond the Common Approximations: How Accurate Is the "Gold Standard," CCSD(T) at the Complete Basis Set Limit?" In: *J. Chem. Theory. Comp.* 9.5 (2013), pp. 2151–2155. URL: https://doi.org/10.1021/ct400057w (cit. on pp. 3, 85, 102).

[17] X. Z. Li, B. Walker, and A. Michaelides. "Quantum nature of the hydrogen bond". In: *PNAS* 108.16 (2011), pp. 6369–6373. URL: https://doi.org/10.1073/pnas.1016653108 (cit. on pp. 3, 116).

[18] J. Guo et al. "Nuclear quantum effects of hydrogen bonds probed by tip-enhanced inelastic electron tunneling". In: *Science* 352.6283 (2016), pp. 321–325. URL: https://doi.org/10.1126/science.aaf2042 (cit. on p. 3).

[19] C. Schran and D. Marx. "Quantum nature of the hydrogen bond from ambient conditions down to ultra-low temperatures". In: *Phys. Chem. Chem. Phys.* 21.45 (2019), pp. 24967–24975. URL: https://doi.org/10.1039/c9cp04795f (cit. on p. 3).

[20] D. M. Wilkins et al. "Nuclear Quantum Effects in Water Reorientation and Hydrogen-Bond Dynamics". In: *J. Phys. Chem. Lett.* 8.12 (2017), pp. 2602–2607. URL: https://doi.org/10.1021/acs.jpclett.7b00979 (cit. on p. 3).

[21] M. Ceriotti et al. "Nuclear quantum effects and hydrogen bond fluctuations in water". In: *PNAS* 110.39 (2013), pp. 15591–15596. URL: https://doi.org/10.1073/pnas.1308560110 (cit. on p. 3).

[22] T. Clark, J. Heske, and T. D. Kühne. "Opposing Electronic and Nuclear Quantum Effects on Hydrogen Bonds in H2O and D2O". In: *Chemphyschem* 20.19 (2019), pp. 2461–2465. URL: https://doi.org/10.1002/cphc.201900839 (cit. on p. 3).

[23] A. Jing, K. Szalewicz, and A. van der Avoird. "Ammonia dimer: extremely fluxional but still hydrogen bonded". In: *Nat. Comm.* 13.1 (2022). URL: https://doi.org/10.1038/s41467-022-28862-z (cit. on p. 3).

[24] T. Meier et al. "Observation of nuclear quantum effects and hydrogen bond symmetrisation in high pressure ice". In: *Nat. Comm.* 9.1 (2018). URL: https://doi.org/10.1038/s41467-018-05164-x (cit. on p. 3).

[25] J. E. Bertie and J. P. Devlin. "Unusual proton transfer patterns in crystalline ammonia hemihydrate (2NH3·H2O)". In: *J. Chem. Phys.* 78.10 (1983), pp. 6203–6208. URL: https://doi.org/10.1063/1.444584 (cit. on p. 3).

[26] C. Drechsel-Grau and D. Marx. "Collective proton transfer in ordinary ice: local environments, temperature dependence and deuteration effects". In: *Phys. Chem. Chem. Phys.* 19.4 (2017), pp. 2623–2635. URL: https://doi.org/10.1039/c6cp05679b (cit. on p. 3).

[27] A. Cahlik et al. "Significance Of Nuclear Quantum Effects In Hydrogen Bonded Molecular Chains". In: *ACS Nano* 15.6 (2021), pp. 10357–10365. URL: https://doi.org/10.1021/acsnano.1c02572 (cit. on p. 3).

[28] K. Liang and A. Nowick. "High-temperature protonic conduction in mixed perovskite ceramics". In: *Solid State Ion.* 61.1-3 (1993), pp. 77–81. URL: https://linkinghub.elsevier.com/retrieve/pii/0167273893903373 (cit. on p. 3).

[29] S. Naito et al. "Isotope effect in the diffusion of hydrogen and deuterium in titanium, Ti88Al12 and Ti3Al". In: *J. Chem. Soc. Faraday Trans.* 92 (1996), pp. 3407–3410 (cit. on pp. 3, 70).

[30] W. Grochala and P. P. Edwards. "Thermal Decomposition of the Non-Interstitial Hydrides for the Storage and Production of Hydrogen". In: *Chem. Rev.* 104.3 (2004), pp. 1283–1316. URL: https://pubs.acs.org/doi/10.1021/cr030691s (cit. on p. 3).

[31] K. D. Kreuer et al. "Transport in Proton Conductors for Fuel-Cell Applications: Simulations, Elementary Reactions, and Phenomenology". In: *Chem. Rev.* 104.10 (2004), pp. 4637–4678. URL: https://pubs.acs.org/doi/10.1021/cr020715f (cit. on p. 3).

[32] M. F. A. Kamaroddin et al. "Membrane-Based Electrolysis for Hydrogen Production: A Review". In: *Membranes* 11.11 (2021), p. 810. URL: https://doi.org/10.3390/membranes11110810 (cit. on p. 3).

[33] M. Rossi, M. Ceriotti, and D. E. Manolopoulos. "Nuclear Quantum Effects in H^+ and OH^- Diffusion along Confined Water Wires". In: *J. Phys. Chem. Lett.* 7.15 (2016), pp. 3001–3007. URL: https://pubs.acs.org/doi/10.1021/acs.jpclett.6b01093 (cit. on pp. 3, 29).

[34] D. Emin. "Phonon-assisted transition rates I. Optical-phonon-assisted hopping in solids". In: *Adv. Phys.* 24.3 (1975), pp. 305–348. URL: https://doi.org/10.1080/00018737500101411 (cit. on pp. 4, 71).

[35] H. Y. Geng, Q. Wu, and Y. Sun. "Prediction of a Mobile Solid State in Dense Hydrogen under High Pressures". In: *J. Phys. Chem. Lett.* 8.1 (2016), pp. 223–228. URL: https://doi.org/10.1021/acs.jpclett.6b02453 (cit. on p. 4).

[36] Y. Wang et al. "High pressure partially ionic phase of water ice". In: *Nat. Comm.* 2.1 (2011). URL: https://doi.org/10.1038/ncomms1566 (cit. on p. 4).

[37] M. Millot et al. "Nanosecond X-ray diffraction of shock-compressed superionic water ice". In: *Nature* 569.7755 (2019), pp. 251–255. URL: https://doi.org/10.1038/s41586-019-1114-6 (cit. on p. 4).

[38] S. Ninet, F. Datchi, and A. M. Saitta. "Proton Disorder and Superionicity in Hot Dense Ammonia Ice". In: *Phys. Rev. Lett.* 108 (16 2012), p. 165702. URL: https://link.aps.org/doi/10.1103/PhysRevLett.108.165702 (cit. on pp. 4, 6, 106).

[39] V. N. Robinson and A. Hermann. "Plastic and superionic phases in ammonia–water mixtures at high pressures and temperatures". In: *J. Phys.: Condens. Matter* 32.18 (2020), p. 184004. URL: https://dx.doi.org/10.1088/1361-648X/ab68f7 (cit. on pp. 4, 7, 116, 141).

[40] M. Caussé, G. Geneste, and P. Loubeyre. "Superionicity of $H^{\delta+}$ in LaH_{10} superhydride". In: *Phys. Rev. B* 107.6 (2023). URL: https://doi.org/10.1103/physrevb.107.l060301 (cit. on p. 4).

[41] . J. E. Rettie et al. "A two-dimensional type I superionic conductor". In: *Nat. Mater.* 20.12 (2021), pp. 1683–1688. URL: https://doi.org/10.1038/s41563-021-01053-9 (cit. on p. 4).

[42] J. S. Loveday and R. J. Nelmes. "The ammonia hydrates—model mixed-hydrogen-bonded systems". In: *High Press. Res.* 24.1 (2004), pp. 45–55. URL: https://doi.org/10.1080/08957950410001661990 (cit. on pp. 4, 7).

[43] A. D. Fortes and M. Choukroun. "Phase Behaviour of Ices and Hydrates". In: *Space Sci. Rev.* 153.1-4 (2010), pp. 185–218. URL: https://doi.org/10.1007/s11214-010-9633-3 (cit. on pp. 4, 5).

[44] Par Léon Andriambariarijaona. "Etude expérimentale des diagrammes de phase de l'hémihydrate et du dihydrate d'ammoniac sous haute pression". In: (2021), p. 202 (cit. on pp. 5, 7, 8, 82, 83, 87–92, 120, 122, 129–132, 134, 137).

[45] J. I. Lunine and D. J. Stevenson. "Clathrate and ammonia hydrates at high pressure: Application to the origin of methane on Titan". In: *Icarus* 70.1 (1987), pp. 61–77. URL: https://doi.org/10.1016/0019-1035(87)90075-3 (cit. on p. 4).

[46] F. Hersant, D. Gautier, and J.I. Lunine. "Enrichment in volatiles in the giant planets of the Solar System". In: *Planet. Space Sci.* 52.7 (2004), pp. 623–641. URL: https://doi.org/10.1016/j.pss.2003.12.011 (cit. on p. 4).

[47] Y. Alibert and O. Mousis. "Formation of Titan in Saturn's subnebula: constraints from *Huygens* probe measurements". In: *Astron. Astrophys.* 465.3 (2007), pp. 1051–1060. URL: https://doi.org/10.1051/0004-6361:20066402 (cit. on p. 4).

[48] S. Stanley and J. Bloxham. "Convective-region geometry as the cause of Uranus' and Neptune's unusual magnetic fields". In: *Nature* 428.6979 (2004), pp. 151–153. URL: https://doi.org/10.1038/nature02376 (cit. on p. 4).

[49] W. B. Hubbard. "Interiors of the Giant Planets". In: *Science* 214.4517 (1981), pp. 145–149. URL: https://doi.org/10.1126/science.214.4517.145 (cit. on p. 5).

[50] C. Cavazzoni et al. "Superionic and Metallic States of Water and Ammonia at Giant Planet Conditions". In: *Science* 283.5398 (1999), pp. 44–46. URL: https://doi.org/10.1126/science.283.5398.44 (cit. on pp. 5, 6).

[51] T. Guillot. "THE INTERIORS OF GIANT PLANETS: Models and Outstanding Questions". In: *Annu. Rev. Earth. Plan. Sci.* 33.1 (2005), pp. 493–530. URL: https://doi.org/10.1146/annurev.earth.32.101802.120325 (cit. on p. 5).

[52] A. D. Fortes et al. “The high-pressure phase diagram of ammonia dihydrate”. In: *High Press. Res.* 27.2 (2007), pp. 201–212. URL: https://doi.org/10.1080/08957950701265029 (cit. on p. 5).

[53] J. S. Loveday et al. “Observation of ammonia dihydrate in the AMH-VI structure at room temperature – possible implications for the outer solar system”. In: *High Press. Res.* 29.3 (2009), pp. 396–404. URL: https://doi.org/10.1080/08957950903162057 (cit. on pp. 5–7).

[54] C. W. Wilson et al. “Pressure-induced dehydration and the structure of ammonia hemihydrate-II”. In: *J. Chem. Phys.* 136.9 (2012), p. 094506. URL: https://doi.org/10.1063/1.3686870 (cit. on pp. 5, 7, 83–85, 87, 91, 93, 101, 102, 118, 121, 122, 131).

[55] X. Li et al. “High-pressure phase stability and elasticity of ammonia hydrate”. In: *Am. Min.* 104.9 (2019), pp. 1307–1314. URL: https://doi.org/10.2138/am-2019-7057 (cit. on p. 5).

[56] H. Zhang et al. “Melting curve and phase diagram of ammonia monohydrate at high pressure and temperature”. In: *J. Chem. Phys.* 153.15 (2020), p. 154503. URL: https://doi.org/10.1063/5.0021207 (cit. on p. 5).

[57] H. Zhang et al. “Observation of a Plastic Crystal in Water–Ammonia Mixtures under High Pressure and Temperature”. In: *J. Phys. Chem. Lett.* 14.9 (2023), pp. 2301–2307. URL: https://doi.org/10.1021/acs.jpclett.3c00092 (cit. on pp. 6, 7, 106, 111).

[58] J. N. Sherwood. *The plastically crystalline state*. John Wiley and Sons, 1979. ISBN: 10:0471997153 (cit. on pp. 6, 122, 141).

[59] J. Timmermans. “Plastic crystals: A historical review”. In: *J. Phys. Chem. Solids* 18.1 (1961), pp. 1–8. URL: https://doi.org/10.1016/0022-3697(61)90076-2 (cit. on p. 6).

[60] E. Hampton, N.C. Lockhart, and J.N. Sherwood. “Temperature dependence of self-diffusion in adamantane”. In: *Chem. Phys. Lett.* 21.1 (1973), pp. 191–193. URL: https://doi.org/10.1016/0009-2614(73)80046-6 (cit. on p. 6).

[61] A. V. Chadwick et al. “Molecular reorientation and self-diffusion in the plastic solid hexamethyldisilane studied using nuclear magnetic resonance and radiotracer techniques”. In: *J. Chem. Soc. Faraday Trans.* 71.0 (1975), p. 1610. URL: https://doi.org/10.1039/f19757101610 (cit. on p. 6).

[62] J. M. Pringle et al. “Organic ionic plastic crystals: recent advances”. In: *J. Mater. Chem.* 20.11 (2010), p. 2056. URL: https://doi.org/10.1039/b920406g (cit. on p. 6).

[63] P. J. Alarco et al. “The plastic-crystalline phase of succinonitrile as a universal matrix for solid-state ionic conductors”. In: *Nat. Mater.* 3.7 (2004), pp. 476–481. URL: https://doi.org/10.1038/nmat1158 (cit. on p. 6).

[64] Y. Takii, K. Koga, and H. Tanaka. “A plastic phase of water from computer simulation”. In: *J. Chem. Phys.* 128.20 (2008). URL: https://doi.org/10.1063/1.2927255 (cit. on p. 6).

[65] J. L. Aragones and C. Vega. "Plastic crystal phases of simple water models". In: *J. Chem. Phys.* 130.24 (2009). URL: https://doi.org/10.1063/1.3156856 (cit. on p. 6).

[66] A. Toffano et al. "Temperature- and pressure-dependence of the hydrogen bond network in plastic ice VII". In: *J. Chem. Phys.* 157.9 (2022), p. 094502. URL: https://doi.org/10.1063/5.0111189 (cit. on pp. 6, 102).

[67] D. Prasad and N. Mitra. "High-temperature and high-pressure plastic phase of ice at the boundary of liquid water and ice VII". In: *Proc. Math. Phys. Eng. Sci. P ROY SOC A-MATH PHY* 478.2260 (2022). URL: https://doi.org/10.1098/rspa.2021.0958 (cit. on p. 6).

[68] L. E. Bove et al. "Translational and Rotational Diffusion in Water in the Gigapascal Range". In: *Phys. Rev. Lett.* 111.18 (2013). URL: https://doi.org/10.1103/physrevlett.111.185901 (cit. on p. 6).

[69] J. S. Loveday and R. J. Nelmes. "Ammonia Monohydrate VI: A Hydrogen-Bonded Molecular Alloy". In: *Phys. Rev. Lett.* 83.21 (1999), pp. 4329–4332. URL: https://doi.org/10.1103/physrevlett.83.4329 (cit. on pp. 6, 7).

[70] C. W. Wilson et al. "On the stability of the disordered molecular alloy phase of ammonia hemihydrate". In: *J. Chem. Phys.* 142.9 (2015), p. 094707. URL: https://doi.org/10.1063/1.4913684 (cit. on pp. 7, 89, 132, 141).

[71] C. Ma et al. "Ammonia molecule rotation of pressure-induced phase transition in ammonia hemihydrates 2NH3·H2O". In: *RSC Adv.* 2.11 (2012), p. 4920. URL: https://doi.org/10.1039/c2ra01156e (cit. on pp. 7, 132).

[72] C. Liu et al. "Topologically frustrated ionisation in a water-ammonia ice mixture". In: *Nat. Comm.* 8.1 (2017). URL: https://doi.org/10.1038/s41467-017-01132-z (cit. on p. 7).

[73] L. Andriambariarijaona et al. *High pressure-temperature phase diagram of ammonia hemihydrate.* 2023. URL: https://arxiv.org/abs/2307.09838 (cit. on pp. 7, 8, 82, 83, 87–92, 120, 122, 129–132, 137, 141).

[74] V. N. Robinson et al. "Stabilization of ammonia-rich hydrate inside icy planets". In: *PNAS* 114.34 (2017), pp. 9003–9008. URL: https://doi.org/10.1073/pnas.1706244114 (cit. on pp. 7, 141).

[75] V. N. Robinson et al. "Novel phases in ammonia-water mixtures under pressure". In: *J. Chem. Phys.* 149.23 (2018), p. 234501. URL: https://doi.org/10.1063/1.5063569 (cit. on pp. 7, 141).

[76] S. Huppert et al. "Simulation of Nuclear Quantum Effects in Condensed Matter Systems via Quantum Baths". In: *App. Sci.* 12.9 (2022), p. 4756. URL: https://doi.org/10.3390/app12094756 (cit. on pp. 8, 18, 25, 41, 47, 85).

[77] F. Brieuc, H. Dammak, and M. Hayoun. "Quantum Thermal Bath for Path Integral Molecular Dynamics Simulation". In: *J. Chem. Theory. Comp.* 12.3 (2016), pp. 1351–1359. URL: https://doi.org/10.1021/acs.jctc.5b01146 (cit. on pp. 8, 37–39).

[78] M. Born and R. Oppenheimer. “Zur Quantentheorie der Molekeln”. In: *Ann. Phys.* 389.20 (1927), pp. 457–484. URL: https://onlinelibrary.wiley.com/doi/abs/10.1002/andp.19273892002 (cit. on p. 13).

[79] D. Marx and J. Hutter. *Ab Initio Molecular Dynamics*. 2009. URL: https://doi.org/10.1017/cbo9780511609633 (cit. on p. 14).

[80] S. Lower and T. Neils. “The Potential-Energy Surface Can Be Calculated Using Quantum Mechanics”. In: (2014). URL: https://chem.libretexts.org/@go/page/14571?pdf (cit. on p. 15).

[81] R. J. Bartlett and G. D. Purvis. “Many-body perturbation theory, coupled-pair many-electron theory, and the importance of quadruple excitations for the correlation problem”. In: *Int. J. Quant. Chem.* 14.5 (Nov. 1978), pp. 561–581. DOI: 10.1002/qua.560140504. URL: https://doi.org/10.1002/qua.560140504 (cit. on p. 15).

[82] W. Kohn and L. J. Sham. “Self-Consistent Equations Including Exchange and Correlation Effects”. In: *Phys. Rev.* 140 (4A 1965), A1133–A1138. URL: https://link.aps.org/doi/10.1103/PhysRev.140.A1133 (cit. on p. 15).

[83] P. Hohenberg and W. Kohn. “Inhomogeneous Electron Gas”. In: *Phys. Rev.* 136 (3B 1964), B864–B871. URL: https://link.aps.org/doi/10.1103/PhysRev.136.B864 (cit. on p. 15).

[84] T. Plé et al. “Routine Molecular Dynamics Simulations Including Nuclear Quantum Effects: From Force Fields to Machine Learning Potentials”. In: *J. Chem. Theory. Comp.* 19.5 (2023), pp. 1432–1445. URL: https://doi.org/10.1021/acs.jctc.2c01233 (cit. on pp. 15–17, 85).

[85] T. Jaffrelot Inizan et al. “High-resolution mining of the SARS-CoV-2 main protease conformational space: supercomputer-driven unsupervised adaptive sampling”. In: *Chem. Sci.* 12.13 (2021), pp. 4889–4907. URL: https://doi.org/10.1039/d1sc00145k (cit. on pp. 15, 17).

[86] K. Vanommeslaeghe, O. Guvench, and A. D. MacKerell. “Molecular Mechanics”. In: *Curr. Pharm. Des.* 20.20 (2014), pp. 3281–3292. URL: https://doi.org/10.2174/13816128113199990600 (cit. on p. 15).

[87] J. Wang et al. “Development and testing of a general amber force field”. In: *J. Comput. Chem.* 25.9 (2004), pp. 1157–1174. URL: https://doi.org/10.1002/jcc.20035 (cit. on p. 16).

[88] W. L. Jorgensen and J. Tirado-Rives. “The OPLS [optimized potentials for liquid simulations] potential functions for proteins, energy minimizations for crystals of cyclic peptides and crambin”. In: *J. Am. Chem. Soc.* 110.6 (1988), pp. 1657–1666. URL: https://doi.org/10.1021/ja00214a001 (cit. on pp. 16, 86).

[89] J. Huang et al. “CHARMM36m: an improved force field for folded and intrinsically disordered proteins”. In: *Nature Meth.* 14.1 (2016), pp. 71–73. URL: https://doi.org/10.1038/nmeth.4067 (cit. on p. 16).

[90] Z. Jing et al. "Polarizable Force Fields for Biomolecular Simulations: Recent Advances and Applications". In: *Annu. Rev. Biophys.* 48.1 (2019), pp. 371–394. URL: https://doi.org/10.1146/annurev-biophys-070317-033349 (cit. on p. 16).

[91] J. W. Ponder et al. "Current Status of the AMOEBA Polarizable Force Field". In: *J. Phys. Chem. B* 114.8 (2010), pp. 2549–2564. URL: https://doi.org/10.1021/jp910674d (cit. on p. 16).

[92] V. L. Deringer, M. A. Caro, and G. Csányi. "Machine Learning Interatomic Potentials as Emerging Tools for Materials Science". In: *Adv. Mater.* 31.46 (2019), p. 1902765. URL: https://doi.org/10.1002/adma.201902765 (cit. on p. 16).

[93] J. Behler. "Four Generations of High-Dimensional Neural Network Potentials". In: *Chem. Rev.* 121.16 (2021), pp. 10037–10072. URL: https://doi.org/10.1021/acs.chemrev.0c00868 (cit. on p. 16).

[94] W. L. Jorgensen, D. S. Maxwell, and J. Tirado-Rives. "Development and Testing of the OPLS All-Atom Force Field on Conformational Energetics and Properties of Organic Liquids". In: *J. Am. Chem. Soc.* 118.45 (1996), pp. 11225–11236. URL: https://doi.org/10.1021/ja9621760 (cit. on pp. 16, 86).

[95] Y. Wu, H. L. Tepper, and G. A. Voth. "Flexible simple point-charge water model with improved liquid-state properties". In: *J. Chem. Phys.* 124.2 (2006), p. 024503. URL: https://doi.org/10.1063/1.2136877 (cit. on pp. 16, 86).

[96] F. Paesani et al. "An accurate and simple quantum model for liquid water". In: *J. Chem. Phys.* 125.18 (2006), p. 184507. URL: https://doi.org/10.1063/1.2386157 (cit. on pp. 16, 86, 116).

[97] L. Lagardère et al. "Tinker-HP: a massively parallel molecular dynamics package for multiscale simulations of large complex systems with advanced point dipole polarizable force fields". In: *Chem. Sci.* 9 (4 2018), pp. 956–972. URL: http://dx.doi.org/10.1039/C7SC04531J (cit. on pp. 16, 85).

[98] D. S. Coombes et al. "Role of Electrostatic Interactions in Determining the Crystal Structures of Polar Organic Molecules. A Distributed Multipole Study". In: *J. Phys. Chem.* 100.18 (1996), pp. 7352–7360. URL: https://doi.org/10.1021/jp960333b (cit. on p. 17).

[99] R. C. Rizzo and W. L. Jorgensen. "OPLS All-Atom Model for Amines: Resolution of the Amine Hydration Problem". In: *J. Am. Chem. Soc.* 121.20 (1999), pp. 4827–4836. URL: https://doi.org/10.1021/ja984106u (cit. on pp. 17, 86).

[100] C. Caleman et al. "Force Field Benchmark of Organic Liquids: Density, Enthalpy of Vaporization, Heat Capacities, Surface Tension, Isothermal Compressibility, Volumetric Expansion Coefficient, and Dielectric Constant". In: *J. Chem. Theory. Comp.* 8.1 (2011), pp. 61–74. URL: https://doi.org/10.1021/ct200731v (cit. on p. 17).

[101] M. J. Robertson et al. "Development and Testing of the OPLS-AA/M Force Field for RNA". In: *J. Chem. Theory. Comp.* 15.4 (2019), pp. 2734–2742. URL: https://doi.org/10.1021/acs.jctc.9b00054 (cit. on p. 17).

[102] W. L. Jorgensen and P. Schyman. "Treatment of Halogen Bonding in the OPLS-AA Force Field: Application to Potent Anti-HIV Agents". In: *J. Chem. Theory. Comp.* 8.10 (2012), pp. 3895–3901. URL: https://doi.org/10.1021/ct300180w (cit. on p. 17).

[103] T. Lewis-Atwell, P. A. Townsend, and M. N. Grayson. "Comparing the Performances of Force Fields in Conformational Searching of Hydrogen-Bond-Donating Catalysts". In: *J. Org. Chem.* 87.9 (2022), pp. 5703–5712. URL: https://doi.org/10.1021/acs.joc.2c00066 (cit. on p. 17).

[104] J.S. Medina et al. "Molecular dynamics simulations of rigid and flexible water models: Temperature dependence of viscosity". In: *Chem. Phys.* 388.1-3 (2011), pp. 9–18. URL: https://doi.org/10.1016/j.chemphys.2011.07.001 (cit. on p. 17).

[105] G. Raabe and R. J. Sadus. "Molecular dynamics simulation of the dielectric constant of water: The effect of bond flexibility". In: *J. Chem. Phys.* 134.23 (2011). URL: https://doi.org/10.1063/1.3600337 (cit. on p. 17).

[106] Z. A. Piskulich and W. H. Thompson. "Examining the Role of Different Molecular Interactions on Activation Energies and Activation Volumes in Liquid Water". In: *J. Chem. Theory. Comp.* 17.5 (2021), pp. 2659–2671. URL: https://doi.org/10.1021/acs.jctc.0c01217 (cit. on p. 17).

[107] Z. Jiao et al. "Effect of model flexibility on the behavior of supercritical water in molecular dynamics simulation". In: *J. Mol. Liq.* 382 (2023), p. 121997. URL: https://doi.org/10.1016/j.molliq.2023.121997 (cit. on p. 17).

[108] V. Prasad K. et al. "Water desalination using graphene nanopores: influence of the water models used in simulations". In: *Phys. Chem. Chem. Phys.* 20.23 (2018), pp. 16005–16011. URL: https://doi.org/10.1039/c8cp00919h (cit. on p. 17).

[109] Gustav-Stresemann-Institut e.V. für Übernationale Bildung und Europäische Zusammenarbeit et al., eds. *Computational soft matter: from synthetic polymers to proteins; Winter School, 29 February - 6 March 2004, Gustav-Stresemann-Institut, Bonn, Germany. 2: Lecture notes.* 23. 2004 (cit. on p. 17).

[110] H. D. Meyer, U. Manthe, and L.S. Cederbaum. "The multi-configurational time-dependent Hartree approach". In: *Chem. Phys. Lett.* 165.1 (1990), pp. 73–78. URL: https://doi.org/10.1016/0009-2614(90)87014-i (cit. on p. 17).

[111] S. Habershon et al. "Ring-Polymer Molecular Dynamics: Quantum Effects in Chemical Dynamics from Classical Trajectories in an Extended Phase Space". In: *Annu. Rev. Phys. Chem.* 64.1 (2013), pp. 387–413. URL: http://www.annualreviews.org/doi/10.1146/annurev-physchem-040412-110122 (cit. on pp. 18, 29).

[112] J. E. Lawrence and D. E. Manolopoulos. "Path integral methods for reaction rates in complex systems". In: *Faraday Discuss.* 221 (2020), pp. 9–29. URL: http://xlink.rsc.org/?DOI=C9FD00084D (cit. on pp. 18, 28–30, 60, 82, 116).

[113] J. Liu, D. Li, and X. Liu. "A simple and accurate algorithm for path integral molecular dynamics with the Langevin thermostat". In: *J. Chem. Phys.* 145.2 (2016), p. 024103. URL: http://aip.scitation.org/doi/10.1063/1.4954990 (cit. on pp. 18, 29).

[114] J. Cao and G. A. Voth. "The formulation of quantum statistical mechanics based on the Feynman path centroid density. III. Phase space formalism and analysis of centroid molecular dynamics". In: *J. Chem. Phys.* 101.7 (1994), pp. 6157–6167. URL: http://aip.scitation.org/doi/10.1063/1.468503 (cit. on pp. 18, 29).

[115] A. Witt et al. "On the applicability of centroid and ring polymer path integral molecular dynamics for vibrational spectroscopy". In: *J. Chem. Phys.* 130.19 (2009), p. 194510. URL: http://aip.scitation.org/doi/10.1063/1.3125009 (cit. on pp. 18, 29).

[116] F. Brieuc et al. "Zero-Point Energy Leakage in Quantum Thermal Bath Molecular Dynamics Simulations". In: *J. Chem. Theory. Comp.* 12.12 (2016), pp. 5688–5697. URL: https://pubs.acs.org/doi/10.1021/acs.jctc.6b00684 (cit. on pp. 18, 34, 35, 61).

[117] E. Mangaud et al. "The Fluctuation–Dissipation Theorem as a Diagnosis and Cure for Zero-Point Energy Leakage in Quantum Thermal Bath Simulations". In: *J. Chem. Theory. Comp.* 15.5 (2019), pp. 2863–2880. URL: https://pubs.acs.org/doi/10.1021/acs.jctc.8b01164 (cit. on pp. 18, 34–37, 82, 116).

[118] N. Mauger et al. "Nuclear Quantum Effects in Liquid Water at Near Classical Computational Cost Using the Adaptive Quantum Thermal Bath". In: *J. Phys. Chem. Lett.* 12.34 (2021), pp. 8285–8291. URL: https://doi.org/10.1021/acs.jpclett.1c01722 (cit. on pp. 18, 37, 62, 69, 85, 86, 116).

[119] N. Mauger et al. "Improving Condensed-Phase Water Dynamics with Explicit Nuclear Quantum Effects: The Polarizable Q-AMOEBA Force Field". In: *J. Phys. Chem. B* 126.43 (2022), pp. 8813–8826. URL: https://doi.org/10.1021/acs.jpcb.2c04454 (cit. on pp. 18, 85, 86).

[120] W. H. Miller. "Classical S Matrix: Numerical Application to Inelastic Collisions". In: *J. Chem. Phys.* 53.9 (1970), pp. 3578–3587. URL: https://doi.org/10.1063/1.1674535 (cit. on p. 18).

[121] T. Plé et al. "Sampling the thermal Wigner density via a generalized Langevin dynamics". In: *J. Chem. Phys.* 151.11 (2019). URL: https://doi.org/10.1063/1.5099246 (cit. on p. 18).

[122] L. Verlet. "Computer "Experiments" on Classical Fluids. I. Thermodynamical Properties of Lennard-Jones Molecules". In: *Phys. Rev.* 159.1 (1967), pp. 98–103. URL: https://link.aps.org/doi/10.1103/PhysRev.159.98 (cit. on p. 19).

[123] R. Zwanzig. "Time-Correlation Functions and Transport Coefficients in Statistical Mechanics". In: *Annu. Rev. Phys. Chem.* 16.1 (1965), pp. 67–102. URL: http://www.annualreviews.org/doi/10.1146/annurev.pc.16.100165.000435 (cit. on p. 19).

[124] M.E. Tuckerman. *Statistical Mechanics: Theory and Molecular Simulation*. 2010. URL: https://books.google.fr/books?id=UMM2NAEACAAJ (cit. on pp. 19, 21, 23–25, 29, 31, 35, 42, 48).

[125] I. R. Craig and D. E. Manolopoulos. "Quantum statistics and classical mechanics: Real time correlation functions from ring polymer molecular dynamics". In: *J. Chem. Phys.* 121.8 (2004), pp. 3368–3373. URL: http://aip.scitation.org/doi/10.1063/1.1777575 (cit. on pp. 19, 29).

[126] H. J. C. Berendsen et al. "Molecular dynamics with coupling to an external bath". In: *J. Chem. Phys.* 81.8 (1984), pp. 3684–3690. URL: http://aip.scitation.org/doi/10.1063/1.448118 (cit. on p. 20).

[127] W. G. Hoover and B. L. Holian. "Kinetic moments method for the canonical ensemble distribution". In: *Phys. Lett. A* 211.5 (1996), pp. 253–257. URL: https://linkinghub.elsevier.com/retrieve/pii/0375960195009736 (visited on 10/07/2020) (cit. on p. 20).

[128] G. J. Martyna, M. L. Klein, and M. Tuckerman. "Nosé–Hoover chains: The canonical ensemble via continuous dynamics". In: *J. Chem. Phys.* 97.4 (1992), pp. 2635–2643. URL: http://aip.scitation.org/doi/10.1063/1.463940 (cit. on p. 20).

[129] H. C. Andersen. "Molecular dynamics simulations at constant pressure and/or temperature". In: *J. Chem. Phys.* 72.4 (1980), pp. 2384–2393. URL: http://aip.scitation.org/doi/10.1063/1.439486 (cit. on p. 20).

[130] G. Bussi, D. Donadio, and M. Parrinello. "Canonical sampling through velocity-rescaling". In: *J. Chem. Phys.* 126.1 (2007), p. 014101. URL: http://arxiv.org/abs/0803.4060 (cit. on p. 20).

[131] S. Nosé. "A unified formulation of the constant temperature molecular dynamics methods". In: *J. Chem. Phys.* 81.1 (1984), pp. 511–519. URL: http://aip.scitation.org/doi/10.1063/1.447334 (cit. on p. 20).

[132] D. S. Lemons and A. Gythiel. "Paul Langevin's 1908 paper "On the Theory of Brownian Motion" ["Sur la théorie du mouvement brownien," C. R. Acad. Sci. (Paris) **146** , 530–533 (1908)]". In: *Am. J. Phys.* 65.11 (1997), pp. 1079–1081. URL: http://aapt.scitation.org/doi/10.1119/1.18725 (cit. on pp. 20, 47, 49).

[133] B. Leimkuhler and C. Matthews. "Rational Construction of Stochastic Numerical Methods for Molecular Sampling". In: *App. Math. Res. eXpress* (2012), abs010. URL: https://academic.oup.com/amrx/article-lookup/doi/10.1093/amrx/abs010 (cit. on pp. 20, 21, 43).

[134] B. Leimkuhler and C. Matthews. "Robust and efficient configurational molecular sampling via Langevin dynamics". In: *J. Chem. Phys.* 138.17 (2013), p. 174102. URL: http://aip.scitation.org/doi/10.1063/1.4802990 (cit. on pp. 20, 21, 43, 86).

[135] B. Leimkuhler and C. Matthews. "Efficient molecular dynamics using geodesic integration and solvent–solute splitting". In: *Proc. Math. Phys. Eng. Sci. P ROY SOC A-MATH PHY* 472.2189 (2016), p. 20160138. URL: https://royalsocietypublishing.org/doi/10.1098/rspa.2016.0138 (cit. on pp. 20, 21, 43, 86).

[136] S. T. Huang and S. Cambanis. "Stochastic and Multiple Wiener Integrals for Gaussian Processes". In: *Ann. Probab.* 6.4 (1978). URL: https://doi.org/10.1214/aop/1176995480 (cit. on p. 21).

[137] G. J. Martyna, D. J. Tobias, and M. L. Klein. "Constant pressure molecular dynamics algorithms". In: *J. Chem. Phys.* 101.5 (1994), pp. 4177–4189. URL: https://doi.org/10.1063/1.467468 (cit. on p. 23).

[138] M. Bernetti and G. Bussi. "Pressure control using stochastic cell rescaling". In: *J. Chem. Phys.* 153.11 (2020). URL: https://doi.org/10.1063/5.0020514 (cit. on p. 23).

[139] S. E. Feller et al. "Constant pressure molecular dynamics simulation: The Langevin piston method". In: *J. Chem. Phys.* 103.11 (1995), pp. 4613–4621. URL: https://doi.org/10.1063/1.470648 (cit. on pp. 23, 86).

[140] H. C. Andersen. "Molecular dynamics simulations at constant pressure and/or temperature". In: *J. Chem. Phys.* 72.4 (1980), pp. 2384–2393. URL: https://doi.org/10.1063/1.439486 (cit. on p. 23).

[141] H. J. C. Berendsen et al. "Molecular dynamics with coupling to an external bath". In: *J. Chem. Phys.* 81.8 (1984), pp. 3684–3690. URL: https://doi.org/10.1063/1.448118 (cit. on p. 23).

[142] R. P. Feynman, Laurie M. L. M. Brown, and P. A. M. Dirac. *Feynman's thesis: a new approach to quantum theory*. 2005 (cit. on p. 25).

[143] J. E. Cohen et al. "Eigenvalue inequalities for products of matrix exponentials". In: *Linear Algebra Appl.* 45 (1982), pp. 55–95. URL: https://linkinghub.elsevier.com/retrieve/pii/0024379582902117 (cit. on pp. 25, 43).

[144] R. Achilles and A. Bonfiglioli. "The early proofs of the theorem of Campbell, Baker, Hausdorff, and Dynkin". In: *Arch. Hist. Exact Sci.* 66.3 (2012), pp. 295–358. URL: http://link.springer.com/10.1007/s00407-012-0095-8 (cit. on pp. 26, 43).

[145] S. Karsten et al. "Simulating vibronic spectra via Matsubara-like dynamics: Coping with the sign problem". In: *J. Chem. Phys.* 149.19 (2018), p. 194103. URL: http://aip.scitation.org/doi/10.1063/1.5046874 (cit. on p. 26).

[146] G. C. Wick. "Properties of Bethe-Salpeter Wave Functions". In: *Phys. Rev.* 96.4 (1954), pp. 1124–1134. URL: https://link.aps.org/doi/10.1103/PhysRev.96.1124 (cit. on p. 27).

[147] D. Chandler and P. G. Wolynes. "Exploiting the isomorphism between quantum theory and classical statistical mechanics of polyatomic fluids". In: *J. Chem. Phys.* 74.7 (1981), pp. 4078–4095. URL: https://doi.org/10.1063/1.441588 (cit. on p. 27).

[148] M. Parrinello and A. Rahman. "Study of an F center in molten KCl". In: *J. Chem. Phys.* 80.2 (1984), pp. 860–867. URL: https://doi.org/10.1063/1.446740 (cit. on p. 27).

[149] B J Berne and D Thirumalai. "On the Simulation of Quantum Systems: Path Integral Methods". In: *Annu. Rev. Phys. Chem.* 37.1 (1986), pp. 401–424. URL: https://doi.org/10.1146/annurev.pc.37.100186.002153 (cit. on p. 27).

[150] M. Ceriotti, D. E. Manolopoulos, and M. Parrinello. "Accelerating the convergence of path integral dynamics with a generalized Langevin equation". In: *J. Chem. Phys.* 134.8 (2011). URL: https://doi.org/10.1063/1.3556661 (cit. on pp. 28, 39, 40).

[151] M. Ceriotti and D. E. Manolopoulos. "Efficient First-Principles Calculation of the Quantum Kinetic Energy and Momentum Distribution of Nuclei". In: *Phys. Rev. Lett.* 109.10 (2012). URL: https://doi.org/10.1103/physrevlett.109.100604 (cit. on pp. 28, 37).

[152] W. H. Miller. "The Semiclassical Initial Value Representation: A Potentially Practical Way for Adding Quantum Effects to Classical Molecular Dynamics Simulations". In: *J. Phys. Chem. A* 105.13 (2001), pp. 2942–2955. URL: https://pubs.acs.org/doi/10.1021/jp003712k (visited on 10/09/2020) (cit. on p. 29).

[153] Mariana Rossi, Michele Ceriotti, and David E. Manolopoulos. "How to remove the spurious resonances from ring polymer molecular dynamics". In: *J. Chem. Phys.* 140.23 (2014). URL: https://doi.org/10.1063/1.4883861 (cit. on p. 29).

[154] R. Kubo. "The fluctuation-dissipation theorem". In: (1966), p. 31 (cit. on pp. 29, 34, 35, 48).

[155] M. F. Herman, E. J. Bruskin, and B. J. Berne. "On path integral Monte Carlo simulations". In: *J. Chem. Phys.* 76.10 (1982), pp. 5150–5155. URL: https://doi.org/10.1063/1.442815 (cit. on p. 31).

[156] Dominik Marx and Michele Parrinello. "Ab initio path integral molecular dynamics: Basic ideas". In: *J. Chem. Phys.* 104.11 (1996), pp. 4077–4082. URL: https://doi.org/10.1063/1.471221 (cit. on p. 31).

[157] M. Ceriotti, J. More, and D. E. Manolopoulos. "i-PI: A Python interface for ab initio path integral molecular dynamics simulations". In: *Comput. Phys. Commun.* 185.3 (2014), pp. 1019–1026. URL: https://doi.org/10.1016/j.cpc.2013.10.027 (cit. on pp. 32, 86).

[158] M. Ceriotti et al. "Efficient stochastic thermostatting of path integral molecular dynamics". In: *J. Chem. Phys.* 133.12 (2010), p. 124104. URL: http://aip.scitation.org/doi/10.1063/1.3489925 (cit. on p. 32).

[159] H. Dammak et al. "Quantum Thermal Bath for Molecular Dynamics Simulation". In: *Phys. Rev. Lett.* 103.19 (2009), p. 190601. URL: https://link.aps.org/doi/10.1103/PhysRevLett.103.190601 (cit. on pp. 32, 35, 62, 63).

[160] M. Ceriotti, G. Bussi, and M. Parrinello. "Nuclear Quantum Effects in Solids Using a Colored-Noise Thermostat". In: *Phys. Rev. Lett.* 103.3 (2009), p. 030603. URL: https://link.aps.org/doi/10.1103/PhysRevLett.103.030603 (cit. on p. 32).

[161] M. Ceriotti, G. Bussi, and M. Parrinello. "Colored-Noise Thermostats à la Carte". In: *J. Chem. Theory. Comp.* 6.4 (2010), pp. 1170–1180. URL: https://pubs.acs.org/doi/10.1021/ct900563s (cit. on p. 32).

[162] J. Łuczka. "Non-Markovian stochastic processes: Colored noise". In: *Chaos* 15.2 (2005). URL: https://doi.org/10.1063/1.1860471 (cit. on p. 34).

[163] H. Dammak et al. "Isotope effects in lithium hydride and lithium deuteride crystals by molecular dynamics simulations". In: *J. Phys.: Condens. Matter* 24.43 (2012), p. 435402. URL: https://iopscience.iop.org/article/10.1088/0953-8984/24/43/435402 (cit. on pp. 35, 70).

[164] Y. Bronstein, P. Depondt, and F. Finocchi. "Thermal and nuclear quantum effects in the hydrogen bond dynamical symmetrization phase transition of δ-AlOOH". In: *EJM* 29.3 (2017), pp. 385–395. URL: https://doi.org/10.1127/ejm/2017/0029-2628 (cit. on p. 35).

[165] F. Calvo, C. Falvo, and P. Parneix. "Atomistic Modeling of Vibrational Action Spectra in Polyatomic Molecules: Nuclear Quantum Effects". In: *J. Phys. Chem. A* 118.29 (2014), pp. 5427–5436. URL: https://doi.org/10.1021/jp5040147 (cit. on p. 35).

[166] W. H. Miller, W. L. Hase, and C. L. Darling. "A simple model for correcting the zero point energy problem in classical trajectory simulations of polyatomic molecules". In: *J. Chem. Phys.* 91.5 (1989), pp. 2863–2868. URL: https://doi.org/10.1063/1.456956 (cit. on p. 35).

[167] S. Habershon and D. E. Manolopoulos. "Zero point energy leakage in condensed phase dynamics: An assessment of quantum simulation methods for liquid water". In: *J. Chem. Phys.* 131.24 (2009). URL: https://doi.org/10.1063/1.3276109 (cit. on p. 35).

[168] O. N. Bedoya-Martinez, J. L. Barrat, and D. Rodney. "Computation of the thermal conductivity using methods based on classical and quantum molecular dynamics". In: *Phys. Rev. B* 89.1 (2014). URL: https://doi.org/10.1103/physrevb.89.014303 (cit. on p. 35).

[169] J. Hernández-Rojas, F. Calvo, and E. Gonzalez Noya. "Applicability of Quantum Thermal Baths to Complex Many-Body Systems with Various Degrees of Anharmonicity". In: *J. Chem. Theory. Comp.* 11.3 (2015), pp. 861–870. URL: https://doi.org/10.1021/ct500678z (cit. on pp. 35, 37).

[170] N. Pottier. *Physique statistique hors d'équilibre: processus irréversibles linéaires*. 2007. URL: https://books.google.fr/books?id=OY3JzcPOqu0C (cit. on pp. 35, 43).

[171] H. B. Callen and T. A. Welton. "Irreversibility and Generalized Noise". In: *Phys. Rev.* 83.1 (1951), pp. 34–40. URL: https://link.aps.org/doi/10.1103/PhysRev.83.34 (cit. on p. 36).

[172] W. C. Swope et al. "A computer simulation method for the calculation of equilibrium constants for the formation of physical clusters of molecules: Application to small water clusters". In: *J. Chem. Phys.* 76.1 (1982), pp. 637–649. URL: http://aip.scitation.org/doi/10.1063/1.442716 (cit. on p. 43).

[173] R. Dupuis et al. "Quantum Nuclear Dynamics of Protons within Layered Hydroxides at High Pressure". In: *Sci. Rep.* 7.1 (2017), p. 4842. URL: http://www.nature.com/articles/s41598-017-04080-2 (cit. on p. 47).

[174] A. Einstein. "Über die von der molekularkinetischen Theorie der Wärme geforderte Bewegung von in ruhenden Flüssigkeiten suspendierten Teilchen". In: *Ann. Phys.* 322.8 (1905), pp. 549–560. URL: http://doi.wiley.com/10.1002/andp.19053220806 (cit. on p. 47).

[175] J. Perrin. *Brownian Movement and Molecular Reality*. 1910. URL: https://books.google.fr/books?id=eARJAAAAIAAJ (cit. on p. 47).

[176] J. L. Garcia-Palacios. "Introduction to the theory of stochastic processes and Brownian motion problems". In: *arXiv:cond-mat/0701242* (2007). URL: http://arxiv.org/abs/cond-mat/0701242 (cit. on p. 48).

[177] S. Arrhenius. "On the reaction rate of the inversion of non-refined sugar upon souring". In: *Z. Phys. Chem. 4* (1889), pp. 226–248 (cit. on p. 50).

[178] K. Laidler. "Chemical Kinetics". In: *Comprehensive Enzyme Kinetics*. 1987, pp. 11–30. URL: https://doi.org/10.1007/0-306-48390-4_2 (cit. on p. 50).

[179] J. L. Bao and D. G. Truhlar. "Variational transition state theory: theoretical framework and recent developments". In: *Chem. Soc. Rev.* 46.24 (2017), pp. 7548–7596. URL: https://doi.org/10.1039/c7cs00602k (cit. on p. 50).

[180] J. O. Richardson. "Ring-polymer instanton theory". In: *Int. Rev. Phys. Chem* . 37.2 (2018), pp. 171–216. URL: https://doi.org/10.1080/0144235x.2018.1472353 (cit. on p. 60).

[181] J. O. Richardson and S. C. Althorpe. "Ring-polymer molecular dynamics rate-theory in the deep-tunneling regime: Connection with semiclassical instanton theory". In: *J. Chem. Phys.* 131.21 (2009). URL: https://doi.org/10.1063/1.3267318 (cit. on p. 60).

[182] F. Angiolari, Simon Huppert, and Riccardo Spezia. "Quantum *versus* classical unimolecular fragmentation rate constants and activation energies at finite temperature from direct dynamics simulations". In: *Phys. Chem. Chem. Phys.* 24.48 (2022), pp. 29357–29370. URL: https://doi.org/10.1039/d2cp03809a (cit. on p. 65).

[183] O. May, J. Fedor, and M. Allan. "Isotope effect in dissociative electron attachment cross sections in acetylene". In: *J. Phys.: Conf. Ser.* 194.5 (2009), p. 052006. URL: https://iopscience.iop.org/article/10.1088/1742-6596/194/5/052006 (cit. on p. 70).

[184] E. Fallacara et al. "Thermal and Nuclear Quantum Effects at the Antiferroelectric to Paraelectric Phase Transition in KOH and KOD Crystals". In: *J. Phys. Chem. C* 125.40 (2021), pp. 22328–22334. URL: https://doi.org/10.1021/acs.jpcc.1c06953 (cit. on p. 70).

[185] S. Schaack et al. "When Quantum Fluctuations Meet Structural Instabilities: The Isotope- and Pressure-Induced Phase Transition in the Quantum Paraelectric NaOH". In: *Phys. Rev. Lett.* 131.12 (2023). URL: https://doi.org/10.1103/physrevlett.131.126101 (cit. on p. 70).

[186] A. L. Samgin. "Lattice-assisted proton hopping in oxides at low temperatures". In: *J. Phys. Chem. Solids* 74.12 (2013), pp. 1661–1668. URL: https://doi.org/10.1016/j.jpcs.2013.05.013 (cit. on p. 71).

[187] A. Luzar and D. Chandler. "Hydrogen-bond kinetics in liquid water". In: *Nature* 379.6560 (1996), pp. 55–57. URL: https://doi.org/10.1038/379055a0 (cit. on pp. 84, 98, 99, 104).

[188] O. Adjoua et al. "Tinker-HP: Accelerating Molecular Dynamics Simulations of Large Complex Systems with Advanced Point Dipole Polarizable Force Fields Using GPUs and Multi-GPU Systems". In: *J. Chem. Theory. Comp.* 17.4 (2021), pp. 2034–2053. URL: https://doi.org/10.1021/acs.jctc.0c01164 (cit. on p. 85).

[189] A. P. Thompson et al. "LAMMPS - a flexible simulation tool for particle-based materials modeling at the atomic, meso, and continuum scales". In: *Comput. Phys. Commun.* 271 (2022), p. 108171. URL: https://doi.org/10.1016/j.cpc.2021.108171 (cit. on p. 86).

[190] G. S. Kell. "Precise representation of volume properties of water at one atmosphere". In: *J. Chem. Eng. Data* 12.1 (1967), pp. 66–69. URL: https://doi.org/10.1021/je60032a018 (cit. on p. 86).

[191] Franz Simon and Gunther Glatzel. "Bemerkungen zur Schmelzdruckkurve". In: *ZAAC* 178.1 (1929), pp. 309–316. URL: https://doi.org/10.1002/zaac.19291780123 (cit. on p. 88).

[192] L. Gašparič, M. Poberžnik, and A. Kokalj. "DFT study of hydrogen bonding between metal hydroxides and organic molecules containing N, O, S, and P heteroatoms: clusters vs. surfaces". In: *Chem. Phys.* 559 (2022), p. 111539. URL: https://doi.org/10.1016/j.chemphys.2022.111539 (cit. on p. 102).